

AD-A145 438

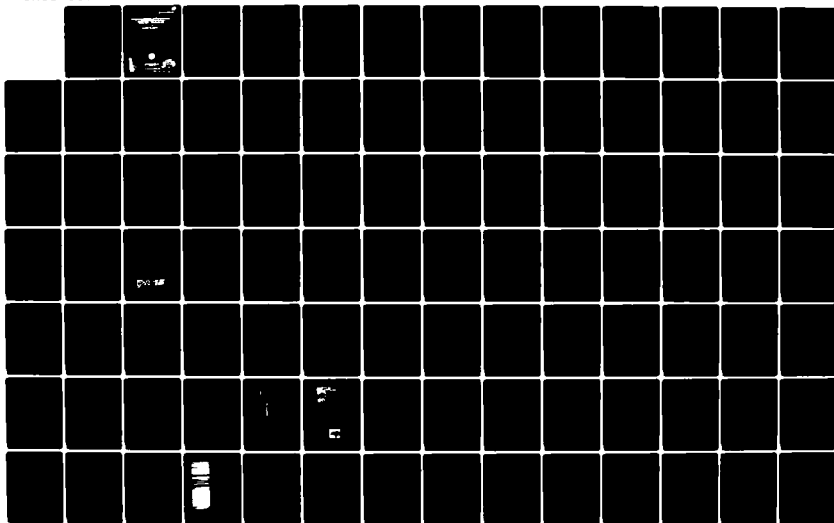
THE USE OF ION IMPLANTATION FOR MATERIALS PROCESSING  
(U) NAVAL RESEARCH LAB WASHINGTON DC F A SMIDT  
23 AUG 84 NRL-MR-5393

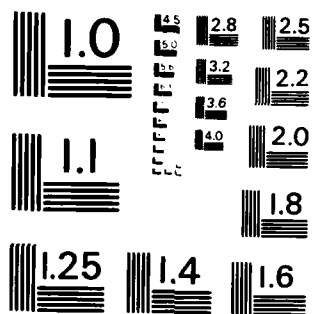
1/2

UNCLASSIFIED

F/G 20/8

NL





MICROCOPY RESOLUTION TEST CHART  
NATIONAL BUREAU OF STANDARDS - 1963-A

AD-A145 438

REPORT DOCUMENTATION PAGE					
1a REPORT SECURITY CLASSIFICATION <b>UNCLASSIFIED</b>			1b RESTRICTIVE MARKINGS		
2a SECURITY CLASSIFICATION AUTHORITY			3 DISTRIBUTION / AVAILABILITY OF REPORT  <b>Approved for public release; distribution unlimited.</b>		
2b DECLASSIFICATION / DOWNGRADING SCHEDULE					
4 PERFORMING ORGANIZATION REPORT NUMBER(S)  <b>NRL Memorandum Report 5393</b>			5 MONITORING ORGANIZATION REPORT NUMBER(S)		
6a NAME OF PERFORMING ORGANIZATION  <b>Naval Research Laboratory</b>		6b OFFICE SYMBOL (If applicable) <b>Code 6670</b>	7a NAME OF MONITORING ORGANIZATION		
6c ADDRESS (City, State, and ZIP Code)  <b>Washington, DC 20375</b>			7b ADDRESS (City, State, and ZIP Code)		
8a NAME OF FUNDING / SPONSORING ORGANIZATION  <b>Office of Naval Research</b>		8b OFFICE SYMBOL (If applicable)	9 PROCUREMENT INSTRUMENT IDENTIFICATION NUMBER		
8c ADDRESS (City, State, and ZIP Code)  <b>Arlington, VA 22217</b>			10 SOURCE OF FUNDING NUMBERS		
			PROGRAM ELEMENT NO (See page ii)	PROJECT NO	TASK NO
			WORK UNIT ACCESSION NO.		
11 TITLE (Include Security Classification) <b>The Use of Ion Implantation for Materials Processing Annual Progress Report for the Period 1 October 1982 — 30 September 1983</b>					
12 PERSONAL AUTHOR(S) <b>Smidt, F. A.</b>					
13a TYPE OF REPORT <b>Progress</b>		13b TIME COVERED FROM <b>10/82</b> TO <b>9/83</b>		14 DATE OF REPORT (Year, Month, Day) <b>1984 August 23</b>	
15 PAGE COUNT <b>191</b>					
16 SUPPLEMENTARY NOTATION					
17 COSATI CODES			18 SUBJECT TERMS (Continue on reverse if necessary and identify by block number)		
FIELD	GROUP	SUB-GROUP	Auger electron spectroscopy Rutherford backscattering Corrosion Ion implantation (Continues)		
19 ABSTRACT (Continue on reverse if necessary and identify by block number)  ➤ An interdisciplinary program on the use of ion implantation for materials processing is being conducted at NRL. This report describes the important factors in ion implantation science and technology and reports progress in the use of ion implantation to modify friction, wear, fatigue, corrosion, optical and magnetic properties of materials.					
20 DISTRIBUTION / AVAILABILITY OF ABSTRACT <input checked="" type="checkbox"/> UNCLASSIFIED/UNLIMITED <input type="checkbox"/> SAME AS RPT <input type="checkbox"/> DTIC USERS			21 ABSTRACT SECURITY CLASSIFICATION <b>UNCLASSIFIED</b>		
22a NAME OF RESPONSIBLE INDIVIDUAL <b>F. A. Smidt</b>			22b TELEPHONE (Include Area Code) <b>(202) 767-4800</b>		22c OFFICE SYMBOL <b>Code 6670</b>

## 10. SOURCE OF FUNDING NUMBERS

PROGRAM ELEMENT NO.	PROJECT NO.	TASK NO.	WORK UNIT ACCESSION NO.
NAVSEA	WR 30827		66-1663-0-2
ONR	RR022-06-42		63-1020-0-3
ONR	RR022-06-42		66-0467-0-3
ONR	RR022-06-42		61-1750-0-3
ONR	RR022-06-42		66-0444-0-3
ONR	RR022-06-42		66-0447-0-3
ONR	RR012-01-42		66-1791-0-3
NAPC 62241N	WF41-401-000		66-0424-A-3
ONR	RR012-01-42		66-0418-0-3
ONR	RR012-01-42		66-1790-0-3
ONR	RR022-06-42		66-1795-0-3
ONR	RR022-06-42		66-0462-0-3

## 18. SUBJECT TERMS (Continued)

Materials processing  
Wear  
Sputtering  
AISI 52100  
Ti-6Al-4V  
M50  
Bearings  
Friction  
Oxidation  
304SS  
9310

SIMS  
Carburization  
Radiation enhanced diffusion  
Cascade mixing  
Preferential sputtering  
Wear testing  
316SS  
Magnetic properties  
HOPG (graphite)  
a-Si  
Co-Cr-WC alloys

Hardness  
Amorphous materials  
Anodic polarization  
Ta  
Cu-Ni alloys  
Surface analysis

Accession For	
NTIS GRA&I	<input checked="" type="checkbox"/>
DTIC TAB	<input type="checkbox"/>
Unannounced	<input type="checkbox"/>
Justification	
By _____	
Distribution/ _____	
Availability Codes	
Dist	Avail and/or Special
A-1	

## CONTENTS

PREFACE - F. A. Smidt .....	vi
SUMMARY .....	1

### RESEARCH PROGRESS

I. ION IMPLANTATION SCIENCE AND TECHNOLOGY	
A. CARBURIZATION OF STEEL SURFACES DURING IMPLANTATION OF Ti IONS AT HIGH FLUENCES .....	11
I. L. Singer	
B. ABSORPTION OF CARBON FROM RESIDUAL GASES DURING Ti IMPLANTATION OF ALLOYS .....	17
I. L. Singer and T. M. Barlak	
C. MODELING OF HIGH FLUENCE TITANIUM ION IMPLANTATION AND VACUUM CARBURIZATION IN STEEL. ....	21
D. Farkas, I. L. Singer, and M. Rangaswamy	
D. BOLTZMANN APPROACH TO CASCADE MIXING .....	29
I. Manning	
E. SURFACE MODIFICATION BY ION BEAM ENHANCED DEPOSITION.....	35
R. A. Kant and B. D. Sartwell.	
F. THE SURFACE BINDING ENERGY FOR A TERNARY ALLOY PRODUCED BY ION IMPLANTATION .....	43
G. W. Reynolds, F. R. Vozzo, R. G. Allas, P. A. Treado and J. M. Lambert	
G. EFFECTS OF NON-NORMAL INCIDENCE ON THE IMPLANTATION OF COPPER WITH GOLD AND TANTALUM .....	49
P. R. Malmberg, R. G. Allas, J. M. Lambert, P. A. Treado, and G. W. Reynolds..	
H. RETENTION OF IONS IMPLANTED AT NON-NORMAL INCIDENCE .....	55
K. S. Grabowski, N.E.W. Hartley, C. R. Gossett, and I. Manning	
I. BINARY COLLISION CASCADE CALCULATION OF SPUTTERING FROM Cu-Ni ALLOYS BY 90 KeV Cu AND Ni IONS .....	63
M. Rosen and R. H. Bassel	

## II. WEAR AND FATIGUE

- A. SURFACE CHEMISTRY AND FRICTION BEHAVIOR OF Ti-IMPLANTED 52100 STEEL ..... 69  
I. L. Singer and R. A. Jeffries
- B. EFFECTS OF IMPLANTATION ENERGY AND CARBON CONCENTRATION ON THE FRICTION AND WEAR OF TITANIUM-IMPLANTED STEEL ..... 75  
I. L. Singer and R. A. Jeffries
- C. WEAR TESTING UNDER HIGH LOAD CONDITIONS ..... 79  
N.E.W. Hartley and J. K. Hirvonen
- D. HARDNESS AS A MEASURE OF WEAR RESISTANCE ..... 89  
W. C. Oliver, R. Hutchings, J. B. Pethica, I. L. Singer and G. K. Hubler
- E. EFFECT OF TITANIUM IMPLANTATION ON THE FRICTION AND SURFACE CHEMISTRY OF A Co-Cr-W-C ALLOY ..... 97  
S. A. Dillich and I. L. Singer
- F. WEAR IMPROVEMENT IN Ti-6Al-4V BY ION IMPLANTATION ..... 107  
R. G. Vardiman

## III. CORROSION AND OXIDATION

- A. AN ELECTROCHEMICAL STUDY OF AMORPHOUS ION IMPLANTED STAINLESS STEELS ..... 115  
C. R. Clayton, Y-F. Wang and G. K. Hubler
- B. MODIFICATION OF THE PASSIVITY OF 316 STAINLESS STEEL BY P AND B IMPLANTATION ..... 123  
C. R. Clayton, Y-F. Wang and G. K. Hubler
- C. MODIFICATION OF THE LOCALIZED CORROSION BEHAVIOR OF AISI 52100 STEEL BY ION IMPLANTATION ..... 135  
C. R. Clayton, W. K. Chan, J. K. Hirvonen, G. K. Hubler and J. R. Reed
- D. ION IMPLANTING BEARING SURFACES FOR CORROSION RESISTANCE.... 151  
R. Valori, D. Popgoshev and G. K. Hubler
- E. HIGH TEMPERATURE OXIDATION OF ION IMPLANTED TANTALUM ..... 161  
E. N. Kaufmann, R. G. Musket, J. J. Truhan, K. S. Grabowski, C. R. Gossett, and I. L. Singer

IV. OTHER EXPLORATORY RESEARCH AREAS

- A. MAGNETIC PROPERTIES OF IRON-IMPLANTED GRAPHITE..... 171  
N. C. Koon, P. Pehrsson, D. Weber, and  
A. I. Schindler
- B. PHYSICAL PROPERTIES OF TWO METASTABLE STATES OF AMORPHOUS  
SILICON ..... 175  
G. K. Hubler, C. N. Waddell, W. G. Spitzer, J. E.  
Fredrickson, and T. A. Kennedy

V. BIBLIOGRAPHY..... 184

## THE USE OF ION IMPLANTATION FOR MATERIALS PROCESSING

Preface - F. A. Smidt

This report is the fifth in a series of Progress Reports on work conducted at the Naval Research Laboratory (NRL) to investigate the use of ion implantation for materials processing. The objective of the program is to develop ion implantation as a viable surface treatment technique for use in applications of interest to the Navy. Attainment of this objective requires both fundamental research to provide an understanding of the physical and metallurgical changes taking place in the implanted region of a material and applications oriented research to demonstrate the benefits of ion implantation.

The work reported here represents a coordinated effort in three divisions at NRL, the Condensed Matter and Radiation Sciences Division (Code 6600), the Chemistry Division (Code 6100) and the Material Science and Technology Division (Code 6300). The work includes in-house basic research conducted under the auspices of the Office of Naval Research, applied research performed for several Navy and DOD sponsors (NAVAIR, NAVSEA) and collaborative work with scientists at other laboratories.

The purpose of this report is to make available in one source the results from all studies at NRL related to the use of ion implantation for materials processing so as to provide a more comprehensive picture of the scope and interrelationship of the research. The report consists of four sections describing the research and a cumulative bibliography of published papers and reports.

THE USE OF ION IMPLANTATION FOR  
MATERIALS PROCESSING

ANNUAL PROGRESS REPORT  
FOR THE PERIOD  
1 OCTOBER 1982 — 30 SEPTEMBER 1983

SUMMARY

I. ION IMPLANTATION SCIENCE AND TECHNOLOGY

Research reported in this section is directed toward a fundamental understanding of the processes and phenomena associated with ion implantation and the development of the technology of ion implantation for materials processing.

A. Carburization Of Steel Surfaces During Implantation Of Ti Ions At High Fluences

I. L. Singer

Auger and nuclear backscattering analyses of ion-implanted steels have shown that surfaces implanted with carbide-forming ions can develop high carbon concentrations well into the implanted layer. A model is presented here in which the residual gases in the vacuum chamber interact with the surface during implantation to carburize the surface. Briefly, (1) implanted Ti ions are "uncovered" by sputtering, (2) they react with residual gases to form surface carbide species, (3) the carbides dissociate, and (4) the carbon atoms diffuse inwards. Composition profiles of steels implanted with Ti ions ( $5-50 \times 10^{16}/\text{cm}^2$  at 55 and 190 keV) were analyzed and shown to support the model. Implications of the vacuum carburization effects on surface alloy chemistry and mechanical properties are discussed.

B. Absorption Of Carbon From Residual Gases During Ti Implantation Of Alloys

I. L. Singer and T. M. Barlak

Secondary ion mass spectrometry (SIMS) has been used to analyze the surface composition of several steel and Ni-plated substrates implanted with Ti ions ( $5 \times 10^{17}$  Ti/cm<sup>2</sup> at 190 keV). SIMS showed clearly the carbonaceous subsurface layer previously reported in Auger and nuclear

Manuscript approved May 25, 1984.

backscattering analyses of Ti-implanted Fe-based alloys. Moreover, substrates implanted in a vacuum which was backfilled with isotopic  $^{13}\text{C}$  gas showed 20 to 50X higher mass 13/ mass 12 ratios for surface concentrations and integrated subsurface doses than substrates implanted in normal vacuum atmospheres at pressures near  $10^{-6}$  Torr. Auger analysis confirmed the subsurface C profile and found no O (<1 at %) below the oxide layer. The experiments provide direct evidence that C atoms can be absorbed from residual gas molecules in a vacuum chamber near room temperatures during implantation of carbide-forming ions.

C. Modeling Of High Fluence Titanium Ion Implantation And Vacuum Carburization In Steel

D. Farkas, I. L. Singer, and M. Rangaswamy

Concentration vs. depth profiles have been calculated for Ti and C in 52100 Ti-implanted steel. Using a computer formalism developed to account for diffusion and mixing processes, as well as sputtering and lattice dilation. A Gaussian distribution of Ti was assumed to be incorporated at each time interval. The effects of sputtering and lattice dilation were then included by means of an appropriate coordinate transformation. C was assumed to be gettered from the vacuum system in a one-to-one ratio with the surface Ti concentration up to a saturation point. Both Ti and C were allowed to diffuse. A series of experimental (Auger) concentration vs. depth profiles of Ti implanted steel were analyzed using the above-mentioned assumptions. A best fit procedure for these curves yielded information on the values of the sputtering yield, range and straggling, as well as the mixing processes that occur during the implantation. The observed values are in excellent agreement with the values predicted by existing theories.

D. Boltzmann Approach To Cascade Mixing

Irwin Manning

The Boltzmann transport equation is used to describe a beam of ions of atomic species 1 bombarding a target modelled as an amorphous mixture of species 2 and species 3 atoms. In a manner familiar in nuclear reactor theory, the method of characteristics is used to integrate the resulting transport equations. An exact expression for the migration flux,  $J_3$ , is obtained in closed form which can be evaluated in terms of a power series in a distance parameter  $s$ . For a slowly varying density of  $\text{N}_3$  atoms, Fick's law is derived as lowest order term of the power series and  $J_3$  is shown to be proportional to the bombarding flux. A closed expression for the mixing parameter in Fick's law is also obtained, which allows a calculation of this quantity for realistic interatomic potentials. A model Kinchin-Pease displacement cascade is proposed, which is expected to allow a reasonable first approximation calculation of the mixing parameter in Fick's law. It is deduced that the mixing parameter will depend sensitively on the lattice displacement energy which provides a physical mechanism for a "chemical effect" in cascade mixing, as well as for the fluence and temperature dependence of cascade mixing.

E. Surface Modification By Ion Beam Enhanced Deposition

R. A. Kant and B. D. Sartwell

Several model experiments were conducted to study sputtering and surface reactions in various combinations of thin film deposition and ion bombardment. Copper films given multiple sequences of Ta implantation and Cu deposition were analyzed using scanning electron microscopy, backscattering, and Auger spectroscopy. Ta retention was 92% following direct implantation while 100% retention was achieved for the same Ta dose if sputtered Cu was replaced during implantation. Lateral migration of Ta and micro-roughness were observed for all cases studied.

F. The Surface Binding Energy For A Ternary Alloy Produced By Ion Implantation

G. W. Reynolds, F. R. Vozzo, R. G. Allas, P. A. Treado and J. M. Lambert

The surface binding energy model proposed by Reynolds for a binary alloy has been extended to a ternary system. From this model extension the steady state atomic surface fractions were calculated for a ternary surface alloy prepared by ion implanting a binary alloy of known composition. These predictions were compared with the results of subsequent ion implantation experiments. The total implantation process was monitored by the observation of light emitted through de-excitation processes from sputtered neutral atoms. Experimental results are reported for a nickel-chromium alloy implanted with 90 keV copper and with tantalum. Rutherford backscattering, particle induced X-ray emission, and Auger surface analysis were used to analyze the composition of the sputtered foils and implanted specimens. The partial sputtering yield for each component, net sputtering yield and surface atomic fractions were determined, and then compared with the predicted values. The different analytical techniques show consistent agreement within experimental error and there is reasonable agreement between the experimental results and the predicted values.

G. Effects Of Non-Normal Incidence On The Implantation Of Copper With Gold And Tantalum

P. R. Malmberg, R. G. Allas, J. M. Lambert, P. A. Treado and G. W. Reynolds

Copper targets were implanted with 125 keV gold and tantalum ions at selected incident angles of the beam relative to the target normal to examine the effect of the incident angle on the sputtering yields, the dose retained in the modified layer, and the atomic surface fractions. Sputtered particles were collected on aluminum foils to measure the angular distribution of the sputtered particles and to determine the partial sputtering yields of the beam and target species. A 1.5 MeV xenon beam implanted markers into the copper targets to determine the average sputtering yield for the surface during the implantation.

Theoretical predictions from a surface binding energy correction model were compared with the experimental results. Although the predictions from the model were not exact, the trends of the data were in agreement with the model. The measured total sputtering yield increases with increasing incident beam angle, and correspondingly, the fluence retained decreases with incident beam angle.

#### H. Retention Of Ions Implanted To High Fluences Into Steel Cylinders

N.E.W. Hartley, K. S. Grabowski, C. R. Gossett and I. Manning

Fixed steel cylinders were implanted by a scanned beam of Ar, Ti, or Ta ions to evaluate the effect of non-normal incidence on the retention of implanted ions. Ions were implanted at 150 keV to fluences up to  $1 \times 10^{18}/\text{cm}^2$ . The cylinders consisted of AISI-M50 and 52100 bearing steels, 304 stainless steel, and Al coated with 160 nm of Fe. Ion retention versus azimuth angle was determined for Ar and Ti implantations by x-ray analysis and for Ta by Rutherford backscattering analysis. Measured retention followed predictions of an analytical model at low ion doses ( $\leq 1 \times 10^{16}/\text{cm}^2$ ) but sometimes deviated from the model at higher fluences, especially for steel cylinders implanted with Ti or Ta ions. This model assumed a constant but angular-dependent sputtering rate during implantation. Experimental results are presented, the analytical model is briefly described, and an explanation for the deviation at higher fluences is proposed.

#### I. Binary Collision Cascade Calculation Of Sputtering From Cu-Ni Alloys By 90 keV Cu And Ni Ions

M. Rosen and R. H. Bassel

The binary collision cascade code MARLOWE was used to calculate the total and elemental sputtering yields, and the angular and energy distributions of sputtered atoms for several Cu-Ni alloys. The calculations were performed as a function of surface composition for the cases of 90 keV Cu and Ni ions striking the alloy targets at normal incidence. The calculations were compared with experimental measurements reported in the literature.

## II. WEAR AND FATIGUE

Research reported in this section involves the application of ion implantation processing to the improvement of surface sensitive mechanical properties such as wear and fatigue, and fundamental investigations of the mechanisms which produce these changes in properties.

#### A. Surface Chemistry And Friction Behavior Of Ti-Implanted 52100 Steel

I. L. Singer and R. A. Jeffries

Auger spectroscopy, EDX, and optical microscopy have been used to analyze the friction and wear behavior of 52100 steel couples, one modified by Ti implantation ( $5\text{-}50 \times 10^{16}/\text{cm}^2$  at 190 keV). A low friction coefficient,  $\mu_k=0.3$ , was measured on surfaces that were carburized by high fluence ( $>16 \times 10^{16}$  Ti/cm<sup>2</sup>) implantation. A fully carburized layer, produced at  $50 \times 10^{16}$  Ti/cm<sup>2</sup>, resisted wear and retained the low friction coupling. Partially carburized layers, produced at 16 and  $20 \times 10^{16}$  Ti/cm<sup>2</sup>, gave an initially low friction coupling  $\mu_k=0.3$ ; but after 6-10 passes, the partially carburized layer was sheared off exposing the underlying Fe-Ti alloy layer, and the friction coefficient rose to  $\mu_k=0.8$ . A high friction coefficient,  $\mu_k=0.8$ , was also measured on initial sliding contact with a surface implanted to a low fluence ( $5 \times 10^{16}$  Ti/cm<sup>2</sup>). High friction is attributed to high adhesion between Fe in the slider and the Fe-Ti alloy found in the surface. Continued sliding contact (in air) against the Fe-Ti surface oxidized the Ti and Fe, and the friction coefficient dropped to a value of  $\mu_k=0.6$ , characteristic of the nonimplanted sliding couples.

#### B. Effects Of Implantation Energy And Carbon Concentration On The Friction And Wear Of Titanium-Implanted Steel

I. L. Singer and R. A. Jeffries

Dry sliding friction and wear measurements were used to evaluate two implantation processes which increase the C concentration in Ti-implanted steels. In the first process, Ti ions were implanted at a low energy (50 keV) in order to enhance the efficiency of vacuum carburization over what is achievable at higher energies (e.g., 190 keV). In the second, a dual implantation process, C ions were implanted into steels already implanted with Ti ions at high energy (190 keV). The first process produced a low friction ( $\mu=0.3$ ), scuff resistant surface at a fluence of  $2 \times 10^{17}/\text{cm}^2$ , 40% lower than the fluence required for similar behavior by 190-keV implants. At fluences of  $2 \times 10^{17}/\text{cm}^2$  each, the dual implantation produced a modest decrease in friction ( $\mu=0.5$ ), accompanied by stick slip, and some wear resistance compared to nonimplanted steel ( $\mu=0.6$ ). Auger spectroscopy and energy-dispersive x-ray analysis were used to analyze the surface composition produced by the two processes at fluences of  $2 \times 10^{17}/\text{cm}^2$ .

#### C. Wear Testing Under High Load Conditions

N.E.W. Hartley and J. K. Hirvonen

The friction and wear behavior of three ion implanted and ion beam mixed steels were investigated under simulated scuffing conditions using a Falex friction and wear tester. The frictional force experienced during wear testing was used to assess the degree of scuffing, and the amount of material worn away was measured on the Falex tester or by

subsequent weight loss determinations. The following ions were evaluated to determine the effects of intermetallic additions (C,N,P), alloy elements (Ti,Cr), and anti-scuff elements (Mo,Ta). In addition some thin (1000 Å) vacuum evaporated layers of Si, V, Ni, Nb, Sn, Mo, Ta and W were prepared and in some cases intermixed with  $N^+$  ions at a fluence of typically  $2 \times 10^{17}/\text{cm}^2$ , to compare with the effects of ion implantation. The 52100 steel (a through-hardened martensitic bearing steel) showed marked improvements after  $Ti^+$  implantation.  $Ta^+$  implantations into 9310 steel (a case-hardened gear steel with 3.0% Ni, 1.4% Cr and 0.55% Mn) reduced the wear rate and scuffing wear. The results are discussed in terms of the probable influence of the various added elements on the metallurgical wear mechanisms of the respective steels.

#### D. Hardness As A Measure Of Wear Resistance

W. C. Oliver, R. Hutchings, J. B. Pethica, I. L. Singer and G. K. Hubler

One measure of the surface mechanical properties of materials can be obtained through microhardness data. The success of microhardness in predicting the improvements in wear resistance of ion implanted metals has been mixed. In this paper the cases of N implantation into 304 S.S. and Ti implantation into 52100 bearing steel are examined. Microhardness data indicates little or no hardness changes whereas large wear rate changes are observed. From these two examples it is clear that the wear mechanism, the chemical nature of the surface, the ductility, and the toughness can be more important than the hardness changes.

#### E. Effect Of Titanium Implantation On The Friction And Surface Chemistry Of A Co-Cr-W-C Alloy

S. A. Dillich and I. L. Singer

The effects of the implantation of titanium ions, to a fluence of  $5 \times 10^{17}$  Ti ions  $\text{cm}^{-2}$  at 190 keV, on the tribological behavior of a centrifugally cast cobalt-based alloy (Stoody 3) were investigated by friction tests against a variety of alloy and carbon counterfaces. Dry sliding friction coefficients were compared with those made on similarly prepared, but non-implanted, and fatty-acid-coated samples. High friction coefficients ( $\mu_k = 0.6$ ) for the alloy-Stoody 3 couples coincided with the formation of debris, with the same composition as the softer of the mating alloys, in the wear scars. Much lower  $\mu_k$  values were measured on titanium-implanted ( $\mu_k = 0.25$ ) and fatty acid-coated ( $\mu_k = 0.1$ ) surfaces. Optical microscopy indicated a change in the surface texture of the implanted surfaces attributable to sputtering. Auger spectroscopy showed that vacuum carburization of both carbide and matrix phases of the Stoody alloy occurred during implantation. The friction and wear mechanisms involved are discussed.

F. Wear Improvement In Ti-6Al-4v By Ion Implantation

R. G. Vardiman

The friction and wear of Ti-6Al-4V are found to be sharply reduced by carbon implantation followed by heat treatment. Optimum wear resistance was developed at 400°C, at which the microstructure of the implanted layer showed a dense array of TiC precipitates up to 60 nm in size. The implanted layer in this case was worn through in a few thousand cycles of the ball on disc test, but by implanting at two energies to achieve a deeper carbide layer, negligible wear was found even after 20,000 cycles. No wear improvement was found for nitrogen implantation.

III. CORROSION AND OXIDATION

Research reported in this section involves the application of ion implantation processing to modify the corrosion and oxidation behavior of surfaces, and fundamental investigations of the mechanisms which produce these changes in properties.

A. An Electrochemical Study Of Amorphous Ion Implanted Stainless Steels

C. R. Clayton, Y-F. Wang and G. K. Hubler

304 and 316 stainless steel were implanted with phosphorous at 40 keV or with boron at 25 keV to a fluence of  $1 \times 10^{17}$  to form amorphous surface alloys. The modification of the corrosion properties of the steels was monitored by dynamic polarization measurements in 0.5M H<sub>2</sub>SO<sub>4</sub> + 0.5M NaCl solutions. Phosphorous was found to reduce the current density at the active-passive transition while Boron was found to increase the pitting potential of both steels.

B. Modification Of The Passivity Of 316 Stainless Steel By P and B Implantation

C. R. Clayton, Y-F. Wang and G. K. Hubler

The nature of the passive films formed on 316 stainless steel (ss) and on amorphous surface alloys formed on 316ss by P and B ion implantation have been studied. The passive films formed on 316ss at +250mV and +550mV (vs SCE) in deaerated 0.5M H<sub>2</sub>SO<sub>4</sub> were found to be crystalline. Under identical conditions the passive films formed on both of the amorphous surface alloys were found to be amorphous. P implantation resulted in self-passivation in 0.5M H<sub>2</sub>SO<sub>4</sub> and 0.5M H<sub>2</sub>SO<sub>4</sub> + 0.5M NaCl, but was less resistant to pitting than 316ss. B implantation, however, had no beneficial effect on the active-passive transition but exhibited a higher pitting resistance than 316ss. An attempt is made to explain the differences in passivity and breakdown of passivity of the two amorphous surface alloys in terms of the composition of their passive films.

C. Modification Of The Localized Corrosion Behavior Of AISI 52100 Steel By Ion Implantation

C. R. Clayton, W. K. Chan, J. K. Hirvonen, G. K. Hubler and J. R. Reed

The pitting resistance of AISI 52100 steel in deaerated 0.01M NaCl (pH 6 buffered) solution was significantly improved following ion implantation with a) Cr, b) Cr + P and c) Ta ions. Cr +P and Ta ion implantation resulted in the formation of amorphous surface alloys. The improvements observed in pitting resistance are discussed in terms of the effect of the ion implantation process on the composition and structure of the carbides and martensitic metal matrix and the nature of the passive films formed on the surface alloys in the Cl<sup>-</sup> solution.

D. Ion Implanting Bearing Surfaces For Corrosion Resistance

R. Valori, D. Popgoshev and G. K. Hubler

A program is currently underway to use ion implantation to improve the tribological and corrosion characteristics of load bearing surfaces in both rolling element bearings and gears used in aircraft propulsion systems. This paper describes that aspect of the program concerned with the use of ion implantation for surface alloying of bearing components in order to alleviate the problem of corrosion in costly M50 steel mainshaft aircraft engine bearings. Results to date indicate that implantation of selected ion species can significantly improve resistance to both generalized and localized (pitting) corrosion without adversely affecting bearing performance or fatigue endurance life.

E. High-Temperature Oxidation Of Ion Implanted Tantalum

E. N. Kaufmann, R. G. Musket, J. J. Truhan, K. S. Grabowski, C. R. Gossett and I. L. Singer

The oxidation of ion implanted Ta in two different high temperature regimes has been studied. Oxidations were carried out at 500°C in Ar/O<sub>2</sub> mixtures, where oxide growth is known to follow a parabolic rate law in initial stages, and at 1000°C in pure O<sub>2</sub>, where a linear-rate behavior is obtained. Implanted species included Al, Ce, Cr, Li, Si and Zr at fluences of the order of 10<sup>17</sup>/cm<sup>2</sup>. Oxidized samples were studied using Rutherford backscattering, nuclear reaction analysis, Auger spectroscopy, secondary-ion mass spectroscopy, X-ray diffraction and optical microscopy. Significant differences among the specimens were noted after the milder 500°C treatment, specifically, in the amount of oxide formed, the degree of oxygen dissolution in the metal beneath the oxide, and in the redistribution behavior of the implanted solutes. Under the severe 1000°C treatment, indications of different solute distributions and of different optical features were found, whereas the overall oxidation rate appeared to be unaffected by the presence of the solute.

#### IV. OTHER RESEARCH AREAS

Research reported in this section includes investigations of ion implantation effects in several areas other than those covered in sections II and III.

##### A. Magnetic Properties Of Iron Implanted Graphite

N. C. Koon, P. Pehrsson, D. Weber, and A. I. Schindler

The magnetic properties of highly oriented pyrolytic graphite (HOPG) implanted with fluences of 25 keV iron atoms ranging from  $10^{16}$  to  $10^{17}$  atoms/cm<sup>2</sup> have been measured. The lowest fluence specimen was paramagnetic down to 2 K, with evidence for clusters of only a few spins, while the highest fluence specimen was clearly ferromagnetic, with magnetization curves resembling those of a set of randomly oriented soft magnetic planes. The critical fluence for formation of a ferromagnetic state appears to be between 1 and  $3 \times 10^{16}$  atoms/cm<sup>2</sup> at 25 keV. These results can be qualitatively understood based on the critical density for percolation of near neighbor exchange interactions.

##### B. Physical Properties Of Two Metastable States Of Amorphous Silicon

G. K. Hubler, C. N. Waddell, W. G. Spitzer, J. E. Fredrickson and T. A. Kennedy

Characterization of the two metastable states of amorphous Si produced by ion implantation were extended to include electron paramagnetic resonance, fundamental absorption edge, and density measurements in addition to infrared reflection. It was found that the properties of the two a-Si states are not dependent upon the mass of the incident ion ( $^{12}\text{C}$ ,  $^{29}\text{Si}$ ,  $^{31}\text{P}$ ,  $^{120}\text{Sn}$ ) or upon the anneal temperature for  $400^\circ\text{C} \leq T_A \leq 600^\circ\text{C}$ . The dangling-bond density decreased by about a factor of 2, the absorption coefficient decreased by more than a factor of 5, but the density did not change when the a-Si went through a transition between the two states.

#### V. BIBLIOGRAPHY

A cumulative bibliography of papers related to ion implantation for materials processing authored or coauthored by NRL staff members is provided.

Section I.A

CARBURIZATION OF STEEL SURFACES DURING IMPLANTATION  
OF Ti IONS AT HIGH FLUENCES

I. L. Singer

Surface Chemistry Branch  
Chemistry Division  
Naval Research Laboratory

This work was supported by the Office of Naval Research.

# Carburization of steel surfaces during implantation of Ti ions at high fluences

I. L. Singer

Chemistry Division (6170), Naval Research Laboratory, Washington, D. C. 20375

(Received 15 November 1982; accepted 22 December 1982)

Auger and nuclear backscattering analyses of ion-implanted steels have shown that surfaces implanted with carbide-forming ions can develop excessively high carbon concentrations well into the implanted layer. A model is presented here in which the residual gases in the vacuum chamber interact with the surface during implantation to carburize the surface. Briefly, (1) implanted Ti ions are "uncovered" by sputtering, (2) they react with residual gases to form surface carbide species, (3) the carbides dissociate, and (4) the carbon atoms diffuse inwards. Composition profiles of steels implanted with Ti ions ( $5\text{--}50 \times 10^{16}/\text{cm}^2$  at 55 and 190 keV) are analyzed and shown to support the model. Carburization occurs at a lower fluence for 55-keV implants than for 190-keV implants, consistent with a nearly energy-independent sputtering yield for Ti into Fe. Implications of the vacuum carburization effects on surface alloy chemistry and mechanical properties are also discussed.

PACS numbers: 81.60.Bn, 82.65.Nz, 61.70.Tm

## I. INTRODUCTION

The ion implantation process is capable of producing virtually any alloy by injecting any ion into a solid surface.<sup>1-3</sup> With the advent of high current implanters, it has become feasible to produce surface alloys with concentrations upwards of 50 at.%. Two consequences of high fluence implantation that have received some attention are the expansion (dilation)<sup>4</sup> and sputtering<sup>5,6</sup> of the implanted surface by incoming ions. A third consequence, only recently discovered, is that the sputtered surface can interact with residual gases in the vacuum system and form unexpected surface alloys. One such alloy was found in Fe and in steel implanted with Ti ions to high influences.<sup>6-8</sup> This alloy had an Fe-Ti-C composition with the unexpected C distributed in a diffusionlike profile from the surface inwards.<sup>6,8</sup> The surface also displayed remarkable tribological<sup>9,10</sup> and chemical<sup>7,12</sup> properties and, in addition, was found to be amorphous.<sup>7,8</sup>

This paper provides a model for the incorporation of C into solid surfaces during high fluence implantation of carbide-forming ions. Composition analyses of Ti-implanted steels are presented in support of the model. Carbon incorporation is attributed to the interaction of the Ti-ion-sputtered surface with residual carbonaceous gas molecules in the vacuum chamber. Auger composition profiles of Ti-implanted steels illustrate the fluence and energy dependence of the carbon incorporation process. This process, because of its analogy with gaseous carburization of steels, will be referred to as vacuum carburization.

## II. EXPERIMENTAL PROCEDURES AND DATA ANALYSIS

### A. Implantation

Implantation of the AISI-52100 steel (Fe-1.5Cr-1C by weight) samples was done with a modified model 200-20A2F Varian/Extrion ion implanter.<sup>6</sup> Disks 0.95 cm in diameter and 0.32-cm thick were heat sunk onto a water-cooled holder and were kept near room temperature ( $< 40^\circ\text{C}$ ) during the implantation. Samples were implanted with 55- or 190-keV

$^{48}\text{Ti}^+$  ions in a target chamber that was cryogenically pumped to pressures of about  $5 \times 10^{-7}$  Torr. The ion beam was scanned electrostatically over the sample holder to give a uniform current density of 10 to  $20 \mu\text{A}/\text{cm}^2$  as measured with a built-in Faraday cup. Several other steels with low carbon content (304SS and 1018) and C-free Fe were also implanted and analyzed.

### B. Chemical analysis

Auger analysis was performed in a UHV chamber equipped with a Perkin-Elmer (PHI) model 545 Auger microprobe, a rasterable ion gun, a Ti sublimator, and liquid nitrogen-cooled cryopanel. The electron gun was operated at 2 kV, with a  $1\text{-}\mu\text{A}$  beam current, rastered over a spot size of  $50 \mu\text{m}$  to reduce the intensity. Auger derivative spectra were recorded either directly or by a peak-height recording multiplexer with a 3-eV modulation amplitude. The ion gun was operated in an Ar atmosphere (about  $5 \times 10^{-8}$  Torr) with a rastered beam of 2-keV  $\text{Ar}^+$  ions, at selected current densities between 2 and  $30 \mu\text{A}/\text{cm}^2$ . Depth profiles were recorded during ion milling with Ti sublimators operating and cryopanel cooled to liquid nitrogen temperature. These procedures reduced contamination of ion-milled surfaces by residual gas vapors to below detectable levels.

Quantitative analysis was performed with the standard normalizing formalism.<sup>13</sup> Auger sensitivity factors  $S$  were obtained from reference samples of known composition<sup>14</sup>; the values are listed in Table I for the principal Auger peaks used to characterize each species (note the shorthand notation, e.g.,  $\text{Ti}_{450}$  meaning the peak-to-peak intensity of the spectrum around 420 eV from Ti Auger electrons). The bulk

TABLE I. Sensitivity factors for Auger peak-to-peak intensities acquired at a modulation amplitude of 3 eV and an energy of 2 keV.

Auger peak	Fe <sub>485</sub>	Cr <sub>575</sub>	Ti <sub>450</sub>	C <sub>285</sub>
S	0.17	0.36	0.48	0.50

C concentration, 4 at.%, was subtracted from the C profile curves in Fig. 1 in order to portray the excess C concentration. In addition, the C-covered oxides present on all surfaces were ignored. Surfaces of steel disks represented in Fig. 1 are actually the metal/oxide interfaces, which are in fact true surfaces during high fluence implantation.

The depth scales for the Auger profiles were established by Michelson interferometry. Auger depth profiles were taken near the edges of partially masked steel surfaces. The depth of an ion-milled step was later measured with a Michelson interferometer to an accuracy of about  $\pm 5$  nm. This procedure gave the depths at which several composition profiles had been terminated. Since no differences were observed in the sputter rates of Ti-implanted and nonimplanted steels, the depth scale was taken to be proportional to milling time.

Energy dispersive x-ray analysis (EDX) was performed with a 20-keV electron beam. At this energy, electrons excite x rays in steel to a depth of about  $1.5 \mu\text{m}$ , which is at least ten times as great as the Ti-implant depth. Hence, the  $\text{Ti}_{K\alpha}/\text{Fe}_{K\beta}$  ratio can be considered proportional to the Ti concentration.

### III. RESULTS AND DISCUSSION

#### A. Titanium and carbon profiles in Ti-implanted steels

Composition versus depth profiles of the near surface region (0–250 nm) of Ti-implanted steels were obtained by Auger electron spectroscopy in conjunction with 2-keV Ar ion milling. Ti profile curves, shown in Fig. 1 for 55 and 190 keV

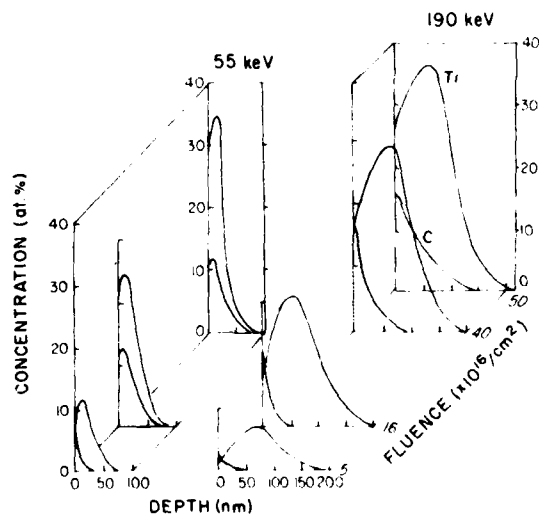


Fig. 1. Concentration vs depth profiles for Ti and C in Ti-implanted 52100 steel at several fluences and energies, (left) 5, 16, and  $40 \times 10^{16} \text{ Ti}^+/\text{cm}^2$  at 55 keV; (right) 5, 16, 40, and  $50 \times 10^{16} \text{ Ti}^+/\text{cm}^2$  at 190 keV. Note bulk C concentration of the steel (4 at.%) was subtracted from data.

implants, evolved from Gaussian-like profiles at low fluences to near sputter-limited profiles at highest fluences. In this fluence regime, an unexpectedly large concentration of C was detected. The profiles are diffusionlike curves, i.e., a high C concentration at or near the surface that falls off into the bulk. (Nondestructive nuclear backscattering analysis was also performed on selected samples and confirmed the diffusionlike C profile.<sup>14</sup> The concentration of carbon [C] in these profiles was independent of the C content of the steel samples, it did have, however, a distinctive dependence on the implantation fluence and energy suggestive of a carburization process.

This dependence of [C] on the Ti fluence and energy can be seen clearly in the composition versus depth profiles appearing in Fig. 1. These profiles were obtained from two sets of 52100 steel samples implanted to fluences of 5, 16, 40, and  $50 \times 10^{16} \text{ Ti}^+/\text{cm}^2$  at energies 55 and 190 keV, respectively. Subsurface [C], barely detectable ( $\sim 1$  at.%) below  $5 \times 10^{16} \text{ Ti}^+/\text{cm}^2$  at 190 keV, rose to a significant fraction of the near surface concentration at a fluence of  $50 \times 10^{16} \text{ Ti}^+/\text{cm}^2$ . At 55 keV, however, [C] comprised a significant fraction of the near surface concentration even at a fluence of  $16 \times 10^{16} \text{ Ti}^+/\text{cm}^2$ . In general, the subsurface C buildup began at lower fluences for lower implantation energies and ultimately saturated at lower fluences for lower energies (compare 16 and  $40 \times 10^{16} \text{ Ti}^+/\text{cm}^2$  for 55 vs 190 keV in Fig. 1). The concentration of C at the surface [C], increased with fluence and energy in the same manner as the subsurface C concentration. This behavior is also expected for a diffusionlike profile.

Ti profiles, as seen in Fig. 1, evolved from Gaussian-like to near sputter-limited curves as the fluence increased. The concentration of Ti at the surface [Ti], also increased with fluence. These concentration profiles are reasonably well understood. Sputtering by Ti ions eroded the sample, placing more and more of the implanted Ti atoms at the inward-moving surface.<sup>5</sup> The [Ti]<sub>s</sub> buildup began at a lower fluence for 55 keV ions than for 190 keV ions (see Fig. 1). This energy dependence reflects the deeper penetration of 190 keV ions than 55 keV ions (projected ranges of 59 and 28 nm, respectively<sup>15</sup>) and not an energy dependence of the sputtering yield.<sup>16</sup>

Sputtering removed much of the Ti in high fluence implants, especially at the 55-keV implantation energy. The retained Ti dose, found by integrating the Ti depth profile curves in Fig. 1, agreed to  $\pm 20\%$  with EDX measurements of the implanted steel surfaces. The shape of the Ti profile at highest fluences suggests that the net removal rate may become less than one atom per ion at high fluences.<sup>4</sup> The subsurface peak in the carbon profiles also suggests that the surface may be expanding outward. These details will be considered in a later paper.

The surface concentrations [Ti]<sub>s</sub> and [C]<sub>s</sub>, therefore, showed similar fluence and energy dependence and, during the early stages of C buildup, were nearly equal in value. Ti and C also bonded chemically at the surface as inferred from Auger line shape analysis. Auger derivative spectra, shown in Fig. 2(a), are representative of spectra obtained from implanted surfaces after ion milling through a thin oxide layer.<sup>17</sup> The line shape of the C(KLL) spectrum is identical to

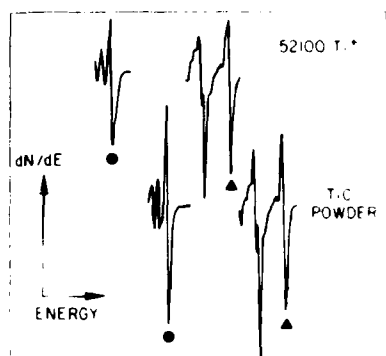


Fig. 2 Auger derivative spectra of C(KLL) and Ti(LMM) energy regions of (upper) Ti-implanted 52100 steel below oxide/metal interface and (lower) ion-milled TiC powder (● indicates 272-eV C peak; ▲, 420-eV Ti peak).

that observed for C(KLL) in TiC,<sup>18</sup> shown in Fig. 2(b), and can easily be distinguished from other forms of carbon,<sup>19</sup> even the carbide present in 52100 steel.<sup>8</sup> The Ti(LMM) spectrum also shows a line shape identical to that observed in TiC,<sup>18</sup> shown in Fig. 2(b). C atoms, therefore, were bonded to Ti atoms at the surface.

The affinity of Ti for C at the surface, the parallel increases of [Ti], and [C], with fluence and energy, and the diffusionlike profile of C can all be explained by a model in which C is gettered from the vacuum chamber by Ti atoms that reach the surface during sputtering. This hypothesis, put forth several years ago,<sup>8</sup> was recently verified.<sup>20</sup> In the experiment, isotopic <sup>13</sup>CO gas was backfilled into a vacuum chamber during Ti implantation of steel surfaces. Secondary ion mass spectroscopy detected <sup>13</sup>C profiles like those shown in Fig. 1 at concentrations two orders of magnitude greater than found in steels implanted without residual <sup>13</sup>CO gas. It has, therefore, been shown that implanted Ti, after sufficient sputtering of the host steel, can getter residual gases from a vacuum chamber. This process will hereafter be referred to as vacuum carburization.

### B. A model for vacuum carburization

Vacuum carburization of Ti-implanted steel can be understood in terms of a four step processes: (1) sputtering uncovers implanted Ti; (2) surface Ti atoms adsorb carbonaceous molecules from residual gases in the vacuum chamber; (3) surface carbide species are formed by dissociation; and (4) surface carbon atoms diffuse inward. Each of these steps will be treated in detail here.

**Sputtering:** During implantation, ions sputter erode the surface in passage to their ultimate resting place. Sputtering is evident in the Ti profiles of Fig. 1, as noted earlier, especially at higher fluences. Ion erosion brings implanted Ti atoms to the surface, the vacuum-solid interface.

**Adsorption:** Once at the surface, Ti atoms are bombarded continually by residual gas molecules present in the vacuum chamber. In chambers routinely opened to air and cycled without baking, carbonaceous gas molecules such as CO and

CO<sub>2</sub> are major constituents of the residual gases.<sup>21</sup> At vacuum pressures of approximately  $p \sim 10^{-6}$  Torr, typical of present day implanters, residual gas molecules strike each surface atom once each second.

Whether or not carbonaceous gas molecules are adsorbed by surface atoms depends on their mutual affinity. Ti is known to have a high affinity for a molecule like CO, and at low surface coverage the sticking probability can be as high as one.<sup>22</sup> To maintain an adsorbed layer, the flux of residual gas molecules which "stuck" must exceed the flux of surface atoms sputtered off. Even under optimal implantation conditions [ $p \sim 1 \times 10^{-6}$  Torr and ion current density  $J = 20 \mu\text{A}/\text{cm}^2$ ], sputtering cannot remove all the adsorbed molecules from surface Ti atoms: for a sputtering yield of  $S = 3$  atoms/ion<sup>16</sup> the erosion flux for  $J = 20 \mu\text{A}/\text{cm}^2$  is  $4 \times 10^{14}$  atoms/ $\text{cm}^2 \text{ s}$ , or 1/3 of the residual gas flux.

**Dissociation:** Adsorbed carbonaceous gas molecules cannot themselves carburize the surface; they must first dissociate forming surface carbide species. In recent years, there have been many surface analytical studies of CO adsorption on Ti, both experimental<sup>19,22</sup> and theoretical,<sup>23</sup> and all have concluded that dissociative adsorption occurs at or above temperatures  $T = 300 \text{ K}$ . Most Auger spectroscopists who have had the occasion to sputter clean reactive metals such as Ti are familiar with the buildup of carbide species adsorbed from residual gases, even in UHV chambers. Moreover, surface carbide species, even under electron and ion bombardment, are quite tenacious unlike surface oxide species, which tend to dissociate and desorb in the presence of electrons (electron stimulated desorption).<sup>24</sup>

**Diffusion:** Surface carbide species are well attached to the surface.<sup>24</sup> They may not desorb, like surface oxide species. They may however dissociate, freeing C atoms to diffuse inwards (as dictated by the thermodynamics). The kinetics of the diffusion problem have not yet been worked out completely; however, the diffusivity of C in Fe at or near room temperature is compatible with measured distances of 100 nm/h.<sup>7</sup>

Several additional effects should be added to this model to account for the profiles obtained in Fig. 1. In addition to sputter eroding the surface, implanted atoms dilate the lattice. The radiation damage produced during implantation can also affect the diffusivity of C in the lattice, so can the presence of implanted Ti, by ternary cross-diffusion effects. Finally, the diffusion equation must be evaluated for a variable surface carbon coverage. Results of such a calculation will be forthcoming.<sup>25</sup>

### C. Other ion-alloy candidates for carburization

The discussion thus far has pertained specifically to implantation of Ti ions. However, as suggested by the model, any carbide-forming ion which produces stable surface carbide species at  $T \sim 300 \text{ K}$  may also lead to a vacuum-carburized surface. Thus, metal ions such as Hf<sup>+</sup>, Zr<sup>+</sup>, Ta<sup>+</sup>, Nb<sup>+</sup>, V<sup>+</sup>, Cr<sup>+</sup>, Mn<sup>+</sup>, and W<sup>+</sup> are potential candidates.<sup>23</sup>

At Naval Research Laboratory, we have observed carburization of a variety of steels (types 52100, 304, M50, 440C, 1018), pure Fe, Ni, and Ta by a variety of ions (Ti<sup>+</sup>, Ta<sup>+</sup>, Cr<sup>+</sup>). Knapp *et al.*<sup>26</sup> have observed carburization of Fe im-

planted with Ti and Chan *et al.*<sup>16</sup> carburization of steel implanted with Cr to high fluences.

Vacuum carburization may also occur when carbide-forming metal surfaces are themselves exposed to radiation in a vacuum. Two examples of surface carbide formation on Ti have already been cited.<sup>17,18</sup> Thomas and Bauer observed carbide formation on Nb surfaces during high temperature ( $T \sim 1000$  K) H irradiation.<sup>17</sup> They speculated that beam-enhanced or beam-induced adsorption and dissociation of residual CO and CO<sub>2</sub> molecules was responsible for carbide formation.

#### D. Implications of vacuum carburization

Vacuum carburization can affect the ion implantation process as well as the chemical and mechanical properties of a sought-after alloy surface. Sputtering produces the erosion by which vacuum carburization occurs. A carburized surface can in turn effect sputtering in several ways: the sputter yields, both atom and ion, will most surely change and the ejection patterns will be different from that of the underlying crystal structure. These may alter not only the retained ion dose and implant profiles but also the information obtainable by metallographic analysis of ion-etched surfaces.<sup>28</sup>

The chemical and mechanical properties of vacuum-carburized surfaces will, of course, be greatly affected. We and others have shown that vacuum-carburized Ti-implanted steel can have much-improved tribological properties,<sup>6,8,11</sup> and dramatically alter corrosion behavior.<sup>12</sup> Microstructures of vacuum-carburized 52100<sup>3</sup> and pure Fe<sup>12</sup> have been shown to be amorphous. It is also quite possible that carburization might have occurred in Ta<sup>12</sup>-implanted Cu which was reported to have produced an amorphous layer at high fluences.<sup>29</sup>

#### IV. SUMMARY AND CONCLUSIONS

Auger composition profiles have demonstrated the dependence that Ti ion fluence and energy exert on the vacuum carburization of steel. A model was presented which accounts for the gettering of carbon from the vacuum system by Ti atoms uncovered during sputtering. Vacuum carburization can produce dramatically different alloys than the intended binary with interesting consequences in chemical and mechanical behavior. Carburization effects should be watched out for when implanting with or into carbide-forming metals or alloys.

#### ACKNOWLEDGMENTS

The author thanks Russ Jeffries for assistance with the Auger analysis and for valuable discussions, Diana Farkas and Irv Manning for discussions on carburization and sput-

tering effects, and NRI's Materials Modification group for implantation.

- <sup>1</sup> *Ion Implantation*, edited by J. K. Hirvonen (Academic, New York, 1980).
- <sup>2</sup> *Ion Implantation Metallurgy*, edited by C. M. Preece and J. K. Hirvonen (Metallurgical Society of AIME, Warrendale, Pennsylvania, 1980).
- <sup>3</sup> *Metastable Materials Formation by Ion Implantation*, edited by S. T. Picraux and W. J. Choyke (Elsevier, Amsterdam, 1982).
- <sup>4</sup> H. Krautle, Nucl. Instrum. Methods **134**, 167 (1976).
- <sup>5</sup> F. Schulz and K. Wittmaack, Radiat. Eff. **29**, 31 (1976).
- <sup>6</sup> C. A. Carosella, I. L. Singer, R. C. Bowers, and C. R. Gossett, *Ion Implantation Metallurgy* (Metallurgical Society of AIME, Warrendale, Pennsylvania, 1980), p. 103.
- <sup>7</sup> J. A. Knapp, D. M. Follstaedt, and S. T. Picraux, *Ion Implantation Metallurgy* (Metallurgical Society of AIME, Warrendale, Pennsylvania, 1980), p. 152; Appl. Phys. Lett. **37**, 330 (1980).
- <sup>8</sup> I. L. Singer, C. A. Carosella, and J. R. Reed, Nucl. Instrum. Methods **182**, 183, 923 (1981).
- <sup>9</sup> I. L. Singer, R. N. Bolster, and C. A. Carosella, Thin Solid Films **73**, 283 (1980).
- <sup>10</sup> I. L. Singer and R. A. Jeffries, J. Vac. Sci. Technol. A (these proceedings).
- <sup>11</sup> F. G. Yost, I. E. Pope, D. M. Follstaedt, J. A. Knapp, and S. T. Picraux, *Metastable Materials Formation by Ion Implantation* (Elsevier, Amsterdam, 1982), p. 261.
- <sup>12</sup> G. K. Hubler, P. Trzaskoma, F. McCafferty, and I. L. Singer, *Ion Implantation into Metals*, edited by V. Ashworth, W. A. Grant and R. P. M. Proctor (Pergamon, Oxford, 1982), p. 24.
- <sup>13</sup> *Handbook of Auger Electron Spectroscopy*, edited by I. E. Davis, N. C. MacDonald, P. W. Palmberg, G. I. Riach, and R. E. Weber (Physical Electronics Industries, Eden Prairie, Minnesota, 1976).
- <sup>14</sup> C. R. Gossett, Nucl. Instrum. Methods **191**, 335 (1981).
- <sup>15</sup> I. Manning and G. P. Mueller, Comp. Phys. Comm. **7**, 84 (1974).
- <sup>16</sup> The sputtering yield of steel by Ti ions with energies 25 to 200 keV is almost constant  $S \sim 2.5 \times 10^{-5}$  if one can extrapolate the yield of Ti from Ar. See: H. H. Anderson and H. I. Bay, in *Sputtering by Particle Bombardment I*, edited by R. Behrisch (Springer, Berlin, 1981), p. 173.
- <sup>17</sup> There is generally some reservation about inferring chemical bonding from ion-eroded surfaces because of potential ion beam effects, e.g., reduction or radiation-enhanced chemistry. However, it would seem that, in the case of ion implantation, the effects of ion erosion do no more than mimic those of ion implantation.
- <sup>18</sup> N. K. Sharma and W. S. Williams, Thin Solid Films **54**, 75 (1978).
- <sup>19</sup> M. P. Hooker and J. I. Grant, Surf. Sci. **62**, 21 (1977).
- <sup>20</sup> I. L. Singer and I. M. Barlak, to be published.
- <sup>21</sup> M. J. Drinkwine and D. Lichtman, *Partial Pressure Analyzers and Analysis*, American Vacuum Society Monograph Series (AVS, New York, 1980), p. 64.
- <sup>22</sup> Y. Fukuda, G. M. Lancaster, I. Honda, and J. W. Rabalais, J. Chem. Phys. **15**, 3447 (1978), and references therein.
- <sup>23</sup> J. B. Benziger, Appl. Surf. Sci. **6**, 105 (1980), and references therein.
- <sup>24</sup> H. J. Mathieu, J. B. Mathieu, D. E. McClure, and D. Landolt, J. Vac. Sci. Technol. **14**, 1023 (1977).
- <sup>25</sup> D. Farkas and I. L. Singer, to be published.
- <sup>26</sup> W. K. Chan, C. R. Clayton, and J. K. Hirvonen, in *Corrosion of Metals Produced by Directed Energy Beams*, edited by C. R. Clayton and C. M. Preece (AIME, New York, 1982), p. 91.
- <sup>27</sup> G. J. Thomas and W. Bauer, J. Vac. Sci. Technol. **12**, 490 (1975).
- <sup>28</sup> I. L. Singer, J. Vac. Sci. Technol. **18**, 175 (1981).
- <sup>29</sup> A. G. Cullis, J. A. Borders, J. K. Hirvonen, and J. M. Poate, Philos. Mag. B **37**, 615 (1978).

Section I.B

ABSORPTION OF CARBON FROM RESIDUAL GASES  
DURING Ti IMPLANTATION OF ALLOYS

I. L. Singer<sup>1</sup>  
T. M. Barlak<sup>2</sup>

<sup>1</sup>Surface Chemistry Branch  
Chemistry Division  
Naval Research Laboratory

<sup>2</sup>Geo-Centers, Incorporated  
Suitland, Maryland 20746

This work was supported by the Office of Naval Research.

# Absorption of carbon from residual gases during Ti implantation of alloys

I. L. Singer

Chemistry Division (6170), Naval Research Laboratory, Washington D. C. 20375

T. M. Barlak

Geo-Centers, Incorporated, Suitland, Maryland 20746

(Received 20 April 1982, accepted for publication 13 June 1983)

Secondary ion mass spectrometry (SIMS) has been used to analyze the surface composition of several steel and Ni-plated substrates implanted with Ti ions ( $5 \times 10^{17}$  Ti/cm<sup>2</sup> at 190 keV). SIMS showed clearly the carbonaceous subsurface layer previously reported in Auger and nuclear backscattering analyses of Ti-implanted Fe-based alloys. Moreover, substrates implanted in a vacuum which was backfilled with isotopic <sup>13</sup>CO gas showed 20 to 50 × higher mass 13/ mass 12 ratios for surface concentrations and integrated subsurface doses than substrates implanted in normal vacuum atmospheres at pressures near  $10^{-6}$  Torr. Auger analysis confirmed the subsurface C profile and found no O (< 1 at. %) below the oxide layer. The experiments provide direct evidence that C atoms can be absorbed from residual gas molecules in a vacuum chamber near room temperatures during implantation of carbide-forming ions. A second possible source of C atoms is also discussed.

PACS numbers: 82.65.My, 81.60.Bn, 61.70.Tm, 82.80.Ms

Anomalous high concentrations (20 at. %) of carbon have been detected in surfaces implanted to high fluences with carbide-forming metal ions.<sup>1-4</sup> Auger depth profile<sup>1,4</sup> and nondestructive nuclear backscattering<sup>2,5,6</sup> analyses of Ti-implanted Fe-based alloys (the most extensively studied system) have revealed a diffusionlike profile of carbon atoms in an amorphous layer which grows inward with increasing fluence. These results have led investigators to speculate that carbon (C) is absorbed from the vacuum chamber during implantation. In this letter we report direct experimental evidence that excess C found in Ti-implanted alloys can originate from residual gas molecules in the implantation vacuum chamber.

The experiment consisted of implanting Ti into substrates exposed to a partial pressure of <sup>13</sup>CO gas, then detecting <sup>13</sup>C atoms in the implanted surface using secondary ion mass spectrometry (SIMS). The <sup>13</sup>C atoms are expected to pass from the gas phase <sup>13</sup>CO molecules to the solid surface by a process we call implant-assisted vacuum carburization.<sup>4</sup> During implantation, incoming ions erode the surface and eventually uncover previously implanted Ti. At the surface, Ti atoms adsorb residual carbonaceous gas molecules, which dissociate to form surface carbide species. These surface carbon atoms in turn migrate inwards during continued implantation bombardment. CO gas was chosen for this experiment because it has a high probability of sticking to Ti at room temperature and dissociatively chemisorbs to form surface carbide species.<sup>7</sup>

Implantation of Ti ions, in NRL's cryopumped Varian/Extrion implanter, is normally performed with the vacuum chamber at pressures from  $1$  to  $4 \times 10^{-6}$  Torr and at current densities of  $J \sim 5$ – $20$   $\mu$ A/cm<sup>2</sup> (Refs. 1 and 3). For the <sup>13</sup>C experiment, the vacuum chamber was pumped overnight and reached a base pressure of  $p = 4 \times 10^{-7}$  Torr. The pressure rose to  $p = 6 \times 10^{-7}$  Torr with the entry of a Ti ion beam (at  $J = 10$   $\mu$ A/cm<sup>2</sup>), then to  $p = 4 \times 10^{-6}$  Torr as <sup>13</sup>CO gas was bled into the chamber. This pressure was maintained

throughout the implantation period by a continuous flow of <sup>13</sup>CO gas.

The sample sets consisted of three polished steel substrates (a high carbon steel, a low carbon steel, and an 18 Cr Ni steel<sup>8</sup> and one Ni-plated substrate. Substrates were pasted to a water-cooled holder (to keep the temperature below 40 °C) then implanted to a fluence of  $5 \times 10^{17}$  Ti/cm<sup>2</sup> at 190 keV. One set was implanted with the <sup>13</sup>CO gas present, a second set at normal vacuum conditions (i.e., without <sup>13</sup>CO gas), and a third set remained nonimplanted.

Composition versus depth profiles of the implanted layer were obtained by Auger electron spectroscopy and SIMS. Auger data were obtained during 2-keV Ar-ion milling with a CMA analyzer with a 3-V modulation voltage and a 2-kV electron beam voltage. SIMS data were acquired on a Cameca ion microscope (Model IMS-300) using a 5.5-keV O<sub>2</sub><sup>+</sup> primary ion beam. The beam was rastered over an area typically  $0.6 \times 0.9$  mm at currents from 500 to 800 nA. The weak positive secondary ion signals of C and O required count times  $100 \times$  longer than the strong positive metal ion signals. All samples were sputter cleaned for 15 s prior to counting to avoid the strong secondary ion peaks resulting from the contaminated oxide surface. The mass 12 intensity is taken to represent <sup>12</sup>C<sup>+</sup> ions. The mass 13 intensity should be principally <sup>13</sup>C<sup>+</sup>, although some CH<sup>+</sup>, also mass 13, may contribute due to the lack of UHV conditions in the SIMS vacuum chamber.

Figures 1(a)–1(c) present selected SIMS profiles for the 18Cr 8Ni steel substrates. The C introduced into the surface by Ti implantation is clearly identified as the mass 12 and mass 13 intensities (i.e., <sup>12</sup>C and <sup>13</sup>C curves) in Figs. 1(a) and 1(b); the cross-hatched and dotted areas indicate the excess C above steady-state values. The excess C concentration found in the nonimplanted substrates [Fig. 1(c)] is quite small, albeit exaggerated by the logarithmic scale; it probably resulted from beam mixing of carbonaceous overlayers found on all surfaces. Both excess carbon curves, <sup>12</sup>C and <sup>13</sup>C, fall to

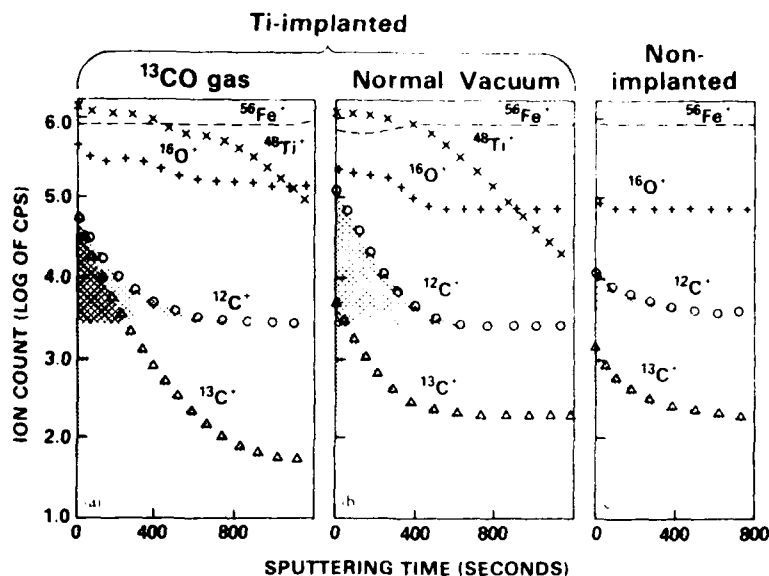


FIG. 1. Positive secondary ion spectra from 18Cr/8Ni steel substrates obtained with 5 keV  $O^+$  beam at current density  $J = 100 \mu A/cm^2$ . (a) Ti implanted in partial pressure of  $^{13}CO$  gas,  $J = 100 \mu A/cm^2$ ; (b) Ti implanted in normal vacuum,  $J = 90 \mu A/cm^2$ ; (c) nonimplanted,  $J = 90 \mu A/cm^2$ .

steady-state (bulk) values with diffusionlike tails, consistent with Auger results (shown below). The steady-state mass 13/mass 12 ratio, however, is less than one-half of the expected isotopic  $^{13}C/^{12}C$  ratio (1.99); we believe that  $CH^+$  may have contributed to the mass 13 intensity.

Figure 1(a) provides direct evidence for the adsorption of C from the gas phase. It shows a much greater proportion of  $^{13}C$  than Fig. 1(b) (the substrate implanted without  $^{13}CO$  gas): the mass 13/mass 12 intensity ratio at the surface, approximately 1:1, is more than 30% greater, and the integrated mass 13/mass 12 dose ratio is approximately 40% greater. Similar ratio values were obtained from the two other steel samples.

The Ni substrates also had excess C after Ti implantation and enhanced mass 13/mass 12 ratios for the substrate implanted in the presence of  $^{13}CO$  gas, as shown in Fig. 2. There were, however, two differences in the spectra of Ti-implanted Ni and Ti-implanted steels. First, more excess C was found in the steels than in the Ni, despite identical implantation conditions and similar Ti concentration profiles. This difference, indicated by the mass 12 or mass 13 to mass 48 ratios in Figs. 1 and 2, has also been verified by Auger composition versus depth profiles (not shown). Vacuum carburization, however, is a complicated interplay of sputtering, chemisorption, and diffusion (probably radiation enhanced), and factors affecting the carburization rates of different metals are not understood. For example, Cr atoms on the 18Cr/8Ni steel surface might provide a second site for C adsorption, thereby enhancing the C absorption rate. A second difference was that the mass 13/mass 12 ratio in the  $^{13}CO$ -on-Ni substrate reached three, but was never more than one for the  $^{13}CO$ -on-steel substrates.

One of the unanswered questions of the SIMS analysis

is why the mass 13/mass 12 is not greater than observed. If the  $^{13}CO$  gas pressure was (as measured) seven times greater than the background pressure and  $^{13}CO$  has a sticking coefficient as high as any other residual gas species (as expected), then the  $^{13}C/^{12}C$  ratio should be at least 7:1. We assume that the ionization yields of  $^{12}C$  and  $^{13}C$  are the same, and we verified that the gas bottle contained 99 mol %  $^{13}CO$ . One possible explanation for the lower ratio is that a large flux of neutral low-energy contaminant molecules (e.g.,  $CO$ ,  $CO_2$ ,  $CH_4$ ) may have "streamed" along with the ion beam. A large increase in the local pressure at the target would be mea-

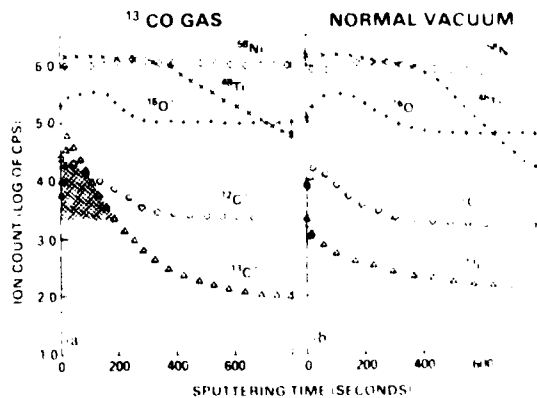


FIG. 2. Positive secondary ion spectra from Ni-plated substrates and  $^{13}CO$  gas implanted with Ti ions: (a) in partial pressure of  $^{13}CO$  gas, (b) in normal vacuum.

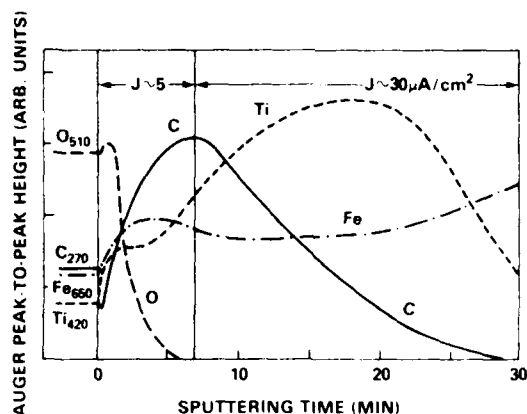


FIG. 3 Auger depth profile of 18Cr8Ni steel implanted with Ti in the presence of  $^{13}\text{CO}$  gas. Note change in sputtering current densities from  $J \sim 5 \mu\text{A}/\text{cm}^2$  initially to  $J \sim 30 \mu\text{A}/\text{cm}^2$  beyond the metal oxide interface.

sured as a small increase in the overall chamber pressure; this "streaming" may account for the rise in background pressure from  $4 \times 10^{-7}$  to  $6 \times 10^{-7}$  Torr when the Ti $^{+}$  beam was turned on.

The relative concentrations of C to O absorbed during Ti implantation in  $^{13}\text{CO}$  gas were obtained from Auger depth profiles of the steel and Ni substrates. Figure 3 presents selected Auger depth profiles of the near surface region of the 18Cr8Ni steel analyzed in Fig. 1(a). The surface oxide/metal interface was profiled slowly ( $J \sim 5 \mu\text{A}/\text{cm}^2$ ) with a 2-keV  $\text{Ar}^{+}$  ion beam. The C signal rises to near maximum value at the oxide/metal interface, where the O signal from the oxide layer falls to negligible intensity (less than 1 at. % concentration). The remaining profile, taken at a faster rate

( $J \sim 30 \mu\text{A}/\text{cm}^2$ ), shows C falling off with a diffusionlike tail and O never reappearing. Therefore, only the C, not the O, is selectively absorbed during the implant-assisted vacuum carburization process.

The main finding of this experiment is that excess carbon in the Ti-implanted surface originated from residual gases in vacuum system. We have shown here that vacuum carburization can occur in Ni as well as Fe alloys, and the C but not O is absorbed. Recently, one of us (ILS) has reported that Cr and Ta implants also carburize metals and suggested that carburization should occur for any strong carbide former implanted to high fluences (Ref. 4, see also Ref. 2). Implant-assisted vacuum carburization is expected to occur so long as the incident flux of residual gas molecules is greater than the sputtering rate by the ion beam. This hypothesis is now being tested at NRL by performing implantations at high dose rates in a UHV chamber, with and without  $^{13}\text{CO}$  gas. These investigations should also reveal whether contaminant streaming contributes to implant-assisted carburization in high vacuum.

We thank Russ Jeffries for assistance with sample preparation and Auger analysis, Bob Olfsky and Randy Walker for assisting with the implantation, and Dave Baldwin and Wayne Rabalais for discussion about streaming contamination.

<sup>1</sup>C. A. Carosella, I. L. Singer, R. C. Bowers, and C. R. Gossett, in *Ion Implantation Metallurgy*, edited by C. M. Preece and J. K. Hirvonen (Metallurgical Society of AIME, Warrendale, PA, 1980), p. 103.

<sup>2</sup>J. A. Knapp, D. M. Follstaedt, and S. T. Picraux Appl. Phys. Lett. **37** (1980) 330; see also in *Ion Implantation Metallurgy*, edited by C. M. Preece and J. K. Hirvonen (Metallurgical Society of AIME, Warrendale, PA, 1980), p. 152.

<sup>3</sup>I. L. Singer, C. A. Carosella, and J. R. Reed, Nucl. Instrum. Methods **182**, 183, 923 (1981).

<sup>4</sup>I. L. Singer, J. Vac. Sci. Technol. A **1**, 419 (1983).

<sup>5</sup>C. R. Gossett, Nucl. Instrum. Methods **191**, 335 (1981).

<sup>6</sup>G. K. Hubler, Nucl. Instrum. Methods **191**, 101 (1981).

<sup>7</sup>M. P. Hooker and J. T. Grant, Surf. Sci. **62**, 21 (1977).

<sup>8</sup>The high carbon steel was type 52100 (Fe1.5Cr1C), the low carbon steel was type 1018 (Fe0.2C), the 18Cr8Ni steel was type 304 (Fe18Cr8Ni0.06C), all given in wt. %.

Section I.C

MODELING OF HIGH FLUENCE TITANIUM ION IMPLANTATION  
AND VACUUM CARBURIZATION IN STEEL

D. Farkas, and M. Rangaswamy<sup>1</sup>  
I. L. Singer<sup>2</sup>

<sup>1</sup>Department of Materials Engineering  
Virginia Polytechnic Inst. & State University  
Blacksburg, VA 24061

<sup>2</sup>Surface Chemistry Branch  
Chemistry Division  
Naval Research Laboratory

Funding for this work was provided by Virginia Polytechnic Institute and State University<sup>1</sup> and by the Office of Naval Research<sup>2</sup>.

## MODELING OF HIGH FLUENCE TITANIUM ION IMPLANTATION AND VACUUM CARBURIZATION IN STEEL

D. Farkas<sup>\*</sup>, I. L. Singer<sup>\*\*</sup>, and M. Rangaswamy<sup>\*</sup>

<sup>\*</sup>Department of Materials Engineering, VPI & SU, Blacksburg, VA 24061

<sup>\*\*</sup>Chemistry Division, Code 6170, Naval Research Laboratory, Washington, DC 20375.

### ABSTRACT

Concentration vs. depth profiles have been calculated for Ti and C in 52100 Ti-implanted steel. A computer formalism was developed to account for diffusion and mixing processes, as well as sputtering and lattice dilation. A Gaussian distribution of Ti was assumed to be incorporated at each time interval. The effects of sputtering and lattice dilation were then included by means of an appropriate coordinate transformation. C was assumed to be gettered from the vacuum system in a one-to-one ratio with the surface Ti concentration up to a saturation point. Both Ti and C were allowed to diffuse. A series of experimental (Auger) concentration vs. depth profiles of Ti implanted steel were analyzed using the above-mentioned assumptions. A best fit procedure for these curves yielded information on the values of the sputtering yield, range and straggling, as well as the mixing processes that occur during the implantation. The observed values are in excellent agreement with the values predicted by existing theories.

### INTRODUCTION

Ions implanted to high fluences ( $> 10^{17}/\text{cm}^2$ ) in metals are capable of creating unique alloys with remarkable mechanical and chemical properties. An example of such an alloy is the wear-resistant amorphous layer formed when Ti is implanted into 52100 steel (1). This layer forms by adsorbing carbon from residual gases in the vacuum chamber (2), assisted by Ti atoms which reach the surface by sputter erosion during implantation.

The present paper describes a computational method for modeling high fluence implantation and presents calculated Ti and C depth profiles which mimic those observed for the above mentioned Ti implantation into 52100 steel. The model accounts for ion collection, sputtering and lattice dilation in a manner similar to the earlier treatments by Schultz and Wittmaak (3) and Krautle (4).

It also considers the diffusion-like transport processes which affect the shape of the evolving profiles and incorporates the vacuum carburization process elucidated by Singer (2). The formalism is based on a numerical solution of the coupled diffusion equations for implanted Ti and adsorbed C. Effective diffusivities for the two species and sputtering yield by Ti ions were obtained by comparison of the calculated and experimental profiles. The experimental data modeled in the present work were obtained by Singer (2).

### THEORETICAL CONSIDERATIONS

The profile of Ti implanted to high fluences is affected by four processes:

- o Ion collection, with a Gaussian distribution

Presented at the Materials Research Society Symposium, Boston, MA, November 1983.

- o Sputter erosion of the surface
- o Lattice dilation as a result of ion collection
- o Diffusion-like broadening resulting from the collision cascades or radiation-enhanced diffusion.

The adsorbed C profiles are affected by two processes:

- o Surface buildup of C as a function of time
- o Diffusion-like penetration

The term "diffusion-like" is used here to denote transport processes that obey Fick's second law (5) which represents thermal and radiation-enhanced diffusion, as well as cascade mixing (6). The diffusion equations were solved for  $D_{Ti}$  and  $D_C$  values which best fit all the experimental curves.

In these calculations  $D_{Ti}$  and  $D_C$  were approximated as constants, as suggested by the calculations of Eltoukhy et al. (7). Non-zero values for  $D_{Ti}$  indicate the relative importance of diffusion-like mixing under the conditions of implantation studied. We emphasize that both  $D_C$  and  $D_{Ti}$  should be considered as effective diffusivities, since they may result from processes other than thermally activated diffusion. The boundary condition is the surface carbon concentration as a function of time, taken from the model for vacuum carburization presented by Singer (2). The model predicts a surface concentration of C that is proportional to the amount of Ti exposed at the surface. As a first approximation it can be assumed that every exposed Ti atom adsorbs a C atom. This assumption is justified by the experimental data for surface contents up to concentrations around 16 at% where there appears to be a saturation of the adsorbed carbon. Therefore, the boundary condition used is that, at the surface, the C and Ti concentrations are equal.

The diffusion equations were solved by a finite difference technique, the Crank-Nicholson method (5,8). At each time step of the calculation a Gaussian distribution of collected Ti was added to the existing profile, which was initially zero. Also, the C concentration at the surface,  $[C]^s$ , was made equal to the Ti concentration for every time increment. In addition, at each time step coordinate transformations were performed that accounted for the sputter erosion of the surface and the lattice dilation.

## RESULTS

The formalism described requires the input of the following parameters:

- o Range and range straggling of Ti ions in steel. These values were obtained from calculations done using LSS theory as described in the Manning and Mueller procedure (9).
- o Flux of the incoming ions which can be obtained from the experimental conditions as fluence per unit time,  $f$ . The Ti flux is converted to added thickness per unit time, using the atomic density of the 52100 steel. ( $f = 9.26 \times 10^{13}$  at/sec  $cm^2$ ,  $n_o = 8.21 \times 10^{22}$  at/ $cm^3$ )
- o Effective diffusivity of C, which was varied in order to obtain a good fit with the experimental C profiles.
- o Effective diffusivity of Ti, which was varied in order to obtain the best fit to the experimental Ti profiles.
- o Sputtering yield ( $S$ ), which can be obtained directly from the experimental data by considering the total area under the profiles. As an additional confirmation the sputtering yield was allowed to vary in a best fit procedure to the experimental profiles. This was done simultaneously with the variation of the Ti diffusivity.

The effect of lattice dilation was found to be very important. Calculations were done without lattice dilation, and it was observed that the only way to get agreement with experimental values was to use a range and range straggling that are very much different from the ones predicted by the

Manning and Mueller formalism. For 190 keV a good fit without the lattice dilation effect required values of  $R_p = 900 \text{ \AA}$  and  $\Delta R_p = 500 \text{ \AA}$ , which are almost double of the LSS values ( $R_p = 590 \text{ \AA}$  and  $\Delta R_p = 230 \text{ \AA}$ ).

Since this discrepancy is unlikely it was concluded that the lattice dilation effect is absolutely necessary to describe high fluence ion implantation profiles.

The next series of calculations included the lattice dilation effect but did not consider a diffusion-like process for Ti. It was observed that the calculated curves were consistently narrower than the experimental ones. This suggested that a diffusion-like process is indeed necessary to account for the observed results. When both diffusion and lattice dilation were included in the calculations, only one combination of  $S$  and  $D_{Ti}$  values resulted in Ti profiles that fit all the seven measured profiles. These values were  $D_{Ti} = 6 \times 10^{-15} \text{ cm}^2/\text{sec.}$  and  $S = 2.0$ .

The sensitivity of the profiles to the value of  $S$  can be seen in Fig. 1 for six of the seven experimental curves studied. (The profile for 190 keV at lowest fluence of  $5 \times 10^{16}$  was found to be insensitive to the variation of the parameters of interest and therefore is not shown). Fig. 1 shows calculated and experimental Ti vs. depth profiles for 3 fluences at each of two energies. As expected, the effect of increasing sputtering yield is to move the profiles closer to the surface. The value of  $S$  that best describes the experimental curves seems to decrease from a value somewhat greater than 2.0 to a value less than 2.0 as the fluence increases. This is consistent with the value of 1.9 derived directly from experimental data. The results of Fig. 1 were calculated for a Ti effective diffusivity of  $6 \times 10^{-15} \text{ cm}^2/\text{sec.}$

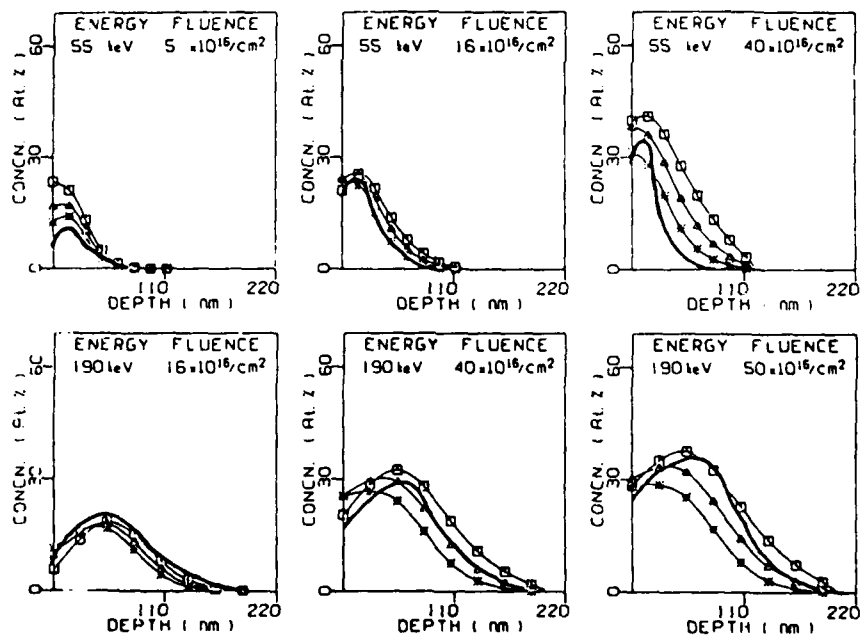


Fig 1 Experimental (heavy line) and calculated Ti profiles for several values of  $S$  [ $\square$  - 1.0,  $\Delta$  - 2.0,  $*$  - 3.0], with  $D_{Ti} = 0.6 \times 10^{-14} \text{ (cm}^2/\text{s)}$ .

The sensitivity of the calculated profiles to the value of  $D_{Ti}$  is shown in Fig. 2. This figure shows calculations done for a sputtering yield of 2.0. These results include the ones obtained in the absence of diffusion broadening, showing that the experimental data are consistently broader. A value of  $D_{Ti}$  different from zero results in better agreement with experiment. An order of magnitude estimate of the transport process present can be obtained from these figures which is approximately,  $D_{Ti} = 6 \times 10^{-15} \text{ cm}^2/\text{sec}$ .

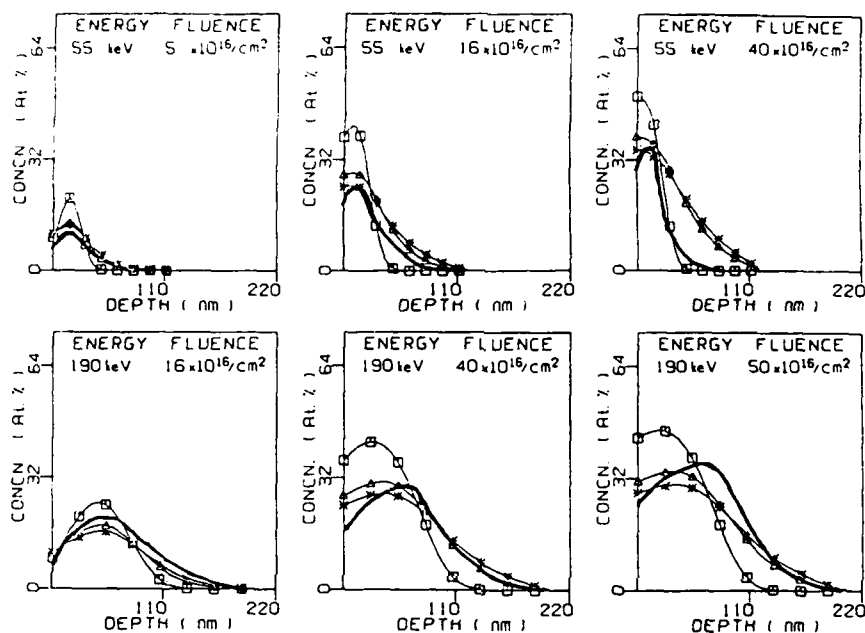


Fig 2 Experimental (heavy line) and calculated Ti profiles for several values of  $D_{Ti}$  [ $(\times 10^{-14} \text{ cm}^2/\text{s}) = -0.0, \Delta - 0.6, * - 1.0$ ], with  $S=2.0$ .

Fig. 3 shows the calculated carbon concentration profiles compared to experiment. In this figure calculations are presented for different values of  $D_C$ , with  $[C]^s$  restricted to  $\leq 16 \text{ at}\%$ . As an order of magnitude estimate it may be concluded that the value of the effective diffusivity of carbon is around,  $D_C = 6 \times 10^{-15} \text{ cm}^2/\text{sec}$ .

#### DISCUSSION

The calculated composition vs. depth profiles are in good agreement with the experimentally determined profiles for high fluences of Ti implanted into steel. The computational method described takes into account the effect of sputtering and lattice dilation, as done by previous investigators. In addition, it is able to describe diffusion-like processes. Other phenomena may also be present in high fluence ion implantation, namely preferential sputtering and radiation induced segregation. The agreement between experimental and calculated profiles that was obtained in the present work suggests that these effects are not very significant in the case studied.

Several conclusions about the implantation alloying process can be drawn from the results of the present work. First, the lattice dilation and

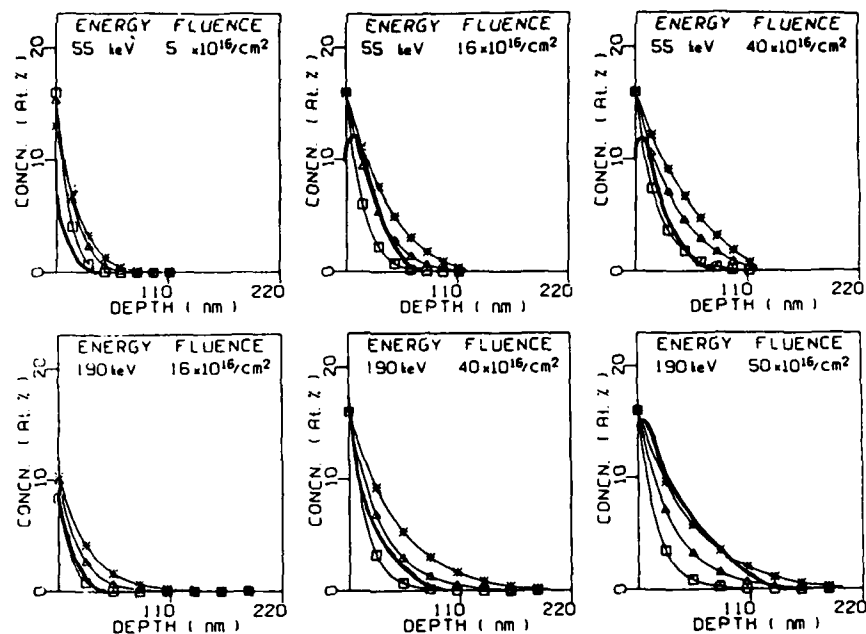


Fig 3 Experimental (heavy line) and calculated C profiles for several values of  $D_C$  [ $\times 10^{-14} \text{ cm}^2/\text{s}$ ]  $\square$  - 0.3,  $\Delta$  - 0.6,  $*$  - 1.0 ], with  $S=2.0$ .

the sputter erosion of the surface must be included in order to obtain reasonable agreement with experiment based on the values for range and straggling given by LSS theory.

Second, the sputtering yield of steel by Ti atoms is approximately 2.0 at fluences below those needed to form a carburized surface, but less than two at higher fluences. A sputtering yield of  $2.5 \pm .5$  has been measured for Ar in Fe and stainless steel targets (10). It is possible that the sputtering yield of Ti is lowered when it is bonded to C. It is even possible that the anomalous dips in the self sputtering yield of reactive metals (V, Ti, Zr, Nb, Hf, Ta) presented by Almen and Bruce (11) over twenty years ago are attributable to carburization effects.

Third, the broadened profiles obtained experimentally can be understood in terms of an effective diffusivity for Ti of  $D_{Ti} = 6 \times 10^{-15}$

$\text{cm}^2/\text{sec}$ . Since this diffusivity occurs thermally at  $580^\circ\text{C}$  (12) it is clear that the diffusivity observed in the present problem is implantation-induced. For typical implantation conditions the effective diffusivity due to collision cascades is known to be of this order of magnitude (13). Furthermore, if following Myers, the effective diffusion coefficient is calculated on the basis of the Kinchin-Pease relation (6) the value obtained is of the same order of magnitude as the one obtained by using the parameters of the present problem.

Finally, a diffusion-like process accounts nicely for the inward migration of C into steel during Ti implantation. The assumption of a saturation value for the C adsorbed on the surface, which resulted in better agreement with experiment, is reasonable for a sputtered surface.

The present model cannot definitely identify the mechanism of the observed effective diffusion of C,  $6 \times 10^{-15} \text{ cm}^2/\text{sec}$ . Three processes can contribute to this effective diffusivity value. These are thermal (non-enhanced) diffusion, radiation enhanced thermal diffusion and cascade

mixing. The thermal diffusion of C in Fe at the sample temperature ( $40^{\circ}\text{C}$ ) is  $10^{-16} \text{ cm}^2/\text{sec}$ . (14), and therefore contributes only 2% of the migration process. A recent Montecarlo type calculation for the collision cascade effect during the carburization of Cr implanted Cr could not account for the majority of the C adsorbed as observed experimentally (15). It appears that in the present case both collision cascades and radiation-enhanced diffusion may contribute to the inward migration of C, although the latter may be more significant. The chemical affinity of C for Ti might also enhance C diffusion.

### CONCLUSIONS

The formalism developed permits quantitative evaluation of several of the dynamic processes present in high fluence reactive ion implantation. For the case of Ti implanted into 52100 steel the following can be concluded: the sputtering yield decreases from a value greater than 2.0 to a value smaller than 2.0 as fluence increases, probably due to the incorporation of carbon with increasing fluence.

It is necessary to account for some mixing process for Ti in order to explain the experimental results. Alternatively a range and straggling that are very different from those predicted by LSS theory have to be assumed. The order of magnitude of this mixing process is characterized by a value of  $D_{\text{Ti}} = 6 \times 10^{-15} \text{ cm}^2/\text{sec}$ , which is consistent with a cascade mixing mechanism.

The mixing process responsible for C penetration can be described by Fick's law and is characterized by an effective diffusion coefficient of  $D_{\text{C}} = 6 \times 10^{-15} \text{ cm}^2/\text{sec}$ . It appears that both radiation enhanced diffusion and cascade mixing contribute to the inward migration of C. The amount of C adsorbed at the surface can be adequately described by a one to one relation with the amount of Ti at the surface up to a certain saturation limit around 16 at. % carbon.

### REFERENCES

1. I. L. Singer, C. A. Carosella, and J. R. Reed, Nucl. Instr. Methods, **182/183**, 923 (1981).
2. I. L. Singer, J. Vac. Sci. Technology, A, **1**, 419 (1983).
3. F. Schulz and K. Wittmaak, Radiat. Eff., **29**, 31 (1976).
4. H. Krautle, Nucl. Instrum. Methods, **134**, 167 (1976).
5. Cranck, "The Mathematics of Diffusion" (Clarendon press, Oxford, 1975).
6. S. M. Myers, Nucl. Instr. Methods, **168**, 265 (1980).
7. A. H. Eltoukhy and J. E. Greene, J. Appl. Phys., **51**, 4444 (1980).
8. A. R. Mitchell, "Computational Methods in Partial Differential Equations", (J. Wiley and Sons, New York 1976) Chapt. 2.
9. I. Manning and G. P. Mueller, Comp. Phys. Comm., **7**, 84 (1974).
10. H. H. Andersen and H. L. Bay, in "Sputtering by Particle Bombardment I", edited by R. Behrisch (Springer Verlag 1981), p. 173.
11. O. Almen and G. Bruce, Nucl. Instr. and Meth., **11**, 257 (1961).
12. Swisher, Trans. AIME, **242**, 2438 (1968).
13. G. Dearnaley, J. H. Freeman, R. S. Nelson, and J. Stephen, "Ion Implantation", (North Holland, Oxford, 1973), p. 228.
14. Smithells, "Metals Reference Book", 3rd edition (Butterworths, Washington, 1962), p. 594.
15. R. H. Bassel, K. S. Grabowski, M. Rosen, M. L. Roush, and F. Davarya, to be published.

Section I.D

BOLTZMANN APPROACH TO CASCADE MIXING

I. Manning

Materials Modification & Analysis Branch  
Condensed Matter & Radiation Sciences Division  
Naval Research Laboratory

This work was supported by the Office of Naval Research.

# BOLTZMANN APPROACH TO CASCADE MIXING

Irwin Manning  
Naval Research Laboratory, Washington, DC 20375

## ABSTRACT

The Boltzmann transport equation is used to describe a beam of ions of atomic species 1 (1-atoms) bombarding a target modelled as an amorphous mixture of 2-atoms and 3-atoms. In a manner familiar in nuclear reactor theory, the method of characteristics is used to integrate the resulting transport equations. An exact expression for the migration flux  $J_3$  of 3-atoms is obtained in closed form. This expression can be evaluated in terms of a power series in a distance parameter  $s$ . For the case of slowly varying density  $N_3$  of 3-atoms, Fick's law, relating  $J_3$  to the gradient of  $N_3$ , is derived from this expression; it is given by the lowest order term of the power series.  $J_3$  is shown to be proportional to the bombarding flux. Concomitantly, a closed expression for the mixing parameter in Fick's law is obtained, which allows a calculation of this quantity for realistic interatomic potentials. A model Kinchin-Pease displacement cascade is proposed, which is expected to allow a reasonable first approximation calculation of the mixing parameter in Fick's law. It is deduced that the mixing parameter will depend sensitively on the lattice displacement energy. This dependence constitutes a physical mechanism for chemical effect in cascade mixing, as well as for fluence and temperature dependence of cascade mixing.

## INTRODUCTION

Haff and Switkowski [1] have proposed a model for cascade mixing in which atomic migration under ion bombardment derives from a mechanism somewhat similar to that of gaseous diffusion driven by concentration gradients. Matteson [2] has examined this process from the point of view of the theory of random flights. In the present work, we propose to discuss this process on the basis of the Boltzmann transport equation.

## REVIEW OF LINEAR TRANSPORT THEORY

It is assumed that the target can be modelled as being amorphous, and that all atomic interactions take place through uncorrelated binary atomic collisions. It is further assumed that, in all atomic collisions, one of the atoms is at rest in the laboratory frame. Consider the case of a beam of atomic species 1 bombarding a target of atomic species 2 containing an impurity of atomic species 3, and let  $\psi_\alpha(\vec{r}, \vec{v}, t) d^3r d^3v$  be the number of atoms of atomic species  $\alpha$  ( $\alpha = 1, 2$ , or 3) located at time  $t$  in space  $d^3r$  about  $\vec{r}$  and having velocity  $d^3v$  about  $\vec{v}$ . Correspondingly,  $\int \psi_\alpha(\vec{r}, \vec{v}, t) \cdot \vec{n} dS d^3v dt$  is the number of  $\alpha$ -atoms (particles of atomic species  $\alpha$ ) with velocity  $d^3v$  around  $\vec{v}$  crossing an element of area  $dS$  with unit normal  $\vec{n}$  in time  $dt$  around  $t$ . Let  $\sigma_{\beta\alpha}(\vec{v}' \rightarrow \vec{v}; \vec{r}) \psi_\beta(\vec{r}, \vec{v}', t) d^3v' d^3r dt$  be the number of  $\alpha$ -atoms emitted into the phase space region  $d^3r d^3v$  about  $\vec{r}$  and  $\vec{v}$  in time  $dt$  due to collisions in which a  $\beta$ -atom of velocity  $d^3v'$  about  $\vec{v}'$  collides with an  $\alpha$ -atom. It follows from these definitions that [3]

$$\sum_\alpha \int \sigma_{\beta\alpha}(\vec{v}' \rightarrow \vec{v}; \vec{r}) d^3v = \sigma_\beta(\vec{v}; \vec{r}), \quad (1)$$

where  $\sigma_\beta$  is the total cross section for  $\beta$ -atoms; that is, the reciprocal mean-free path of these atoms. Let  $q_\alpha(\vec{r}, \vec{v}, t) d^3r d^3v dt$  be the number of  $\alpha$ -atoms inserted into the phase space region  $d^3r d^3v$  about  $\vec{r}$  and  $\vec{v}$  by external sources in time  $dt$  about  $t$ , and let  $Q_{\beta\alpha}(\vec{r}, \vec{v}, t) d^3r d^3v dt$  be the corresponding number of  $\alpha$ -atoms inserted by collision in which a  $\beta$ -atom strikes an  $\alpha$ -atom. From the above definitions one has

$$Q_{\beta\alpha}(\vec{r}, \vec{v}, t) = \int \sigma_{\beta\alpha}(\vec{v}' \rightarrow \vec{v}; \vec{r}) \psi_\beta(\vec{r}, \vec{v}', t) d^3v'. \quad (2)$$

Simple conservation of particles leads to the Boltzmann equation [3]

$$\frac{\partial \psi_a}{\partial t} + \bar{v} \cdot \bar{\nabla} \psi_a + v \sigma_a \psi_a = q_a + \sum_{\beta} Q_{\beta a}. \quad (3)$$

In a manner familiar in nuclear reactor theory, the method of characteristics of the theory of partial differential equations can be applied to integrate the above Boltzmann equation [4]. A characteristic or ray in  $(\bar{r}, t)$  space is determined; in our case it turns out to be the line

$$\left. \begin{aligned} \bar{r} &= \bar{r}_0 + s \bar{\Omega} \\ t &= t_0 + \frac{s}{v} \end{aligned} \right\} \quad (4)$$

where  $\bar{\Omega}$  is the unit vector defined by  $\bar{v} = v \bar{\Omega}$ , and  $s$  is a parameter determining arc length along the ray (4). Along this ray  $\psi_a(\bar{r}, \bar{v}, t)$  becomes a function  $\psi_a(s, \bar{v})$  of  $s$  and  $\bar{v}$ , with  $\psi_a(s, \bar{v}) = \psi_a(\bar{r}_0 + s \bar{\Omega}, \bar{v}, t_0 + s/v)$ . For different choices of initial conditions  $(\bar{r}_0, t_0)$  the rays (4) map out all of  $(\bar{r}, t)$  space. Along the ray (4), the Boltzmann equation (3) becomes

$$v \frac{d\psi_a}{ds} + v \sigma_a \psi_a = q_a + \sum_{\beta} Q_{\beta a}, \quad (5)$$

which is easily integrated to yield

$$\psi_a(s, \bar{v}) = c e^{-F(s)} + \frac{1}{v} e^{-F(s)} \int_0^s e^{F(s')} [q_a(s') + \sum_{\beta} Q_{\beta a}(s')] ds', \quad (6)$$

with

$$F(s) = \int_0^s \sigma_a(s') ds'. \quad (7)$$

We shall be concerned with the steady state, which is obtained by considering the bombarding beam to be constant in time and doing the integration in (6) for  $-\infty < s' \leq 0$ , which corresponds to times  $-\infty < t \leq 0$ . Upon making the change of variable  $-s'$  to  $s'$ , one obtains for the steady-state density function

$$\psi_a(0) = \frac{1}{v} \int_0^{\infty} e^{-F(s')} [q_a(-s') + \sum_{\beta} Q_{\beta a}(-s')] ds' \quad (8)$$

with

$$F(s) = \int_0^s \sigma_a(-s') ds'. \quad (9)$$

#### FICK'S LAW FOR CASCADE MIXING

Consider the flux of impurity atoms due to atomic collisions during ion bombardment. From the definitions above one has for this flux

$$\bar{J}_3(\bar{r}, t) = \int \bar{v} \psi_3(\bar{r}, \bar{v}, t) d^3 v. \quad (10)$$

The  $\bar{r}$  dependence of the collision cross section derives from the spatial variation of atomic densities  $N_a$  in the target, which is explicitly displayed by writing

$$\sigma_{\beta a}(\bar{v} \rightarrow \bar{v}'; \bar{r}) = N_a(\bar{r}) K_{\beta a}(\bar{v} \rightarrow \bar{v}'). \quad (11)$$

A key point of the present work is the observation that the integral form of the Boltzmann equation immediately yields the atomic migration currents in closed form. For the steady-state flux, one has from Eq. (8)

$$\bar{J}_3(\bar{r}_0) = \sum_{\beta} \int d^3 v \bar{\Omega} \int_0^{\infty} ds' e^{-F(s')} \int d^3 v' N_3(-s') K_{\beta 3}(\bar{v}' \rightarrow \bar{v}) \psi_{\beta}(-s', \bar{v}') d^3 v', \quad (12)$$

with

$$F(s) = \int_0^s \sigma_3(-s') ds'. \quad (13)$$

The term in Eq. (12) for  $\beta = 1$  describes recoil implantation effects as well as effects in which implanted atoms participate in cascades. If one describes primary knock-on production by source terms  $q_\beta(\vec{r}, \vec{v}, t)$  then, in the zero-fluence limit, this  $\beta = 1$  term represents purely recoil implantation effects.

Subject only to the assumptions of uncorrelated binary collisions in an amorphous target, Eq. (12) is exact.

Now arrange the coordinate system so that the incoming beam is along the  $z$  axis and, in order to fix ideas, let the beam and target have plane symmetry and perpendicular incidence. One contribution to  $J_3$  in Eq. (12) is the variation in  $N_3(-s') = N_3(\vec{r}_0 - s'\vec{\Omega})$ . Suppose that  $N_3$  increases in the positive  $z$  direction. Then, at a fixed point  $\vec{r}_0$  there will be more particles arriving at  $\vec{r}_0$  which originate from collisions in the positive  $z$  direction (where  $N_3$  is larger) than there are from the negative  $z$  direction, and this gives rise to a net flux. The particle density functions  $\psi_\beta$  in the integrand of Eq. (12) will also make a contribution to  $J_3$  because they depend on  $N_\beta$  and, correspondingly, they will have a directional dependence. The parameter  $s'$  measures the distance from  $\vec{r}_0$  to where these particles originate, and they are attenuated by the factor  $e^{-F(s')}$ , where  $F(s')$  is the average number of mean-free paths these particles travel in going from the point  $\vec{r}_0 - s'\vec{\Omega}$ , where they are created by collisions, to the point  $\vec{r}_0$ , where they make their contribution to  $J_3$ .

Now expand the integral of Eq. (12) in a power series in  $s'$ , and keep only the lowest-order term. That term comes from the spatial dependence of the factor  $N_3$  which, to lowest order, is

$$N_3(-s) = N_3(\vec{r}_0) - s \vec{\Omega} \cdot \vec{\nabla} N_3(\vec{r}_0). \quad (14)$$

The result is

$$\vec{J}_3 = -D \vec{\nabla} N_3(\vec{r}_0) \quad (15)$$

with

$$D = \sum_\beta \int d^3v \Omega^2 \frac{1}{\sigma^2(\vec{v}, \vec{r}_0)} \int d^3v' K_{\beta 3}(\vec{v}' - \vec{v}) v' \psi_\beta(\vec{r}_0, \vec{v}'). \quad (16)$$

In obtaining this result, one uses the identity  $\int_0^\infty ds' s' e^{-\sigma s'} = 1/\sigma^2$ , and the fact that the integrand of Eq. (12) is cylindrically symmetric about the  $z$  axis. In Eq. (16), the particle densities  $\psi_\beta$  are all proportional to the bombarding fluence  $\phi$ , so the diffusion coefficient  $D_0$  of Eq. (16) can be written

$$D = D_0 \phi, \quad (17)$$

with the mixing parameter  $D_0$  independent of the bombarding flux.

Equation (15) is Fick's law for atomic migration, and is obtained as the lowest-order approximation to Eq. (12). This approximation is valid only when the variation of  $N_3(\vec{r})$  over a mean-free path is small compared to  $N_3$ . When this is not true, one must include more terms in the power series expansion in  $s'$ . These higher terms will involve powers of  $N_3$  and also the spatial variations of  $\psi_\beta(\vec{r}, \vec{v})$  due to the spatial variations of  $N_\beta(\vec{r})$ .

On account of the (averaging) integrations  $\int d^3v$  and  $\int d^3v'$  in expression (16), we can expect the result to be insensitive to the details of the density functions  $\psi_\beta$  for the recoil cascades, rather crude approximations will probably suffice. On the other hand, Eq. (16) indicates that  $D$  is highly sensitive to the atomic collision cross sections, and this expression allows the calculation for realistic interatomic potentials.

#### MODEL KINCHIN-PEASE CASCADE

In order to calculate the mixing coefficient  $D_0$ , one needs the density functions  $\psi_\beta(\vec{r}_0, \vec{v}')$  for the displacement cascades. In another work, we plan to show how the integral form (6) can be used to formulate an iteration procedure for these functions which will allow the calculation of  $D_0$  by successive approximations. Here, we formulate a model for  $\psi_\beta$  which allows a first approximation to  $D_0$ . We consider the case of an infinitely dilute impurity, and let us agree to ignore recoil implantation effects. In these circumstances, the terms  $\beta = 1$  and  $\beta = 3$  drop out in Eq. (16), leaving only the term  $\beta = 2$ .

The quantity needed is the density function  $\psi_2(\vec{r}, \vec{v}, t)$  for the cascade of 2-atoms under steady-state bombardment by 1-atoms, which is obtained as follows: Let  $G(\vec{r}, \vec{v}, t; \vec{r}_0, \vec{v}_0, t_0)$  be the density function for the displacement cascade created by a primary knock-on atom (PKA) of energy  $E_0$ , velocity  $\vec{v}_0$  created at time  $t_0$  at the location  $\vec{r}_0$ . We will construct  $G$  to represent a simple implementation of the Kinchin-Pease cascade [5]. Let  $G(\vec{r}, \vec{v}; \vec{r}_0, \vec{v}_0)$  be the density function for the displacement cascades in steady state, where the above PKA's have been created at a constant rate for a long time. One can show from the time-translation invariance of these Green's functions that

$$G(\vec{r}, \vec{v}; \vec{r}_0, \vec{v}_0) = \int_0^\infty G(\vec{r}, \vec{v}, t; \vec{r}_0, \vec{v}_0, t_0 = 0) dt, \quad (18)$$

which will be used to obtain  $G$  from  $G$ . Let  $q_2(\vec{r}_0, \vec{v}_0)$  be the steady-state creation rates for PKA's of velocity  $\vec{v}_0$ . The density function to be used in Eq. (16) will then be

$$\psi_2(\vec{r}, \vec{v}) = \int G(\vec{r}, \vec{v}; \vec{r}_0, \vec{v}_0) q_2(\vec{r}_0, \vec{v}_0) d^3v_0. \quad (19)$$

Thus,  $\psi_2(\vec{r}, \vec{v}, t)$  can be obtained if one has the density function  $G$  for a single cascade.

For our first approximation to  $D_0$ , we will use for  $G$  a simple implementation of the Kinchin-Pease cascade [5]. The cascade is considered to consist of  $m$  steps. At the  $k$ -th step, there are  $2^k$  recoils, each of energy  $E_0/2^k$ , velocity

$$v_k = v_0/2^{k/2}, \quad (20)$$

and isotropically distributed in direction. This step lasts an interval of time

$$\Delta_k = \frac{1}{\sigma(\vec{v})v_k}, \quad (21)$$

where  $\sigma$  is the reciprocal of mean free path, which can be obtained from the actual realistic interatomic potential. The total number  $m$  of such steps is given by the condition

$$E_d = \frac{E_0}{2^m}, \quad (22)$$

where  $E_d$  is the displacement energy. The spatial dependence of the cascade is ignored, since it is expected to make a contribution to  $D_0$  only in higher orders. Define the points in time  $t_k$  by

$$t_k = t_0 + \sum_{i=1}^k \Delta_i. \quad (23)$$

Then  $G$  can be written

$$G(\vec{r}, \vec{v}, t) = \delta(\vec{r} - \vec{r}_0) 2^k \frac{\delta(\vec{v} - \vec{v}_k)}{4\pi v_k^2} \quad (24)$$

for  $t_k \leq t \leq t_{k+1}$ , with  $G = 0$  for  $t > t_m$ .

The steady-state Green's function is obtained from Eq. (18) as

$$G(\vec{r}, \vec{v}) = -\frac{\delta(\vec{r} - \vec{r}_0)}{4\pi} \sum_{k=1}^m \frac{2^k}{\sigma(\vec{v}_k)} \frac{\delta(\vec{v} - \vec{v}_k)}{v_k}. \quad (25)$$

The above  $G$  will make a contribution to the calculation (16) of  $D_0$  via the form  $v' \psi_2(\vec{r}, \vec{v}') d^3v'$ . We can assess this contribution by considering the quantity

$$A \equiv \int v' G(\vec{r}, \vec{v}') d^3v' = \delta(\vec{r} - \vec{r}_0) \sum_{k=1}^m \frac{2^k}{\sigma(\vec{v}_k)}. \quad (26)$$

For  $\sigma(\vec{v}_k)$  a constant, 50% of the total contribution to  $A$  comes from the last step  $k = m$ , 75% from the last two steps, 87.5% from the last three steps, 93.75% from the last four steps, and so on. This shows that the final steps of the cascade will dominate the contributions of  $\psi_2(\vec{r}, \vec{v})$  to the mixing coefficient  $D_0$ . This corresponds to the low-velocity region of  $\psi_2(\vec{r}, \vec{v})$ , where the density function constructed above can be expected to be not a bad approximation. Recall also that the expression (16) is relatively insensitive to the details of  $\psi_2(\vec{r}, \vec{v})$ . These two facts together lead us to expect that the above  $\psi_2(\vec{r}, \vec{v})$  will provide a reasonable first approximation to  $D_0$ .

The above argument also shows that the  $D$  of Eq. (16) will be highly sensitive to the displacement energy  $E_d$ , which determines  $m$  via Eq. (22). Now, instead of the dilute solvent case  $N_3 \ll N_2$ , consider the general case of arbitrary  $N_3$ . If the displacement energy should then depend on the compositions  $N_3$  and  $N_2$  of the target, then so will the mixing coefficient  $D_0$ . This will be a chemical effect in cascade mixing. Furthermore,  $D_0$  will have a (complex) dependence on  $N_1, N_2$ , and  $N_3$ , and therefore will vary with fluence. In addition, if  $E_d$  varies with temperature, then so will  $D_0$ .

#### DISCUSSION

The physical origin of cascade mixing in the present work is the same as that of Haff and Switkowski [1], and this work can be considered a refinement of their approach. Their model of cascades has one velocity and one mean free path, and they find  $D = v f / 3 \sigma$ , with  $f$  a certain fraction. We have the exact expression (12) involving the actual velocity distribution, which allows a derivation of Fick's law and the closed expression (16) for the mixing coefficient.

Emphasis should be placed on the deduction of the previous section that the mixing parameter  $D_0$  will depend sensitively on the displacement energy  $E_d$ . If actual calculation bears out this deduction, then this constitutes a physical mechanism for chemical effect in cascade mixing. In addition, cascade mixing will depend on  $N_1, N_2$ , and  $N_3$  (and therefore fluence) and on temperature.

#### ACKNOWLEDGMENT

I'm grateful to K. Grabowski, G.H. Herling, and G. K. Hubler for stimulating and helpful conversations, and to G.H. Herling for reading the manuscript.

#### REFERENCES

1. P.K. Haff and Z.E. Switkowski, J. Appl. Phys. 48, 3383 (1977).
2. S. Matteson, Appl. Phys. Lett. 39, 288 (1981).
3. K.M. Case and P.L. Zweifel, Linear Transport Theory (Addison-Wesley, 1977).
4. G.I. Bell and S. Glasstone, Nuclear Reactor Theory (Van Nostrand, 1970).
5. G.H. Kinchin and R.S. Pease, Rep. Prog. Phys. 18, 1 (1955).

Section I.E

SURFACE MODIFICATION BY ION BEAM ENHANCED DEPOSITION

R. A. Kant and B. D. Sartwell

Materials Modification & Analysis Branch  
Condensed Matter & Radiation Sciences Division  
Naval Research Laboratory

This work was supported by the Office of Naval Research.

## SURFACE MODIFICATION BY ION BEAM ENHANCED DEPOSITION

R. A. KANT AND B. D. SARTWELL

U.S. Naval Research Laboratory, Washington, D.C., 20375

### ABSTRACT

Copper films given multiple sequences of Ta implantation and Cu depositions were analyzed using electron microscopy, backscattering, and Auger spectroscopy. Ta retention is 92% following direct implantation, and 100% retention was achieved for the same Ta dose if sputtered Cu is replaced during implantation. Lateral migration of Ta and micro-roughness were observed for all cases studied. Evidence for TaC formation is presented.

### INTRODUCTION

The use of concurrent ion irradiation and vapor deposition to achieve enhanced thin film properties and to improve coating adherence has, for the most part, been studied using ion beams with energies less than 5 keV [1-3]. The reasons for using low-energy ions as opposed to beams of moderate-energy ions that are obtained from ion implantation systems include (1) energy deposition will be very near the surface, (2) low energy ion sources are readily available and reasonably inexpensive and (3) sputtering is reduced at low energies. If, however, the negative aspects of increased sputtering could be overcome, then there would be several advantages to using higher energy ion beams available from an implanter. Principle among these are that the ion beam can consist of any element and is not limited to gaseous species as is frequently the case for low energy ion guns. Because of the increased energy available, the dose required to produce the same energy deposition is reduced. In addition, the combined ion implantation and deposition technique offers a new approach for the study of sputtering phenomena. Ordinarily the measurement of a sputtering rate is complicated by an increase in concentration of the implanted element at the surface. If, however, the target material is continuously being replenished by vapor deposition during the sputtering process, the surface fraction of the implanted element can be kept arbitrarily low. Another interesting potential application of the combined technique is to use vapor deposition to precisely offset sputtering. If this can be done, then the maximum concentration of an implanted specie should no longer be fixed by the "sputtering limit" and the fraction of the implanted dose that is retained could be increased significantly. In the process, a completely new range of material compositions would become accessible via ion implantation.

To establish the feasibility of combining vapor deposition techniques and moderate energy ion implantation, a long range systematic study has been initiated. The preliminary results of that study are reported here. An initial goal is to determine the extent to which conventional models for implanted systems are applicable to ion beam enhanced deposition (IBED) systems. For this initial phase of the study, copper was implanted with tantalum while copper was being deposited to replace the sputtered atoms. This system was selected because the sputtering rate for Ta on Cu is high, and because Ta is insoluble in and forms no compounds with Cu.

## EXPERIMENTAL APPARATUS AND TECHNIQUES

For these treatments, the sample is positioned in the center of a chamber 30 cm above an electron beam evaporator and can be rotated about a horizontal axis in order to expose it to either the evaporant from below or the ion beam from the side. The samples are affixed to a cylinder of circular or square cross section or in some cases are themselves cylinders. In order to maintain a high degree of control over the relative arrival rates of the evaporant atoms and the beam ions, the treatment process is broken into two completely isolated steps. First a small fraction of the total intended dose is implanted. Then the sample is rotated into the evaporant stream where a correspondingly thin coating of the desired element is deposited. This process is then repeated until the desired film thickness or ion dose is achieved. If small variations in the relative arrival rates can be ignored, or if an external means of controlling the two fluxes is provided, then the sample is simply rotated continuously through the two beams. The chamber is equipped with two variable apertures which will eventually be used to adjust the relative arrival rates of ions and evaporant atoms, but for this work, these apertures were used to mask different portions of the sample from each beam. The evaporator is diffusion pumped and is isolated from the sample by a set of differential pumping apertures. A cryogenic pump is mounted directly opposite the sample which is itself surrounded by a cold wall held at 77 K.

In order to evaluate the extent to which the effects of the sputtering of copper by tantalum can be offset by concurrent evaporation of copper, three types of samples were prepared. For all three cases investigated, the substrate was a 12 mm diameter aluminum disk on which 63 nm of Cu had been deposited. The first treatment (case I) consisted of normal incidence implantation of 50 keV Ta to a fluence that was believed to be sufficient to sputter 48 nm of Cu or four times the range of the Ta ions. Assuming a sputtering rate of 18 atoms/ion for 50 keV Ta on Cu, this required a fluence of  $2.26 \times 10^{16}$  ions/cm<sup>2</sup> to remove the necessary amount of Cu. For the second treatment (case II), the same Ta fluence was implanted, but this time in 12 equal increments. Between each increment, 4 nm of Cu were deposited, which was approximately the thickness required to replace the Cu sputtered during each implant increment, assuming a sputtering yield of 18 atoms/ion. For case III, the sample received a total of 48 increments, each identical to those used in case II. Thus the total fluence of Ta for this sample was  $9.04 \times 10^{16}$  ions/cm<sup>2</sup> and the total equivalent thickness of deposited copper during the implantation was 188 nm (47 increments).

These samples were evaluated using Rutherford backscattering (RBS), scanning electron microscopy (SEM), and Auger electron spectroscopy (AES) combined with low-energy argon ion bombardment. For the RBS measurements, 2 MeV alpha particles were normally incident on the samples, with the back-scattered ions being detected at an angle of 135 degrees. Scanning electron microscopy was performed in an ISI model SX30 equipped with energy dispersive X-ray analysis and a Coates and Welter Cwicscan 106A. Auger electron spectra were obtained using a single-pass cylindrical mirror analyzer, with an incident electron beam energy of 3 keV and current of 0.05 mA. Depth profiles of the films were obtained by sequential Auger analysis and sputtering with 3 keV argon ions incident at an angle of 60 degrees with respect to the sample normal.

## RESULTS AND DISCUSSION

Analysis of the RBS spectrum of the direct Ta-implanted Cu film (case I) (Fig. 1A) indicated that the average thickness of copper removed was 43 nm (nearly the equivalent of four times the calculated range of the implanted Ta) and that the average sputtering yield was 16.4. It is, therefore, remarkable that the RBS spectrum also indicated that approximately 90% of the implanted Ta had been retained. The RBS spectrum for the second case, 4 nm of Cu deposited between each of the 12 incremental doses of Ta (Fig. 1B), showed that essentially 100% of the implanted Ta had been retained. For this case, nearly exact replacement of the sputtered Cu had been achieved and the apparent sputtering rate was 18.3. It should be noted that these determinations of the amount of Ta and Cu present are uncertain to 10 to 15%; thus the difference between the amounts of retained Ta for the two cases should not be viewed as significant. The amount of Cu on this second type of sample was essentially identical, within experimental uncertainty, to the amount present before implantation. For the third case (48 increments of Ta implantation plus 47 evaporations of 4 nm of Cu), the RBS revealed that the system no longer was retaining all of the implanted Ta and that the Cu depositions were increasing the film thickness more rapidly than the Cu was being sputtered away. The sputtering yield for this case was 18.3, 16% of Cu deposited during implantation remains, and retained Ta is 84% of that implanted.

Scanning electron microscopy of these samples (Fig. 2) revealed that considerable roughening of the surface had taken place in all three cases. Fig. 2C shows the surface for case III viewed at an angle of 79 degrees with respect to the surface normal. Energy dispersive X-ray analysis was used to examine the light and dark areas shown in Fig. 2B. The ratios of the X-ray yields in the light areas to that in the dark areas for Ta, Cu and Al are 1.6:1, 3.5:1 and .5:1 respectively.

The relative peak heights of the derivative Auger spectra plotted as a function of sputtering time for the three samples are shown in Fig. 3. An Auger depth profile of the unimplanted 63 nm thick copper film (not shown) indicated that it required approximately 20 minutes of sputtering to remove the film and observe the Al KLL peak. Small amounts of oxygen and carbon (less than 5 at.%) were incorporated into the film. For each of the profiles shown, it is assumed that approximately 2-3 minutes of sputtering was required to remove the surface contamination produced when the samples were exposed to the atmosphere. Thus, the 2-3 minute Auger peak heights should be considered to represent the "surface" as it existed before being removed from the IBED vacuum chamber.

When viewed collectively, the above results suggest the following interpretation. The RBS data indicate that there is Al very close to the surface. The gradual slope of the near surface Al signal in the RBS spectra (particularly for case III) suggests that the thickness of the film is not constant, a result that is certainly supported by the SEM pictures. These results, together with the X-ray data, indicate that the ridges that have developed are rich in Ta and have resisted sputtering while the valleys between the ridges have been preferentially sputtered, thereby exposing the Al substrate. The nonuniformity of the Ta indicates that significant lateral migration has occurred. In addition, the AES data indicate that significant Cu concentration occurs at the surface. This supports the view that the Ta has segregated on the surface leaving exposed regions of Cu. Analysis of the C KLL Auger line shape indicates that the C was present as a carbide. Applying sensitivity

factors to the C and Ta Auger peak heights indicated that there was approximately a 1:1 correspondence between the concentrations of those two elements throughout the implanted region. This supports the contention that a carburization process has resulted in the formation of TaC. The amount of sputtering that has taken place during the Ta implantation is well illustrated in Fig. 3A. Ta is still observed after all the Cu had been removed by sputtering or during AES analysis, indicating that some Ta was implanted into the Al substrate. Also, the fact that the ratio of the Al Auger peak at the "surface" (after 3 minutes of sputtering) to that obtained at saturation is 0.3 indicates that 30% of the aluminum substrate was exposed during the implantation. This uncovering of Al was reduced substantially for case II sample but reappears for case III.

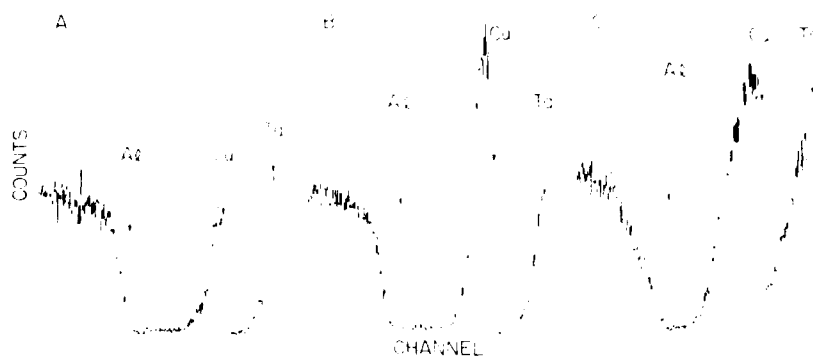


FIG. 1. Rutherford backscattering spectra of Cu films on Al following A)  $2.26 \times 10^{16}$  Ta/cm<sup>2</sup>; B) same Ta dose delivered 12 increments separated by 11 Cu depositions of 4 nm each; and C)  $9 \times 10^{16}$  Ta/cm<sup>2</sup> in 48 increments separated by 47 Cu depositions.

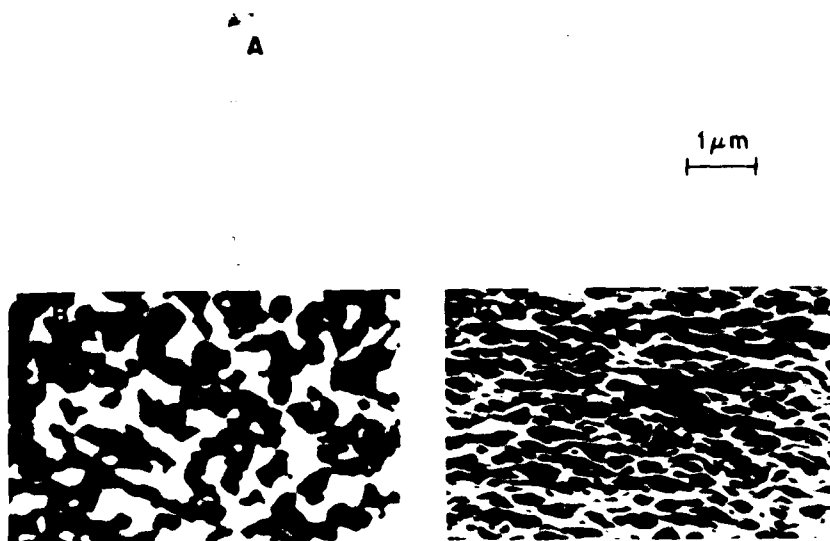


FIG. 2. Scanning electron micrographs: A) unimplanted Cu film; B) following 48 Ta implantations with Cu deposited; and C) same as B but viewed at 79 degrees to surface normal.

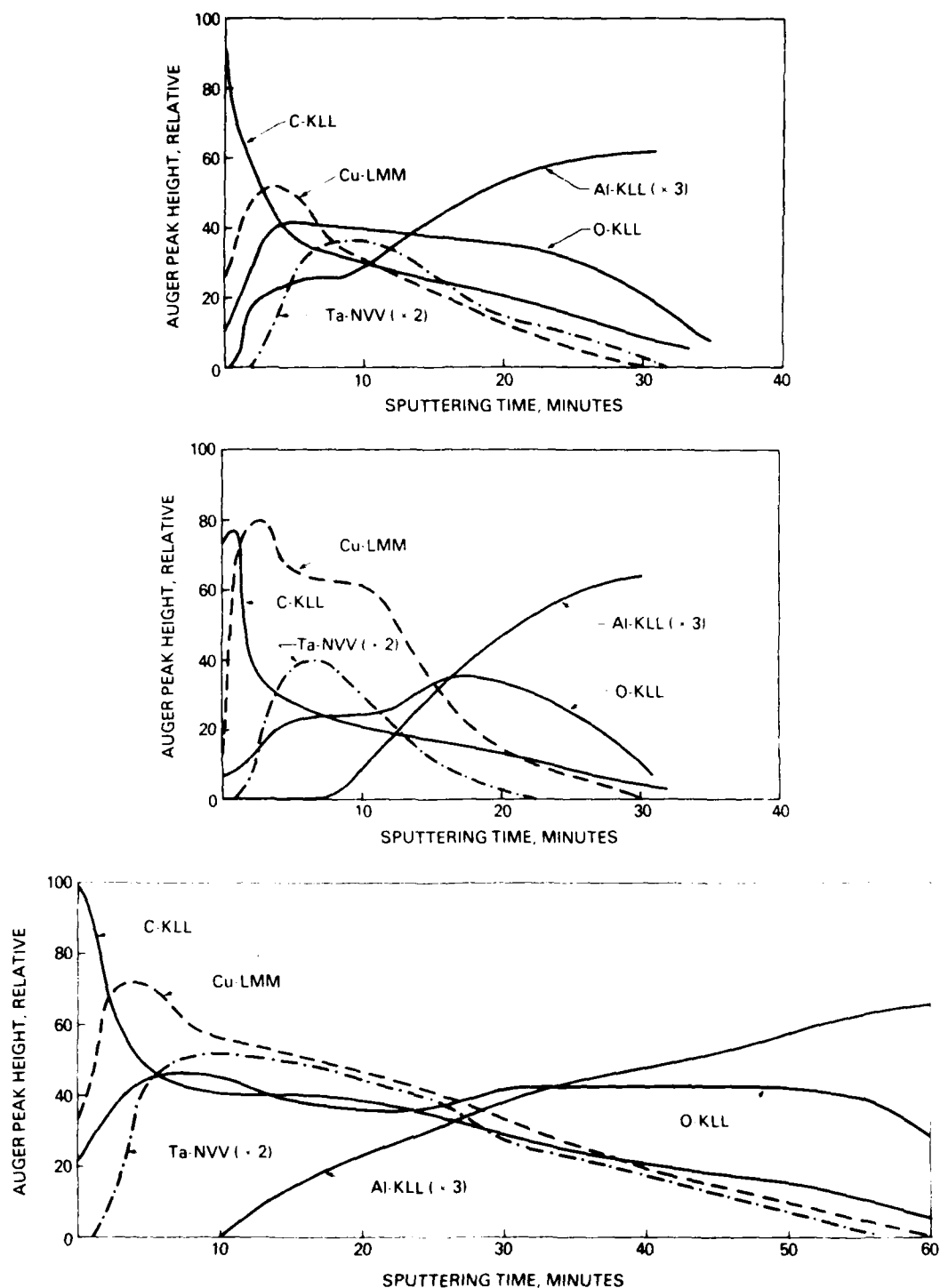


FIG. 3. Auger electron peak heights for Ta, Cu, C, and O versus Ar sputtering time. A) Ta implantation only; B) and C) sequential deposition and implantation of  $2.26 \times 10^{16}$  and  $9 \times 10^{16}$  Ta/cm<sup>2</sup> respectively.

## CONCLUSIONS

The interpretations presented above lead to the following conclusions. During the early stages of the Ta implantation, two mechanisms may be contributing to development of the roughened topography which subsequently dominates the evolution of the system. First, there is the usual development of hills and valleys due to sputtering. This development is enhanced by the segregation of the exposed Ta which forms TaC layers over the hills which further reduces the sputtering rate in these regions. It is apparent that the Cu deposited between Ta implantations has had an influence on the total retained Ta, but this added Cu has not significantly altered the development of surface roughness. This result has significant implications for the use of the combined technique for generating thick layers. Since the development of micro-roughness has not been substantially mediated by the deposition of additional Cu during implantation, it may be necessary to avoid applying the technique to systems with high sputtering rates. At the very least, such roughness severely complicates the interpretation of various surface analytical techniques such as AES. For example, without topographical information, one might conclude from the Auger depth profiles that intermixing between the Cu and Al had occurred. The results of these experiments also demonstrate the potential value of the IBED technique as a tool for the investigation of sputtering processes. Note, for example, that small changes in the sputtering rates become magnified if deposition is employed during implantation. This is illustrated by comparing the average thicknesses of the Cu film following 12 increments of implanted Ta with that following 48 such implants. A change in the sputtering rate of less than ten percent has lead to a readily detectable accumulation of several hundred angstroms of copper over the course of the 48 Ta implants.

## ACKNOWLEDGMENTS

We would like to thank Dr. A. R. Knudson for generating the RBS spectra and R. A. Walker for his skillful operation of the ion implanter.

## REFERENCES

1. C. Weissmantel, Thin Solid Films 58, 101-105 (1979).
2. L. Pranevicious, Thin Solid Films 63, 77-85 (1979).
3. J. J. Cuomo, J. M. E. Harper, C. R. Guarnieri, D. S. Yee, L. J. Attanasio, J. Angillello, and C. T. Wu, J. Vac. Sci. Technol., 20(3), 349-354 (1982).

Section I.F

THE SURFACE BINDING ENERGY FOR A TERNARY ALLOY  
PRODUCED BY ION IMPLANTATION

G. W. Reynolds<sup>1</sup>

F. R. Vozzo<sup>2</sup>

R. G. Allas<sup>† 3</sup>

P. A. Treado and J. M. Lambert<sup>4</sup>

<sup>1</sup>State University of New York at Albany

Albany, New York

and

Materials Modification & Analysis Branch  
Condensed Matter & Radiation Sciences Division  
Naval Research Laboratory

<sup>2</sup>State University of New York

Albany, New York

<sup>3</sup>Materials Modification & Analysis Branch  
Condensed Matter & Radiation Sciences Division  
Naval Research Laboratory

<sup>4</sup>Georgetown University

Washington, D. C.

and

Materials Modification & Analysis Branch  
Condensed Matter & Radiation Sciences Division  
Naval Research Laboratory

† Deceased

This work was supported by the Office of Naval Research.

## THE SURFACE BINDING ENERGY FOR A TERNARY ALLOY PRODUCED BY ION IMPLANTATION

G.W. REYNOLDS

*Naval Research Laboratory, Washington, DC, USA and SUNY at Albany, New York, USA*

F.R. VOZZO

*SUNY, Albany, New York, USA*

R.G. ALLAS<sup>†</sup>

*Naval Research Laboratory, Washington, DC, USA*

P.A. TREADO and J.M. LAMBERT

*Naval Research Laboratory, Washington, DC, USA and Georgetown University, Washington, DC, USA*

In this paper the surface binding energy model proposed by Reynolds for a binary alloy has been extended to a ternary system. From this model extension the steady state atomic surface fractions were calculated for a ternary surface alloy to be prepared by ion implanting a binary alloy of known composition. These predictions were compared with the results of the subsequent ion implantation experiments. The total implantation process was monitored by the observation of light emitted through de-excitation processes from sputtered neutral atoms. The experimental results reported are for nickel-chromium alloy implanted with 90 keV copper and tantalum and were analyzed using Rutherford backscattering, particle induced X-ray emission, and Auger surface analysis. From these results the partial sputtering yield for each component, net sputtering yield and surface atomic fractions were determined, and then compared with the predicted values. The different analytical techniques show consistent agreement within experimental error and there is reasonable agreement between the experimental results and the predicted values.

### 1. Introduction

In earlier papers [1,2] it has been shown that the changing surface during ion implantation alters the expected fluence in attaining steady state conditions (i.e., the partial sputtering yield of the implanted species is equal to one) and that the resulting atomic surface of the implanted species in general is not the reciprocal of the self ion sputtering yield as indicated in earlier literature [3]. Recently Reynolds calculated the average binding energy for surface atoms as a function of the atomic surface fractions for the copper-nickel system and proposed a binding energy correction factor determining the partial sputtering yields during ion implantation [2].

In this paper those concepts are extended more generally to alloy targets and in particular to ternary systems, that is, a metallic ion species implanted into a binary alloy of known composition not containing the beam species. The alloy selected was commercial nickel chromium (78:22) and was implanted with

metallic ions, copper and tantalum, at 90 keV energy. The beam species were selected to illustrate expected differences due to beam ion mass and the altered surface binding energy during ion implantation.

### 2. Surface energy model

Reynolds [2] has defined interaction parameters associated with the three nearest neighbor sets and calculated the average surface energy for the component atoms in the target surface. For the implanted species the average surface binding energy was

$$U_0 = n_0 U_0 + n_1 (U_1 - U_0), \quad (1)$$

where  $n$  is the atomic surface fraction, and the subscripts "0" and "1" refer, respectively, to the implanted species and the initial target species.  $U_1$  is the surface binding energy for the pure element as calculated by Jackson [4]. For the implanted species forming a binary system this expression works well and can be used to predict the steady state surface fractions. This formula-

<sup>†</sup> Deceased

tion is not directly extendable to ternary or higher order systems.

More properly the average surface binding energy for a component is

$$\bar{U}_i = z n_i U_{ii} + z n_j U_{ij}, \quad (2)$$

where  $i$  and  $j$  designate the component and  $U_i$  is the average binding energy of that component. Parameter  $z$  is the coordination or interaction number as described below and  $U_{ii}$ ,  $U_{ij}$  are the respective binding energies per interaction. The coordination or interaction number is related to the number of nearest neighbors used to determine the surface binding energy for each atom in the surface [2]. In a uniformly distributed minor component in a solid solution there is an equal probability for the solute atom to be placed anywhere in the set of  $N$  atoms comprising the nearest neighbor sets from which the individual atomic surface binding energy is calculated. Then one can assume that there is little or no difference between a regular lattice site with three distinct nearest neighbor sets and a hypothetical lattice of  $N-1$  neighbors plus the interacting atom equidistant from the subject site. The parameter  $z$  is then the total number ( $N$ ) of neighbors and

$$U_{ii} = U_i/z, \quad (3)$$

where  $U_{ii}$  is the binding energy per interaction in the hypothetical lattice and  $U_i$  is the elemental surface binding energy. In any system

$$U_{ii} \neq U_{ij} \neq U_{jj}, \quad (4)$$

The binding energy per interaction between dissimilar atoms,  $U_{ij}$ , may be estimated by one of the following three techniques:

- Comparing the single diatomic molecular bond strengths of the pure element and the combination, where available, to provide a factor for modifying the surface binding energy of the element appropriately.
- Using the simple average of the elemental surface binding energy of the two elements.
- Comparing the atomic sizes of the two atoms to provide a factor modifying the simple binding energy average towards the smaller atomic size.

Thus for any system, the average surface binding energy for a particular species becomes

$$\bar{U}_i = \sum_j z n_j U_{ij}, \quad (5)$$

where  $i$  is the species of interest at the binding site,  $j$  is the index of all species in the surface and the neighbor set,  $n_j$  is the atomic surface fraction of " $j$ " species in the set, and  $U_{ij}$  is the binding energy per interaction of the fixed hypothetical lattice of  $z$  interactions.

For a ternary system prepared by ion implantation the average binding energy has the following representation.

$$\begin{bmatrix} U_{i0} \\ U_{i1} \\ U_{i2} \end{bmatrix} = Z \begin{bmatrix} U_{i00} & U_{i01} & U_{i02} \\ U_{i10} & U_{i11} & U_{i12} \\ U_{i20} & U_{i21} & U_{i22} \end{bmatrix} \begin{bmatrix} n_1 \\ n_2 \\ n_3 \end{bmatrix}, \quad (6)$$

### 3. Sputtering of the binary alloy surface

At the onset of ion implantation of a third species into a binary alloy, the following conditions exist and continue to exist throughout the entire implantation. The sum of the atomic fractions is one, e.g.,

$$\sum_i n_i \approx 1. \quad (7)$$

The total sputtering yield for the bombarded surface is equal to the sum of the partial sputtering yields:

$$S_{tot} = \sum_i s_i, \quad (8)$$

where  $i$  is the index for all species in the bombarded surface.

The enhancement factor for preferential sputtering in binary alloys as defined by Anderson [5] is,

$$f_{12} = \frac{s_1/n_1}{s_2/n_2}, \quad (9)$$

and is constant throughout implantation. Subscripts 1 and 2 refer to the initial components of the binary alloy.

The partial sputtering yield is defined as:

$$s_i = n_i C_i S_{0i}, \quad (10)$$

where  $S_{0i}$  is the elemental sputtering yield calculated after Sigmund [6] and  $C_i$  is the surface binding energy correction term,

$$C_i = U_i/U_j, \quad (11)$$

At the steady state condition two additional constraints are placed on the system,

$$s_{0i} = 1, \text{ and} \quad (12)$$

$$s_1/s_2 = \lambda_1/\lambda_2, \quad (13)$$

where subscripts: 0, 1, 2, refer to the beam species and the initial target species respectively and  $\lambda_1$  and  $\lambda_2$  are the bulk atomic fractions of the initial binary alloy.

From these conditions one can predict which component of the binary alloy will be preferentially sputtered and can also predict the surface atomic fractions when the steady state is attained during the ion implantation.

### 4. The experiments

Nickel-chromium (78:22) alloy was implanted with 90 keV copper and tantalum ions to a fluence of  $2 \times 10^{17}$  ions/cm<sup>2</sup> prior to the insertion of high purity aluminum collector foils for collection of the sputtered products at

X. MINING

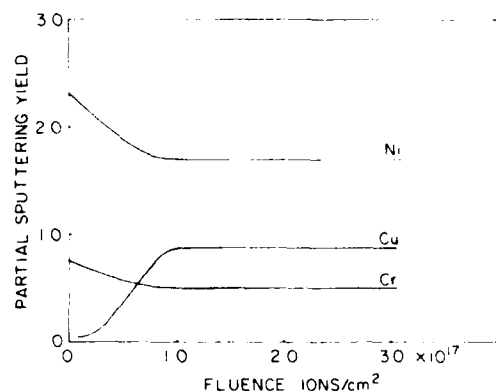


Fig. 1. Partial sputtering yields vs Fluence determined from optical Monitor (90 keV  $\text{Cu}^+ \rightarrow \text{Ni-Cr}$ )

the steady state or near steady state conditions. Throughout the implantation, the optical signals emitted from the excited sputtered atoms were monitored and used to confirm the near steady state conditions. Fig. 1 is the optical record for a copper ion implantation into nickel-chromium alloy, which the partial sputtering yields change during implantation.

The collector foils were analyzed using both PIXE

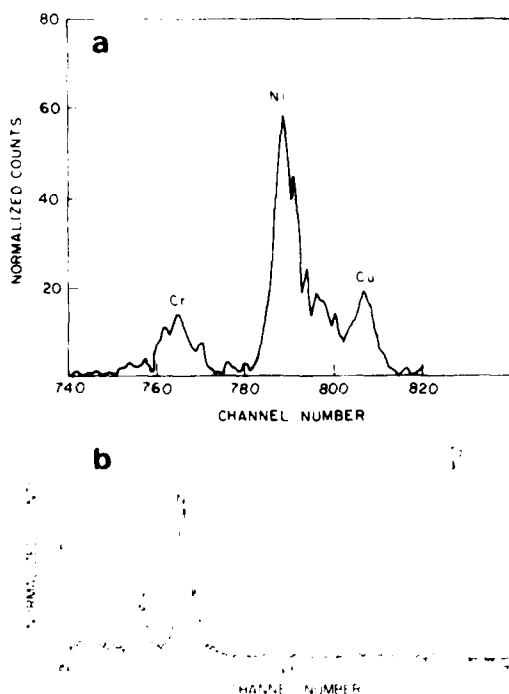


Fig. 2. RBS spectra of sputtered materials on Al collector foil: (a)  $\text{Cu}^+ \rightarrow \text{Ni-Cr}$  implantation and (b)  $\text{Ta}^+ \rightarrow \text{Ni-Cr}$  implantation

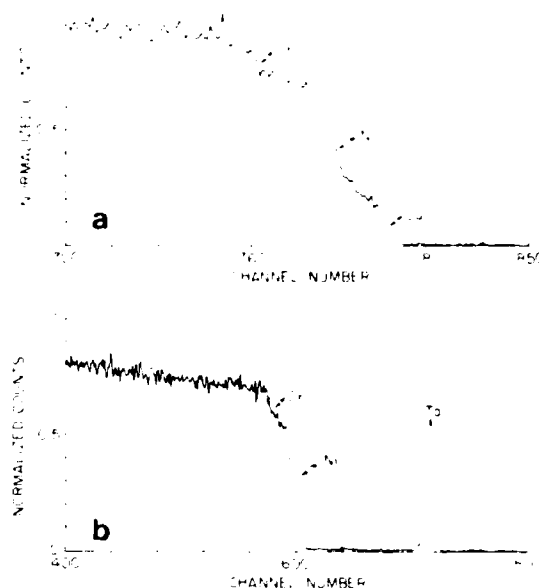


Fig. 3. RBS spectra of implanted region of alloy target: (a)  $\text{Cu}^+ \rightarrow \text{Ni-Cr}$  implantation, (b)  $\text{Ta}^+ \rightarrow \text{Ni-Cr}$  implantation

and RBS to ascertain both the distribution of the sputtered material and the partial sputtering yields at the near steady state condition. Figs. 2a and b are representative regions of the RBS spectra of sputtered products collected on the catcher foil for copper ion implanted nickel-chromium and for tantalum ion implanted nickel-chromium.

The targets were analyzed by RBS and AES sputter profile techniques to determine the profile of the implanted species and to determine the atomic surface fractions. Figs. 3a and b are typical RBS spectra for copper ion implanted nickel-chromium and for tantalum ion implanted nickel-chromium.

The apparatus and techniques used throughout these experiments have been previously described [7,1]. Table 1 summarizes the predicted parameters for the two systems and the experimental results.

From the experimental results it is apparent that the steady state condition was not reached during the implantation, though initial calculations of the fluence and the optical monitor chart indicated that the experiment should have been at steady state or very near steady state. Although the measured partial yields tend to support the use of measured values of elemental sputtering and the measured surface fractions support the use of the theoretically calculated values of the elemental yields, there is very strong evidence in support of the binding energy correction factor as determined from the modified surface binding energy. This model does not

Table 1

Comparison of steady state predicted values with experiment.

(a) 90 keV  $\text{Cu}^+ \rightarrow \text{Ni-Cr}$  (78:22) alloy.

Enhancement factor 1.16 chromium sputters preferentially.

		Initial conditions <sup>a1</sup>		Predicted results <sup>a1</sup>		Experimental results <sup>a1</sup>				
		Theory	Measured	Theory	Measured	Folios		Targets		Optical Monitor
						RBS	PIXE	RBS	AES	
Partial yield	Cu	0	0	1.00	1.00	0.7	0.4	0.6 <sup>b1</sup>	0.5 <sup>b1</sup>	0.8
Partial yield	Cr	1.57	0.71	1.22	0.50	0.7	0.5	0.5 <sup>b1</sup>	0.5 <sup>b1</sup>	0.5
Partial yield	Ni	6.52	2.27	4.31	1.82	2.3	1.6	2.1 <sup>b1</sup>	2.1 <sup>b1</sup>	1.7
Total yield		8.09	2.98	6.53	3.32	3.7	2.5	3.2	3.1	3.1
Surface fraction	Cu	0	0	0.137	0.221	0.17 <sup>b1</sup>	0.09 <sup>b1</sup>	0.14	0.11	0.19 <sup>b1</sup>
Surface fraction	Cr	0.22	0.23 ± 0.02	0.185	0.194	0.20 <sup>b1</sup>	0.15 <sup>b1</sup>	0.15	0.14	0.15 <sup>b1</sup>
Surface fraction	Ni	0.78	0.77 ± 0.04	0.677	0.585	0.75 <sup>b1</sup>	0.56 <sup>b1</sup>	0.71	0.68	0.53 <sup>b1</sup>
									0.06 <sup>d1</sup>	

(b) 90 keV  $\text{Ta}^+ \rightarrow \text{Ni-Cr}$  (78:22) alloy.

Enhancement factor 1.05 chromium sputters preferentially.

		Initial conditions <sup>a1</sup>		Predicted results <sup>a1</sup>		Experimental results <sup>a1</sup>		
		Theory		Theory <sup>a1</sup>		Folios	Targets	Optical monitor
						RBS	RBS	
Partial yield	Ta	0		1.00		0.7	1.7 <sup>b1</sup>	
Partial yield	Cr	2.65		2.35		2.4	1.9 <sup>b1</sup>	1.9
Partial yield	Ni	9.04		8.49		4.9	8.5 <sup>b1</sup>	6.8
Total yield		11.67		11.84		8.0	12.1	
Surface fraction	Ta	0		0.058		0.04 <sup>b1</sup>	0.10	<sup>b1</sup>
Surface fraction	Cr	0.22		0.199		0.20 <sup>b1</sup>	0.17	0.16 <sup>b1</sup>
Surface fraction	Ni	0.78		0.743		0.43 <sup>b1</sup>	0.73	0.60 <sup>b1</sup>

<sup>a1</sup> Theoretical values calculated after Sigmund [6] and measured values calculated from results [7,1].<sup>b1</sup> Values calculated from fraction or yields this column.<sup>c1</sup> Experimental errors ± 40%.<sup>d1</sup> Atomic surface fraction carbon (C).

consider large perturbations in the binding energy attributable to the formation of a strong chemical bond. The atomic surface fraction of carbon measured by AES was noted to be the compound chromium carbide, which does change the surface binding energy of all materials in the surface.

## 5. Summary

A model has been presented for calculating the average surface binding energy for each species in an alloy surface and has been used to determine surface binding

energy correction factors in calculating partial sputtering yields for surface components during ion implantation of an alloy of known composition. The steady state atomic surface fractions may be predicted and the total fluence to reach the steady state can be more precisely estimated. The optical monitor record clearly illustrates the behavior of each surface component during implantation, demonstrating the influence of the bombarding ions on the surface behavior.

Additional experiments in a broader spectrum of alloys is necessary to ascertain the general applicability of this model.

**References**

- [1] G.W. Reynolds et al., *Mat. Res. Soc. Symp. Proc.* 7 (1982) 51.
- [2] G.W. Reynolds, *Nucl. Instr. and Meth.* 209-210 (1983) 57.
- [3] J.K. Hirvonen, *Treatise on materials science and technology*, ed., J.K. Hirvonen (Academic Press, New York, 1980).
- [4] D.O. Jackson, *Radiat. Eff.* 18 (1973) 185.
- [5] H.H. Anderson, *Proc. of Symp. on the physics of ionized gases*, Boris Kidric Inst. Nucl. Sci., ed., M. Matic (1980) pp. 421-483.
- [6] P. Sigmund, in: *Sputtering by ion bombardment*, ed., R. Behrisch, vol. 1 (Springer, Berlin, 1982) ch. 2.
- [7] R.G. Allas et al., *Nucl. Instr. and Meth.* 194 (1982) 615.

Section I.G

EFFECTS OF NON-NORMAL INCIDENCE ON THE IMPLANTATION  
OF COPPER WITH GOLD AND TANTALUM

P. R. Malmberg and R. G. Allast<sup>1</sup>  
J. M. Lambert and P. A. Treado<sup>2</sup>  
G. W. Reynolds<sup>3</sup>

<sup>1</sup>Materials Modification & Analysis Branch  
Condensed Matter & Radiation Sciences Division  
Naval Research Laboratory

<sup>2</sup>Georgetown University  
Washington, D. C. 20057  
and

Materials Modification & Analysis Branch  
Condensed Matter & Radiation Sciences Division  
Naval Research Laboratory

<sup>3</sup>State University at Albany  
Albany, N. Y. 12222  
and

Materials Modification & Analysis Branch  
Condensed Matter & Radiation Sciences Division  
Naval Research Laboratory

+ Deceased

This work was supported by the Office of Naval Research.

## EFFECTS OF NON-NORMAL INCIDENCE ON THE IMPLANTATION OF COPPER WITH GOLD AND TANTALUM

P.R. MALMBERG and R.G. ALLAS<sup>1</sup>

*US Naval Research Laboratory, Washington, D.C. 20375, USA*

J.M. LAMBERT and P.A. TREADO

*US Naval Research Laboratory and Georgetown University, Washington, D.C. 20057, USA*

G.W. REYNOLDS

*US Naval Research Laboratory and SUNY at Albany, Albany, NY 12222, USA*

Copper targets were implanted with 125 keV gold and tantalum ions at selected incident angles of the beam relative to the target normal to examine the effect of the incident angle on the sputtering yields, the dose retained in the modified layer, and the atomic surface fractions. Sputtered particles were collected on aluminum foils to measure the angular distribution of the sputtered particles and to determine the partial sputtering yields of the beam and target species. A 1.5 MeV xenon beam implanted markers into the copper targets to determine the average sputtering yield for the surface during the implantation. Theoretical predictions from a surface binding energy correction model were compared with the experimental results. Although the predictions from the model were not exact, the trends of the data were in agreement with the model. The measured total sputtering yield increases with increasing incident beam angle, and, correspondingly, the fluence retained decreases with incident beam angle.

### 1. Introduction

The process of modifying metallic surface properties by the ion implantation of additional metallic species is rapidly becoming a significant technological process as a post-manufacturing surface treatment of materials [1,2]. The effects of non-normal incidence of the ion beam relative to the target surfaces being modified become important because most surfaces being treated are not planar. The most important effects of non-normal beam incidence are the depth and distribution of the implanted species in the surface layer, the quantity of the beam species retained compared with the quantity incident to the surface, and the erosion rate (sputtering yields) of the surface during the implantation. This paper presents information on two implant systems in which these effects were studied and compared with predictions from existing models and theory. The systems selected were 125 keV gold ions and 125 keV tantalum ions implanted into high purity polycrystalline copper targets. Copper was selected as a relatively non-reactive target material and the two beam species were selected because their masses are approximately equivalent while one is non-reactive and the other is reactive in the vacuum environment [3].

<sup>1</sup> Deceased.

Varga et al. [4] and Berisch [5,6] have edited recent reviews relative to sputtering processes. These references and a review of the more recent literature indicate a limited number of experiments in this higher energy region with heavy metallic ion beams. The theoretical formalism as proposed by Sigmund (ref. [5], ch. 2) and modified by the model proposed by Reynolds [7] was used to calculate the elemental yields, partial sputtering yields during the implantation, and the steady state atomic surface fractions.

### 2. Experiment

The experimental apparatus, procedures and analytic methods have been discussed previously [8,9]. A scanned beam (average current 200 to 400 nA) defined by a 3 mm  $\times$  5 mm aperture was used to implant to an initial dose, and then a cylindrical aluminum collector foil was inserted to collect sputtered particles throughout the remaining fluence implanted. The beam angles investigated were 0°, 30°, 45°, and 60° measured from the target normal. Prior to implanting with the metal ion beams each copper target was preimplanted with a 1.5 MeV xenon beam to a fluence of  $2 \times 10^{16}$  ions cm<sup>-2</sup> as a marker to measure total erosion in the modified region. The collected sputtered particle distributions

were used to determine partial and net sputtering yields. The collector foils were analyzed both by 1 MeV proton induced X-ray emission (PIXE) and 3.5 MeV helium Rutherford backscattering spectroscopy (RBS). The targets were analyzed using RBS to determine net sputtering yields, implanted profiles, atomic surface fractions, and the dose retained. When designing the experiments the pre-collector foil fluences were estimated from previous experience and from yields extrapolated from the review by Andersen and Bay (ref. [5], ch. 4). The additional fluence after insertion of the foil was estimated to produce approximately  $10^{14}$  beam particles per  $\text{cm}^2$  on the collector foil for analysis. The expected partial yields and surface fractions at the steady state condition were calculated after the implantations were scheduled and did not permit desired changes in estimated fluences.

### 3. Model calculations

The theoretical approach proposed by Sigmund (ref. [5], ch. 2) has been used to calculate the elemental sputtering yields for these experiments. Based on previous experience we recognize that the yields so calculated may be incorrect by nearly a factor of two [10]. The use of theoretical values was done for consistency because a complete set of experimental values was not available at this energy. The elemental yields were then corrected for modified surface binding energy to determine the partial sputtering yields in the manner proposed by Reynolds [7].

The elemental yields  $\{Y(1)\}$  for both the beam species and target species were determined applying (ref. [5], ch. 4)

$$Y(1)_i = \frac{0.042\alpha(M_i/M_0, \theta)S_n(E, Z_0, Z_i)}{NU_i} \quad (1)$$

where  $M$  is the atomic mass,  $Z$  is the nuclear charge,  $S_n$  is the nuclear stopping power at the surface for beam particles of energy  $E$ ,  $N$  is the atomic density of the target,  $\theta$  is the angle of the beam with respect to the target normal, and  $U$  is the surface binding energy. The subscripts 0 and  $i$  refer to the beam atom and target atom, respectively. The constant  $\alpha$  is taken from an earlier paper by Sigmund [11] in which the variation with angle is given as  $\sec^{-1}\theta$ .

The partial sputtering yields were then calculated applying [7]

$$Y_i = n_i C_i Y(1)_i \quad (2)$$

with

$$Y_{\text{net}} = \sum_i Y_i \quad (3)$$

where  $n$  is the atomic surface fraction,  $C$  is the surface

binding energy correction term and  $i$  is the index of species present in the target including the beam species.

The surface binding energy correction term is one of three corrections that may be applied to determine the partial sputtering yields as the surface region and the implanted region are altered by implantation of the beam species. The effects of the beam species have been observed when the atomic surface fraction for the implanted species is less than 0.005 [10]. The surface binding energy correction term is of the form

$$C_i = U_i/U_i(n), \quad (4)$$

where  $U_i$  is the surface binding energy used in eq. (1) and corresponds to the sublimation energy per atom or to the surface binding energy per atom as calculated by Jackson [12]. The average surface binding energy,  $U_i(n)$ , as a function of the atomic surface fractions is determined from

$$U_i(n) = \sum_j n_j z U_{ij} \quad (5)$$

The index  $j$  is over all components in the target surface and  $z$  is the number of binding interactions used in determining the binding energy per interaction. In solid solutions the number assigned to  $z$  corresponds to the number of atoms in the nearest neighbor set for an atom in the target surface. The binding energy per interaction,  $U_{ij}$ , is calculated in the following manner

$$U_{ij} = U_i(z) - U_j(z), \quad (6)$$

$$U_i(z) = \left[ \frac{U_i + U_{ii}}{2} \right] \left[ 1 + \left( \frac{r_i - r_{ii}}{r_i + r_{ii}} \right) \right], \quad (7)$$

where  $r$  is the atomic radius of the indexed species.

This surface binding correction term does not consider effects due to chemical bonding (covalent or electrovalent) that occur when compounds form. A similar term may be derived to correct the atomic density term,  $N$ , in eq. (1), but this has not been applied in the calculations which are presented in table 1 as the effect was considered small for the reported implantations. The correction to the stopping power,  $S_n$ , has also been neglected. For a two component system neglecting the latter two corrections, the partial yield equations may be solved for the steady state conditions (i.e.,  $Y_i = 1$ ). These calculations are presented in table 1.

### 4. Discussion of results

Figs. 1a and 1b show the angular distributions for the gold beam of the sputtered particles relative to the target normal for the four incident angles of the beam. The sputtered particle distributions for the tantalum implant have about the same appearance. Within experimental errors the distributions appear symmetrical

Table 1  
Comparison of calculated values with experimental data

Beam angle	Calculated theory - model				Experimental data			
	0	30	45	60	0	30	45	60
<i>125 keV gold into copper</i>								
$Y(1)_{Au}$	28.4	36.1	50.6	90.1	not measured this experiment			
$Y(1)_{Cu}$	15.3	19.4	27.3	48.6	not measured this experiment			
$Y_{ss}$ at steady state	1	1	1	1	0.6 <sup>a)</sup>	0.8 <sup>a)</sup>	0.8 <sup>a)</sup>	0.9 <sup>a)</sup>
$Y_{ss}$ at steady state	14.7	18.8	26.8	48.2	15 <sup>a)</sup>	26 <sup>a)</sup>	34 <sup>a)</sup>	43 <sup>a)</sup>
$Y_{net}$ at steady state	15.7	19.8	27.8	49.2	19 <sup>b)</sup>	24 <sup>b)</sup>	35 <sup>b)</sup>	55 <sup>b)</sup>
$n_{ss}$ at steady state	0.040	0.031	0.022	0.012	0.038 <sup>c)</sup>	0.027 <sup>c)</sup>	0.025 <sup>c)</sup>	0.018 <sup>c)</sup>
Fluence <sup>d)</sup> for steady state	34.8	23.7	13.9	5.54				
Predose fluence <sup>d)</sup>					21.7	17.9	11.9	6.4
Total fluence <sup>d)</sup>					35.4	37.2	25.1	13.1
Retained dose <sup>d)</sup>	26.0	17.9	10.3	4.33	16.6	11.9	7.6	4.2
Half profile depth (Å)	200	163	126	82	315	236	231	205
<i>125 keV tantalum into copper</i>								
$Y(1)_{Ta}$	12.6	15.9	22.4	39.8	not measured this experiment			
$Y(1)_{Cu}$	15.4	19.5	27.4	48.7	not measured this experiment			
$Y_{ss}$ at steady state	1	1	1	1	0.4 <sup>a)</sup>	0.7 <sup>a)</sup>	0.4 <sup>a)</sup>	0.6 <sup>a)</sup>
$Y_{ss}$ at steady state	11.2	17.9	25.9	47.2	13 <sup>a)</sup>	17 <sup>a)</sup>	14 <sup>a)</sup>	32 <sup>a)</sup>
$Y_{net}$ at steady state	12.2	18.9	26.9	48.2	9 <sup>b)</sup>	22 <sup>b)</sup>	15 <sup>b)</sup>	56 <sup>b)</sup>
$n_{ss}$ at steady state	0.149	0.115	0.080	0.044	0.047 <sup>c)</sup>	0.047 <sup>c)</sup>	0.045 <sup>c)</sup>	0.018 <sup>c)</sup>
Fluence <sup>d)</sup> for steady state	38.6	27.3	12.3	5.75				
Predose fluence <sup>d)</sup>					25.8	25.3	14.7	8.33
Total fluence <sup>d)</sup>					59.2	49.1	35.4	20.8
Retained dose <sup>d)</sup>	32.7	21.4	10.4	3.7	47.5	30.7	24.2	3.0
Half profile depth (Å)	208	180	174	104	300	240	188	157

<sup>a)</sup> Not steady-state conditions, an average value for fluence region in which collected

<sup>b)</sup> Determined from marker shift for the total dose

<sup>c)</sup> Determined from profile data

<sup>d)</sup> Units of  $10^{17}$  cm<sup>-2</sup>

about the target normal and appear to be about cosine squared distributions.

The experimental partial yields were determined from the distribution data, these are presented in table 1 along with other experimental data. For only 3 cases (60° Au, 45° Ta, 60° Ta) did the pre-foil fluence exceed the predicted steady state fluence requirement. Since steady state had not been achieved one expects experimental partial yields for the beam species to be less than one, and correspondingly, partial yields for the copper to be larger than expected steady state values.

Fig. 2 compares the beam species depth profiles for both experiments as a function of the incident beam angle. All implantations were expected to reach the steady state as these profiles result from analyses of the targets after the total implantation. For the profiles one observes that only the 60° gold implantation is at steady state and that the 60° tantalum implantation is at near

steady state. The remaining profiles are indicative of non-steady state conditions and there are significant differences between the two experiments. The gold implantation into the copper is typical of the solid state solution where there are negligible chemical effects, whereas the asymmetry of the profile in the tantalum implant with the much steeper slope near the surface is indicative of additional chemical effects in the surface region. Singer [13,14] and Hartley [3] have observed similar beam profiles where the reactive species has formed a carbide at the surface which is subsequently recoil implanted, mixed, and diffused in the near surface region. The observed greater range than expected increases the fluence necessary to reach steady state, effectively reducing the net and partial sputtering yields at this fluence. The extended range may be the result of cascade mixing diffusion, recoil implantation and low energy channeling all effective altering the nuclear stop-

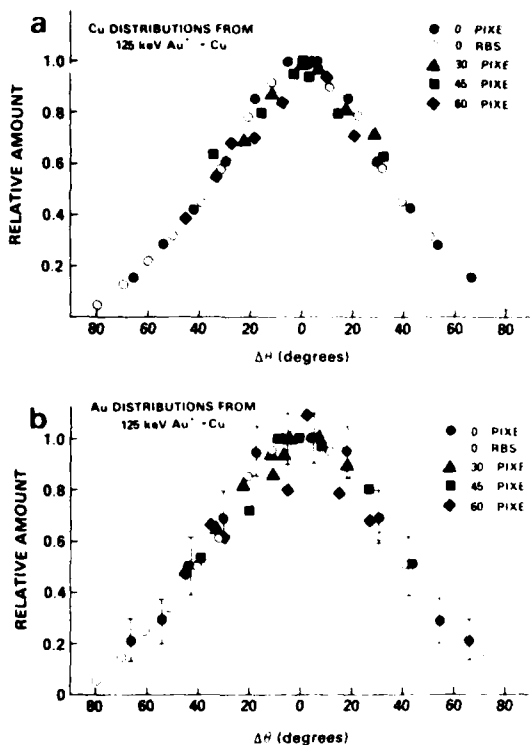


Fig. 1. Normalized angular distributions of sputtered particles for incident beam angles. a) Copper distribution vs angle from target normal. b) Gold distribution vs angle from target normal.

ping power in this region.

From the data collected, when the appropriate corrections for the effect of the beam species are included, the sputtering yield is seen to approximately match

$$Y(\theta) = Y(0)\sec^5 \theta \quad (8)$$

in general agreement with the Sigmund theory. The retained dose, correspondingly, decreases with an increasing incident angle requiring careful consideration of implantation geometries when modifying industrial components by ion implantation.

## 5. Summary

For the two systems studied, we have demonstrated the effect of the incident beam angle on both sputtering yields and the portion of the fluence retained in the target post implantation. The effect of the beam species on the implantation process is also observable. The model calculations for this effect begin with the onset of implantation although experimentally the effect is

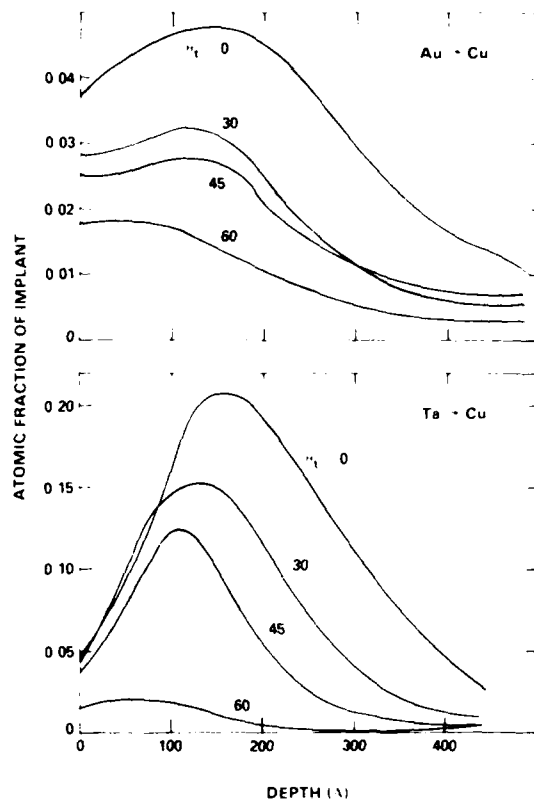


Fig. 2. Beam species depth profiles in target post implantation for incident beam angles.

noticeable when the atomic surface fraction for the beam species is small. The observations and calculations confirm that one cannot neglect the effects of the implanted species in the sputtering regardless of the beam species or beam energy. In comparing the implanted profiles of gold and tantalum, there is evidence of a chemical interaction near the surface in the case of tantalum which could be vacuum environment related. Although the model used does not completely predict the surface and implanted region behavior, it is a step toward being able to develop a more complete model. Additional improvements in the model incorporating additional corrections and additional experiments are necessary to determine the exact nature of the chemical interaction occurring during the tantalum implantation.

## References

- [1] G.K. Hubler, *Metastable Materials Formation by Ion Implantation*, eds. S.T. Picraux and W.J. Choyke, Materials Research Society Proceedings, Vol. 7 (North-Holland, Amsterdam, 1982) p. 34.

- [2] R.E. Fromson and R. Kossowsky, *Metastable Materials Formation by Ion Implantation*, eds., S.T. Picraux and W.J. Choyke, Materials Research Society Proc. vol. 7 (North-Holland, Amsterdam, 1983) p. 355.
- [3] N.E.W. Hartley, K.S. Grabowski, C.R. Gossett and J. Manning, Materials Research Society Proc. (1983) submitted.
- [4] P. Varga, G. Betz and F.P. Viehbock, eds., *Proc. Symp. on Sputtering*, Institute für Allgemeine Physik, Technische Universität Wien, Austria (1980).
- [5] R. Behrisch, ed., *Sputtering by Particle Bombardment I* (Springer, Berlin, 1981).
- [6] R. Behrisch, ed., *Sputtering by Particle Bombardment II*, (Springer, Berlin, 1983) to be published.
- [7] G.W. Reynolds, Nucl. Instr. and Meth. 209/210 (1983) 57.
- [8] R.G. Allas, A.R. Knudson, J.M. Lambert, P.A. Treado and G.W. Reynolds, Nucl. Instr. and Meth. 194 (1982) 615.
- [9] J.M. Lambert, P.A. Treado, D. Trbojevic, R.G. Allas, A.R. Knudson, G.W. Reynolds and F.R. Vozzo, IEEE Trans. Nucl. Sci. NS-30 (1982) 1285.
- [10] G.W. Reynolds, F.R. Vozzo, R.G. Allas, A.R. Knudson, J.M. Lambert and P.A. Treado, Materials Research Society Proc., vol. 7 (North-Holland, Amsterdam, 1982) p. 51.
- [11] P. Sigmund, Phys. Rev. 184 (1969) 383.
- [12] D.P. Jackson, Rad. Eff. 37 (1973) 185.
- [13] I.L. Singer, C.A. Carosella and J.R. Reed, Nucl. Instr. and Meth. 182/183 (1981) 923.
- [14] I.L. Singer, J. Vac. Technol. to be published.

Section I.H

RETENTION OF IONS IMPLANTED AT NON-NORMAL INCIDENCE

K. S. Grabowski<sup>1</sup>  
N.E.W. Hartley<sup>2</sup>  
C. R. Gossett and I. Manning<sup>1</sup>

<sup>1</sup>Materials Modification & Analysis Branch  
Condensed Matter & Radiation Sciences Division  
Naval Research Laboratory

<sup>2</sup>Research was performed while on sabbatical to:  
Department of Physics  
Georgetown University  
Washington, D. C. 20057

Permanent Address:  
AERE, Harwell  
Didcot, Oxfordshire  
Great Britain

This work was supported by the Office of Naval Research.

## RETENTION OF IONS IMPLANTED AT NON-NORMAL INCIDENCE

K.S. GRABOWSKI\*, N.E.W. HARTLEY\*\*, C. R. GOSSETT\*, and I. MANNING\*

\*Naval Research Laboratory, Washington, D.C. 20375, \*\*Georgetown University, Washington, D.C. 20007 (Present address: AERE Harwell, UK)

### ABSTRACT

Future applications of ion implantation require a knowledge of how the retention of implanted ions varies with angle of ion incidence. In this work the retention of 150-keV Ar, Ti, Cr, and Ta ions in AISI-M50 and 52100 bearing steels was measured for incidence angles up to 60° off normal. Fluences between  $3 \times 10^{15}$  and  $3 \times 10^{17}/\text{cm}^2$  were used, typically on 3/8" diameter cylindrical samples. Retention was measured for Ar, Ti, and Cr by ion induced x-ray emission and for Ta by backscattering of He ions. Range and sputtering parameters needed for model calculations were experimentally determined from Ta-implanted thin Fe film samples. Generally, at the low-fluence limit a near-cos  $\theta$  dependence obtained while at the high-fluence limit a (cos  $\theta$ )<sup>8/3</sup> dependence applied where  $\theta$  is the angle between the sample normal and the beam direction.

### INTRODUCTION

It is clear that in practical applications it will be necessary to ion implant some metal workpieces at non-normal angles of incidence. Not surprisingly, there is concern that large angles of incidence may limit the benefits obtainable by line-of-site ion implantation. Singer and Jeffries [1] have provided recent evidence that the angle of incidence can be an important factor in determining the friction and wear properties of Ti-implanted steel, substantiating some of these concerns.

Since the benefits of ion implantation are typically related to the concentration of the ions at the surface, and the durability of this improvement is likely related to the depth of the distribution, it is appropriate to consider the integrated quantity of implanted ions remaining in the target (the retained dose). This work addresses how the retained dose of Ar, Ti, Cr, and Ta ions implanted into steel depends on the incidence angle of the ion beam.

### EXPERIMENTAL PROCEDURE

The angle of beam incidence was controlled by implanting a scanned ion beam into symmetrically curved surfaces and into flat samples inclined to the beam. In the majority of this work, Ar, Ti, and Ta ions were implanted into stationary 3/8" diameter cylinders of AISI-M50 and 52100 martensitic bearing steels. M50 has a composition of Fe-4Cr-4Mo-1V-0.8C (in weight percent) and 52100 has a composition of Fe-1.5Cr-1.0C. Both steels were in a hardened and polished condition. A Ta slit 3/16" wide limited the 150-keV ion beams to a specific band across each cylinder. The slit was translated along the cylinder's axis to obtain separate bands for fluences between  $3 \times 10^{15}$  and  $3 \times 10^{17}/\text{cm}^2$  (all fluences specified are for normal incidence). Typically, the chamber pressure was  $3 \times 10^{-6}$  torr and the beam current density was between 1 and 15  $\mu\text{A}/\text{cm}^2$  during these implantations.

Other steel samples were implanted under similar conditions. Flat disks of 52100 steel were inclined at various angles up to  $40^\circ$  to the beam and collectively implanted with 145-keV Ta ions to a fluence of  $2 \times 10^{17}/\text{cm}^2$ . An M50 steel inner-ring raceway of a ball bearing (2-cm bore diameter, 7.94-mm ball diameter) was implanted with 150-keV Cr ions to a fluence of  $2 \times 10^{17}/\text{cm}^2$ . This was the only concave surface examined. Additionally, 150-keV Ti ions were implanted to a fluence of  $1 \times 10^{18}/\text{cm}^2$  into a 1/4" diameter half cylinder of 304 stainless steel (Fe-18 Cr-8Ni).

Fe thin-film samples were also Ta-ion implanted. An Al cylinder (3/8" diameter) was coated with 1600Å of evaporated Fe and implanted with  $1 \times 10^{17}\text{Ta}/\text{cm}^2$  at 145 keV in a 3/16" wide band. This sample enabled measurement of both Ta retention and sputtering yields for Ta and Fe as a function of incident angle. Sputtering yields and retention were also examined as a function of fluence at normal incidence using 1900Å-thick Fe films on a sapphire substrate. Fluences of  $1 - 18 \times 10^{16}/\text{cm}^2$  were examined.

The retention of implanted Ar, Cr, and Ti ions was determined by proton or alpha-induced x-ray emission (PIXE), and of implanted Ta ions by 2-MeV Rutherford backscattering (RBS) of  $\text{He}^+$ . During the analysis, the 3/8"-diameter cylinders were rotated about their axis to select a specific incidence angle of the various implanted ions. The M50 bearing race was rotated during analysis so that the angle of Cr incidence was examined in the ball raceway at one radial section of the inner ring. The incidence angle on the 1/4"-diameter 304 s.s. half cylinder was selected by translating the cylinder diameter across the beam during analysis. This latter technique was somewhat less accurate and was therefore abandoned in later work. It was not possible to analyze implanted Ti in M50 due to overlap with the V signal from the bulk. For RBS analysis a scattering angle of  $135^\circ$  was used, and for the PIXE work an angle of  $90^\circ$  between the detector and beam direction was used, except for the Cr in M50 bearing analysis where an angle of  $65^\circ$  was used. The PIXE determinations of retained dose were all normalized to the retention at  $0^\circ$  incidence, whereas the absolute retention (in ions/ $\text{cm}^2$ ) was obtained from the RBS measurements. As mentioned RBS measurements also provided the Fe and Ta sputter yields from the Fe thin-film samples.

## RESULTS AND DISCUSSION

### Theoretical

A rather simple dependence of the retained implantation dose on angle of incidence can be derived at both low-dose and high-dose (or steady-state) limits, using the model of Schulz and Wittmaack [2] for the evolution of the concentration-versus-depth profile from high-dose ion implantation. This model assumes that the implanted ion occupies no volume (i.e. no swelling occurs), the sputter coefficient and projected range remain constant, and no ion mixing or diffusion occurs. Although these assumptions appear quite restrictive, they do not prevent the model from identifying to first order the functional dependence of ion retention on incidence angle.

Fig. 1 shows the evolution of an implantation profile with increasing fluence based on the Schulz and Wittmaack model.  $R_p$  and  $\sigma$  represent the projected range and straggling of the incident ion, respectively,  $S$  the constant sputter coefficient,  $F_{\text{ion}}$  the atomic fraction of ions in the target, and  $w$  the thickness of material sputtered off ( $S\Phi/N$ ) relative to  $R_p$  after an implantation fluence  $\Phi$  (ions/ $\text{cm}^2$ ).  $N$  is the constant target atomic density (at./ $\text{cm}^3$ ). This figure represents implantations for which  $R_p/\sigma = 6/\sqrt{2}$ .

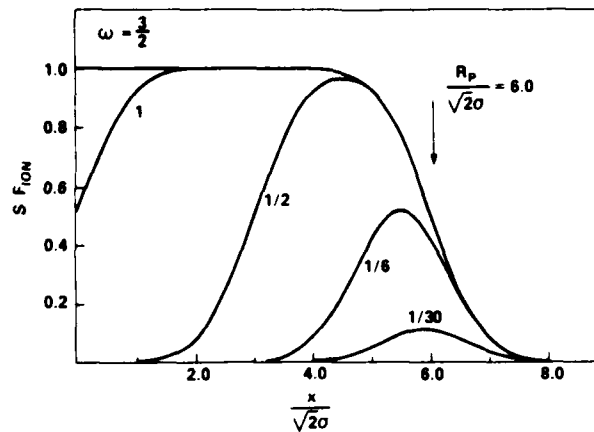


Fig. 1 Development of implanted ion distribution with increasing fluence for case of  $R_p/\sigma = 6\sqrt{2}$ .  $\omega$  is the amount of material sputtered away relative to the projected range,  $R_p$ .

In the low-fluence limit for this value of  $R_p/\sigma$ , all implanted ions are retained beneath the surface, as is evident from Fig. 1. For an incident fluence,  $\Phi_0$ , specified for normal incidence, the actual fluence is  $\Phi_0 \cos \theta$  where  $\theta$  is the angle between the beam direction and the surface normal. Therefore, the retention,  $R$  (ions/cm<sup>2</sup>), at low fluences should be

$$R_0 = \Phi_0 \cos \theta \quad (1)$$

In the high-fluence limit, the retention of ions is related to the area under the curve shown in Fig. 1 with  $\omega=3/2$ . Approximating this area by a step function of height  $S F_{ion}$  with the step at  $X=R_p$  leads to  $R=NR_p/S$ . At non-normal incidence,  $R_p$  shortens to  $X_p=R_p \cos \theta$  and  $S$  increases. Sigmund [3] has estimated that  $S$  depends on  $\theta$  according to  $S=S_0/\cos^f \theta$  with  $f$  approximately equal to 5/3 for target masses less than about 3 times the ion mass, a condition met in all of the present work. Combining these angular dependences leads to a high-fluence limit of

$$R_\infty = \frac{NR_p}{S_0} (\cos \theta)^{8/3} \quad (2)$$

At intermediate fluences,  $R$  should vary with  $\theta$  so as to fall between the two limits set by Eqs. 1 and 2.

A more realistic description of the evolution of an implantation profile is shown in Fig. 2, where  $R_p/\sigma = \sqrt{2}$ . This value of  $R_p/\sigma$  is more in line with the values of 1.7 - 2.8 expected for normal incidence and the ions and targets studied here. Even in Fig. 2, however, close examination reveals that in the high fluence limit ( $\omega=3$ ), the area under the curve can be closely approximated by a step function of height  $S F_{ion}$  and width  $X=R_p$ . However, conditions may worsen at non-normal incidence since  $X_p/\sigma$  is smaller. Similarly, the retention at low fluences may deviate from the  $\cos \theta$  dependence due to an increase of ion loss from backscattering at large incidence angles.

Fig. 3 shows the extent to which Eqs. 1 and 2 deviate from the low and high-fluence limits expected from the complete Schulz and Wittmaack model of retention during implantation of 145-keV Ta into Fe. The model calculation

used measured values for  $R_p$ ,  $\sigma$ , and  $S_0$  of 106Å, 122Å, and 6.0, respectively, and assumed  $X_p = R_p \cos \theta$ . The dashed lines in Fig. 3 represent values at low fluence from Eq. 1, normalized at  $\theta = 0^\circ$ , and at high fluence directly from Eq. 2. In the low-fluence limit, even though  $\omega$  is only 0.1 at  $0^\circ$ , retention falls off more quickly than  $\cos \theta$  with increasing angle due to an increase in ion backscattering. In the high-fluence limit, however, the simple approximations of Eq. 2 seem to hold quite well. This was found to be true for all cases of the present work.

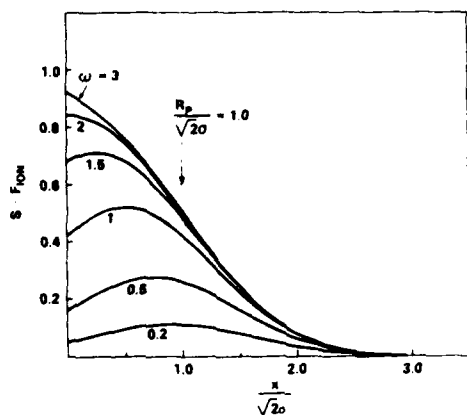


Fig. 2. Development of implanted ion distribution with increasing fluence for  $R_p/\sigma = \sqrt{2}$ .

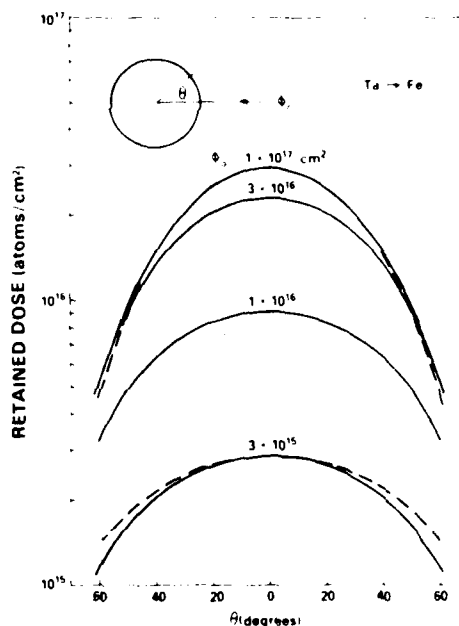


Fig. 3. Theoretical retention of implanted Ta ions as a function of incidence angle and normal fluence. Dashed lines are simplified versions of theory for low and high-dose limits. Measured values for  $R_p$ ,  $\sigma$  and  $S_0$  were 206Å, 122Å, and 6.0, respectively.

### Experimental

Because theory predicted a more general result for retention in the high-fluence limit, comparison with experiment was first conducted in that regime. Fig. 4 shows the retention of various ions normalized to unity at  $\theta = 0^\circ$ . All fluences were selected to produce a steady state distribution in the target. For Ar- and Cr-implanted samples good agreement between theory and experiment was obtained. The slight discrepancy near  $60^\circ$  for the 304 stainless steel target implanted by Ti is believed caused by difficulties in the experimental measurement. These were associated with the small cylinder diameter and the translation approach to selecting  $\theta$ . Conversely, the slightly narrower shape to the distribution observed in Ti-implanted 52100 and somewhat more so in Ta-implanted M50 is believed to

be real. A similar narrower shape was also observed from Ta-implanted 52100 flat samples, the Ta-implanted 52100 cylinder, and the Ta-implanted Fe film on Al cylinder.

To assess where the model was failing in Ti and Ta-implanted steel, the absolute retention of Ta in M50 and 52100 cylinders was determined as a function of incident angle and fluence. Only results for the 52100 cylinder are shown in Fig. 5, although analogous results were obtained from the M50 cylinder. For fluences up to about  $1 \times 10^{16}/\text{cm}^2$ , theory agreed within experimental accuracy with the data. However, at higher fluences where sputtering becomes important, much more retention was measured at all angles than was predicted by the Schulz and Wittmaack theory, even though the input values for  $R_p$ ,  $\sigma$  and  $S_0$  had been measured in Fe thin-film samples.

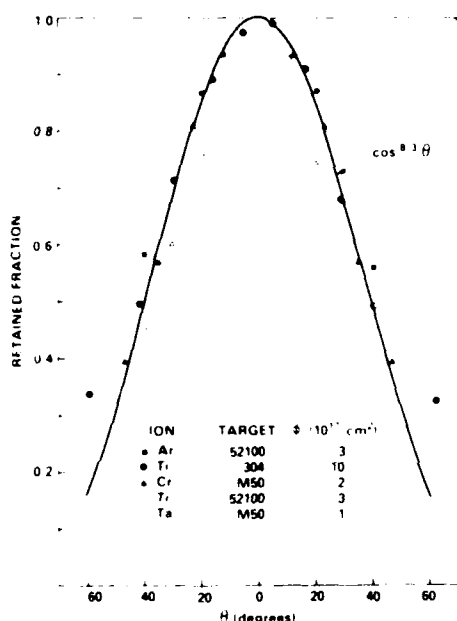


Fig. 4. Normalized retained dose in the high-dose limit from simplified theory and from measurements on steel cylinders. Data points at normal incidence were not plotted.

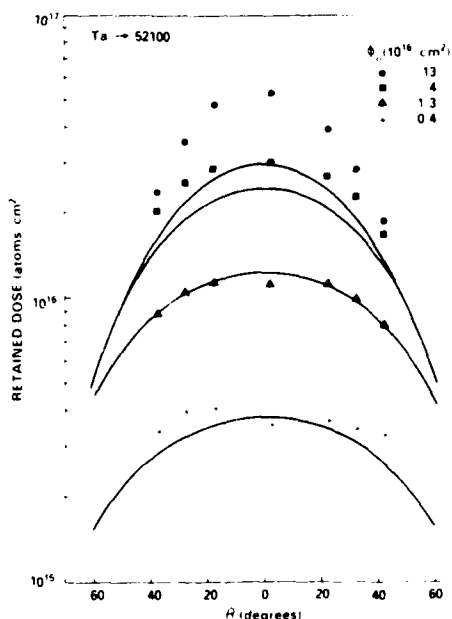


Fig. 5. Retention of implanted Ta in 52100 cylinder as function of fluence and incidence angle for theory and experiment. Theory used measured  $R_p$ ,  $\sigma$  and  $S_0$  as input and same fluences as experiment.

A more elaborate calculation of retention versus fluence at normal incidence was performed for Ta implantation, based on the model of Krautle [4]. This model includes the effects of target swelling, range shortening, and preferential sputtering, but not migration. This model, like the Schulz and Wittmaack model, predicts a plateau level for the atomic fraction of beam atoms beneath the surface. This level is equal to  $1/S$  where  $S$  is the total sputtering coefficient of both ion and target atoms. Target swelling and range shortening alone reduced the saturation retained dose of Ta by about 5%. Including preferential sputtering (which alters  $S$ ) could drive theoretical retention towards the experimental results, but the change in  $S$

required was unrealistic when compared to the values measured from Fe thin-film samples.

A plausible explanation of the discrepancy shown in Fig. 5, then, is that preferential removal of Fe combined with ion mixing resulted in the increased retention of Ta, distributed over about the range of the incident ion. This is in fact the model discussed by Liao and Mayer [5]. From this model it can be shown that the steady state distribution of implanted ions can again be represented by a step function of width about  $R_p$  and height (in atom fraction of beam atoms) equal to  $1/S_{ion}$ , where  $S_{ion}$  is the sputter coefficient for ions incident on themselves as a pure target. Therefore, this new model predicts approximately the same dependence on angle as described by Eq. 2, with the amplitude scaled by approximately the ratio of  $S$  to  $S_{ion}$ . In the present work this implies that  $S_{ion}$  for Ta should be about 3. Ongoing research at NRL will attempt to determine whether this assessment is correct. Considering this latter model to be correct, perhaps the slight discrepancy between experiment and Eq. 2 in Fig. 4 is caused by variations in the preferential removal of Fe or in ion mixing, with changing angles of incidence. This might be related to the carburization process which is known to occur during the implantation of Fe by reactive metal ions like  $Ti^+$  and  $Ta^+$ .

## CONCLUSIONS

The experimental data suggest that the preferential removal of Fe combined with ion mixing during implantation with Ta is necessary to explain the fluence dependence of Ta retention observed in steels. It is not clear from the present results whether these processes also occur during the implantation of Ar, Ti, or Cr ions into these same steels.

Nevertheless, in the high-fluence limit the retention of all these ions follows quite closely a  $(\cos \theta)^{8/3}$  dependence, where  $\theta$  is the angle between the beam direction and the surface normal. A slightly stronger decay with increasing angle of incidence does appear to occur for Ta and sometimes Ti-ion implantations. At lower fluences the retained dose falls off more gradually with increasing  $\theta$  but may never quite approach the  $\cos \theta$  dependence expected at low fluences from simple arguments, since an increase in ion backscattering occurs at large angles of incidence.

## ACKNOWLEDGMENTS

The authors are indebted to R.A. Jeffries for early x-ray measurements, C.M. Davisson for her model calculations, and to F.D. Correll for his help with some RBS measurements.

## REFERENCES

1. I.L. Singer and R.A. Jeffries, these proceedings.
2. F. Schulz and K. Wittmaack, Rad. Eff. 29, 31(1976).
3. P. Sigmund, Phys. Rev. 184, 383(1969).
4. H. Krautle, Nucl. Instrum. Methods 134, 167(1976).
5. Z.L. Liao and J.W. Mayer in: Treatise on Materials Science and Technology, Vol. 18, Ion Implantation, J.K. Hirvonen, ed. (Academic, New York 1980) ch. 2, pp. 17-50.

Section I.I.

BINARY COLLISION CASCADE CALCULATION OF SPUTTERING FROM  
Cu-Ni ALLOYS BY 90 KeV Cu and Ni IONS

M. Rosen<sup>1</sup>  
R. H. Bassel<sup>2</sup>

<sup>1</sup>Radiation Matter Interactions Branch  
Condensed Matter & Radiation Sciences Division  
Naval Research Laboratory

<sup>2</sup>Materials Modification & Analysis Branch  
Condensed Matter & Radiation Sciences Division  
Naval Research Laboratory

This work was supported by the Office of Naval Research.

## BINARY COLLISION CASCADE CALCULATION OF SPUTTERING FROM Cu-Ni ALLOYS BY 90 keV Cu AND Ni IONS

Mervine ROSEN and Robert H. BASSEL

Naval Research Laboratory, Washington, DC 20375, USA

Total and elemental sputtering yields, and angular and energy distributions of sputtered atoms, are calculated as a function of surface composition for the cases of 90 keV Cu and Ni ions, respectively, normally incident on Cu-Ni binary alloy targets using the binary collision cascade code MARLOWE. The results are compared with experiment.

### 1. Introduction

The use of ion implantation for modifying metallic surfaces is becoming an accepted technique for the production of specialized alloy structures in industrial applications. High energy, large fluence irradiations are required for these processes. In order to gain an understanding of the mechanisms involved, it is important to study the mutual dependence of the changing atomic surface fractions and target sputtering yields in this high fluence regime. Experimental results have recently been reported for the high fluence implantation of polycrystalline elemental Cu and Ni targets by 90 keV Ni and Cu ions, respectively [1-3]. Sputtering yields, atomic surface fractions and angular distributions were measured as a function of fluence up through the steady state. We have examined these data using the binary collision cascade code MARLOWE (version 11) [4-6]. We discuss the model used in section 2, below, and the total and partial sputtering yields obtained in section 3. The angular and energy distributions we obtained for the sputtered atoms are examined in section 4.

### 2. The computational model

The computational model used by the code MARLOWE for sputtering calculations is amply described in refs. [4-6]. As in our earlier study of the self sputtering of Cu and Ni at 90 keV [7], we used targets having finite thickness (11 lattice spacings). For both Cu and Ni we took the low energy cut off and the minimum displacement energy to be 5 eV. All the MARLOWE calculations were performed using a zero surface binding energy,  $U_s$ , and an auxiliary code used to impose a planar surface binding energy condition on the atoms that had escaped the surface. In this way sputtering yields, angular and energy distributions could be explored easily as a function of  $U_s$ . The Moliere

interatomic potential was used with the screening radius of ref. [4].

We modeled the target as a polycrystalline binary mixture of Cu and Ni. The probability that during any collision a target atom was of a particular species (or the other) was determined stochastically by the atomic fraction of that species, i.e. the collisions were stoichiometric and we assumed a uniform stoichiometry throughout the target. This is reasonable since our calculations in ref. [7] show that, in the cascade model, the sputtering is not significantly affected at this energy by collisions that occur more than approximately 11 lattice spacings below the surface. This is also found in the present calculation as seen in fig. 5 below. In addition Reynolds et al. [8] have shown that for 90 keV implantation, the steady state implanted species depth profile does not begin to drop off till a depth of approximately 10 nm.

The lattice spacings used in this calculation were a weighted linear average of the elemental lattice spacings the weights being the respective atomic fractions (Vegard's Law).

### 3. Sputtering yields

We calculated partial and total sputtering yields for three stoichiometries (including the steady state) for 90 keV Cu ions normally incident on an originally elemental Ni target (corresponding to three incident fluences) and for the steady state surface fraction for Ni incident on Cu. The atomic fractions used were obtained from the optical emission spectra of Reynolds [3]. This was justified by the results of Reynolds et al. [8] who showed that the optical emissions tracked the surface atomic fractions well.

For the Cu on Ni irradiation, we calculated the yields for the atomic fractions (94% Ni, 6% Cu), (88% Ni, 12% Cu) and (77% Ni, 23% Cu), the last set being the steady state atomic surface fraction. As a compar-

Table 1

Sputtering yields ( $S$ ) from MARLOWE for 90 keV Cu incident on Ni and Ni incident on Cu, respectively, as a function of the atomic surface fraction of Cu

Cu fraction (%)	$S(\text{Ni})$	$S(\text{Cu})$	$S(\text{total})$
<b>Cu on Ni</b>			
6	$3.52 \pm 0.5$	$0.22 \pm 0.05$	$3.74 \pm 0.5$
12	$3.41 \pm 0.5$	$0.53 \pm 0.1$	$3.94 \pm 0.5$
23	$3.42 \pm 0.4$	$0.97 \pm 0.1$	$4.39 \pm 0.4$
<b>Ni on Cu</b>			
77	$1.07 \pm 0.16$	$3.20 \pm 0.38$	$4.27 \pm 0.4$

son, for the Ni irradiation we used the steady state fraction (23% Ni, 77% Cu). Values of surface binding energy are not well known. In order to fit the self sputtering yields (and angular distributions) for Cu and Ni, values for  $U_s$  of 5.0 eV and 6.0 eV, respectively, were used. For our present calculations we found it adequate to use a common value for both Cu and Ni of 5.5 eV. The results are shown in table 1.

The sputtering yields are seen to be stoichiometric, e.g. for the Ni on Cu steady state yield shown, the Cu partial sputtering yield is 75% of the total yield. Similar results obtain for the Cu on Ni irradiations. Indeed we found that this result holds independently of the surface binding energy. We varied  $U_s$  from 4.5 eV to 7.0 eV for each case and found, as expected, that both partial and total sputtering yields varied approximately inversely with  $U_s$  and that the yields were always distributed stoichiometrically. This seems to imply that the sputtered Cu and Ni angular and energy distributions are indeed very much alike. We shall see below that this is so. The last two rows in table 1 corroborate the experimental finding that these two are the steady state surface fractions.

It is interesting to compare these results with those predicted by the formula of Haff and Switkowski [9] which predicts similar behavior. These are given in table 2. The agreement of the partial scattering yields is clear.

Table 2

Sputtering yields ( $S$ ) from Haff and Switkowski [9] for  $U_s = 5.5$  eV

Cu fraction (%)	$S(\text{Ni})$	$S(\text{Cu})$	$S(\text{total})$
<b>Cu on Ni</b>			
6	4.22	0.27	4.51
12	3.96	0.54	4.50
23	3.49	1.04	4.53
<b>Ni on Cu</b>			
77	1.07	3.59	4.66

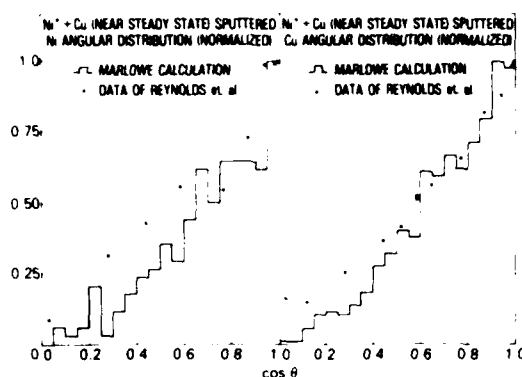


Fig. 1. The angular distributions of sputtered Ni and Cu atoms for the case of 90 keV Ni implantation of Cu near steady state fluence. The data are that of Reynolds et al. [1]. Both experimental and calculated distributions are normalized to unity at zero exit angle.

#### 4. Angular and energy distributions

Reynolds et al. [1] have measured the angular distributions of sputtered Cu and Ni atoms at near steady state fluence for 90 keV Ni ions incident on Cu. Their results are depicted in fig. 1, together with the results of the MARLOWE calculation. The experimental distribution was normalized to unity at zero exit angle, and so we have normalized the MARLOWE distribution in the same way. Due to a statistical fluctuation in the lowest exit angle bin, this had the effect of artificially pushing the whole calculated Ni distribution down a bit too much. With this in mind, the general agreement is clear, both distributions being very similar. Within statistical errors, both experimental and calculated distributions

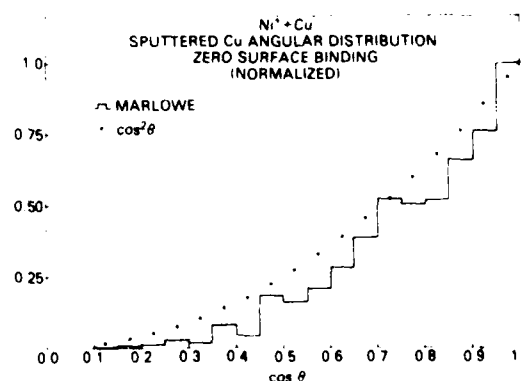


Fig. 2. The calculated sputtered Cu angular distribution for the case of 90 keV Ni implantation of Cu at near steady state fluence. Zero surface binding energy was assumed for this distribution.

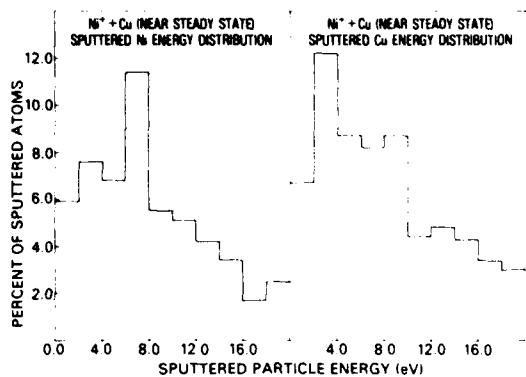


Fig. 3. Calculated energy spectra for sputtered Ni and Cu atoms in the low energy regime (less than 20 eV) for the case of 90 keV Ni implantation of Cu at near steady state fluence.

show a  $\cos \theta$  dependence for both atomic species. This is not independent of the surface binding energy, however. If zero surface binding is assumed, the calculated angular distribution exhibits a  $\cos^2 \theta$  dependence on the sputtering angle. This is illustrated in fig. 2 for near steady state fluence.

The calculated energy distributions of both sputtered species for the steady state implantation of Ni into Cu are shown in figs. 3 and 4 for the low energy (less than 20 eV) and high energy (up to 140 eV) regimes, respectively. In both regimes, the distributions for both Cu

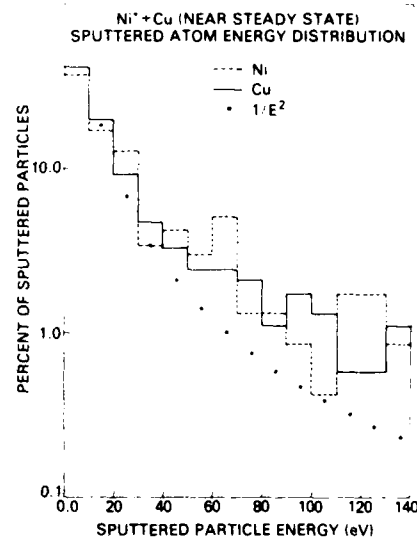


Fig. 4. Energy spectra in the high energy regime (up to 140 eV) for the same case as in Fig. 3.

and Ni are much the same. This, and the similarity in the angular distributions are in line with the conclusions of Anderson and Sigmund [10] that the only significant deviations from stoichiometry occur for the case of extreme mass ratios, and is probably also the explanation for the surface binding energy independence of the

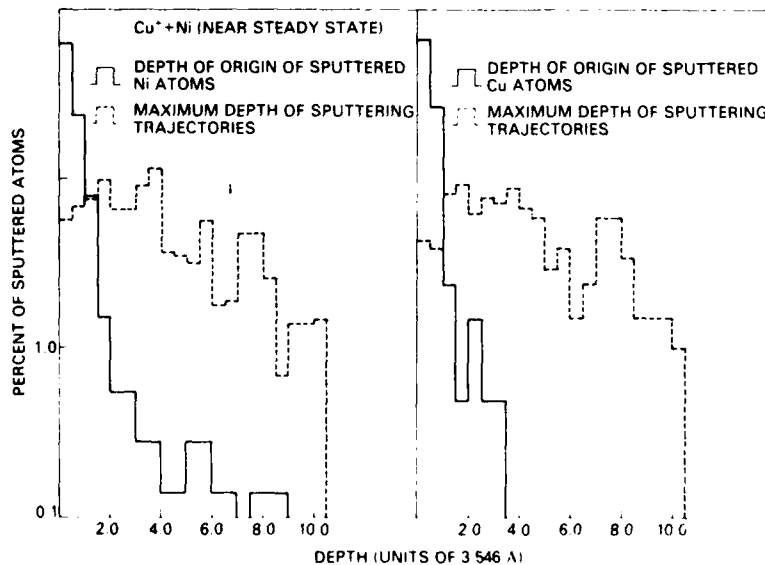


Fig. 5. Comparison of calculated depth distributions of sites of origin of sputtered Ni and Cu atoms to the distribution of maximum depths of their respective sputtering trajectories for the near steady state implantation of Ni by 90 keV Cu.

stoichiometric splitting of the total sputtering yields among the partial yields of the sputtered atoms. It is interesting to note that the low energy distribution for a 90 keV implantation of Ni, as shown in fig. 3, is very much the same as that calculated for 0.9 keV Ar atoms normally incident on amorphous Cu [6] and, as shown in that reference, with the distribution measured from polycrystalline Cu by Oechsner [11].

We have also examined the sputtering cascades for both the Cu and Ni irradiations. We trace the chain of collisions back from each sputtered atom, collision by collision, to the deepest point in the target that the chain reaches - this we call a sputtering trajectory [7]. The set of such trajectories we term a sputtering cascade. In fig. 5 we show for the Cu on Ni irradiation, the distributions of the depths of origin of both the sputtered Cu and Ni atoms and the distributions of the maximum depths of the sputtering trajectories. Again the Cu and Ni distributions are essentially the same and also are similar to the distributions found for self ion sputtering [7]. We did find a decrease (from 20% to 15%) in the number of Cu and Ni sputtering trajectories that contain replacement sequences of length 3 or greater from the number found for self ion sputtering. Although one expects this value to be sensitive to mass differences, the change found here may be just a statistical fluctuation.

## 5. Conclusions

We have shown that high energy heavy atom binary alloy sputtering angular distributions and sputtering yields can be accounted for by a binary collision cascade

model such as that used in MARLOWE. The partial sputtering yields calculated were found to be stoichiometric for all the atomic surface fractions we considered, independent of the surface binding energy. The energy and angular distributions and the structure of the sputtering cascades of both sputtered species were found to be alike.

## References

- [1] G.W. Reynolds, F.R. Vozzo, R.G. Allas, A.R. Knudson, J.M. Lambert and P.A. Treado, in *Metastable materials formation by ion implantation*, eds., S.T. Picraux and W.J. Choyke (North-Holland, Amsterdam, 1982) p. 198.
- [2] J.M. Lambert, P.A. Treado, D. Trbojevic, R.G. Allas, A.R. Knudson, G.W. Reynolds and F.R. Vozzo, *IEEE Trans. Nucl. Sci.* NS-30 (1983) 1285.
- [3] G.W. Reynolds, *Nucl. Instr. and Meth.* 209/210 (1982) 57.
- [4] M.T. Robinson and I.M. Torrens, *Phys. Rev. B* 9 (1974) 5008.
- [5] M. Hou and M.T. Robinson, *Nucl. Instr. and Meth.* 132 (1976) 641.
- [6] M. Hou and M.T. Robinson, *Appl. Phys.* 18 (1979) 381.
- [7] M. Rosen, G.P. Mueller and W.A. Fraser, *Nucl. Instr. and Meth.* 209/210 (1983) 63.
- [8] G.W. Reynolds, A.R. Knudson and C.R. Gossett, *Nucl. Instr. and Meth.* 182/183 (1981) 179.
- [9] P.K. Haff and Z.E. Switkowski, *Appl. Phys. Lett.* 29 (1976) 549.
- [10] N. Anderson and P. Sigmund, *Mat. Fys. Medd. Dan. Vid. Selsk.* 39 (1974) no. 3.
- [11] H. Oechsner, *Z. Physik* 238 (1970) 433.

Section II.A

SURFACE CHEMISTRY AND FRICTION BEHAVIOR  
OF Ti-IMPLANTED 52100 STEEL

I. L. Singer<sup>1</sup>  
R. A. Jeffries<sup>2</sup>

<sup>1</sup>Surface Chemistry Branch  
Chemistry Division  
Naval Research Laboratory

<sup>2</sup>Geo-Centers, Inc.  
Suitland, Maryland 20746

This work was supported by the Office of Naval Research.

# Surface chemistry and friction behavior of Ti-implanted 52100 steel

I. L. Singer

Chemistry Division, Naval Research Laboratory, Washington, D.C. 20375

R. A. Jeffries

Geo-Centers, Inc., Suitland, Maryland 20746

(Received 5 October 1982; accepted 9 November 1982)

Auger spectroscopy, EDX, and optical microscopy have been used to analyze the friction and wear behavior of 52100 steel couples, one modified by Ti implantation ( $5 \times 10^{16}$  Ti/cm<sup>2</sup> at 190 keV). A low friction coefficient,  $\mu_k = 0.3$ , was measured on surfaces that were carburized by high fluence ( $> 16 \times 10^{16}$  Ti/cm<sup>2</sup>) implantation. A fully carburized layer, produced at  $50 \times 10^{16}$  Ti/cm<sup>2</sup>, resisted wear and retained the low friction coupling. Partially carburized layers, produced at 16 and  $20 \times 10^{16}$  Ti/cm<sup>2</sup>, gave an initially low friction coupling,  $\mu_k = 0.3$ , but after 6–10 passes, the partially carburized layer was sheared off exposing the underlying Fe–Ti alloy layer, and the friction coefficient rose to  $\mu_k = 0.8$ . A high friction coefficient,  $\mu_k = 0.8$ , was also measured on initial sliding contact with a surface implanted to a low fluence ( $5 \times 10^{16}$  Ti/cm<sup>2</sup>). High friction is attributed to high adhesion between Fe in the slider and the Fe–Ti alloy found in the surface. Continued sliding contact (in air) against the Fe–Ti surface oxidized the Ti and Fe, and the friction coefficient dropped to a value of  $\mu_k = 0.6$ , characteristic of the nonimplanted sliding couples.

## I. INTRODUCTION

Applications of ion implantation to tribology have been mainly concerned with finding the appropriate implant species to improve the tribological properties of materials.<sup>1–4</sup> One of the more successful candidates for reducing friction and wear of steels has been Ti implantation. High fluence Ti implants have produced low friction,<sup>1–5</sup> abrasion resistant,<sup>6</sup> and scuff resistant surfaces.<sup>4,7</sup> Low fluence Ti implants, however, appear to give anomalously high friction coefficients and exhibit considerable surface wear.<sup>4</sup>

In this paper we examine the tribological behavior of alloyed surfaces, using ion implantation to change the composition of a hardened steel surface. We intend to establish a chemical basis for the aforementioned friction and wear behavior of Ti-implanted steel. Auger electron spectroscopy (AES) and energy dispersive x-ray analysis (EDX) are used to examine the composition of as-implanted surfaces and scars produced by low speed, unlubricated ball-on-flat sliding conditions. Scanning electron microscopy (SEM) and several optical interference microscopies are used to examine surface textures.

## II. EXPERIMENTAL

### A. Kinetic coefficient of friction

Friction measurements were carried out in air ( $\sim 50\%$  RH) at room temperatures at a sliding velocity of 0.1 mm/s. The sliders were 1.27 cm diameter AISI 52100 steel balls which were in contact with steel disks 0.95 cm in diameter and 0.32 cm thick. The applied force was 9.8 N. The first passes were 5 mm in length; subsequent passes over the same track were 3 mm each.

Disks were hardened ( $R_c = 60$ ) AISI 52100 steels (1 C, 1.5

Cr, balance Fe) polished to a metallographic finish. During implantation in NRL's modified Varian/Extrion implanter, disks were heat sunk onto a water-cooled holder and kept near room temperature ( $< 40^\circ\text{C}$ ). Samples were implanted to fluences ranging between  $5$  and  $50 \times 10^{16}$  Ti/cm<sup>2</sup> with a 190-keV <sup>48</sup>Ti<sup>+</sup>-beam rastered to give current densities of  $J = 10$ – $20 \mu\text{A}/\text{cm}^2$ . The target chamber was cryogenically pumped to base pressures of 7 mPa ( $\sim 5 \times 10^{-7}$  Torr).

### B. Chemical analysis

Auger analyses were performed in one of two UHV chambers: one equipped with a Perkin-Elmer (PHI) model of 545 microprobe, the other with a model 590 microprobe (spatial resolution  $< 1 \mu\text{m}$ ). Auger derivative spectra were taken with electron beam energies  $V_e = 2$  or  $5 \text{ keV}$  and recorded at  $V_{mod} = 3$  or  $6 \text{ eV}$  modulation amplitudes either directly or by a peak-height recording multiplexer. Depth profiles were recorded during ion milling with a rastered 2-keV-Ar-ion beam.

Quantitative Auger analysis was performed with the standard normalizing formalism<sup>8</sup>:

$$\chi_i = \frac{I_i/S_i}{\sum_j I_j/S_j}$$

where  $\chi_i$  is the atomic concentration of element  $i$ ,  $I_i$  is the Auger peak to peak intensity and  $S_i$  is the Auger sensitivity factor for a given Auger peak.

Sensitivity factors for Fe<sub>650</sub>, Ti<sub>420</sub>, and C<sub>272</sub> lines were obtained by analyzing reference compounds as well as using nuclear backscattering data of the implanted steels.<sup>9,4</sup> The Fe<sub>650</sub> and Ti<sub>420</sub> require different sensitivity values for oxides and metal; Ti<sub>420</sub> uses the same value for both metal and car-

TABLE I. Auger peak-to-peak sensitivity factor for C, Ti, O, and metal (or carbide) and oxide-like spectra of Ti and Fe

$V_e$ (keV)	$V_{mod}$ (eV)	C	O	Ti(420 eV)		Fe(650 eV)	
				metal	oxide	metal	oxide
2	3	0.50	0.50	0.48	0.42	0.17	0.21
5	3	0.35	0.48	0.34	0.30	0.18	0.22
5	6	0.31	0.39	0.21	0.19	0.15	0.18

bide. The values used to calculate atomic concentrations are listed in Table I. Sensitivity factors were determined for  $V_e = 2$  and 5 keV electron beams and a modulation voltage of 3 eV; they were later scaled for a 5-keV-beam and a modulation voltage of 6 eV.<sup>9</sup>

Energy dispersive x-ray analysis (EDX) was performed on an Advanced Metal Research model 1000 scanning electron microscope (SEM) fitted with a Kevex model 5100 spectrometer. The electron gun provided a 20-keV-beam on incidence 45° from normal. At this energy, electrons excite x-rays to a depth of about 1.5  $\mu\text{m}$  in steel.<sup>10</sup> Since this excitation depth is about ten times greater than the Ti implant depth, we may take the  $Ti_{K\alpha}/Fe_{K\beta}$  ratio proportional to the Ti concentration.

Surface textures were examined in wear tracks using differential interference contrast and Michelson interference objectives. Depth scales for ion-milled surfaces were established by masking surfaces, then measuring crater depths with interferometry.

### III. RESULTS

#### A. Chemistry of the as-implanted surface

The composition of a Ti-implanted steel depends strongly on the ion energy and fluence chosen, because of sputtering effects and the incorporation of carbon from the vacuum system.<sup>4,11</sup> At low fluences an implant-alloyed surface consists solely of the implanted Ti plus the host constituents. At higher fluences, a third component C can enter the surface from the vacuum system. This carburization effect with increasing fluence can be observed in the composition profiles of Fig. 1, which depict the Ti and excess carbon concentrations<sup>12</sup> obtained by Auger analysis for 52100 steel implanted at 190 keV to fluences of 5, 16, and 50  $\times 10^{16}$  Ti/cm<sup>2</sup>. At 5  $\times 10^{16}$ /cm<sup>2</sup>, the surface is principally an Fe-Ti alloy; at 50  $\times 10^{16}$ /cm<sup>2</sup> the Fe-Ti alloy has been carburized; at 16  $\times 10^{16}$ /cm<sup>2</sup> the alloy is only partially carburized. Similar Ti and C profiles have been obtained independently by nuclear backscattering analyses.<sup>1,11</sup> Not indicated in Fig. 1 are the oxide layers which are typically as thick as those formed on polished steels ( $\sim 3$  nm),<sup>14</sup> but contain a thin TiO<sub>2</sub> layer directly below the Fe oxide layer. The TiO<sub>2</sub> layers had Ti concentrations approximately that of the Ti concentration at the metal oxide/metal interface. More details of the composition and chemical states of the Ti and C are given in Ref. 4. Hereafter, we denote surfaces implanted to fluences approximately those of Figs. 1(a)-(c) as "low, medium, and high" fluence surfaces.

#### B. Tribological behavior

High and low fluence surfaces gave two extremes in friction contact between a 52100 steel ball sliding against a Ti-implanted surface. High fluence surfaces had a nearly constant coefficient of friction ( $\mu_k \sim 0.3$ ) from the first pass on. In addition, no wear occurred as indicated by the nearly identical textures inside and outside the wear track and by the parallel lines in the interferogram of the track [Fig. 2(c)]. Occasionally an abrasivelike scratch could be found, but the friction coefficient was unaffected.

Low fluence surfaces showed initially (one to three passes) a high friction coefficient which dropped asymptotically (in three to seven passes) to a value of  $\mu = 0.6$ , identical to that of 52100 steel sliding against itself. Fine (submicrometer) debris flakes were distributed across the wear tracks after one pass; yet no measurable ( $< 5$  nm) wear could be seen on interferograms [Fig. 2(a)]. Subsequent passes produced larger and thicker debris flakes ( $\sim 500$  nm) but still no substantial wear ( $< 10$  nm) of the surface. A debris flake (Fig. 3) which formed on a ball after five passes had a thickness of 500 nm.

Medium fluence surfaces exhibited a friction coefficient which was initially low, occasionally with stick-slip, but rose linearly with each pass to a value of  $\mu_k = 0.8$  (after six to ten passes). Wear tracks were initially unblemished, except for some circular patches from stick-slip events. By the time the high friction plateau was reached, the wear tracks had developed scars 30–50 nm deep (depending on fluence) [Fig. 2(b)].

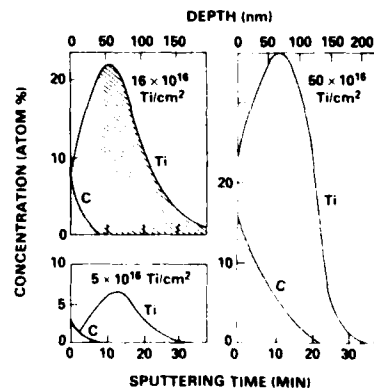


FIG. 1. Auger composition vs depth profiles of Ti and excess C (i.e., above bulk 4 at %) in 52100 steel implanted with Ti to three fluences at 190 keV (see the text for significance of cross-hatched area). Depth scales are from interferograms of ion-milled craters.

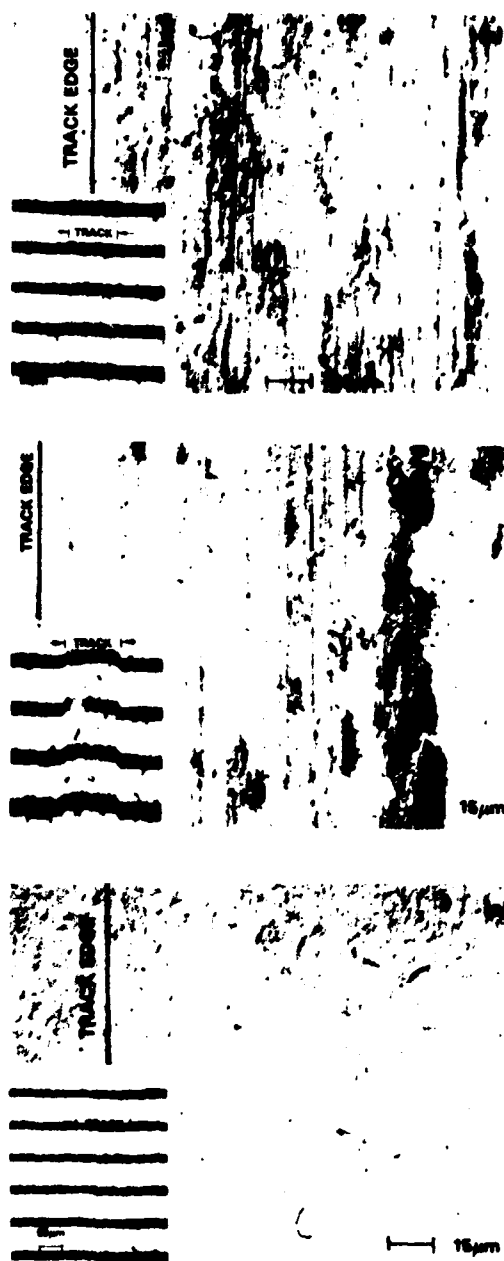


FIG. 2 Optical micrographs of wear tracks on Ti-implanted 52100 steel disks. Differential interference contrast photos with interferograms in insets (fringe spacing = 273 nm). (a) Low fluence (first pass  $\mu_k = 0.6$ ), (b) medium fluence (tenth pass  $\mu_k = 0.8$ ), (c) high fluence (fifteenth pass  $\mu_k = 0.3$ ).

The tracks were rectangular troughs, i.e., uniformly deep across their width, not semicircular as would conform to plowing by the ball; they also contained a few patches of debris [Fig. 2(b)]. After remaining at the plateau level for four to six passes, the friction coefficient dropped asymptotically to a steady state value of  $\mu_k \approx 0.6$ . At steady state, the wear tracks retained their rectangular trough scars (40–60 nm deep) but accumulated more debris flakes.

### C. Composition of wear tracks and debris

Low fluence surfaces were heavily disturbed by sliding contact yet showed no apparent wear. Energy dispersive x-ray analysis (EDX) in and out of debris-free regions of the tracks gave identical  $Ti_{K\alpha}/Fe_{K\beta}$  ratios ( $\pm 10\%$ ) confirming that no significant amount of material had been removed.

Nonetheless, a debris flake approximately 500 nm thick had built up on a ball after five passes against a low fluence surface. A SEM micrograph of the flake, shown in Fig. 3(a), indicates layers stacked on top of one another. An Auger depth profile of a spot (10  $\mu m$  in diameter) on the flake quickly reached the steady state spectrum shown in Fig. 3(b). This spectrum had a  $Ti_{KLL}$  line shape of  $TiO_2$ <sup>15</sup> and a  $Fe_{MIV}$  line shape of oxidized Fe.<sup>16</sup> The composition, determined from Auger sensitivity factors, was  $Fe_4Ti_3O_{11}$ , or taking into account the chemistry, 3%  $TiO_2$  in an Fe/Fe oxide matrix.<sup>17</sup>

Auger analysis of the as-implanted oxide layer also indicated a  $TiO_2$  concentration of 3 at.%, reflecting a 1 at.% Ti at the metal oxide/metal interface [Fig. 1(a)]. The debris and the oxide layer, therefore, have approximately the same composition.

Medium fluence surfaces were analyzed by both EDX and Auger spectroscopy in tracks representing the high friction plateau and in tracks formed after the friction coefficient reached steady state. EDX analyses of debris-free regions in the high friction track shown in Fig. 2(b) found two thirds the Ti detected in the as-implanted surface. Two thirds of the Ti in the implanted surface resides below a depth of 45 nm, as indicated by the cross-hatched area of Fig. 1(b); the outer third is in the partially carburized surface layer. Therefore, the 45-nm-track depth after ten passes is due to wear, and not to plastic deformation. Repetitive sliding contact appears to have "sheared" off the partially carburized layer, which would explain the rectangular-trough shape of the track.

Auger analysis also confirmed that partially carburized layers were sheared off medium fluence surfaces. Auger depth profiles from regions in and out of a 14 pass track (steady state  $\mu_k = 0.6$ ) are presented in Fig. 4. All three profiles were obtained concurrently during 2-keV-Ar ion milling. The as-implanted surface (spot a) and debris-free region of the track (spot b) both show a bell-shaped Ti concentration profile. The partially carburized layer, however, is missing from the in-track profile as the greatly reduced excess carbon profile attests. The in-track profile, however, does contain more oxygen and to a greater depth than the as-implanted surface. The track also sputtered somewhat slower than the as-implanted surface (presumably because oxides sputter slower than metals) which obscured an expected 50 nm se-



FIG. 3. SEM photos of debris flake on ball after five passes against a 52100 steel flat implanted to  $5 \times 10^{17} \text{ Ti}^{3+} \text{ cm}^{-2}$ . Inset: Auger derivative spectrum of spot during Ar ion sputtering. Auger conditions:  $E_{\text{ion}} = 5 \text{ keV}$ ,  $I_{\text{ion}} = 1 \text{ nA}$ .

paration of Ti peak depths based on track depth measurements. EDX analysis indicated that the debris-free region of this track had 60% as much Ti as the as-implanted surface.

Debris flakes covered a substantial portion ( $\sim 20\%$ ) of this track. An Auger depth profile of a typical debris flake (spot cf) is shown in Fig. 4. The composition which quickly reached steady state was  $\text{Fe}_{10}\text{Ti}_1\text{O}_{11}\text{C}_{11}$ . The  $\text{Ti}_{\text{AKL}}$  spectrum [in Fig. 4(c)] is that of  $\text{TiO}_2$ , which suggests that the debris had 21 at.%  $\text{TiO}_2$  mixed in with metallic Fe and Fe oxide. A sampling of debris flakes in medium fluence tracks and on balls gave  $\text{TiO}_2$  concentrations from 10–30 at. %

#### IV. DISCUSSION

The tribological behavior of Ti-implanted steels depends on the final composition of the implanted surface; more specifically, it depends on the degree to which the surface develops a carburized layer. In accordance with Fig. 1, surfaces implanted at an energy of 190 keV/ion to fluences of 5, 16, and 50 ions/ $\text{cm}^2$  can be considered noncarburized, partially carburized, and highly carburized. (At lower energies, similar degrees of carburization can be produced at lower fluences.)<sup>1b</sup> Highly carburized surfaces have low friction co-

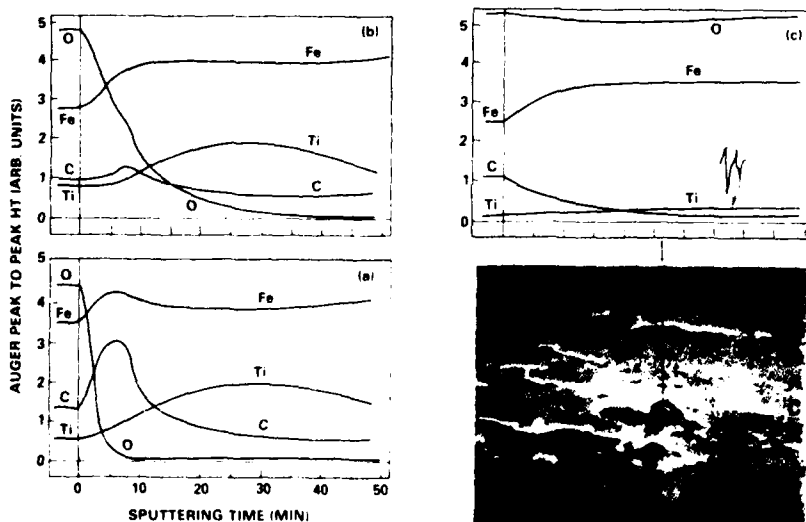


FIG. 4. Auger microprobe analysis of wear track. SEM photo of track area in medium fluence disk worn to steady state (14 passes). Auger microprobe spectra: (a) out of track, (b) debris-free in track, (c) debris flake in track. [Auger conditions:  $E_{\text{ion}} = 5 \text{ keV}$ ,  $I_{\text{ion}} = 3 \text{ nA}$  for  $\text{Ti}_{\text{AKL}}$  and  $\text{O}_{\text{AKL}}$ ,  $E_{\text{exc}} = 6 \text{ eV}$  for  $\text{C}_{\text{AKL}}$  and  $\text{Fe}_{\text{AKL}}$ ].

efficients ( $\mu_k \sim 0.3$ ) and resist wear in sliding contact with steel. Low or noncarburized surfaces, by contrast, have high friction coefficients and are heavily textured by sliding contact. Partially carburized surfaces can display both behaviors; initially the surface resists wear, and except for occasional stick-slip, gives a low friction coefficient [ $\mu_k$  (average)  $\sim 0.3$ ]. During the next six to ten passes, however, a 30–50-nm-thick layer is worn off the track and the friction rises to  $\mu_k \sim 0.8$ . Auger and EDX analyses have shown that this wear corresponds to shearing off the partially carburized layer. Sliding in this track, as during initial contact with the low fluence track, brings steel in contact with an Fe–Ti alloy.

The high coefficients of friction ( $\mu_k \sim 0.8$ ) can be attributed to the contact of steel (plus debris) against the Fe–Ti alloy. Miyoshi and Buckley have studied the friction and adhesion of several Fe-based alloys.<sup>19</sup> They found that Fe–Ti alloys are more adherent than Fe itself, and the enhanced adhesion leads to higher friction during sliding. Buckley attributes the high adhesion of the Fe–Ti alloy addition to the high chemical activity of the Ti (more specifically, to the low percentage of *d*-band metallic bonding).<sup>20</sup>

The wear associated with enhanced adhesion of the Fe–Ti alloy surfaces appears to be a form of mild adhesive wear,<sup>21,22</sup> in which the oxide of the Fe–Ti surface adhered to the ball and was sheared off the flat at the metal oxide/metal interface. Wear debris began to form early during high friction sliding contact [Fig. 2(a)]. Fine debris accumulated on the ball and, even after five passes, the flake which formed was only approximately 500 nm thick. Yet, little if any wear ( $< 10$  nm) could be detected on the flat. Very little metal is lost, however, during oxide wear. Even though an oxide formed on steel at room temperature is 3 nm thick,<sup>14</sup> it has twice the molecular volume per atom as Fe<sup>2+</sup> and more than 1/2 of its composition is oxygen from the air. Thus for every 3 nm of oxide removed, less than 1 nm of metal is consumed at a time.

This condition of oxide wear with high friction does not continue for long, as witnessed by the drop in friction to the steady state coefficient  $\mu_k = 0.6$ . At this point, the friction and wear behavior appear to be controlled principally by debris flakes on the ball sliding against debris flakes in a partially oxidized track. Auger analysis has shown that Fe oxide debris found on both low and medium fluence tracks contained from 3 to 30 at.% TiO<sub>2</sub> and the track itself has Ti. If, as claimed earlier, Ti alloy additions increase the adhesion and friction of Fe, why should debris containing 1%–10% Ti produce the same friction as the Ti-free debris? We suggest that oxidation neutralizes the excess chemical activity of Ti, and the friction is that of Fe/Fe oxide debris contact found in nonimplanted steel-on-steel ( $\mu_k = 0.6$ ).

In the present investigation, the implanted flats were subjected to what might be considered extreme sliding conditions matched in practice only by, for example, low speed cutting. We refer to the high Hertzian stresses (0.57 GPa), unlubricated sliding at very low speeds (0.1 mm/s). Under less severe conditions, even the medium fluence implants might survive more than the 6–10 passes which sheared the partially carburized layer in our severe wear test.

## V. CONCLUSIONS

(1) The tribological behavior of Ti-implanted AISI 52100 bearing steel depends critically on composition via the fluence.

(2) Low friction, no wear surfaces can be formed by implanting Ti at sufficiently high fluences to produce a highly carburized surface.

(3) Low or noncarburized surfaces give high friction contact, consistent with enhanced adhesion of Fe–Ti alloys, but mild adhesive wear.

(4) Partially carburized surfaces initially respond as low friction surfaces. However, after the carburized layer is removed and the underlying Fe–Ti is exposed, the friction coupling is that of an Fe–Ti alloy.

## ACKNOWLEDGMENTS

We thank Carmine Carosella for contributing to the early phase of this research, the Surface Modification and Materials Analysis Group at NRI for their cooperation with implantation, Ron Lee at Naval Surface Weapons Center for use of the 590 Auger microprobe and Elaine Shafrin for assistance with the Auger analysis.

<sup>1</sup> N. L. W. Hartley, *Ion Implantation* edited by J. K. Hirvonen, Academic, New York, 1980, p. 32.

<sup>2</sup> G. Dearnaley, in *Ion Implantation in Metallurgy* edited by C. M. Preece and J. K. Hirvonen, Metallurgical Society of AIME, Warrendale, 1980, p. 1. C. A. Carosella, I. L. Singer, R. C. Bowers, and C. R. Gossett, *Ion Implantation in Metallurgy*, Metallurgical Society of AIME, Warrendale, 1980, p. 105.

<sup>3</sup> I. L. Singer, C. A. Carosella, and J. R. Reed, *Nucl. Instrum. Methods* **182**, 183, 923 (1981).

<sup>4</sup> E. G. Yost, E. E. Pope, D. M. Tollstaedt, J. A. Knapp, and S. T. Pietrav, *Metastable Materials Formation by Ion Implantation* edited by S. T. Pietrav and W. J. Choyke, Elsevier, Amsterdam, 1982, p. 261.

<sup>5</sup> I. L. Singer, R. N. Bolster, and C. A. Carosella, *Thin Solid Films* **73**, 283 (1980).

<sup>6</sup> N. L. W. Hartley, to be published.

<sup>7</sup> *Handbook of Auger Electron Spectroscopy* edited by I. L. Davis, Physical Electronics Industries, Eden Prairie, Minnesota, 1976.

<sup>8</sup> G. E. McGuire, *Auger Electron Spectroscopy Reference Manual*, Plenum, New York, 1979.

<sup>9</sup> C. A. Anderson, in *The Electron Microscope*, Wiley, New York, 1966, p. 62.

<sup>10</sup> I. L. Singer and D. Larkas, *J. Vac. Sci. Technol. A*, these proceedings.

The bulk carbon concentration, 4 at.%, has been subtracted out.

<sup>11</sup> C. R. Gossett, *Nucl. Instrum. Methods* **191**, 335 (1981).

<sup>12</sup> K. Asami, K. Hashimoto, and S. Shimodaira, *Corrosion Sci.* **17**, 713 (1977).

<sup>13</sup> J. S. Solomon and W. L. Baum, *Surf. Sci.* **51**, 228 (1975).

<sup>14</sup> M. Seo, J. B. Tinsden, and R. W. Staehle, *Surf. Sci.* **50**, 541 (1975).

<sup>15</sup> The phases of Fe or Fe oxide cannot be determined from the composition analysis because of preferential oxygen sputtering; moreover, the debris may be a mixture of metallic and oxidized Fe.

<sup>16</sup> I. L. Singer and R. A. Jeffries, to be published.

<sup>17</sup> K. Miyoshi and D. H. Buckley, *NASA TP 1604*, 1980.

<sup>18</sup> D. H. Buckley, *Surface Effects on Adhesion, Friction, Wear and Lubrication*, Elsevier, Amsterdam, 1981, p. 391.

<sup>19</sup> E. Rabinowicz, *Friction and Wear of Materials*, Wiley, New York, 1965, p. 125.

<sup>20</sup> D. H. Buckley, *Surface Effects on Adhesion, Friction, Wear and Lubrication*, Elsevier, Amsterdam, 1981, p. 446.

<sup>21</sup> O. Kubaschewski and B. L. Hopkins, *Oxidation of Metals and Alloys*, Butterworths, London, 1962, p. 10.

Section II.B

EFFECTS OF IMPLANTATION ENERGY AND CARBON CONCENTRATION  
ON THE FRICTION AND WEAR OF TITANIUM-IMPLANTED STEEL

I. L. Singer<sup>1</sup>  
R. A. Jeffries<sup>2</sup>

<sup>1</sup>Surface Chemistry Branch  
Chemistry Division  
Naval Research Laboratory

<sup>2</sup>Geo-Centers, Incorporated  
Suitland, Maryland 20746

This work was supported by the Office of Naval Research and the NAVSEA Manufacturing Technology Program.

## Effects of implantation energy and carbon concentration on the friction and wear of titanium-implanted steel

I. L. Singer

Chemistry Division, Naval Research Laboratory, Washington, D.C. 20375

R. A. Jeffries

Geo Centers, Incorporated, Suitland, Maryland 20746

(Received 2 February 1983; accepted for publication 30 August 1983)

Dry sliding friction and wear measurements were used to evaluate two implantation processes which increase the C concentration in Ti-implanted steels. In the first process, Ti ions were implanted at a low energy (50 keV) in order to enhance the efficiency of vacuum carburization over what is achievable at higher energies (e.g., 190 keV). In the second, a dual implantation process, C ions were implanted into steels already implanted with Ti ions at high energy (190 keV). The first process produced a low friction ( $\mu = 0.3$ ), scuff resistant surface at a fluence of  $2 \times 10^{17}/\text{cm}^2$ , 40% lower than the fluence required for similar behavior by 190-keV implants. At fluences of  $2 \times 10^{17}/\text{cm}^2$  each, the dual implantation produced a modest decrease in friction ( $\mu = 0.5$ ), accompanied by stick slip, and some wear resistance compared to nonimplanted steel ( $\mu = 0.6$ ). Auger spectroscopy and energy-dispersive x-ray analysis were used to analyze the surface composition produced by the two processes at fluences of  $2 \times 10^{17}/\text{cm}^2$ . The dual implanted surface had more Ti, more C, and a greater C/Ti ratio than the low-energy implanted surface. The latter, however, had more C derived from vacuum carburization than the dual implanted surface. Both processes resulted in identical surface C concentrations. We concluded, therefore, that the improved tribological surface of Ti-implanted steel results from vacuum carburization and not just the presence of excess C.

PACS numbers: 61.70.Tm, 81.40.Pq, 82.80.Pv, 64.80.Eh

Ion implantation of metals is moving out of the laboratory and into practice as a surface processing technique for improving the wear life of engineering components. While much emphasis has been placed on N implantation for improving knives, dies, and punches subjected to mild abrasive and adhesive wear environments,<sup>1-3</sup> Ti implantation is receiving considerable attention in the bearing and tool steel community<sup>4,5</sup> because of its ability to reduce friction and wear on hardenable steels subjected to severe wear conditions.<sup>6-9</sup>

The improved tribological properties of Ti-implanted steels have been attributed to a unique surface alloy produced by high fluence Ti implantation. The alloy is a mixture of Fe-Ti-C<sup>8,10</sup> with a microstructure shown to be amorphous.<sup>8,10</sup> The carbon (C) enters the solid from the vacuum chamber by a process which can be described as implant-assisted vacuum carburization.<sup>8,11</sup> During implantation, sputtering erodes the surface and uncovers implanted Ti, which reacts with residual gases in the vacuum chamber, producing surface carbide species. These carbon atoms then migrate inwards, producing the Fe-Ti-C surface alloy. It is not known, however, whether it is the presence of C itself or the process by which C enters the surface that is responsible for creating this remarkable tribological surface. Dual implants of C and Ti have also produced low wear and low friction surfaces.<sup>6,12,13</sup>

The purpose of this study was to investigate two different ion implantation processes which increase the C concentration in Ti-implanted steels. In one process, separate implantations of Ti and C were performed at energies resulting in similar depth distribution for Ti (190 keV) and C (50 keV)

atoms. In the second, Ti was implanted at an energy considerably lower (50 keV) than used previously (190 keV). A recent study of the energy dependence of the Ti implantation process<sup>11</sup> has shown that at lower energies, vacuum carburization is initiated sooner and a more fully carburized layer is produced at a lower fluence. Dry sliding friction and wear measurements were used to evaluate these two processes and compare them to a third, the original high fluence ( $5 \times 10^{17}/\text{cm}^2$ ) high-energy (190 keV) process. Compositions of surfaces implanted with Ti ions to a fluence of  $2 \times 10^{17}/\text{cm}^2$  will be presented in order to illustrate the effects of the processing methods on the Ti and C distributions.

Steel disks were metallographically polished, then implanted with Ti, Ti and C, or C ions. The disks were carefully heat sunk to prevent heating by the ion beam during implantation ( $T_{\text{max}} < 50^\circ\text{C}$ ). Ti ions were implanted to fluences from 0.5 to  $5 \times 10^{17}/\text{cm}^2$  at 50 or 190 keV, and C ions to  $2 \times 10^{17}/\text{cm}^2$  at 50 keV.

Kinetic friction coefficients ( $\mu_k$ ) were measured under rather severe sliding conditions: low speed (0.1 mm/s), dry sliding contact in air. The geometry was a 1.27-cm-diam ball sliding against an implanted disk flat (both AISI 52100 steel of hardness  $R_c \sim 60$ ). The ball was loaded to 9.8 N (1 kgf), and up to 20 unidirectional passes were made over the same track. The severity of wear produced during sliding was evaluated by optical (differential interference contrast and interferometry) and electron microscopies.

Table I summarizes the friction and wear results for the three implantation processing treatments. Low friction ( $\mu \sim 0.3$ ) values were obtained for all three treatments at fluences of  $5 \times 10^{17}$  Ti/cm<sup>2</sup>, but only for the low-energy (50

TABLE I Maximum friction coefficients and wear track damage (*n* = none, *m* = mild, *s* = severe) for three Ti-implantation processes as a function of ion energy and fluence.

Process	Energy (keV)	Fluence ( $\times 10^{16}$ Ti/cm <sup>2</sup> )		
		5	20	50
Low-energy Ti	50	0.6/s	0.3/n	0.3/n
High-energy Ti	190	0.8/s	0.8/s	0.3/n
Dual implant: Ti	190	0.7/s	0.5/m	0.3/n
C	50			

keV) treatment at a fluence of  $2 \times 10^{17}/\text{cm}^2$ . In each of the four low friction surfaces, damage in the "wear" track was negligible. Debris and/or severe wear ( $> 50$  nm) was observed on all other tracks<sup>14</sup> except for the Ti + C implant at  $2 \times 10^{17}/\text{cm}^2$ , whose track had a smeared layer but only mild ( $\sim 20$  nm) wear. This dual implanted surface displayed stick slip in its friction ( $\Delta\mu_k \sim \pm 0.1$ ). Similar friction and wear behavior resulted when the order of implantation was reversed (i.e., C first, then Ti). Nonimplanted and C (alone) implanted disks had high  $\mu_{k, \text{max}}$  values, 0.6 and 0.7, respectively and severely damaged wear tracks. Thus, at fluences of  $2 \times 10^{17}$  Ti/cm<sup>2</sup>, the low energy implantation process produced a better tribological surface than the dual implantation process.

Compositions produced by the three processing treatments at a fluence of  $2 \times 10^{17}$  Ti/cm<sup>2</sup> were obtained by Auger sputter profiles with depth scales quantified by interferometry; quantitative analysis of Auger data was based on reference compounds.<sup>6,8</sup> Figure 1 presents profiles of Ti and excess C (the 4 at. % of C found in the bulk alloy has been subtracted out). The high-energy implant (disk 1) in Fig. 1(a) shows a Ti profile which peaks at about 60 nm and a vacuum carburized layer about 50 nm deep. The non-Gaussian shape of the Ti profile indicates that the surface was sputtered during implantation.<sup>15</sup> The dual implant (disk 2) in Fig. 1(b)

TABLE II Retained Ti dose and C/Ti ratio for three disks implanted to  $2 \times 10^{17}/\text{cm}^2$

	High-energy Ti disk 1	Dual implant disk 2	Low-energy Ti disk 3
Retained Ti ( $\times 10^{16}/\text{cm}^2$ ) <sup>a</sup>	13	13	9
C/Ti ratio	0.060	1.0	0.23

<sup>a</sup> By EDX, calibrated against a Ti-implanted steel ( $5 \times 10^{16}$  Ti/cm<sup>2</sup> at 190 keV) for which the retention was observed to be almost 100%.

shows a similar Ti profile with implanted C and Ti overlapping one-to-one. (The concentration of Ti in disk 2 is about 20% less than in disk 1 because implanted C dilutes the Fe-Ti alloy.) The low-energy implant (disk 3) in Fig. 1(c) also shows a sputtered Ti profile which peaked nearer the surface and possessed a more fully carburized layer than the high-energy implant, disk 1. The surface C concentrations, coincidentally, were the same for the dual implant and the low-energy implant.

The composition profiles shown in Fig. 1 are readily explained in terms of implanted ion ranges,<sup>16</sup> sputtering,<sup>15</sup> and vacuum carburization<sup>11</sup> effects. At low energies, implanted atoms are concentrated nearer the surface because the ion ranges are shorter. As the fluence is increased, more of the Ti atoms implanted at low energy are removed by sputtering. (The sputtering rate of steel should be nearly the same at energies of 50 and 190 keV.<sup>17</sup>) However, carburization occurs sooner with low-energy Ti implantation because the Ti atoms reach the surface sooner. Thus, in the low-energy Ti implantation process, less Ti was retained, but with a higher peak Ti concentration and a more fully carburized layer.

Energy dispersive x-ray analysis (EDX) of Ti in the three disks, presented in Table II, confirmed that a smaller percentage of Ti was retained by the low-energy implant (disk 3) than by the high-energy implants, disks 2 and 1. Retained Ti doses were also determined by graphical integration of Fig. 1 and agreed to 15% with the EDX values in Table II. Doses of incorporated C were also obtained by graphical integration. The C to Ti dose ratios for the three disks are listed in Table II. It is clear from Fig. 1 and Table II that the low-energy implant (disk 3) was more carburized than the high-energy implant (disk 1), but that it had less C, less Ti, and a smaller C/Ti ratio than the dual implant (disk 2). The low-energy implant also had a larger peak Ti concentration than the high-energy implant (32 at. % vs 22 at. %); however, previous studies have indicated that Ti without sufficient C has a deleterious effect on friction and wear.<sup>8,14</sup> We therefore believe that the larger peak Ti concentration obtained by low-energy implantation did not play a significant role in the improved friction behavior; this, however, needs further investigation.

In summary, we have evaluated two ion implantation processes which increase the C concentration in Ti-implanted layers above that of the original treatment. Dry sliding friction and wear studies have demonstrated that low-energy (50 keV) Ti implantation produces a superior tribological surface at a lower fluence than dual implantations (Ti at 190

#### CONCENTRATION PROFILES OF STEEL IMPLANTED TO $2 \times 10^{17}/\text{cm}^2$

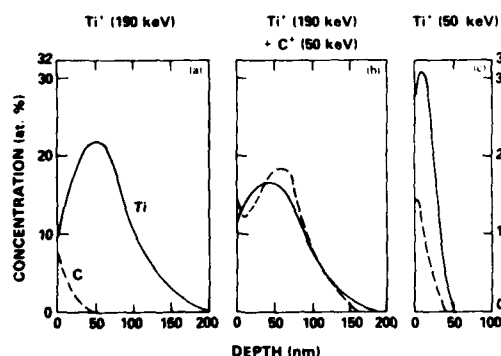


FIG. 1 Auger composition vs depth profiles of Ti and excess C (i.e., above bulk 4 at. % in 52100 steel) implanted to a fluence of  $2 \times 10^{17}/\text{cm}^2$  with (a) disk 1, Ti<sup>+</sup> (190 keV); (b) disk 2, Ti<sup>+</sup> (190 keV) + C<sup>+</sup> (50 keV); (c) disk 3, Ti<sup>+</sup> (50 keV).

keV plus C at 50 keV). Based on a comparison of the compositions of the implanted layers, we conclude that the Fe-Ti-C layer produced during the vacuum carburization process imparts the tribological improvement and not the C concentration alone. Hence, a vacuum carburized layer is more effective than implanted carbon in forming a superior tribological surface Ti-implanted steel.

We have also demonstrated that the fluence required to produce a fully carburized layer decreases as the energy of the implanted Ti decreases. This is of great practical importance for the ion implantation processing of materials: lower fluences reduce production time and lower energies cut down beam heating problems. It also suggests that if sequential implants are to be performed at several energies,<sup>11</sup> e.g., to produce more uniform composition versus depth profile, that the lowest energy implant should be done first. Dual implants of C and Ti had a somewhat beneficial effect in a bearing steel. We suggest they may prove even more valuable in softer steels where friction reduction by the Ti-induced carburized layer and solid solution strengthening by the C might combine to improve tribological behavior.

We thank the Surface Modification and Analyses Branch at NRL for their support and cooperation with implantation and the NAVSEA Manufacturing Technology Program for partial funding of this research.

<sup>11</sup>G. Dearnaley, *J. Metals* **34**, 18 (1982).

<sup>12</sup>G. Dearnaley, *Rad. Eff.* **63**, 1 (1982).

<sup>13</sup>R. E. Fromson and R. Kossowsky, in *Metastable Materials Formation by Ion Implantation*, edited by S. T. Picraux and W. J. Choyke (Elsevier, Amsterdam, 1982), p. 355.

<sup>14</sup>J. A. Smidt, J. K. Hirvonen, and S. Ramalingham, NRI Memorandum Report 4616, September 25, 1981.

<sup>15</sup>Piran Siwashani (Spire Corp., Bedford, Mass.) reported at Metallurgical Coatings Conference, San Diego, CA, April 1983.

<sup>16</sup>C. A. Carosella, I. I. Singer, R. C. Bowers, and C. R. Gossett, in *Ion Implantation Metallurgy*, edited by C. M. Preece and J. K. Hirvonen (Metallurgical Society of AIME, Warrendale, PA, 1980), p. 103.

<sup>17</sup>I. I. Singer, R. N. Bolster, and C. A. Carosella, *Thin Solid Films* **73**, 283 (1980).

<sup>18</sup>I. I. Singer, C. A. Carosella, and J. R. Reed, *Nucl. Instrum. Methods* **182**, 183, 923 (1981).

<sup>19</sup>T. E. Fischer, M. J. Euton, J. M. Williams, C. W. White, and B. R. Appleton, *ASLE Trans.* **26**, 466 (1983).

<sup>20</sup>J. A. Knapp, D. M. Follstaedt, and S. T. Picraux, in *Ion Implantation Metallurgy*, edited by C. M. Preece and J. K. Hirvonen (Metallurgical Society of AIME, Warrendale, PA, 1980), p. 152; *Appl. Phys. Lett.* **37**, 330 (1980).

<sup>21</sup>I. I. Singer, *J. Vac. Sci. Technol. A* **1**, 419 (1983).

<sup>22</sup>J. K. Hirvonen, C. A. Carosella, R. A. Kant, I. I. Singer, R. Vardiman, and B. B. Rath, *Thin Solid Films* **63**, 5 (1979).

<sup>23</sup>F. G. Yost, L. E. Pope, D. M. Follstaedt, J. A. Knapp, and S. T. Picraux, in *Metastable Materials Formation by Ion Implantation*, edited by S. T. Picraux and W. J. Choyke (Elsevier, Amsterdam, 1982), p. 261.

<sup>24</sup>A detailed study of the friction and wear behavior of 190 keV Ti implants is reported in I. I. Singer and R. A. Jeffries, *J. Vac. Sci. Technol. A* **1**, 317 (1983).

<sup>25</sup>F. Schulz and K. Wittmaack, *Rad. Eff.* **29**, 31 (1976).

<sup>26</sup>P. D. Townsend, J. C. Kelly, and N. F. W. Hartley, *Ion Implantation, Sputtering and their Applications* (Academic, New York, 1976), Chaps. 2 and 6.

<sup>27</sup>The sputtering yield of steel by Ti ions with energies 25–200 keV should be constant ( $S = 2.5 \pm 0.5$ ) if one can extrapolate the yield by Ti from Ar and Fe.<sup>28</sup> See H. H. Anderson and H. T. Bay in *Sputtering by Atomic Bombardment I*, edited by R. Behrisch (Springer, Berlin, 1981), p. 173.

Section II.C

WEAR TESTING UNDER HIGH LOAD CONDITIONS

N.E.W. Hartley<sup>1</sup>  
J.K. Hirvonen<sup>2</sup>

<sup>1</sup>Research performed while on sabbatical to:  
Department of Physics  
Georgetown University  
Washington, D. C. 20057

Permanent Address:  
AERE, Harwell  
Didcot, Oxfordshire  
Great Britain

<sup>2</sup>Materials Modification & Analysis Branch  
Condensed Matter & Radiation Sciences Division  
Naval Research Laboratory

Present address:  
Zymet Corporation  
Danvers, MA 01923

This work was supported by the Office of Naval Research and U.S. Naval Air Propulsion Center.

**WEAR TESTING UNDER HIGH LOAD CONDITIONS**  
**The effect of "anti-scuff" additions to AISI 3135, 52100 and 9310 steels introduced by ion implantation and ion beam mixing**

**N.E.W. HARTLEY \***

*Department of Physics, Georgetown University, Washington, D.C. 20057, USA*

**J.K. HIRVONEN \*\***

*U.S. Naval Research Laboratory, Code 6671, Washington, D.C. 20375, USA*

There is a need to eliminate the sudden onset of severe adhesive wear ("scuffing") in high performance hardened steels (e.g., AISI 9310) under arduous load conditions. We have investigated the friction and wear behavior of three ion implanted and ion beam mixed steels under simulated scuffing conditions using a Falex friction and wear tester. This machine enabled tests to be carried out at a load of 700 lb (318 kg), corresponding to a mean contact pressure of approximately 20000 psi (i.e.,  $1 \times 10^8 \text{ N/m}^2$ ) which was sufficient to induce scuffing. A series of lower load tests at 200 lb (91 kg) load ( $5.2 \times 10^7 \text{ N/m}^2$ ) enabled the longer term wear performance of various ion/substrate combinations to be measured. The frictional force experienced during wear testing was used to assess the degree of scuffing, and the amount of material worn away was measured on the Falex tester or by subsequent weight loss determinations, depending on the type of test. The following ions were implanted:  $\text{C}^+$ ,  $\text{N}^+$ ,  $\text{P}^+$ ,  $\text{Ti}^+$ ,  $\text{Cr}^+$ ,  $\text{Mo}^+$ , and  $\text{Ta}^+$ , chosen in order to evaluate the effects of intermetallic additions (C, N, P), alloy elements (Ti, Cr), and anti-scuff elements (Mo, Ta). In addition some thin ( $\sim 1000 \text{ \AA}$ ) vacuum evaporated layers of Si, V, Ni, Nb, Sn, Mo, Ta and W were prepared, and in some cases intermixed with  $\text{N}^+$  ions at a fluence of typically  $2 \times 10^{17}/\text{cm}^2$ , to compare with the effects of ion implantation. Under the low load conditions the wear rate of AISI 3135 steel (1.5% Ni, 0.65% Cr alloy tool steel) was found to be reduced by a factor 3 as a result of  $\text{N}^+$  implantation under low load, in agreement with previous work reported elsewhere, whereas other ions gave inconclusive results. The 52100 steel (a through-hardened martensitic bearing steel) showed marked improvements after  $\text{Ti}^+$  implantation, revealing a sensitivity to fluence which correlated with known dry sliding behaviour of this steel modified by titanium implantations.  $\text{Ta}^+$  and  $\text{Mo}^+$  implantations into 9310 steel (a case-hardened gear steel with 3.0% Ni, 1.4% Cr and 0.55% Mn) reduced the wear rate (in  $\mu\text{g}$  per second) under the low load parameters from 4.2 to 0.15 and 0.26 respectively. Under simulated scuffing,  $\text{Ta}^+$  was effective whereas  $\text{Mo}^+$  was not. SEM examination of the implanted AISI-9310 steel wear pins tested to 200 lb (91 kg) showed extensive smoothing in the implanted worn zones, implying a different wear process. On all the steels, mixed overlayers showed improved friction and wear behavior compared to unmixed layers. The results are discussed in terms of the probable influence of the various added elements on the metallurgical wear mechanisms of the respective steels.

## 1. Introduction

Scuffing is defined as gross damage characterized by the formation of local welds between sliding surfaces [1]. The phenomenon can be troublesome, because of its unpredictability, and costly to live with because of the catastrophic damage which rapidly ensues after scuffing initially occurs, for example within a gear box. The beneficial effects of ion implantation in friction and wear reduction in a variety of steels are now well enough known to not require further com-

ment. In the work described below, the intention was to assess a possible new role for ion implantation in a practical problem area in which there is great reluctance to alter the base material.

Scuffing is usually simulated on specially designed machines in which high loads (1000 lb: 454 kg), high relative sliding velocities ( $10 \text{ ft s}^{-1}$ :  $3 \text{ ms}^{-1}$ ) and extremely thin lubricant layers ( $4.0 \times 10^{-6} \text{ inch}$ :  $0.10 \mu\text{m}$ ) are present. It was decided in the present study to use a commonly used Falex wear tester in a preliminary study of "wear under high load conditions," principally because the necessary sample geometries are considerably smaller for this type of machine, but also because it would be inopportune to evaluate true scuffing components without some preliminary screening.

\* Permanent address: Building 329 AERE Harwell, Oxfordshire OX11 0RA, UK.

\*\* Now at Zymet, Inc., Liberty Square, Danvers, MA 01923, USA.

## 2. Experiments

### 2.1. Wear

The Falex wear tester in ion implantation experiments has been previously described by Hale [2,3]. It uses a cylindrical pin-in-V-block arrangement and is primarily designed to evaluate lubricants. However, with careful sample preparation and experimental procedure it is quite possible to use the machine as a materials wear tester, as Hale et al. have already demonstrated [3]. In essence, the machine rotates a test pin at the fixed rate of 290 revolutions per minute in a vertical axis and the frictional force exerted by the pin against 2 V-blocks clamped against it is recorded as a torque. The torque reading is simply related to a friction coefficient by an equation which can be derived from the machine dimensions and geometry:

$$\mu = \frac{2.97 \times \text{Torque (lb)}}{\text{Load (lb)}}$$

The load was read off from a spring loading gage attached to the loading arms and was monitored continuously throughout the test.

Standard Falex test pins with nominal compositions as shown in table 1 were obtained for this study.

Two types of wear tests using the Falex machine were carried out, designated i) "low load tests" and ii) "high load tests".

#### 2.1.1. Low load tests

The objective of these tests was to observe the effects of some selected ions on the weight loss behavior of 3135, 52100, and 9310 steels and to compare the results with those of Hale et al. [2], reported earlier, for closely equivalent wear conditions.

This test required that a load of 200 lb (91 kg) be maintained on the rotating pin for 90 min. The

weight loss experienced during the test was recorded. Measurements were also made of the width of the grooves in the V-blocks, with more wear corresponding to a wider groove.

#### 2.1.2. High load tests

Most of the wear testing reported in this paper was carried out under these conditions, which follow the ASTM D267067 procedure for evaluating lubricants. After an initial run-in period of 5 min at 250 lb (114 kg), the load was increased to 700 lb for 15 min by using the ratchet mechanism intrinsic to the machine. The test was then stopped. This load-time history produced occasional rapid excursions in the friction coefficient for untreated 9310 and 52100 steels (see figs. 4, 6, and 7), although not in 3135 steel. These excursions were frequently accompanied by audible squeaking and are identified here as scuffing events.

A comparison between the low and high load test parameters is given in table 2.

Before wear testing, each pin was successively degreased in i) acetone, ii) naphtha, iii) toluene and iv) methanol. An identical cleaning procedure was applied to the V-blocks, which were always not implanted. Ion implanted (or vacuum deposited) pins were stored under clean conditions in methanol prior to testing. The AISI-52100 and 9310 test pins were run against 52100 and 9310 steel V-blocks, respectively. The 3135 pins were run against AISI-1137 steel blocks. This steel is a low-carbon free cutting steel which is invariably used with the 3135 steel pin in this machine (e.g., Hale, [2]). Under high load conditions the maximum temperature reached was typically 180°C. Under low load conditions the maximum temperature reached was about 80°C. All the wear tests were carried out in fresh Herculube A, a synthetic lubricant based on pentaerythritol tetrahexanoate.

Table 1  
Test pin compositions (wt. %)

AISI	C	Mn	P	S	Ni	Cr	Si	Mo
3135	0.065	-	-	-	1.25	0.025	-	-
9310	0.85 <sup>41</sup>	0.55	0.025	0.025	3.25	1.25	0.25	0.12
52100	0.96	0.36	-	0.012	1.36	0.22	-	-

<sup>41</sup> Carburized.

Table 2  
Summary of test conditions

Low load	High load	Data points (figs. 4, 6, 7)
"Non scuffing"	"Scuffing"	
1) Initial loading at 200 lb	1) Initial loading at 250 lb	1-5
	2) Run-in at 250 lb	6-10
	3) Increase load to 700 lb	11-19
2) Maintain load at 200 lb for 90 min	4) Maintain load at 700 lb for 15 min	20-34
Additional parameter pin weight loss		

## 2.2 Surface treatments

### 2.2.1 Ion implantation

An Extrion medium current implanter at NRL was used for the implantations. A rotating stage was made so that 4, and occasionally 5, pins could be implanted simultaneously. The beam was rastered to cover all samples, which were arranged so as not to obscure one another. Since the whole of one side of a given wear pin was exposed to the beam, the ions arrived at all angles between 0 and 90° to the surface. Their temperature during implantation was monitored remotely using an infrared pyrometer, and was not allowed to exceed 150 °C.

### 2.2.2 Vacuum deposition

A second rotating stage was constructed in order that a maximum of 8 pins could be evenly coated, using sputter deposition, under UHV conditions. In practice 4 pins were coated at any one time in order to avoid non-uniformities in deposition caused by the increasingly large distances of the outermost pins from the source of sputtered ions. Sputter deposition for Si, Nb and Mo layers was carried out in a UHV rig at NRL. The target stage was typically a 4" (10 cm) diameter pure plate of the element to be deposited, positioned about 2" (5.0 cm) above the array of rotating pins. Typical base pressure was  $5.8 \times 10^{-9}$  Torr; an Ar plasma discharge at 65 mTorr (1100 W, 1900 V target bias) was applied for between 5 and 15 min de-

pending on the sputter deposition rate.

An electron-beam evaporation unit was used for the deposition of the refractory metals Ta, V and W. The Sn and Ni layers were applied using a thermal evaporation unit at NRL for 10 to 20 min, depending on the element. Thickness measurements were made by Rutherford backscattering or interferometry.

## 3. Results

### 3.1. Low load wear tests

Fig. 1 shows the friction coefficient for 9310 gear steel as a function of time for Mo and Ta implantations ( $1 \times 10^{17}$  per  $\text{cm}^2$ ) compared to an unimplanted sample. The rate of weight loss from the pin (i.e., wear) is also included and it is clear that a considerable reduction in surface damage has resulted from the ion implantation treatment, particularly for the Ta<sup>+</sup> treatment.

Fig. 2 shows equivalent data for 52100 steel. In this example, the 52100 steel was treated with Ti<sup>+</sup> ions to a fluence of  $4.6 \times 10^{17}$  per  $\text{cm}^2$ , which has been shown to reduce friction under dry sliding conditions [4].

Ion implanted AISI 3135 steel pins were treated with Ta<sup>+</sup> and Mo<sup>+</sup> ions, to a fluence of  $4.1 \times 10^{17}$  per  $\text{cm}^2$ . The N<sup>+</sup> treatment reduced the wear rate by a factor 3, in close agreement with the result of Hale et al. [1], but the Mo<sup>+</sup> and Ta<sup>+</sup> treatments gave no change in wear rate, as shown in table 3. (In general, wear tests on 3135 steel were found to be less reproducible than 52100 and 9310 tests, possibly because this steel is softer.)

A Sloan Instruments Dektak surface profilometer was used to record the surface roughness of the pin surface across the worn/unworn zone, and the results are shown in fig. 3 for 9310 steel. It can be seen that on the 9310 alloy, the surface is considerably more smooth in the Ta implanted region. Scanning electron micrographs on the worn 9310 surface of the control pin and the worn surface of the Ta<sup>+</sup> implanted pin (fig. 4b) show that a totally different surface structure is present in the worn zone of the implanted sample [figs. 4(a) and (b)]. Surface roughness profiles were also obtained from the 52100 and 3135 steels. These showed significant differences between implanted and unimplanted wear zones, but for brevity the data are

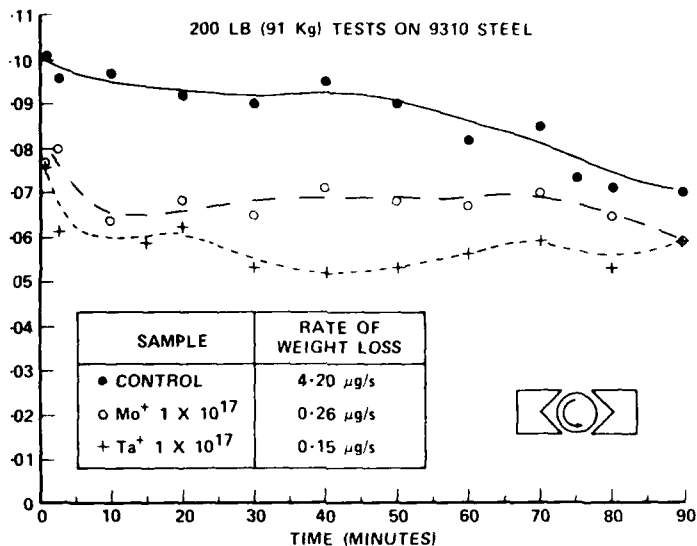


Fig. 1. Coefficient of friction of carburized 9310 gear steel as a function of time for  $\text{Mo}^+$  and  $\text{Ta}^+$  implantations, 200 lb (91 kg) Falex testing in Hercolube A lubricating oil.

not presented here but are tabulated in table 3.

In addition to the pin weight loss, a measurement was also made of the groove width on the contacting V-blocks for each of the tests shown in the previous figures. For scuffing resistance it is

required that the wear on both surfaces (i.e., pin and V-block) is minimized, ideally under the lowest possible coefficient of friction. These results are also summarized in table 3.

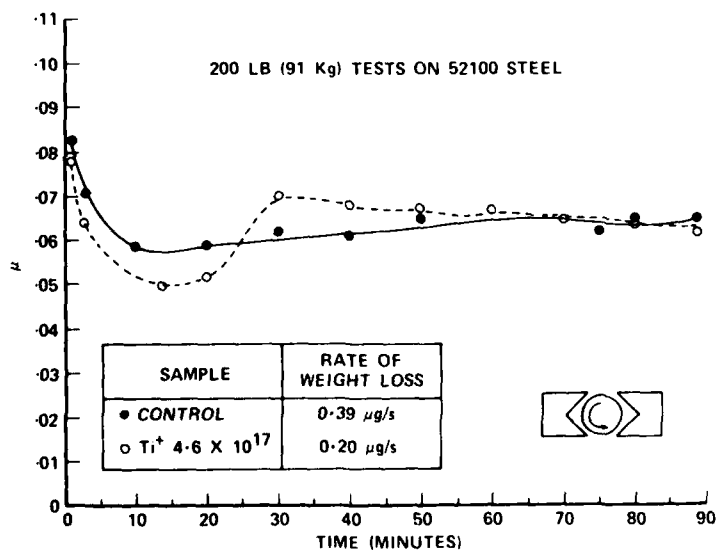


Fig. 2. Coefficient of friction of 52100 bearing steel as a function of time for  $\text{Ti}^+$  implantation, 200 lb (91 kg) Falex testing in Hercolube A lubricating oil.

Table 3  
Results of low load tests, 200 lb (91 kg) 90 min duration

	Ion beam	Wear rate ( $\mu\text{g/s}$ )	V-block groove width ( $\mu\text{m}$ )	Friction coefficient $\mu$ at 20 min	Dektak trace
9310		4.20	$480 \pm 90$	0.092	rough
	Mo <sup>+</sup>	0.26	$390 \pm 40$	0.068	smooth valleys
	Ta <sup>+</sup>	0.15	$360 \pm 20$	0.062	very smooth
52100		0.39	$310 \pm 20$	0.059	intermediate
	Ti <sup>+</sup>	0.20	$380 \pm 30$	0.052	rough
3135		3.09	$350 \pm 90$	0.053	very rough
	N <sup>+</sup>	0.96	$740 \pm 70$	0.067	intermediate
	Mo <sup>+</sup>	3.06	$335 \pm 30$	0.048	very rough
	Ta <sup>+</sup>	3.19	$325 \pm 30$	0.048	very rough

### 3.2. High load ("scuffing") tests

#### 3.2.1. Ion implanted test pins

**9310 steel:** The coefficient of friction for the shorter duration, high load, scuffing tests is shown in fig. 5 for various ions implanted into 9310 steel. For clarity, the horizontal axis is plotted in "data points"; individual points can be related to the loading sequence with reference to the regimes listed in table 3. It can be seen that for the control pin, Cr<sup>+</sup> and Mo<sup>+</sup> implantations all led to scuffing events. Ta<sup>+</sup> implantation appeared to be the

most effective in lowering the coefficient of friction ( $\mu$ ) and in preventing excessive wear of the V-blocks. Profilometer traces of all the worn surfaces were obtained, but for brevity only the Ta<sup>+</sup> and Mo<sup>+</sup> implant results are included here, with reference to the unimplanted control (fig. 6). In general it was found that the implanted ions which gave the highest frictional values (N, C) also led to substantial V-block wear, which is not unexpected intuitively.

**52100 steel:** High load friction/scuffing results for ion implanted 52100 test pins are presented in fig. 7. For this steel there was little systematic variation in the friction dependence, with the exception of Ti<sup>+</sup> implantations which show a sensitivity to fluence. The coefficient of friction and the degree of wear on the V-blocks did not correlate.

**3135 steel:** A very limited set of tests were carried out on 3135 steel because the initial screening under 200 lb (91 kg) maximum load showed little promise.

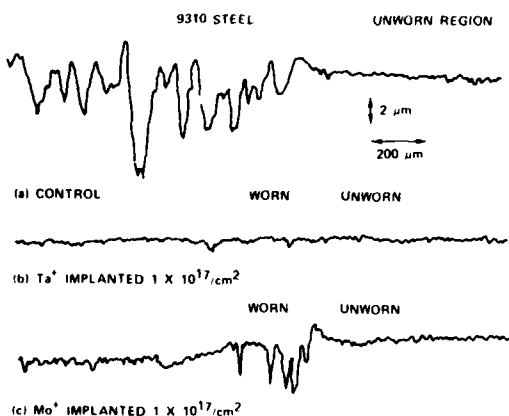


Fig. 3. Dektak surface profiles of wear zones on implanted and unimplanted test pins of 9310 steel after low load testing.

#### 3.2.2. Overlayer and intermixed coatings

Constraints on accelerator use and technical difficulties experienced during the deposition of some of the overlayers meant that only a very limited number of systems were examined for wear behavior. Fig. 7 includes the result obtained with a single vacuum deposited Ta film on 52100. Fig. 8 shows the data for V, Ta and Sn layers on 9310 steel. The 3135 steel was vacuum deposited with Si only, and the frictional dependence thus measured was virtually identical to unimplanted steel.

## VII. METALS

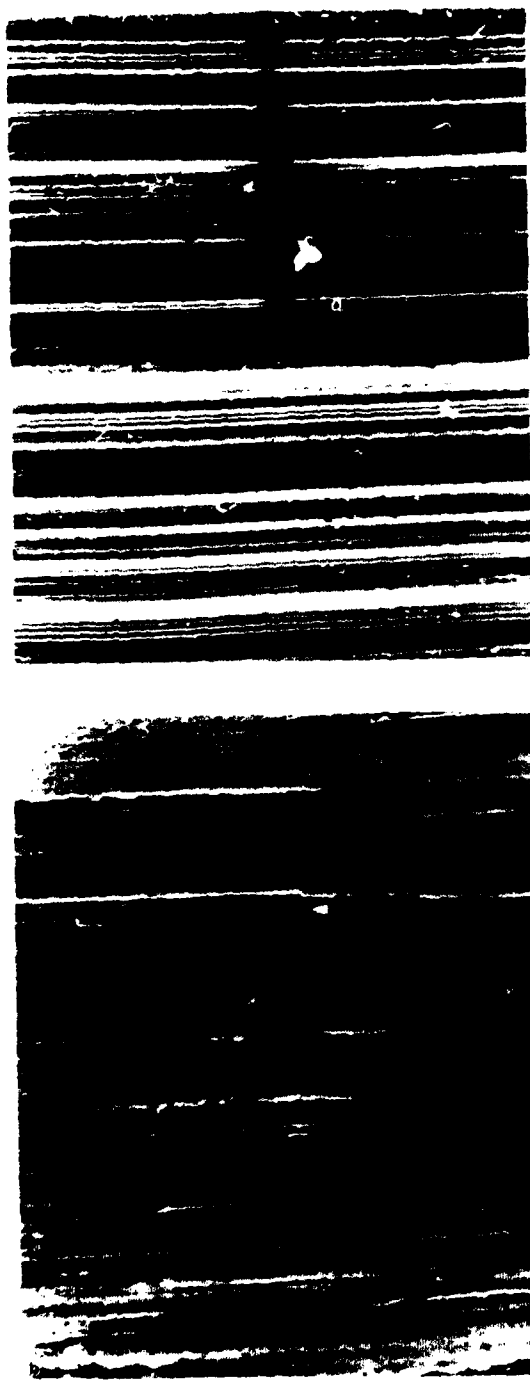


Fig. 4. Scanning Electron Micrographs of the wear zones of (a) unimplanted and (b)  $Ta^+$  implanted 9310 steel wear pins after 200 lb (91 kg) Falex tests.  $500\times$ .

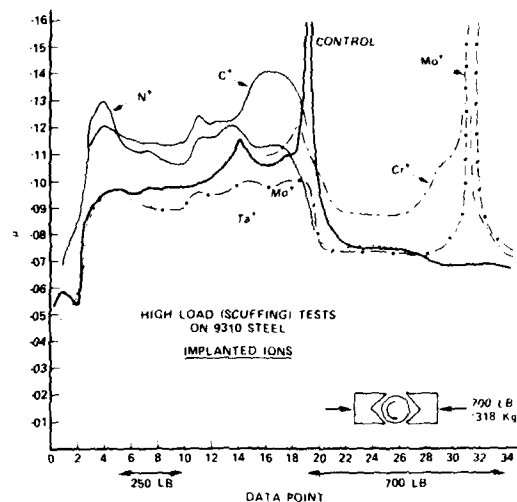


Fig. 5. Coefficient of friction of carburized 9310 gear steel under high load (700 lb, 318 kg) Falex testing in Herculube A lubricating oil. (Key to data points given in table 2.)

#### 4. Discussion

Since scuffing is initiated by very localized plastic flow, the problem reduces to avoiding metal-to-metal contact and eliminating gross deformation. The three ways to prevent scuffing are (i) increase the surface hardness, (ii) use extreme pressure (EP) additives in the lubricant so that a monolayer of polar liquid is firmly attached to the metal surfaces, and (iii) prevent the formation of

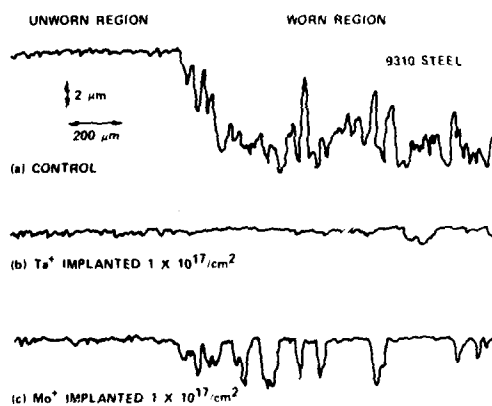


Fig. 6. Dektak surface profiles of wear zones on implanted and unimplanted test pins of 9310 steel after high load testing

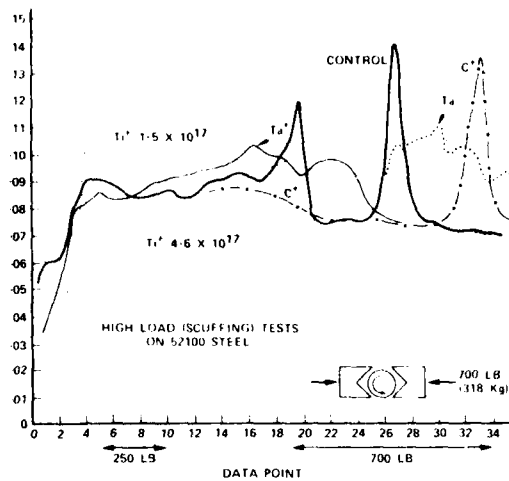


Fig. 7. Coefficient of friction of 52100 gear steel under high load (700 lb, 318 kg) Falex testing in Herculube A lubricating oil. (Key to data points given in table 2.)

the more ductile austenitic phase of ferrous alloys. In addition, it has become clear recently that the role of oxides may be crucial in the first stages of scuffing [5]. However, there is insufficient knowledge at present to correlate all the possible physical and chemical parameters of the various oxides which may be present to subsequent scuffing behavior. In this study we have directed our attention to simpler ideas centering on surface hardness and austenite prevention.

Additional hardness can be provided in case-hardened 9310 steel by trapping the carbon atoms effectively. Tantalum and molybdenum both form carbides with higher enthalpies than either  $\text{Cr}_2\text{C}_6$  or  $\text{Fe}_3\text{C}$  [6]. In addition, molybdenum forms a range of oxides which have beneficial lubricious properties. The lowered friction and decreased wear rate observed in ion implanted 9310, fig. 1, may be attributable to these effects. The surface profiles, fig. 3, imply strongly that the surface has been hardened since the gross damage seen on untreated 9310 is not present. Moreover, the original position of the surface is almost completely retained ( $\text{Ta}$ ), or penetrated only in specific regions ( $\text{Mo}$ ).

However, under "scuffing" conditions, molybdenum implantation is unsatisfactory (fig. 5). Thus, if s ft oxides are present, in combination with enhanced carbide production, they are insufficient

to prevent metal-to-metal adhesion.

It is noteworthy also that high load scuffing is not prevented by  $\text{Cr}^+$ , and both nitrogen and carbon implantation provide significant increases in  $\mu$  which are probably detrimental to wear performance. N and C are strong austenite formers (ref. 6, p. 59), and Cr has only a slight effect on hardenability in ferrite. It would therefore seem to be important to avoid the austenite forming elements (Zn, Cu, Ni, Mn, N, C) and to enhance ferrite formers (Si, Be, Al, Mo, W, Nb, V, P, Sn, Ti, Zr). However, it is not sufficient merely to provide evaporated layers of these latter species (e.g., V, Sn), as these are presumably scraped off during high load wear, fig. 8.

Ion mixing seems to be beneficial by providing for a more integral surface modified zone. Auger electron spectroscopy analysis of these nitrogen bombarded layers showed that nitrides had not been formed, and in fact the nitrogen implantation had only barely approached the Sn/9310 interface. This implies that only a minor degree of subsequent bombardment is sufficient to considerably enhance the tenacity of deposited overlayers.

52100 steel cannot be hardened by "interstitial" (i.e. C, N) ion bombardment because of its fully through-hardened state [4,7]. Titanium is effective due to the formation of a  $\text{TiC}$ -like region, with excess carbon becoming entrained during implantation due to gettering by Ti [4]; significantly lowered friction and wear have been observed as a

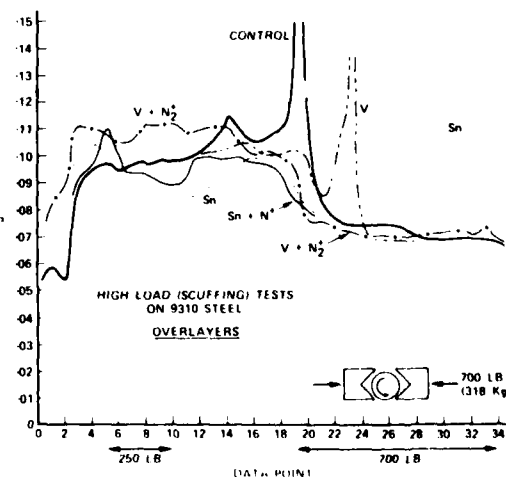


Fig. 8. Coefficient of friction of carburized 9310 gear steel, as fig. 5, for various overlayer and N-mixed coatings

result. This is consistent with the low load observations in the present study, fig. 2 and 6. Ta<sup>+</sup> implantation to  $1 \times 10^{17}$  ions per cm<sup>2</sup> is roughly equivalent initially to Ti<sup>+</sup> implanted at  $1 \times 10^{17}$  per cm<sup>2</sup> (fig. 7), but it is noteworthy that the friction decreases with time for the Ta treatment. TiC has a formation enthalpy slightly higher than TaC (80 KJ mol<sup>-1</sup>). Note also that Ta as an overlayer (fig. 7) does not prevent the occurrence of friction peaks.

## 5. Conclusions

This study has shown that even under the relatively severe conditions of wear testing using a Falex lubricant tester, implanted metal ions and some ion-bombarded overlayers can provide lower friction and improved wear performance. The most significant findings were that Ta and Mo implantation into case-hardened 9310 steel reduce the friction by as much as 30%; also, the wear rates are reduced by as much as a factor of 28 and 16, respectively. Titanium implantation into 52100 was also effective in wear reduction, by a factor 2, but friction improvement was less marked.

Under simulated scuffing conditions, 9310 steel was most improved by Ta<sup>+</sup> treatment and 52100 steel was improved by high fluence (i.e.,  $4.6 \times 10^{17}$ ) Ti<sup>+</sup> implantation.

Of the very limited number of overlayers examined, it was found that ion bombardment eliminated the tendency for such films to become removed.

The results are generally consistent with the formation of hard intermetallic phases, and the suppression of austenite. However, there is no doubt a secondary effect due to oxide formation. This aspect of the reported improvements has not been addressed here.

There is clearly a considerable amount of further exploratory work to be undertaken in this field to compare (i) additional overlayer and implanted elements, (ii) the effects of "reactive" (i.e.,

N) with "unreactive" (i.e., Ne) intermixants, and (iii) the role of carburized (9310) versus uncarburized surfaces, and the question of whether or not this affects the diffusion kinetics, (iv) the chemical state of the intermixed and implanted layers, and (v) the role of oxides on scuffing prevention.

This study has shown that some of the more pressing problems of scuffing prevention on advanced iron alloys may be addressed by using ion beam methods.

The authors wish to acknowledge numerous discussions with members of the ion implantation group at NRL, also Irwin Singer and Russ Jeffries of the NRL Chemistry Division. The implantations were performed by Randy Walker. Deposition experiments, not all of which have been reported here, were carried out by Wendy Fuller, Deborah van Vechten and Arnold Singer at NRL, and also by Dale Jacobson at Bell Telephone Laboratories. A grant to Georgetown University from NRL is acknowledged as is the leave-of-absence provision from the UKAEA for NEWH. Partial support for this work by the U.S. Naval Air Propulsion Center is gratefully acknowledged.

## References

- [1] A. Dyson, in *Wear*, ed., D. Scott, Treatise on Materials Science and Technology, vol. 13 (Academic Press, New York, 1979) pp. 175-216.
- [2] E.D. Hale et al., in: *Ion implantation into Metals*, eds., V. Ashworth, W.A. Grant and R.P.M. Procter (Pergamon, London, 1982) pp. 111-116.
- [3] E.D. Hale et al., *Rev. Sci. Instr.* (August 1982).
- [4] I.L. Singer and R.N. Bolster, in *Ion Implantation Metallurgy*, Eds., C.M. Preece and J.K. Hirvonen (AIME, 1980) p. 116.
- [5] K.C. Ludema, Univ. of Ann Arbor, private communication.
- [6] R.W.K. Honeycombe, *Steels - Microstructure and Properties*, (ASM, 1981) pp. 224, 58-62.
- [7] G.K. Hubler, in *Metastable Materials Formation by Ion implantation*, eds., S.T. Picraux and W.K. Choyke (MRS, 1981) pp. 341-345.

Section II.D

HARDNESS AS A MEASURE OF WEAR RESISTNCE

W. C. Oliver<sup>1</sup>

R. Hutchings<sup>2</sup>

J. B. Pethica<sup>3</sup>

I. L. Singer<sup>4</sup> and G. K. Hubler<sup>5</sup>

<sup>1</sup>United Technologies Research Center  
E. Hartford, CT 06108

<sup>2</sup>Brown Boveri Research Center  
CH-5405 Baden, Switzerland

<sup>3</sup>Cavendish Laboratory  
Cambridge, CB3 0HE, U.K.

<sup>4</sup>Surface Chemistry Branch  
Chemistry Division  
Naval Research Laboratory

<sup>5</sup>Materials Modification & Analysis Branch  
Condensed Matter & Radiation Sciences Division  
Naval Research Laboratory

The portion of this work performed at Naval Research Laboratory was supported by the Office of Naval Research. Other contributions included corporate R & D funding by Brown Boveri<sup>1,2,3</sup> and by United Technologies.

## HARDNESS AS A MEASURE OF WEAR RESISTANCE

W.C. OLIVER<sup>1</sup>, R. HUTCHINGS<sup>2</sup>, J.B. PETHICA<sup>3</sup>, I.L. SINGER<sup>4</sup>, AND  
G.K. Hubler<sup>5</sup>

<sup>1</sup>United Technologies Research Center, E. Hartford, CT 06108

<sup>2</sup>Brown Boveri Research Center, CH-5405 Baden, Switzerland;

<sup>3</sup>Cavendish Lab., Cambridge, CB3 0HE, U.K;

<sup>4,5</sup>Naval Research Laboratory, U.S.A.

### ABSTRACT

One measure of the surface mechanical properties of materials can be obtained through microhardness data. The success of microhardness in predicting the improvements in wear resistance of ion implanted metals has been mixed. In this paper the cases of N implantation into 304 S.S. and Ti implantation into 52100 bearing steel will be examined. Microhardness data indicates little or no hardness changes whereas large wear rate changes are observed. From these two examples it is clear that the wear mechanism, the chemical nature of the surface, the ductility, and the toughness can be more important than the hardness changes.

### INTRODUCTION

Two tribological systems of technological interest that have been studied extensively are N implanted 304 S.S. and Ti implanted 52100 bearing steel. Much of the early work on these systems involved extensive wear testing and little evidence was collected concerning the mechanism by which the improvements might occur. General explanations involving increased hardness of the implanted surface as giving rise to better wear resistance have been offered.

The hardness of a material does affect its wear rate; however, other parameters can be more important. Hardness gives some indication of strength. Other mechanical properties of a material that help determine its wear rate are ductility, toughness and the temperature dependence of these quantities. Hornbogen [1] and Atkins [2] consider the effects of some of these parameters on wear rates. The mechanical structure of the surface is also important. For example, a very hard surface on a very soft substrate does not result in high wear resistance if high contact stresses occur. Finally, chemical effects between each component of the wear couple and the atmosphere and between the two components themselves can also be extremely important.

Many of these properties are very difficult to measure. Ease of measurement has led to hardness being used extensively when considering wear experiments and modeling of wear processes. In the case of ion implanted surfaces, even hardness is very difficult to measure.

A hardness tester that is capable of sampling the very thin implanted layers has been constructed and used to measure the hardness of implanted surfaces [3-5]. The results of these tests, wear data, and microanalysis results for a range of implanted metals have been presented [6].

By comparing hardness and wear data, it has been shown that indentation hardness is qualitatively correct in predicting pin on disc wear property improvements. The magnitude of the improvements is much less predictable from the hardness data. In fact, in the cases where dramatic improvements in wear properties are observed, the improvements are too large to be explained through the effect of hardness on a given wear mechanism. For the cases of Ti-6Al-4V and hard electroplated chromium, N implantation can cause a change in the dominant wear mechanism [6]. The important point is, if the hardness of a surface is increased through implantation, some increase in wear resistance can be expected; however, other properties of the surface may also effect the wear rate.

With this discussion as background, we shall now proceed to two specific cases for which the evidence appears to be conflicting. These are nitrogen implanted 304 S.S. and titanium implanted 52100 bearing steel. The data in question concerns the indentation hardness, the surface abrasion resistance, and pin on disc type wear data that has been collected for these two systems.

The surface abrasion, relative wear resistance (R.W.R.) test was introduced by Bolster and Singer [7] as a relatively simple way to get some indication of the hardness of thin surface layers. This is a reasonable approach if all the parameters, other than hardness, that effect abrasive wear are held constant. The apparent inconsistencies arise when actual indentation hardness tests, taken using the machine mentioned above, do not match the R.W.R. results.

The hardness data presented here will highlight these apparent inconsistencies. The discussion of the results will help explain them.

## EXPERIMENTAL

The 52100 specimens were implanted at the Naval Research Laboratory (N.R.L.). The conditions for the Ti implantation of the 52100 steel specimens have been previously reported [8]. The carbon was implanted at 40 keV to a dose of  $2 \times 10^{21}$  ions/m<sup>2</sup>. The Ta was implanted to a dose of  $1.8 \times 10^{21}$  ions/m<sup>2</sup>.

One 304 stainless steel specimen was polished to a 9  $\mu$ m diamond abrasive finish. Part of the surface was electropolished and part was ion milled with 1 keV Ar ions. Part of the resulting surface was then implanted with  $1 \times 10^{21}$  N<sup>+</sup>/m<sup>2</sup> at 40 keV. Thus the sample had surfaces treated as shown in Figure 2 available for hardness testing.

The other 304 S.S. specimen was polished to a 1  $\mu$ m diamond finish and one section of the surface was implanted with N<sub>2</sub><sup>+</sup> at 90 keV to a dose of  $2.5 \times 10^{21}$  ions/m<sup>2</sup>.

## RESULTS AND DISCUSSION

First let us consider 52100 bearing steel. This materials is used in the through hardened and slightly tempered condition. It has been shown that nitrogen implantation is not effective at hardening the surface of this material or improving its wear resistance [6,9]. For this reason extensive work has been carried out at the Naval Research Laboratory on Ti, Ta and Ti+C implantations of this materials [8-13]. Positive improvements in wear life have been achieved. In addition the surface sensitive abrasive wear test used at N.R.L. indicated a factor of 6 increase in the relative wear

resistance (R.W.R.) of the Ti implanted surfaces [8]. A dose of  $5 \times 10^{21}$  ions/m titanium is known to produce an amorphous film on 52100 bearing steel [11]. It has been established that the titanium implantations are most effective when a significant amount of carbon is gettered from the atmosphere. Auger results have shown that the carbon is bound to the titanium in the same way as in TiC; however, there is no evidence that TiC exists as a second phase.

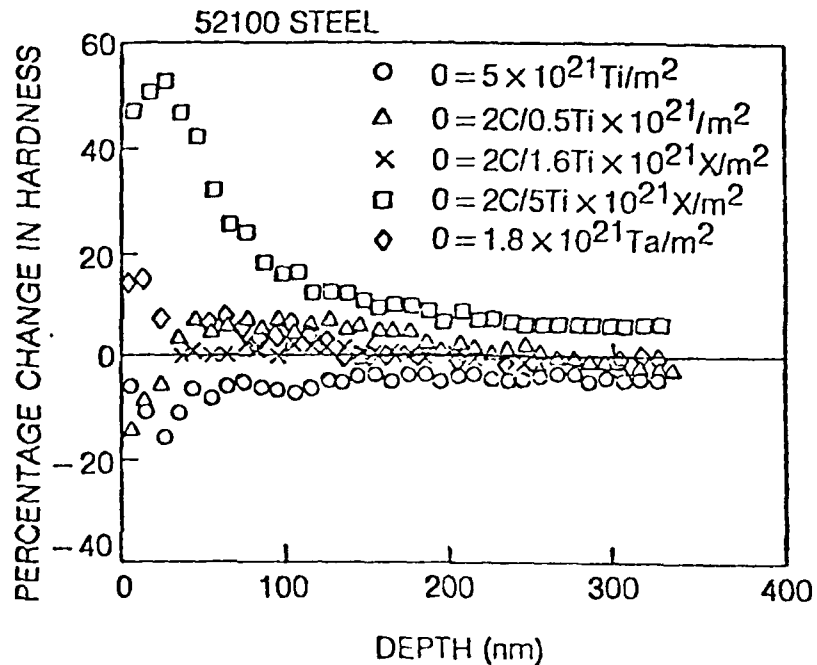


Figure 1

To confirm that the surface of 52100 bearing steel is hardened by Ti and Ta implantation, five samples were tested for indentation hardness versus depth. This data is presented in Figure 1. The first surprising result shown in Figure 1 is that Ti or Ta implanted by themselves did not increase the hardness of 52100 steel. In fact, the only effective hardening process was implanting with  $2 \times 10^{21}$  ions/m<sup>2</sup> C and  $5 \times 10^{21}$  ions/m<sup>2</sup> of Ti. This dose level of titanium corresponds well with the critical level for positive wear results which have been reported; however the wear results were determined without C implantation. It is clear that a minimum amount of both carbon and titanium are required for positive hardness results. In the presence of  $2 \times 10^{21}$  ions/m<sup>2</sup> of C the threshold for hardness increases is between 1.6 and  $5 \times 10^{21}$  ions/m<sup>2</sup> of Ti. The wear improvements demonstrated in both the abrasive

wear test (R.W.R.) and the pin on plate tests were from samples that according to Figure 1 should not have significantly hardened surfaces; thus, hardness changes cannot be responsible. This is a clear example of the dangers of interpreting abrasive wear resistance directly in terms of hardness. The dose level associated with wear property improvements correlates with the dose required to obtain an amorphous layer. It may be some property of that layer that is important. Some possibilities are ductility or toughness. The hardness data indicates that further wear property improvements might be obtained if the surface was hardened by dual implantation of C and Ti.

The apparent inconsistency in the data for this material, (that is improvements in R.W.R., no hardness increase, and pin on plate wear improvements), are rationalized when two facts are considered. First, R.W.R. is actually a wear test. Second, properties other than hardness can be important in determining wear rates.

The second material we will discuss is 304 S.S. Significant increases in pin on disc wear resistance have been reported through N implantation of this material [6,14]. Figure 2 shows the indentation hardness versus depth curves for a 304 S.S. surface modified in several ways. The base line (0% change) is the hardness of electropolished, ion milled, unimplanted surface. The error in the measurements at less than 40 nm depth is large, particularly for this specimen which was only polished with 9  $\mu\text{m}$  diamond. The data in this region should be considered with caution. It is clear that implanting electropolished 304 S.S. increases the near surface hardness. This has been measured to cause an increase of at least 50% at 40 nm on two separate specimens. The change in hardness on implantation of the mechanically polished 304 S.S. shown in Figure 2 is more difficult to interpret due to a lack of a mechanically polished base line. The change in hardness due to N implantation of a 1  $\mu\text{m}$  diamond polished 304 S.S. sample is shown in Figure 3. It is clear that N implantation increased the surface hardness of this specimen by about 40-60%. The change for the mechanically polished material shown in Figure 2 is certainly no greater than 25% and perhaps significantly less. However, if one interprets the previously reported R.W.R. results for mechanically polished 304 S.S. [7] in terms of hardness one would expect a 50% decrease. This does not agree with the 40-60% increase shown in Figure 3 or the data presented in Figure 2. It is clear from Figure 2 that the hardness at 400 nm is greatly increased ( $\approx 50\%$ ) by mechanical polishing. It seems that the easiest way to harden the surface of 304 S.S. is through cold work.

The decrease in relative wear resistance near the surface of the implanted material has been explained by a reversion of a work-hardened surface martensite to softer austenite [7]. It is clear that strain induced martensite does revert to austenite due to nitrogen implantation [14]; however, it is not clear under what polishing conditions the surface will contain a large fraction of martensite. The samples used to measure the R.W.R. and indentation hardness results were polished using vibratory and wheel techniques, respectively. This in itself could explain the discrepancy between these results. It is also possible the implanted austenite is as hard or harder than the martensite from which it is formed. Other properties than hardness may cause the decrease in R.W.R. and increase in pin on disc wear properties.

BASE LINE: ELECTRO POLISH AND ION MILLED

○ BASE LINE +  $1 \times 10^{21} \text{N}^+ / \text{m}^2$  AT 40 KeV

△ 9 $\mu\text{m}$  MECH POLISH +  $1 \times 10^{21} \text{N}^+ / \text{m}^2$  AT 40 KeV

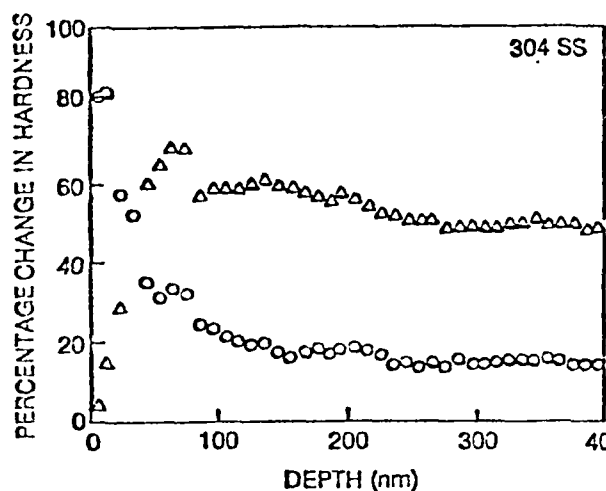


Figure 2

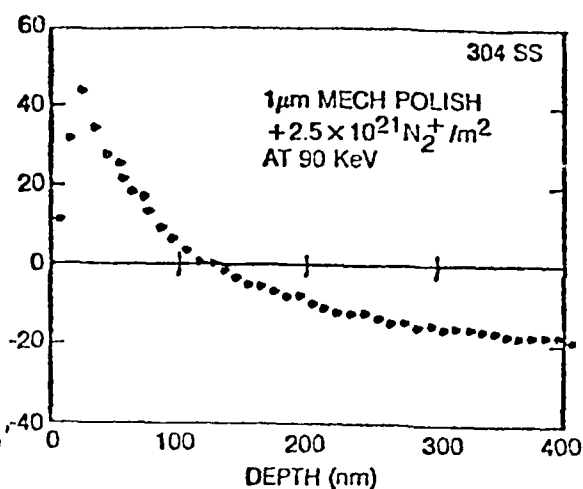


Figure 3

The two examples discussed above illustrate the errors obtained if one interprets surface abrasive wear results in terms of hardness changes. The R.W.R. test is an important tool for learning about the abrasive wear properties of implanted layers. Any consistent model of the behavior of such layers should be able to explain R.W.R. and pin disc results; however, what effect hardness has on the results can easily be masked by other effects.

## CONCLUSIONS

1. Hardness is not the important property through which the wear properties of 304 S.S. or 52100 are improved by N and Ti implantation, respectively.
2. The surface hardness of 52100 steel can be increased by dual implantation of C and Ti.
3. The surface hardness of electropolished 304 S.S. can be increased by at least 50% through nitrogen implantation; however, the surface of mechanically polished 304 S.S. is only increased at most by 10-20%.
4. Indirect estimates of hardness through abrasive wear tests can yield misleading results.

## REFERENCES

1. E. Hornbogen, Wear 33, 251 (1975).
2. A.G. Atkins, Wear 61, 183 (1980)
3. J.B. Pethica and W.C. Oliver, "Metastable Materials Formation By Ion Implantation", S.T. Picraux and W.J. Choyke, eds., Elsevier, New York (1982) p. 373.
4. J.B. Pethica: "Ion Implantation into Metals", V. Ashworth, W.A. Grant, and R.P.M. Proctor, eds., Pergamon Press, New York (1982) p. 147.
5. J.B. Pethica, R. Hutchings and W.C. Oliver, Phil. Mag., in press.
6. R. Hutchings, W.C. Oliver, and J.B. Pethica, to be published in Proc. of NATO/ASI on "Surface Engineering", Les Arcs, France, 1983.
7. R.N. Bolster and I.L. Singer, ASLE 24, 526 (1981).
8. I.L. Singer, R.N. Bolster and C.A. Carosella, Thin Solid Films 73, 283 (1980).
9. I.L. Singer and R.A. Jeffries, J. Vac. Sci. Technol. A1, 317 (1983).
10. C.A. Carosella, I.L. Singer, R.C. Bowers, and C.R. Gossett, "Ion Implantation Metallurgy", Eds., C. Preece and J.K. Hirvonen, AIME, (1980) p. 103.
11. I.L. Singer, J. Vac. Sci. Technol. A1, 419 (1983).
12. I.L. Singer, C.A. Carosella, and J.R. Reed, Nucl. Inst. and Meth. 182/183, 923 (1981).
13. I.L. Singer and R.A. Jeffries, Appl. Phys. Lett. 43, 925 (1983).
14. R.G. Vardiman and I.L. Singer, Mater. Lett. 2, 150 (1983).

Section II.E

EFFECT OF TITANIUM IMPLANTATION ON THE FRICTION  
AND SURFACE CHEMISTRY OF A Co-Cr-W-C ALLOY

S. A. Dillich\* and I. L. Singer

Surface Chemistry Branch  
Chemistry Division  
Naval Research Laboratory

\*National Research Council Research Associate

This work was supported by the Office of Naval Research and the National Research Council.

AD-A145 438

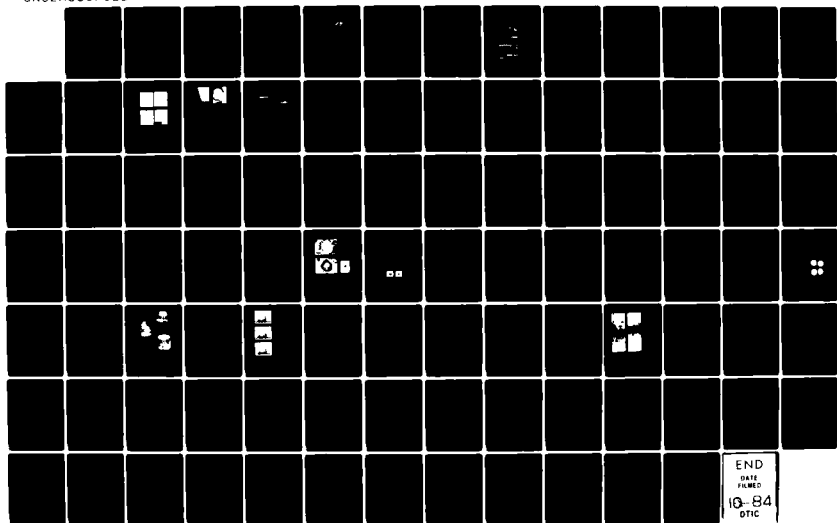
THE USE OF ION IMPLANTATION FOR MATERIALS PROCESSING  
(U) NAVAL RESEARCH LAB WASHINGTON DC F A SMIDT  
23 AUG 84 NRL-MR-5393

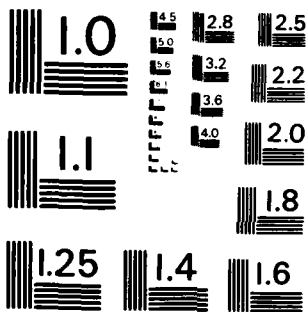
2/2

UNCLASSIFIED

F/G 20/8

NL





MICROCOPY RESOLUTION TEST CHART  
NATIONAL BUREAU OF STANDARDS-1963-A

## EFFECT OF TITANIUM IMPLANTATION ON THE FRICTION AND SURFACE CHEMISTRY OF A Co-Cr-W-C ALLOY\*

S. A. DILLICH† AND I. L. SINGER

*Naval Research Laboratory, Code 6170, Washington, DC 20375 (U.S.A.)*

(Received April 18, 1983; accepted May 19, 1983)

The effects of the implantation of titanium ions, to a fluence of  $5 \times 10^{17}$  Ti ions  $\text{cm}^{-2}$  at 190 keV, on the tribological behavior of a centrifugally cast cobalt-based alloy (Stoody 3) were investigated by friction tests against a variety of alloy and carbon counterfaces. Dry sliding friction coefficients were compared with those made on similarly prepared, but non-implanted, and fatty-acid-coated samples. High friction coefficients ( $\mu_k \approx 0.6$ ) for the alloy–Stoody 3 couples coincided with the formation of debris, with the same composition as the softer of the mating alloys, in the wear scars. Much lower  $\mu_k$  values were measured on titanium-implanted ( $\mu_k \approx 0.25$ ) and acid-coated ( $\mu_k \approx 0.1$ ) surfaces. Optical microscopy indicated a change in the surface texture of the implanted surfaces attributable to sputtering. Auger spectroscopy showed that vacuum carburization of both carbide and matrix phases of the Stoody alloy occurred during implantation. The friction and wear mechanisms involved are discussed.

### 1. INTRODUCTION

Centrifugally cast cobalt-based alloys exhibit high wear resistance, attributed to the presence of fine and evenly dispersed carbides (chromium and tungsten) in a softer, more ductile cobalt-rich matrix. These alloys can, however, show severe wear under detrimental sliding conditions<sup>1,2</sup>. Our investigations were intended to lead to an understanding of the wear modes of these cobalt-based alloys and to develop surface treatments to protect against wear.

Ion implantation is a process which holds promise as a surface treatment for wear resistance<sup>3</sup>. The high fluence implantation of titanium ions, for example, is capable of producing reduced friction<sup>4</sup> and reduced abrasive<sup>5</sup> and adhesive<sup>6</sup> wear in hardened steels such as AISI 52100, a high carbon chromium steel. It is not known, however, whether titanium implantation can improve the tribological behavior of multiphase alloys composed of large (10  $\mu\text{m}$  or more in length) complex carbides in a

\* Paper presented at the International Conference on Metallurgical Coatings, San Diego, CA, U.S.A., April 18–22, 1983.

† National Research Council–Naval Research Laboratory Research Associate.

much softer matrix. In the present study we examine the effects of high fluence titanium implantation on the dry sliding friction and wear behavior of a centrifugally cast cobalt-based alloy (50% Co, 31% Cr, 12.5% W, 2.2% C), hereafter referred to by its commercial designation Stoodly 3.

The wear scars and surface textures were examined using optical and scanning electron microscopies. Energy-dispersive X-ray analysis (EDX) and Auger electron spectroscopy were used to identify the compositions of as-implanted surfaces and wear debris in the tracks.

## 2. EXPERIMENTAL PROCEDURE

### 2.1. Friction testing

Kinetic friction coefficient measurements were made using a slider-on-disk test configuration. The Stoodly 3 disks made contact with hard bearing steels such as 52100, 440C stainless steel and M50, as well as 302 stainless steel and low carbon mild steel. Two cobalt-based alloys, Stoodly 2 and Stellite 3, with compositions very similar to that of Stoodly 3 were tested, as well as an extremely hard cobalt-cemented tungsten carbide. Since in many tribological applications cobalt-based alloys mate with carbon soft faces, it was of interest to investigate the friction characteristics of carbon-Stoodly 3 couples. Thus, two grades of carbon, one a porous synthetic graphite and the other a hard carbon-graphite with a resin impregnant, were also tested against the Stoodly 3 alloy. The nominal compositions and hardnesses of the materials used, as specified by the manufacturers, are shown in Table I.

The sliders, alloy balls 1.27 cm in diameter and carbon pins of 1.27 cm length and 0.62 cm diameter with truncated hemispherical tips, rode against Stoodly 3 disks 1.27 cm in diameter and 0.32 cm thick. Friction measurements were made in air (30%–50% relative humidity) at room temperatures, with a normal load of 9.8 N, at a very slow sliding speed of  $0.1 \text{ mm s}^{-1}$ . Test durations were limited to 20 successive unidirectional traverses of the sliders over the same path on the Stoodly 3 disks.

### 2.2. Sample preparation and titanium implantation

The Stoodly 3 disks were polished to a metallographic finish before testing. The

TABLE I  
NOMINAL COMPOSITION AND HARDNESS OF ALLOYS AND CARBONS

Designation	Composition (wt.%)	Hardness
52100	Fe-1.5Cr-1C	60–65 HRC
440C stainless steel	Fe-17Cr-1C	58–62 HRC
M50	Fe-4Cr-4Mo-0.8C	66–65 HRC
302 stainless steel	Fe-18Cr-8Ni-0.1C	35–29 HRC
Mild steel	Fe-0.2C	18–20 HRC
Stellite 3	Co-31Cr-12.5W-2.3C	50–54 HRC
Stoodly 2	Co-33Cr-19W-2.5C	58–63 HRC
Stoodly 3	Co-31Cr-12.5W-2.2C	51–58 HRC
WC	WC-6Co	90.5–91.5 HRA
P03	Graphite	Scleroscope 75
P658RC	Carbon-graphite	Scleroscope 95

alloy balls, with surface finishes of about 0.03  $\mu\text{m}$ , were degreased with benzene in a Soxhlet extractor and stored in toluene. Prior to testing, disks and balls were ultrasonically cleaned in acetone and rinsed with 2-propanol. Later, in the course of research, it was found desirable to add toluene cleaning of the disks to the preparation procedure in order to ensure the complete removal of the polishing compounds from the sliding surfaces. The hemispherical tips of the carbon pins were polished to a metallographic finish, providing a sliding surface of about 2 mm diameter.

A close-packed monolayer of eicosanoic acid ( $\text{C}_{19}\text{H}_{39}\text{COOH}$ ), hereafter designated  $\text{C}_{20}$  acid, was applied to several disks by retraction from the melt at 76 °C. The state of packing of each  $\text{C}_{20}$  acid coating was characterized by measuring the contact angle  $\theta$  exhibited by methylene iodide ( $\text{CH}_2\text{I}_2$ )<sup>7</sup>.

Implantations of the Stoodly 3 samples were done in a modified model 200-20A2F Varion-Extrion ion implanter with a hot cathode arc discharge type of ion source. The disks were heat sunk onto a water-cooled holder and implanted with  $^{48}\text{Ti}$  ions at 190 keV, to a fluence of  $5 \times 10^{17}$  Ti ions  $\text{cm}^{-2}$ . The target chamber was cryogenically pumped to pressures of about  $3 \times 10^{-6}$  Torr or better.

### 2.3. Surface inspection and chemical analysis

Auger analysis of Stoodly 3 disks was performed with several scanning Auger microprobes, one a PHI model 590 with a spatial resolution of better than 1  $\mu\text{m}$ . Depth profiles were recorded during ion milling with a rastered 2 keV argon ion beam. Elemental concentrations were determined from peak height data using a linear normalizing procedure<sup>8</sup> with sensitivity factors obtained from reference compounds<sup>6</sup>. Depth scales for ion-milled surfaces were established by measuring crater depths by interferometry.

Wear tracks on the Stoodly 3 surfaces were examined using scanning electron microscopy (SEM) and optical microscopy with differential interference contrast (DIC). EDX of the wear tracks was done on an Advanced Metal Research model 1000 scanning electron microscope equipped with a Kevex mode 5100 spectrometer.

## 3. RESULTS

### 3.1. Surface chemistry and texture

Titanium ions implanted into Stoodly 3 to  $5 \times 10^{17}$   $\text{cm}^{-2}$  at 190 keV produced a (Ti + C)-enriched surface layer extending almost 200 nm into the disk. The Auger depth profile, shown in Fig. 1, indicates a near-saturation profile of titanium and a diffusion-like profile for carbon. Only carbon in excess of bulk carbon is depicted in the profile. These compositions were found in both the chromium-rich carbide phase and the cobalt-rich matrix phase of the alloy. The chemical affinity of the implanted titanium for the excess carbon, inferred from their Auger line shapes, is summarized along the curves in Fig. 1. The profiles and chemistry of titanium and carbon in Stoodly 3 are identical with those found in steels implanted under the same conditions<sup>4,5</sup>. It has recently been demonstrated that the excess carbon is absorbed from residual gases in the vacuum chamber<sup>9</sup>. Implanted titanium atoms, brought to the surface by sputter erosion of the substrate, are believed to be responsible for gettering the carbon atoms.

The texture of the multiphased Stoddy 3 surface was also changed by this high fluence titanium implantation (see Fig. 1(b)). The tops of carbides, raised above the cobalt-rich matrix by polishing, were rounded by high angle sputtering at their edges. Sputter-deposited carbide is believed to form a raised perimeter a short distance from the carbide-matrix interfaces, producing the high contrast borders seen around carbides in the DIC micrograph of Fig. 1.

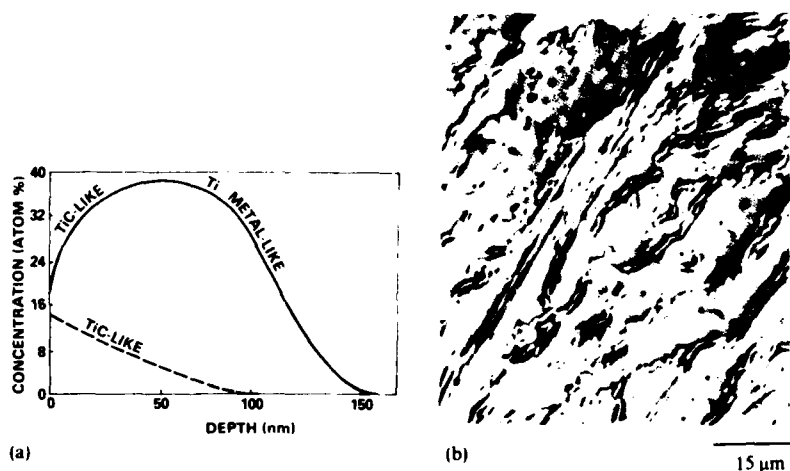


Fig. 1. (a) Auger depth profile of titanium-implanted Stoddy 3 ( $5 \times 10^{17} \text{ cm}^{-2}$  at 190 keV): —, Ti LMM; ---, C KLL. (b) DIC micrograph of the as-implanted surface.

### 3.2. Contact angle measurements

Contact angles measured on Stoddy 3 disks with adsorbed  $\text{C}_{20}$  acid monolayers ranged from  $66^\circ$  to  $74^\circ$ . These compare favorably with values ( $\theta = 70^\circ, 71^\circ$ ) reported as measured on close-packed monolayers<sup>10</sup>. Contact angles of between  $41^\circ$  and  $50^\circ$  were measured on implanted disks, while values ranging from  $44^\circ$  to  $63^\circ$  were observed on Stoddy 3 surfaces cleaned with organic solvents. A contact angle of zero, i.e. complete wettability, would be expected on a contamination-free metal surface. Thus it seems that implanted surfaces were less contaminated than those cleaned with organic solvents. It is not clear, however, whether titanium implantation forms a material with a lower energy surface or simply sputter cleans the surface free of contaminants.

### 3.3. Friction tests

#### 3.3.1. Alloy balls-Stoddy 3

Results of friction tests made on the three classes of Stoddy 3 disks, non-implanted, titanium implanted and  $\text{C}_{20}$  acid coated, are summarized in Table II. Unless otherwise noted, two to nine tests were made for each slider-Stoddy 3 combination. The highest values of the kinetic coefficient of friction  $\mu_k$  measured on the first and twentieth passes of each slider-disk couple are listed in Table II. In general, the highest coefficients of friction were observed on non-implanted disks which were cleaned with toluene as part of the preparation procedure.

TABLE II  
COEFFICIENTS OF KINETIC FRICTION OF ALLOY BALLS AND CARBON PINS SLIDING AGAINST STOODY 3

Slider	Non-implanted			Ti implanted			C <sub>70</sub> acid monolayer		
	$\mu_k$		Debris <sup>a</sup> in track	$\mu_k$		Debris <sup>a</sup> in track	$\mu_k$		Debris <sup>a</sup> in track
	1st pass	20th pass		1st pass	20th pass		1st pass	20th pass	
52100	0.32	0.56	Co-Cr-W	0.14	0.19	None	0.09	0.10	None
440C stainless steel	0.22	0.54	Co-Cr-W	0.13 <sup>b</sup>	0.14 <sup>b</sup>	None	0.06 <sup>b</sup>	0.08 <sup>b</sup>	None
M50	0.31	0.64	Co-Cr-W	0.16 <sup>b</sup>	0.20 <sup>b</sup>	None	0.08	0.08	None
302 stainless steel	0.24	0.58	Fe-Cr-Ni	0.17	0.51	Fe Cr Ni			
Mild steel	0.23	0.50	Fe	0.13	0.33	Fe			
Stellite 3	0.20	0.57	Co-Cr-W	0.10 <sup>b</sup>	0.16 <sup>b</sup>	None			
Stoody 2	0.24	0.60	Co-Cr-W	0.15	0.22	Co Cr W	0.09 <sup>b</sup>	0.08 <sup>b</sup>	None
WC	0.20	0.62	Co-Cr-W	0.14 <sup>b</sup>	0.27 <sup>b</sup>	Co Cr W			
P03 graphite	0.16	0.24	None	0.15	0.16	None	0.10	0.21	None
P638RC carbon-graphite resin	0.13	0.14	None	0.11	0.13	None	0.08	0.10	None

<sup>a</sup> Identified by EDX.

<sup>b</sup> One test only.

Friction during the first pass of the alloy balls on the non-implanted disks was generally low ( $\mu_k \approx 0.25$ ). Optical microscope inspection of tracks on the disks revealed that, even during the first pass, considerable scratching and plastic deformation of the Stoddy 3 sliding surface occurred (Fig. 2(a)). With successive passes, the friction coefficient  $\mu_k$  rose to about 0.6 and the tracks became debris

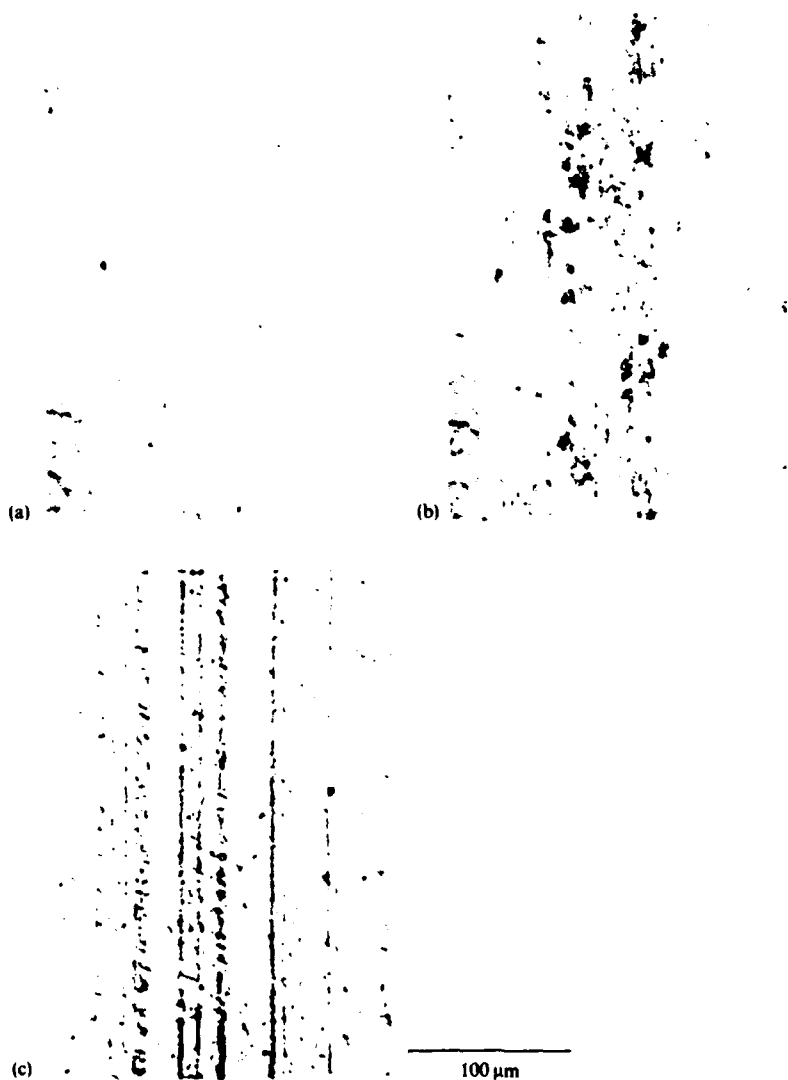


Fig. 2. Wear tracks of 52100 steel sliding against non-implanted and titanium-implanted Stoddy 3 disks: (a) plastic deformation of the Stoddy 3 occurred immediately on the first passes of the 52100 balls on non-implanted disks ( $\mu_k = 0.25$ ); (b) by the twentieth pass, the tracks were covered with wear debris ( $\mu_k = 0.56$ ); (c) plastic deformation, but no debris, was seen on tracks on implanted disks ( $\mu_k = 0.19$ ).

laden (Fig. 2(b)). SEM-EDX of wear tracks showed the debris to be composed of materials from the softer of the ball-disk couple (Fig. 3).

Coefficients of friction significantly lower (by a half to two thirds at the twentieth pass) than those observed for non-implanted disks were measured for the titanium-implanted disks tested against balls of hardness approximately equal to or harder than that of Stoddy 3. After 20 passes, plastic deformation was apparent on all tracks (see, for example, Fig. 2(c)). Wear debris formation, when it occurred (Table II), was light compared with that of the non-implanted tracks. Stoddy 2 and tungsten carbide produced the most severe deformation on the implanted disks. Debris particles, although few in number, where visible were of the same composition as the Stoddy 3 disks. The highest  $\mu_k$  values of the implanted disks were

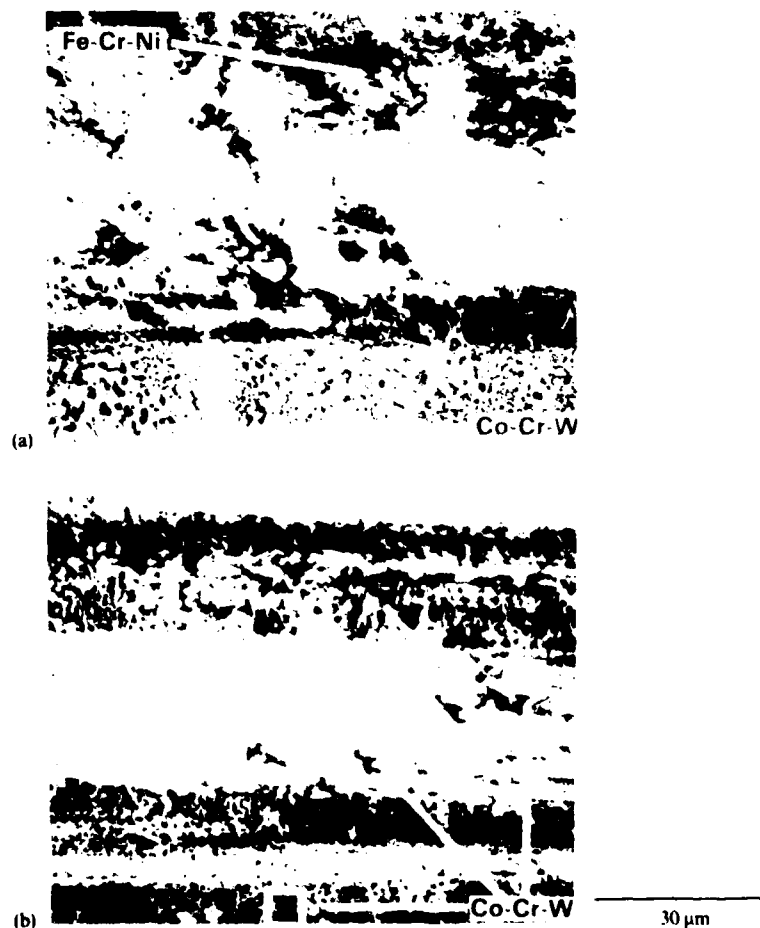


Fig. 3. SEM-EDX of (a) 302 stainless steel ball tracks and (b) 440C stainless steel ball tracks on Stoddy 3 disks. The debris in the 302 stainless steel track had the same composition as the ball, whereas the debris on the 440C track had the same composition as the disk.

measured while testing against the mild steel and 302 stainless steel balls. Analogous to the non-implanted disk tests, some ball material was transferred to the disks.

The lowest coefficients of friction ( $\mu_k \leq 0.1$ ) were observed during testing against Stoddy 3 disks covered by an adsorbed  $C_{20}$  acid monolayer (Table II). Low friction persisted through the twentieth pass for all alloy sliders. Faint scratches were produced on the Stoddy 3 disks, but no debris could be found in the wear tracks.

### 3.3.2. Carbon pins-Stoddy 3

Titanium implantation reduced the friction coefficient of the P03-Stoddy 3 couples by 30% but had little effect on the P658RC-Stoddy 3 couples. Unlike the titanium-implanted surfaces, however, the  $C_{20}$  acid monolayers were not able to maintain low friction through the twentieth pass for the graphite pins. For all surfaces tested, the graphite friction was consistently higher than that of the resin-impregnated carbon-graphite. Both types of carbons occasionally produced faint scratches on the non-implanted disks but not on the implanted Stoddy 3 surfaces.

## 4. DISCUSSION

The implantation of titanium to high fluences produced low wear, low friction contact surfaces which endured the rather severe sliding contact of harder alloy balls by deforming plastically but not delaminating or spalling. Softer alloy balls (302 and mild steel) degraded during sliding, leaving wear debris on the tracks. Wear debris coincided with higher friction, as was the case for non-implanted disks. Thus, harder alloys gave low  $\mu_k$  values but softer alloys had less dramatic reductions in friction.

The low friction coefficients observed with titanium implantation cannot be explained by the presence of a lubricious contamination on the surface, as the low contact angles observed on the implanted disks confirmed. The implantation process must therefore have induced changes in the Stoddy 3 chemistry and microstructure which affected the surface mechanical properties of the disks. Titanium implantation into Stoddy 3 produced the vacuum-carburized titanium layer depicted in Fig. 1, in both matrix and carbide phases. Identical Ti + C layers found in titanium-implanted 52100 steel were shown to be amorphous<sup>4</sup>. For reasons not well understood, these layers produced low friction wear-resistant surfaces in both 52100 steel and Stoddy 3.

During implantation, a pronounced texture, distinct from that seen on the polished samples, was produced by titanium ion sputtering of the Stoddy 3 surface. However, what role, if any, the implantation-induced texture played in effecting the improvement in the tribological behavior of the alloy is not known.

## 5. CONCLUSIONS

(1) Titanium-implanted vacuum-carburized Stoddy 3 surfaces show a dramatic improvement in friction and wear properties when in contact with alloys of similar or greater hardness.

(2) The high friction coefficients ( $\mu_k \approx 0.6$ ) of alloy-Stoddy 3 couples have been correlated with the presence of wear debris of the softer material in the wear scars.

(3) Monolayer films of  $C_{20}$  acid are durable boundary lubricants on Stoddy 3 surfaces.

# ACKNOWLEDGMENTS

We thank the Surface Modification and Materials Analysis Group at the Naval Research Laboratory for their cooperation with implantation, Ron Lee at the Naval Surface Weapons Center for use of the 590 microprobe, and Marianne K. Bennett for her assistance with the application and characterization of the C<sub>20</sub> acid monolayers. We would especially like to thank the Stooddy Company, Wear Resistant Alloy Parts Division, and The Pure Carbon Company for their generous donations of the materials used in this investigation. This project was supported in part by the Office of Naval Research.

# REFERENCES

- 1 K. C. Antony, *J. Met.*, **35** (2) (1983) 52.
- 2 R. I. Blombery and C. M. Perrot, *J. Aust. Inst. Met.*, **19** (1974) 254.
- 3 N. E. W. Hartley, Ion implantation, *Treatise Mater. Sci. Technol.*, **18** (1980) 321.
- 4 I. L. Singer, C. A. Carosella and J. R. Reed, *Nucl. Instrum. Methods*, **182-183** (1981) 923.
- 5 I. L. Singer, R. N. Bolster and C. A. Carosella, *Thin Solid Films*, **73** (1980) 283.
- 6 I. L. Singer and R. A. Jeffries, *J. Vac. Sci. Technol. A*, **1** (1983) 317.
- 7 W. A. Zisman, in *Contact Angle, Wettability and Adhesion*, American Chemical Society, Washington, DC, 1964, p. 107.
- 8 L. E. Davis, N. C. McDonald, P. W. Palmberg, G. E. Riach and R. E. Weber, *Handbook of Auger Electron Spectroscopy*, Physical Electronics Industries, Eden Prairie, MN, 1976.
- 9 I. L. Singer, *J. Vac. Sci. Technol. A*, **1** (1983) 419.
- 10 O. Levine and W. A. Zisman, *J. Phys. Chem.*, **61** (1957) 1188.

Section II.F

WEAR IMPROVEMENT IN Ti-6Al-4V BY ION IMPLANTATION

R. G. Vardiman

Physical Metallurgy Branch  
Material Science and Technology Division  
Naval Research Laboratory

This work was supported by the Office of Naval Research.

## WEAR IMPROVEMENT IN Ti-6Al-4V BY ION IMPLANTATION

R.G. Vardiman  
Naval Research Laboratory  
Washington, D.C. 20375

### ABSTRACT

The friction and wear of Ti-6Al-4V are found to be sharply reduced by carbon implantation followed by heat treatment. Optimum wear resistance is developed at 400°C, at which the microstructure of the implanted layer shows a dense array of TiC precipitates up to 60 nm in size. The implanted layer in this case is worn through in a few thousand cycles of the ball on disc test, but by implanting at two energies to achieve a deeper carbide layer, negligible wear was found even after 20,000 cycles. No wear improvement was found for nitrogen implantation.

### INTRODUCTION

Titanium alloys have always presented a particular problem with regard to wear, yet many applications involve fretting or wear situations. Most standard coating methods do not work well on titanium usually because of adhesion problems [1]. It is not always possible to lubricate the surfaces, and under unlubricated conditions rapid material transfer and severe wear can occur with even moderate loads [2].

Ion implantation creates a surface layer with no adhesion problems, since the affected layer is continuous with the underlying material. Wear improvement has been achieved in a variety of materials by implantation, usually with nitrogen [3]. Two recent studies [4,5] have reported substantial wear improvement in Ti-6Al-4V with nitrogen implantation.

The present work uses carbon implantation with post-implantation heat treatment to produce a low friction, wear resisting surface. Variations in the implanted layer microstructure are seen to correlate with wear behavior. A dual energy implant, increasing the depth of the affected layer, produces a larger than expected improvement in wear rate. A nitrogen implanted specimen tested for comparison did not show any wear improvement.

### Experimental Methods

The starting material was  $\alpha$ - $\beta$  processed (mill annealed) Ti-6Al-4V. This microstructure is characterized by equiaxed  $\alpha$  grains and smaller, elongated  $\beta$  grains [6]. Wear discs were cut approximately 2.6 cm square and 0.45 cm thick, and the surface polished to 3  $\mu$ m diamond. For transmission electron microscopy (TEM), 3 mm discs were mechanically polished to 100-150  $\mu$ m thickness, then electropolished on one side before implantation. Final thinning was from the opposite side, with the implanted surface masked.

For implantation, wear specimens were clamped to an aluminum plate, while TEM specimens were attached with silver paint. Heat sinking was good in both cases, and maximum temperature during implantation is not expected to exceed 150°C. Two types of carbon implantation were used. First,  $2 \times 10^{17}$

at./cm<sup>2</sup> was implanted at 75 keV. All TEM specimens received this treatment, and one set of wear discs. One wear disc was first implanted to  $3 \times 10^{17}$  at./cm<sup>2</sup> at 175 keV, followed by the above treatment, in order to give a much deeper layer of carbon. Nitrogen was implanted to  $2 \times 10^{17}$  at./cm<sup>2</sup> at 100 keV, following the procedure of ref 4.

All material was heat treated in ultra-high vacuum. The cold vacuum was normally  $1 \times 10^{-9}$  torr, rising to roughly  $2 \times 10^{-8}$  torr at temperature. Temperature regulation was typically  $\pm 2^\circ\text{C}$ . Heat treatments were for one hour at 300, 400, or 500°C.

TEM examination was performed on a 200 kV instrument equipped with an electron energy loss spectrometer (EELS). Both EELS analysis and the observation of the highly strained appearance characteristic of an implanted layer confirmed that the material under examination was from the implantation layer.

The wear test used here was a simple ball on disc test. The ball was 12.7 mm diameter 440C stainless steel. The position of the ball was adjusted to give wear tracks with diameters between 14 mm and 23 mm. The rotation rate of the disc was adjusted to give a constant speed of 1.35 cm/sec of the ball relative to the disc. The friction force was recorded continuously, and calibrated before and after each test. The disc surface was covered with hexadecane, a poor lubricant which was used to give a more constant surface environment than laboratory air. The normal load was 100 g, with one run done at 300 g.

## RESULTS

### Microstructural Characterization

The microstructure of the 75 keV implants as seen in TEM shows the presence of TiC in all cases. The electron diffraction pattern shows in addition to the titanium spots diffuse rings corresponding to a FCC phase of the expected lattice parameter for TiC. The evenness of the ring intensities indicates the carbides are incoherent with the matrix. Dark field micrographs using portions of the (111) and (200) rings are shown in Fig. 1. The particles in the as implanted case have a maximum size of about 10 nm. After one hour at 300°C, there is only a small change in maximum size, but the density appears greater. One hour at 400°C produces a large change, with the maximum particle size increased to roughly 60 nm, while few particles of 10-20 nm size are seen. The overall density of carbides can be more clearly seen in the bright field micrograph of Fig. 2(a). After the 500°C heat treatment, few small particles are visible (Fig. 1(d)), while precipitates of the size 0.5-2.0  $\mu\text{m}$  are found every two or three grains. A typical large carbide is shown in Fig. 2(b).

### Wear Behavior

Friction and wear of the unimplanted material were found to be as expected [2]; the friction coefficient varying between approximately 0.4 and 0.5 (see Fig. 4(a)), heavy titanium transfer to the steel ball so that the wear couple was essentially titanium on titanium, and rapid removal of material from the disc wear track even at the relatively light load of 100 g.

Wear of the carbon implanted surface showed a low friction coefficient initially but after about 100 cycles changed to that of the unimplanted material, and after 1000 cycles no difference in total wear could be discerned. After the 300°C heat treatment, the low friction coefficient persisted for approximately 500 cycles, and for the 400°C specimens, for 2500 cycles. Prior to the transition in friction, the amount of wear was not discernable; that is, the wear track was indistinguishable from the surface roughness when measured on a surface profilometer. Wear of the 500°C specimen was similar to the as implanted surface; that is, a transition at around 100 cycles. The number of cycles before the transition is plotted in Fig. 3 as a function of heat treatment temperature.

The friction coefficient in the low wear mode was sometimes constant around 0.17, a value similar to that found in other investigations of implantation improved wear in Ti-6Al-4V [5,6]. In some cases, however, the friction coefficient varied around the wear track from 0.17 to values as high as 0.35. These higher friction areas were found to be associated with small grooves whose presence did not appear to affect the wear behavior. Fig. 4 shows examples of the various types of friction behavior which were found in this study.

By implanting at more than one energy, the implant species concentration can be made nearly constant for extended depths. In order to see the effect of a thicker implanted layer on the wear behavior, one disc was implanted at two energies, as described above, then heat treated one hour at 400°C to optimize wear resistance. Normal loads of 100 and 300 g were used, and even with the 300 g load, no transition occurred after 20,000 cycles, when the test was stopped. No wear was measurable, but the track showed considerable discoloration indicating that the surface had oxidized there.

The nitrogen implanted specimen showed wear characteristics identical to unimplanted material. Tests run with mineral oil as well as hexadecane showed no difference.

#### DISCUSSION AND CONCLUSIONS

The dual energy implant produces a high concentration carbon layer three to four times thicker than the 75 keV implant. The number of cycles to break through this layer is obviously much greater than the thickness ratio would suggest. The strengthening of a greater depth of material probably contributes strongly to this extra wear resistance. The formation of an oxide layer in the wear track also should decrease the wear rate [5].

Neither nitrogen or carbon improved wear resistance in the as implanted state under the conditions of this experiment. Hutchings and Oliver [5] found that higher concentrations of nitrogen were required to substantially improve wear resistance in Ti-6Al-4V, although Shepard and Suh [4] found wear improvement at the dose and energy used here. The finding here that precipitate growth is needed to improve wear resistance with carbon implantation agrees with the lack of improvement by nitrogen implantation. Heat treatment would not be expected to affect the wear of the nitrogen implanted surface, as temperatures up to 500°C have been found to have little effect on nitride size [6].

In summary, the friction and wear behavior of Ti-6Al-4V is found to change sharply when implanted with carbon and heat treated to increase carbide size. Optimum size and density of precipitates to resist wear is found after heat treatment at 400°C. Even more extensive improvement is achieved by using more than one implantation energy to increase the thickness of the carbide layer.

#### ACKNOWLEDGMENTS

I wish to thank Dr. I.L. Singer for many stimulating discussions, and the NRL ion implantation group for doing the implantations.

#### REFERENCES

1. N.J. Finch and J.E. Bowers, B.N.F.M.R.A. Research Report A1536 (1965).
2. S.R. Nutt and A.W. Ruff in Wear of Materials 1983, ed. K.E. Ludema (ASME, New York, 1983) pp. 426-433.
3. N.E.W. Hartley, Thin Solid Films 64, 177-190 (1979).
4. S.R. Shepard and N.P. Suh, J. Lubr. Technol. 104, 29-38 (1982).
5. R. Hutchings and W.C. Oliver, Wear, in press.
6. R.G. Vardiman and R.A. Kant, J. Appl. Phys. 53, 690-694 (1982).

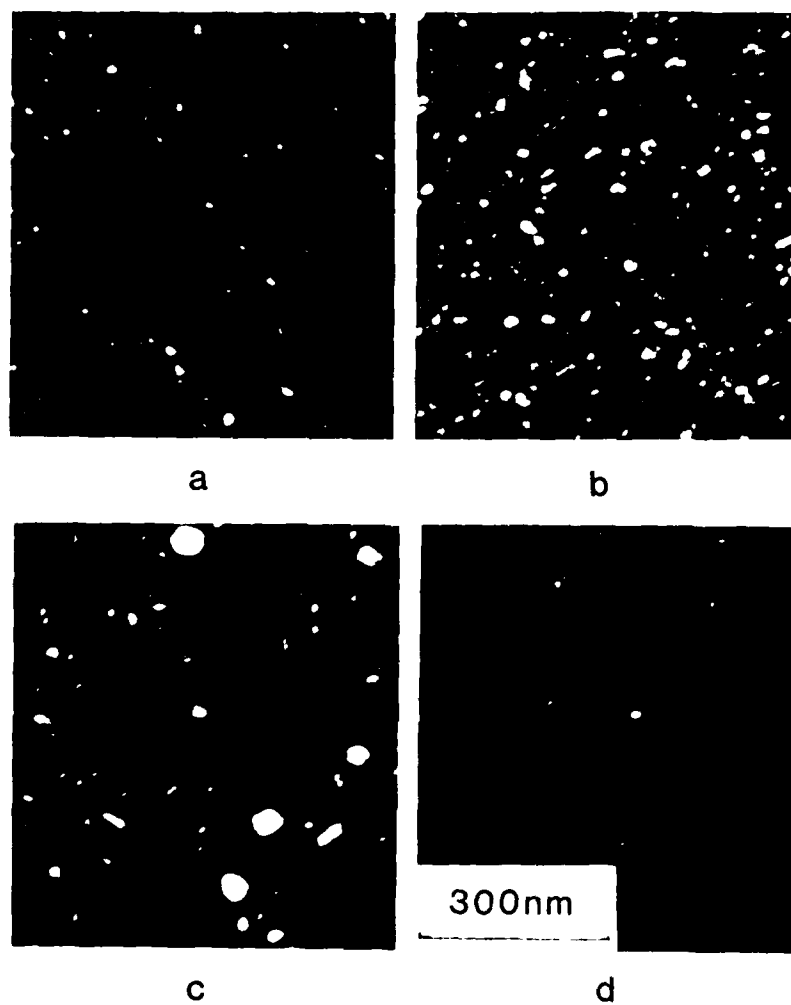


FIG. 1. Dark field TEM showing carbides in the implanted layer: (a) as implanted, (b) one hour at  $300^{\circ}\text{C}$ , (c) one hour at  $400^{\circ}\text{C}$ , and (d) one hour at  $500^{\circ}\text{C}$ .

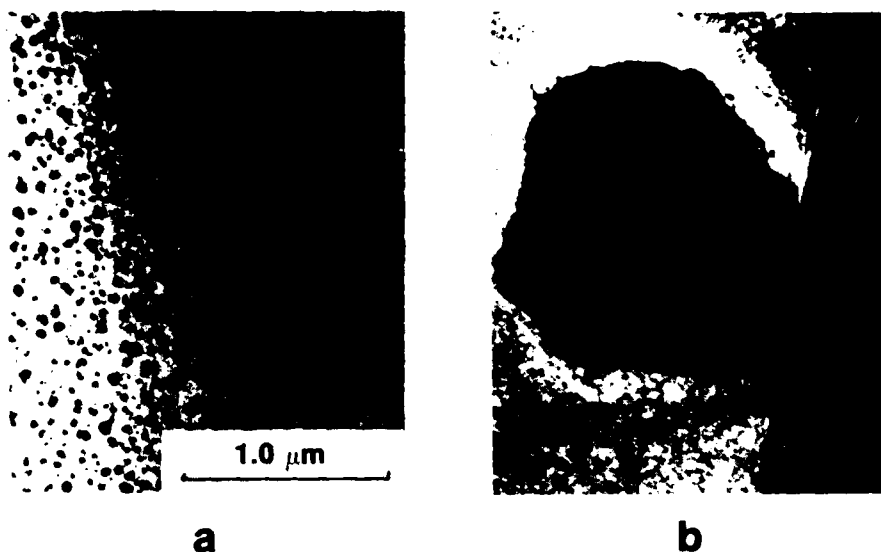


FIG. 2. Bright field TEM showing carbides after (a) one hour at 400°C and (b) one hour at 500°C.

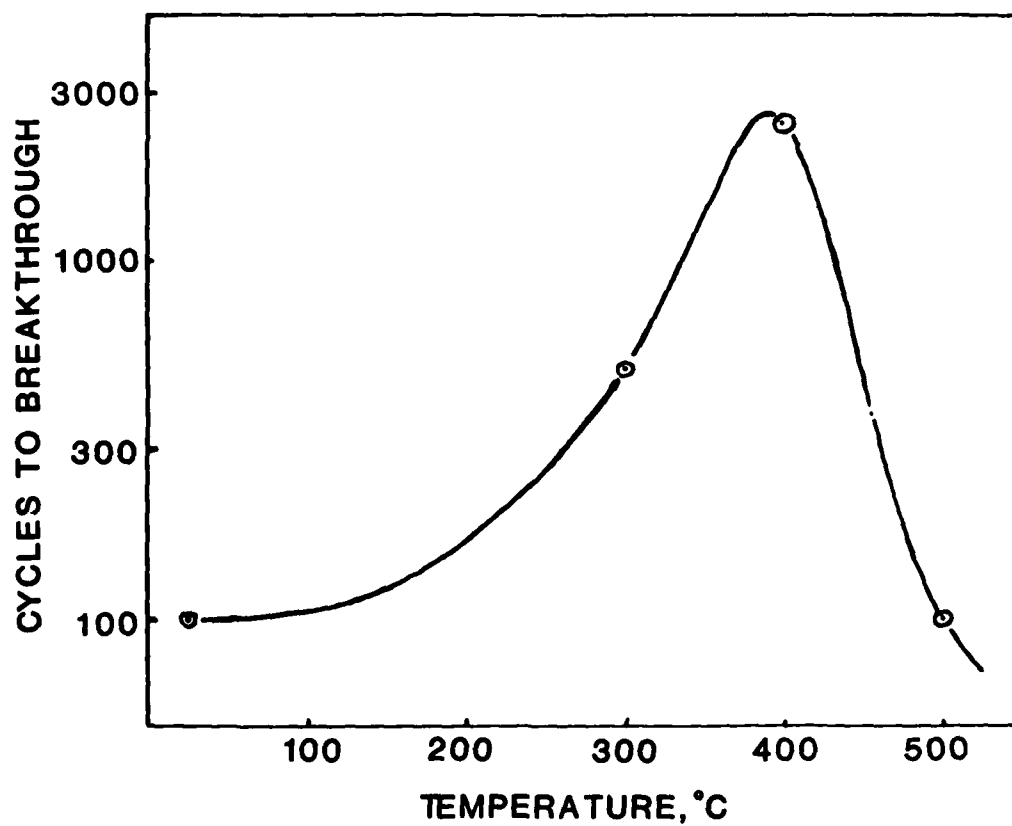


FIG. 3. Cycles to breakthrough of implanted layer vs temperature of heat treatment.

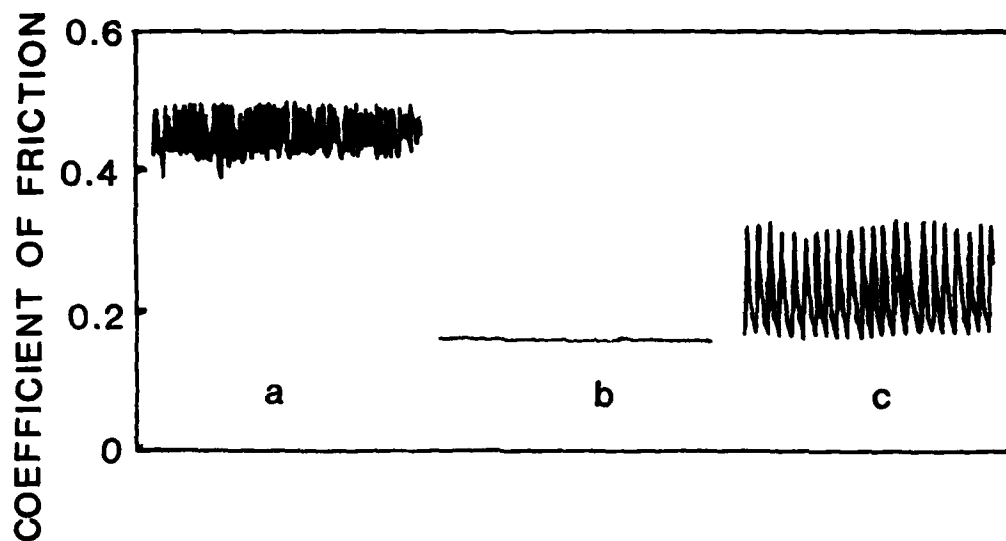


FIG. 4. Coefficient of friction for various conditions: (a) unimplanted surface; (b) and (c) different friction behavior found after carbon implantation plus one hour at 400°C.

Section III.A

AN ELECTROCHEMICAL STUDY OF AMORPHOUS  
ION IMPLANTED STAINLESS STEELS

C. R. Clayton and Y-F. Wang<sup>1</sup>  
G. K. Hubler<sup>2</sup>

<sup>1</sup>Department of Materials Science and Engineering  
State University of New York  
Stony Brook, N.Y. 11794

<sup>2</sup>Materials Modification & Analysis Branch  
Condensed Matter & Radiation Sciences Division  
Naval Research Laboratory

This work was supported at State University of New York by the Office of Naval Research, under the contract #N0001477C0424 and at NRL by the Office of Naval Research.

AN ELECTROCHEMICAL STUDY OF AMORPHOUS ION IMPLANTED STAINLESS STEELS

C. R. CLAYTON<sup>1</sup>, Y-F. WANG<sup>1</sup>, AND G. K. HUBLER<sup>2</sup>

<sup>1</sup> Department of Materials Science and Engineering, State University of New York,  
Stony Brook, N.Y. 11794, USA

<sup>2</sup> Naval Research Laboratory, Washington, D.C. 20375, USA

ABSTRACT

304 and 316 stainless steel was implanted with phosphorous at 40 keV or with boron at 25 keV to a fluence of  $1 \times 10^{17}$  to form amorphous surface alloys. The modification of the corrosion properties of the steels was monitored by dynamic polarization.

INTRODUCTION

It has been shown by Hashimoto (ref.1) that the addition of metalloid elements is necessary to obtain an amorphous structure in alloys formed by rapid quenching techniques. Among those metalloid elements, phosphorous and boron are important to ensure good corrosion resistance of amorphous iron-based alloys containing chromium. Recently ion implantation has been used extensively to modify the properties of the surface layers of pure metals and alloys. Implantation is capable of producing a wide range of metastable surface alloys. With proper selection of implant element and implantation parameters, an amorphous surface alloy may be formed (ref.2,3,4). In this work, 304 and 316 stainless steel (ss) have been implanted with phosphorous at 40 keV to a fluence of  $1 \times 10^{17}$  ions  $\text{cm}^{-2}$  or with boron at 25 keV to a fluence of  $1 \times 10^{17}$  ions  $\text{cm}^{-2}$ . In each case, this resulted in the formation of an amorphous surface alloy (ref.2,3,5). Combined implantation of B and P was also carried out. Anodic polarization studies were carried out to determine the effects of P and B implantation on the active-passive behavior and pitting resistance of 304 and 316 ss in deaerated solutions of 0.5M  $\text{H}_2\text{SO}_4$  and 0.5M  $\text{H}_2\text{SO}_4$  + 0.5M NaCl.

EXPERIMENTAL

The chemical composition of 304 and 316 ss is given below. The depth profiles of P and B in 304 and 316 ss were obtained by Auger Spectroscopy with 6keV argon or 2keV xenon ion sputtering. The distribution of P and B in 304 and 316 ss were very similar. The distributions of P and B in the 304 ss samples are shown in figures 1a and 1b. It is seen from the B profile, figure 1b, that a slight enrichment of Fe and Cr occurs within the first 20 nm. This is thought to be due to radiation enhanced diffusion rather than selective sputtering.

TABLE 1.

Composition of 304 and 316 stainless steels

Steel	% Cr	% Ni	% Mn	% Si	% Mo	% C	% N	% S	% P	% Fe
304	18.18	8.48	1.75	0.5	0.36	0.051	0.05	0.005	0.028	balance
316	17.25	10.82	2.0	0.6	2.28	0.05	0.03	0.030	0.032	balance

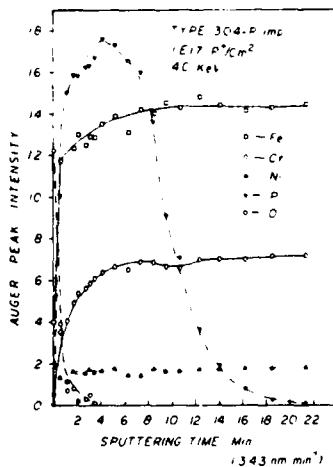


Fig. 1a.

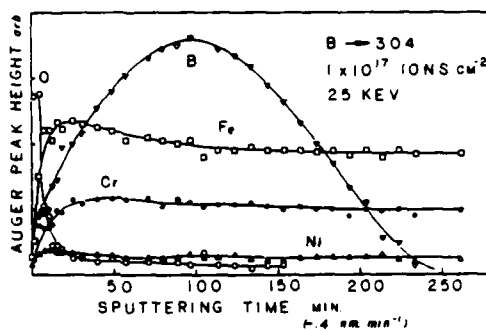


Fig. 1b.

Fig. 1. AES composition depth profiles of P (1a.) and B (1b.) implanted 304 stainless steel.

Anodic polarization was carried out in argon deaerated solutions of 0.5M H<sub>2</sub>SO<sub>4</sub> and 0.5M H<sub>2</sub>SO<sub>4</sub> + 0.5M NaCl using a conventional Greene cell. The implanted samples were masked with epoxy resin to prevent attack on unimplanted surfaces. All potentials were recorded relative to a saturated calomel electrode (SCE). The samples were cathodically treated at 1mA/cm<sup>2</sup> (150–200 mV below E<sub>ocp</sub>) for 30 minutes to remove the air formed film on the surfaces. Samples were then anodic polarized with a scanning rate of 1mV/sec.

## RESULTS AND DISCUSSION

Anodic Polarization in 0.5M H<sub>2</sub>SO<sub>4</sub>

The anodic polarization curves of implanted and unimplanted 304 and 316 ss in 0.5M H<sub>2</sub>SO<sub>4</sub> are given in figure 2 and figure 3 with the corresponding parameters given in Table 2. All the implanted steels show a reduction in the critical current density ( $i_c$ ). In the case of the 304 ss samples, the passivation potential ( $E_p$ ) shifted to more negative values and a small decrease in the transpassive potential ( $E_T$ ) is observed. The elevation of the slope of the transpassive curve indicated that P-implantation reduces the rate of transpassive dissolution. In the passive potential region Phosphorous tended to form a more stable film as indicated by a lower passive current density ( $i_{pp}$ ). Boron implanted steel showed a higher current density in the same potential region. A second current maximum ( $E_p'$ ) was observed on each of the implanted steels. The polarization behaviour of the P and B multi-implanted steel is midway between that of both P and B implanted steel. Therefore there appears to be no synergistic effect on the anodic behaviour of 304 ss from mixing P and B.

P-implantation of 316 ss results in the complete removal of the active region. A single anodic maximum is observed at +33mV. The transpassive potential and the slope of the transpassive branch is slightly increased. B implantation provides no evident improvement in the anodic characteristics of 316 ss, but instead leads to a slight positive increase in the passivation potential.

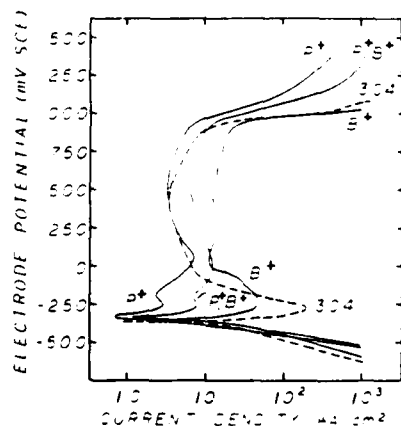


Fig. 2.

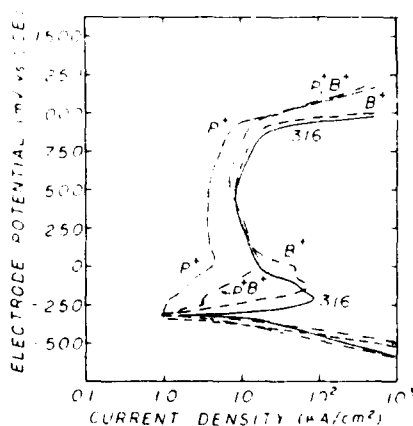


Fig. 3.

Fig. 2. Anodic polarization curves of unimplanted and implanted 304 ss in 0.5M H<sub>2</sub>SO<sub>4</sub> solution.

Fig. 3. Anodic polarization curves of unimplanted and implanted 316 ss in 0.5M H<sub>2</sub>SO<sub>4</sub>.

TABLE 2

Anodic polarization parameters determined in deaerated 0.5M H<sub>2</sub>SO<sub>4</sub>

Steel	Potential (mV vs SCE)				Current Density ( $\mu$ A cm <sup>-2</sup> )		
	E <sub>ocp</sub>	E <sub>p</sub>	E <sub>p</sub> '	E <sub>T</sub>	I <sub>c</sub>	I <sub>c</sub> '	I <sub>pp</sub>
304	-370	-225	—	+945	200.0	—	3.4
304-P	-330	-250	+50	+930	4.2	7.1	3.3
304-B	-375	-263	+200	+910	42.0	12.5	11.0
304-P,B	-330	-250	0	+933	8.2	12.4	6.6
316	-314	-206	—	+904	84.0	—	8.4
316-P	-325	—	+33	+900	—	4.5	3.7
316-B	-305	-125	-5	+935	70.0	50.0	8.4
316-B,P	-282	-245	32	+962	3.2	16.5	7.2

Anodic polarization in 0.5M H<sub>2</sub>SO<sub>4</sub> + 0.5M NaCl

The anodic polarization curves for implanted and unimplanted 304 and 316 ss in the acid/chloride solutions are presented in figures 4 and 5. The corresponding parameters are given in Table 3. The beneficial effect of P-implantation on the active-passive transition is repeated in the acid/chloride solution as is the lowering of the critical current density for 304 passivation. As before, B increased the passivation potential both for 304 and 316 ss in the positive direction. P-implantation appears to have little beneficial effect upon the pitting resistance of 304 and 316 ss, while B significantly raises the pitting potential (E<sub>b</sub>) of both steels. The multiple P and B implantation treatment combines the beneficial effect of P on the active-passive transition, and the beneficial effect of B on the breakdown potential (E<sub>b</sub>).

It is interesting to note that Mo is added to stainless steels to improve pitting resistance. However, it is well known that Mo also tends to increase the activity of the stainless steel slightly. Therefore Mo and B appear to have some similar characteristics. At this stage the exact effect Mo and B may have on the properties of the passive film and on the metal layer interfacing the film is not known. A more comprehensive study to include the composition analysis of the passive films and the underlying alloy of both unimplanted and implanted stainless steel is currently underway and will be reported elsewhere.

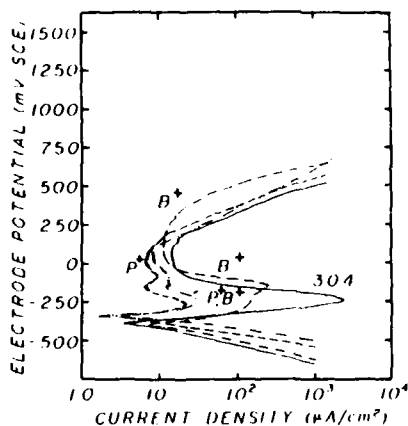


Fig. 4.

Fig. 4. Anodic polarization curves of unimplanted and implanted 304 ss in 0.5M H<sub>2</sub>SO<sub>4</sub> + 0.5M NaCl.

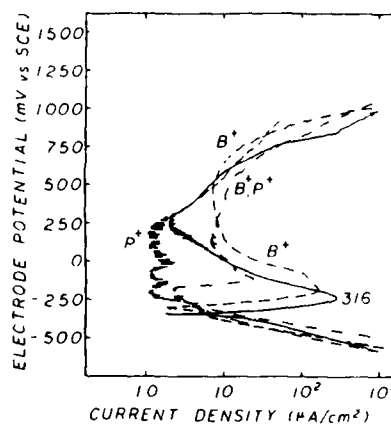


Fig. 5.

Fig. 5. Anodic polarization curves of unimplanted and implanted 316 ss in 0.5M H<sub>2</sub>SO<sub>4</sub> + 0.5M NaCl.

TABLE 3

Anodic polarization parameters determined in deaerated 0.5M H<sub>2</sub>SO<sub>4</sub> + 0.5M NaCl.

Steel	Potential (mV vs SCE)				Current Density (μA cm <sup>-2</sup> )		
	E <sub>ocp</sub>	E <sub>p</sub>	E <sub>p</sub> '	E <sub>b</sub>	I <sub>c</sub>	I <sub>c</sub> '	I <sub>pp</sub>
304	-390	-243	—	+150	2600	—	15.0
304-P	-345	-263	-80	+160	23	9.6	6.5
304-B	-375	-145	—	+350	195	—	11.5
304-P,B	-342	-237	-80	+110	30	16.0	8.3
316	-340	-236	—	+305	280	—	2.2
316-P	-250	-135	0	+225	1.6	2.2	1.3
316-B	-295	-180	-75	+692	160	120.0	7.0
316-P,B	-250	-112	—	+640	25	25.0	7.1

## CONCLUSIONS

- \* P-implantation improved the active-passive behavior of 304 and 316 ss in solutions of 0.5M H<sub>2</sub>SO<sub>4</sub> and 0.5M H<sub>2</sub>SO<sub>4</sub> + 0.5M NaCl.
- \* B-implantation had no beneficial effect on the active-passive behavior of 304 and 316 ss in both test electrolytes.
- \* B significantly increased the pitting resistance of 304 and 316 ss in the 0.5 H<sub>2</sub>SO<sub>4</sub> + 0.5M NaCl solution.
- \* The beneficial effects of P and B were combined in the multiple implantation treatment.

## ACKNOWLEDGMENTS

This work was support by the U.S Office of Naval Research, Arlington, Virginia, under the contract # N0001477C0424.

## REFERENCE

- 1 K. Hashimoto, M. Naka, J. Nugichi, K. Asami, and T. Masumoto. Passivity of Metals, Ed. R.P. Frankenthal and J. Kruger (Proc. of Fourth Int. Symp. on Passivity, 1977) p. 156 The Electrochem. Soc. Inc., Princeton, N.J. (1978)
- 2 C. R. Clayton, K. G. K. Doss, Y-F Wang, J. B. Warren and G. K. Hubler. Ion Implantation Into Metal, Ed. V. Ashworth et al. Pergamon Press, Oxford and New York. 1982.
- 3 C. R. Clayton, K. G. K. Doss, H. Herman, S. Prasad, Y-F Wang, J. K. Hirvonen and G. K. Hubler. Ion Implantation Metallurgy, Ed. C. M. Preece and J. K. Hirvonen, TMS-AIME 1980
- 4 C. R. Clayton, Nuclear Instruments and Methods 182/183, p.865-873 (1981)
- 5 Chen Qing-Ming et al., Proc. IBMM-82 Grenoble, France, September, 1982.

Section III.B

MODIFICATION OF THE PASSIVITY OF 316 STAINLESS  
STEEL BY P AND B IMPLANTATION

C. R. Clayton and Y-F. Wang<sup>1</sup>  
G. K. Hubler<sup>2</sup>

<sup>1</sup>Department of Materials Science and Engineering  
State University of New York  
Stony Brook, N.Y. 11794

<sup>2</sup>Materials Modification & Analysis Branch  
Condensed Matter & Radiation Sciences Division  
Naval Research Laboratory

This work was supported at State University of New York by the Office of Naval Research, contract #N0001477C0424 and National Science Foundation DMR 8106499A01 and at Naval Research Laboratory by the Office of Naval Research.

MODIFICATION OF THE PASSIVITY OF 316 STAINLESS STEEL  
BY P AND B IMPLANTATION

C. R. Clayton<sup>1</sup>, Y-F Wang<sup>1</sup>, and G. K. Hubler<sup>2</sup>

1. Department of Materials Science and Engineering  
State University of New York, Stony Brook, N.Y. 11794 USA
2. Naval Research Laboratory, Washington, D. C. 20375, USA

Abstract

The nature of the passive films formed on 316 stainless steel (ss) and on amorphous surface alloys formed on 316ss by P and B ion implantation have been studied. The passive films formed on 316ss at +250mV and +550mV (vs SCE) in de-aerated 0.5M H<sub>2</sub>SO<sub>4</sub> were found to be crystalline. Under identical conditions the passive films formed on both of the amorphous surface alloys were found to be amorphous. P implantation resulted in self-passivation in 0.5M H<sub>2</sub>SO<sub>4</sub> and 0.5M H<sub>2</sub>SO<sub>4</sub> + 0.5M NaCl, but was less resistant to pitting than 316ss. B implantation, however, had no beneficial effect on the active-passive transition but exhibited a higher pitting resistance than 316ss. An attempt is made to explain the differences in passivity and breakdown of passivity of the two amorphous surface alloys in terms of the composition of their passive films.

Introduction

Ion implantation is emerging as a specialized corrosion protection treatment in which pure metals and engineering alloys may be doped with metals or metalloids in order to modify anodic and cathodic processes (1). Ion Implantation provides wide scope for producing a range of metastable surface alloys, some of which are amorphous. To form amorphous surface alloys care is taken to choose an implant species which either has a very low miscibility in the host element eg. Ta-Fe (or steel) or which may form a deep eutectic eg. P or B-Fe (or steel).

In this paper we consider improving the general and localized corrosion resistance of 316ss by producing amorphous surface alloys by implantation with

- a) P implantation at  $10^{17} \text{ P cm}^{-2}$  and 40 KeV
  - and b) B implantation at  $10^{17} \text{ B cm}^{-2}$  and 25 KeV.
- In previous communications we have considered the structure and composition of the passive films formed on P-304ss (2,3) and have compared the electrochemical behavior of P and B implanted 304 and 316ss (4). In this work we are concerned in part with the effect of P and B implantation on the structure, thickness and composition of the passive films formed on 316ss in deaerated 0.5M H<sub>2</sub>SO<sub>4</sub> under controlled potential conditions.

### Experimental

The chemical composition of 316ss is given in Table 1

Table 1

Composition of 316 Stainless Steel in wt%

Cr.	Ni.	Mn.	Si.	Mo.	C.	N.	S	P	Fe
17.25	10.82	2.00	0.60	2.28	0.05	0.03	0.03	0.03	Bal

The samples were mechanically polished up the grades finishing with a 0.5  $\mu\text{m}$  chromium oxide paste polish. Samples were then washed in methanol. Following ion implantation the composition of the surface alloys was determined by auger depth profiling. The profiles obtained are presented in figure 1. Structural analysis consisted of Reflection High Energy Electron Diffraction (RHEED) of the as-implanted surfaces. The electrochemical behavior of the unimplanted and implanted steels was determined by potentiodynamic polarization using a PAR Model 173 potentiostat.

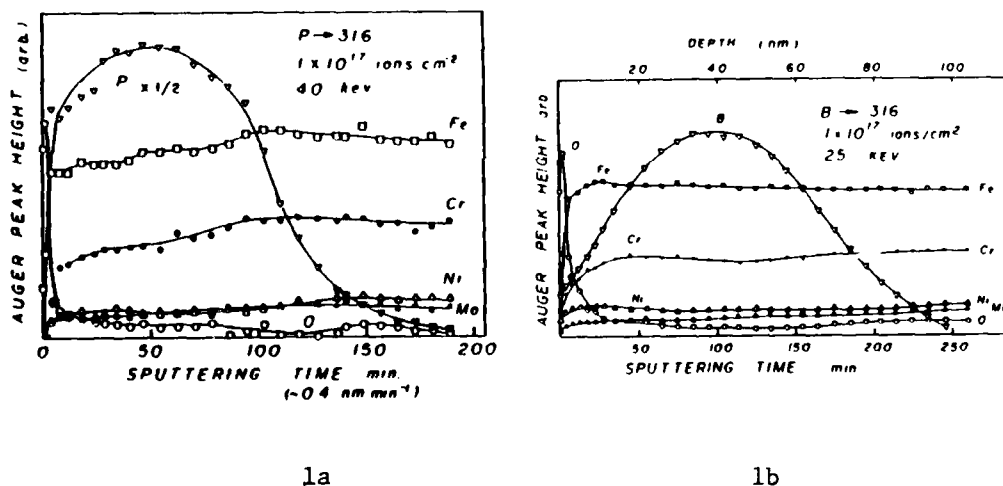


Fig. 1. AES Composition depth profiles of P (1a) and B (1b) implanted 316 stainless steel

Potentiodynamic polarization was carried out in argon deaerated solutions of 0.5M  $\text{H}_2\text{SO}_4$  and 0.5M  $\text{H}_2\text{SO}_4$  + 0.5M NaCl using a conventional Greene cell. The implanted samples were masked with epoxy resin to prevent attack on unimplanted surfaces. All potentials were recorded relative to a saturated calomel electrode (SCE). The samples were cathodically treated at  $1\text{mA cm}^{-2}$  (150-200 mV below  $E_{\text{ocp}}$ ) for 30 minutes to remove the air formed film on the surfaces. Samples were then

anodically polarized with a scanning rate of  $1\text{mV sec}^{-1}$ . The resulting polarization curves are presented in figure 2.

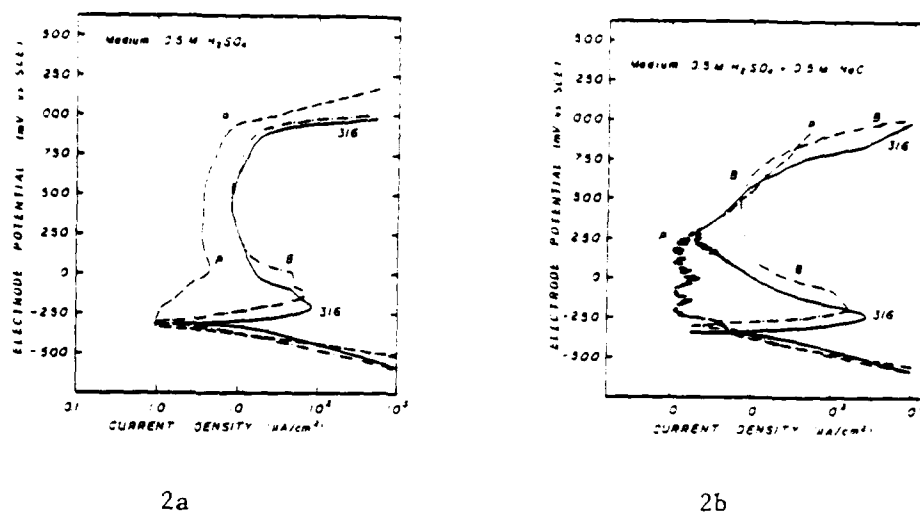


Fig. 2. Anodic polarization curves for 316ss and 316ss implanted with P and B in 0.5M H<sub>2</sub>SO<sub>4</sub> (2a) and 0.5M H<sub>2</sub>SO<sub>4</sub> + 0.5M NaCl solution (2b)

Passive films were prepared on the unimplanted and implanted steel in 0.5M H<sub>2</sub>SO<sub>4</sub> potentiostating at +250mV and +550mV for 1 hour which insured the attainment of steady state. Comprehensive characterization of the passive films included: - structural analysis determined by RHEED; film thickness and elemental distribution analysis by AES with 2KeV Xe ion sputtering and specific oxidation state information from components within the film and at the metal-film interface by non-destructive variable angle XPS (5). The RHEED data is summarized in Table 2 and the Auger depth profiles in figure 3. RHEED Patterns were obtained using a Phillips EM 300 Transmission Electron Microscope at 100KeV. Sample mounting onto the RHEED holder and transfer to the electron microscope was carried out under an argon atmosphere. Structural information was obtained by calculating the interplanar spacings employing a thin film of gold as a standard to calculate the camera constant. Electron spectroscopy was performed on a combined V. G. Scientific ESCA 3MK II, SAM unit controlled by a V. G. Scientific Data-system 1000. XPS spectra were corrected for charge shifting taking the adventitious surface carbon 1s spectrum at 284.6eV.

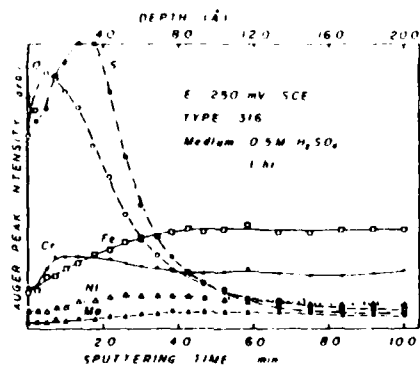
Table 2  
Summary of RHEED analysis of Passive Films formed in deaerated  
0.5M H<sub>2</sub>SO<sub>4</sub>

Sample	+250mV, 1 hr.	+550mV, 1 hr.
316ss	Cr(OH) <sub>3</sub> Green Rust II	Cr(OH) <sub>3</sub> Green Rust II γ Fe OOH Mo <sub>2</sub> S <sub>3</sub>
B→316ss	Non crystalline	Non crystalline
P→316ss	Non crystalline	Non crystalline

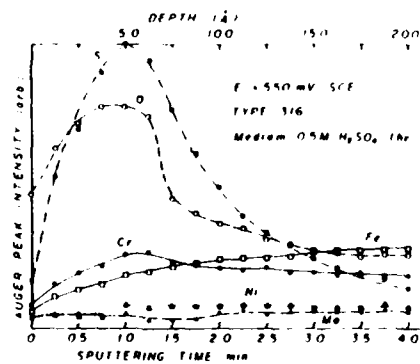
### Results and Discussion

It is apparent from the auger depth profiles of the ion implanted steel samples (figure 1) that the peak concentration of the P surface alloy was 50 at% and the surface concentration 37 at%. The peak concentration of B was found to be 20at% and the surface concentration 5at%. No evidence was found of selective sputtering or radiation enhanced diffusion resulting from the implantation process. There was also no evidence of excessive surface oxidation or carburization that had previously been reported for Cr implantation (6). It has previously been shown that P and B implantation of stainless steel, using the parameters employed in this study resulted in amorphous surface alloys (7). From Figure 2 it can be seen that P implantation resulted in self-passivity in 0.5M H<sub>2</sub>SO<sub>4</sub> solution and a marked reduction in the critical current density in the acidic SO<sub>4</sub><sup>=</sup>/Cl<sup>-</sup> solution. In 0.5M H<sub>2</sub>SO<sub>4</sub> the passive current density was also reduced. However, in the acidic SO<sub>4</sub><sup>=</sup>/Cl<sup>-</sup> solution fluctuations in the passive current density were observed at the onset of passivity and a lowering of breakdown potential was recorded. B implantation had no beneficial effects on the active-passive transition or passive current density. However, B implantation resulted in a very significant increase in the breakdown potential.

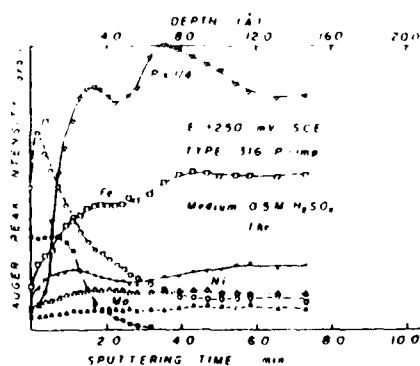
RHEED analysis rendered no evidence of crystallinity in the passive films formed on the P and B surface alloys. However, the implanted steel produced a crystalline film consisting of Cr(OH)<sub>3</sub> and Green Rust II at +250mV. In addition to these phases, Mo<sub>2</sub>S<sub>3</sub> and γ-FeOOH was observed at +550mV. The appearance of Mo<sub>2</sub>S<sub>3</sub> was confirmed by variable angle XPS which detected sulphide at the metal oxide interface. This is shown in Figure 4. SO<sub>4</sub><sup>=</sup> was also observed, as shown in Figure 4, and was associated with FeSO<sub>4</sub> in Green Rust II i.e.



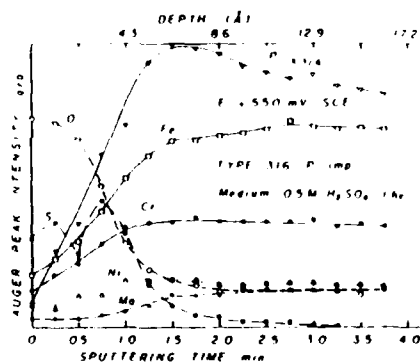
a



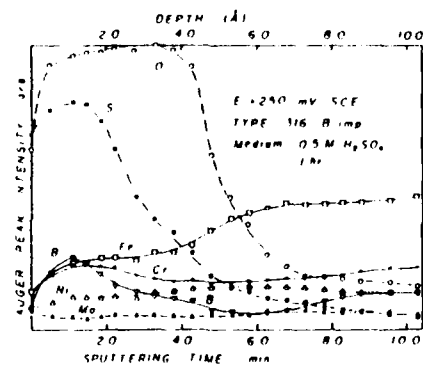
b



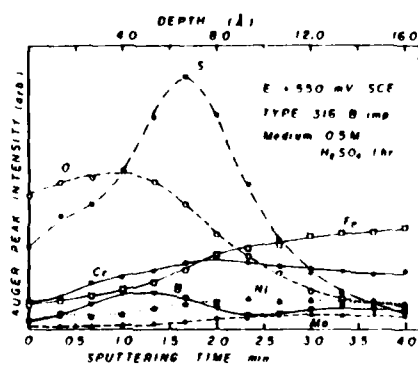
c



d



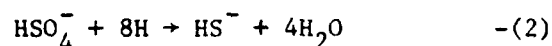
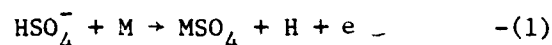
e



f

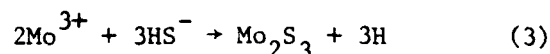
Fig. 3. AES composition profiles of the anodic films formed on 316ss. (a, b) 316ss implanted with P (c, d) and B (e, f) in 0.5M  $H_2SO_4$  at +250mV and + 550mV SCE

$4\text{Fe}(\text{OH})_2 \cdot 2\text{Fe}(\text{OH})_3 \cdot \text{FeSO}_4 \cdot \text{XH}_2\text{O}$  (8). Both  $\text{FeSO}_4$  and  $\text{Mo}_2\text{S}_3$  may form by the decomposition of the anion  $\text{HSO}_4^-$  to  $\text{HS}^-$  as follows:



where M may be Fe.

The sparingly soluble  $\text{Mo}_2\text{S}_3$  may be formed as follows:



Reactions (1) and (2) have been discussed by Droste and Feller in the anodic dissolution of Ni in 0.5M  $\text{H}_2\text{SO}_4$  (9). We note that in their work both NiS and  $\text{Ni}_3\text{S}_2$  was detected on Ni electrodes by electron diffraction.

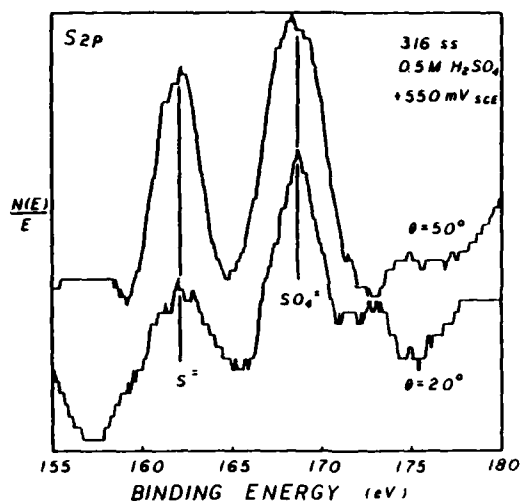


Fig. 4. S 2p photoelectron spectra measured for anodic film formed on 316ss in 0.5M  $\text{H}_2\text{SO}_4$  at +550mV SCE

By varying the photoelectron take-off angle to enhance the spectrum of the near surface atoms, i.e. to  $20^\circ$  (measured from the plane of the sample) and  $50^\circ$  to enhance the metal-film interface spectrum, it was possible to detect two S 2p spectra: (a)  $\text{SO}_4^{2-}$  (B.E. = 168.8eV) detected throughout the film and (b)  $\text{S}^{2-}$  (B.E. = 162.4eV) which was detected at the metal-film interface of Boron and unimplanted steel. The phosphorus implanted steel revealed only a trace of sulphide at +250mV. No sulphide was detected at 550mV. It was also noted that at +550mV the sulphide content was highest in the B → 316ss.

The XPS analysis suggests that the appearance of sulphide is indicated in the Auger depth profiles of the passive films formed on 316ss and B-316ss as a maximum in the S distribution. In considering the mechanism by which P may suppress sulphide formation it is possible that the formation of  $\text{Fe}_3(\text{PO}_4)_2$  which is more soluble than  $\text{FeSO}_4$ , was produced at a higher rate than the sulphate thus effectively stifling reaction (2) and ultimately reaction (3). It has been postulated by Hashimoto that the efficient dissolution of iron phosphate formed during the anodic dissolution of amorphous alloys containing Fe, P and Cr, leads to rapid surface enrichment of Cr and ultimately the formation of a Cr-rich passive film (10). In the same context, Hashimoto has also found that B is not as effective as P and thus presumably iron borate is not so readily formed at low potentials (11). This would suggest that B implantation of 316ss would neither be expected to suppress sulphide formation nor to induce spontaneous passivation in 0.5M  $\text{H}_2\text{SO}_4$ .

An alternative source of S may be that contained in the steel as an impurity (0.03wt%). Marcus and Oudar have shown that S impurities in Ni can become surface segregated during anodic dissolution (12). We note that the significantly lower passive current density associated with P implantation would tend to reduce the degree of sulphur enrichment at the metal-oxide interface. B, however, tends to increase the passive current density in 0.5M  $\text{H}_2\text{SO}_4$  and, therefore, could explain the higher level of sulphide retention compared to the unimplanted steel. Clearly a more detailed study of the source of sulphide is needed.

The appearance of  $\text{Mo}_2\text{S}_3$  at the metal-film interface of 316ss and B-316ss suggests the possibility that this compound may act as a primary passive layer which may slow down the dissolution rate of Cr allowing accumulation of  $\text{Cr}^{3+}$  and  $\text{OH}^-$  ions and thereby aid in the formation and retention of  $\text{Cr}(\text{OH})_3$ . It has been suggested by Hashimoto and co-workers that Mo in amorphous alloys and crystalline ferrous alloys aids in the establishment of a Cr-rich passive film via the formation of a Mo-rich corrosion product layer in the manner described above (13). However, the instability of the Mo-bearing corrosion products leads to oxidation to the soluble  $\text{Mo}^{6+}$  cation leaving little trace of Mo in the film. By contrast in this study the Mo-product is relatively stable at least to +550mV. Some traces of  $\text{Mo}^{6+}$  were found in the passive films by XPS indicating perhaps some evidence of breakdown of the sulphide.

B implantation appears to enhance the formation of interfacial sulphide at +550mV. It does not, however, increase the  $\text{Cr}^{3+}$  content in the film or alter film thickness. Unlike 316ss, B-316 ss produces an amorphous passive film which is contaminated with a low concentration of  $\text{BO}_3^{4-}$  anions. The three characteristics of the passive films formed on B-316 ss that appear to correlate with improved pitting resistance are:

- a) the amorphous structure of the film
- b) increased retention of  $\text{OH}^-$
- c) enrichment of  $\text{Mo}_2\text{S}_3$  at the metal-oxide interface.

Amorphylicity plays an important role in improving pitting resistance by reducing ionic mobility. Such films may also be highly hydrated. A high degree of bound water is beneficial to the repair of active sites caused by aggressive anions (14). The exact role of the sulphide layer on passivity is unknown, however, it is possible that the inner sulphide layer may aid in the retention of bound water in an outer hydroxide-type passive film by partially screening the outer layers from the high anodic electric field which otherwise activates deprotonation. It is also conceivable that the sulphide layer acts as an effective barrier against  $\text{Cl}^-$  ions centering at weak points in the outer hydroxide layer.

Of the two metalloids studied, it is apparent from passive film analysis that  $\text{PO}_4^{3-}$  retention is much higher than  $\text{SO}_3^{2-}$ . This is in part due to the higher concentration of P retained in 316ss following the high fluence implantations necessary to form the amorphous surface alloys. The high concentration of P at the metal-oxide interface found in the auger depth profiles indicates the location of surface phosphates, observed by XPS, which provide passivity. It was also noted that Cr retention in the films formed on P-316ss was surprisingly lower than 316ss and B-316ss despite the excellent passivation behavior observed in 0.5M  $\text{H}_2\text{SO}_4$ . This would suggest that insoluble phosphates of Fe and Cr provide a salt layer as the main constituent of the passive film. This barrier layer may also accommodate the formation of a relatively small concentration of amorphous  $\text{Cr}(\text{OH})_3$ . In an earlier paper we discussed a similar mechanism for the passivity of P-304ss in 0.5M  $\text{H}_2\text{SO}_4$  following detection of  $\text{CrPO}_4$  and  $\text{Fe}(\text{PO}_3)_3$  in the passive films formed at +250mV and +550mV (3). In the same paper evidence from XPS analysis was presented of the displacement of  $\text{PO}_4^{3-}$  anions by  $\text{Cl}^-$  ions following  $\text{Cl}^-$  ion inoculation experiments at +550mV in 0.5M  $\text{H}_2\text{SO}_4$ . This process may be responsible for the breakdown of passivity of P-316ss.

#### Conclusions

1. RHEED analysis suggested that the passive films formed on 316ss in 0.5M  $\text{H}_2\text{SO}_4$  were crystalline, containing  $\text{Cr}(\text{OH})_3$  and Green Rust II at both potentials studied. In addition  $\text{Mo}_2\text{S}_3$  and  $\gamma\text{-FeOOH}$  were observed at +550mV. XPS suggested that sulphide was also present at +250mV at the metal-oxide interface.
2. P implanted 316ss spontaneously passivates in 0.5M  $\text{H}_2\text{SO}_4$  by formation of an amorphous film of insoluble Fe and Cr phosphates. In acidic  $\text{SO}_4^{2-}/\text{Cl}^-$  solutions the phosphate barrier film was readily attacked by  $\text{Cl}^-$  ions and pitting occurred at a lower potential than 316ss.

3. B-implanted 316ss passivated at a more noble potential than 316ss in 0.5M  $H_2SO_4$ . The passive film was amorphous consisting of Cr and Fe hydroxides. The film was very similar to that formed on 316ss having the same thickness and Cr concentration. However, it was more highly hydrated. An inner layer of sulphide was also observed by electron spectroscopy. Pitting in anodic  $SO_4^{2-}/Cl^-$  solution occurred at higher potentials than 316ss. This was attributed both to the amorphous structure and higher bound water content of the passive film.

#### Acknowledgments

Portions of this work were supported from grants from the Office of Naval Research N0001477C0424 and National Science Foundation DMR 8106499A01. The VGS ESCA 3MK2 and VGS Datasystem were purchased from an equipment grant from the National Science Foundation. Thanks are due to K.G.K. Doss for help with RHEED analysis.

#### References

1. Corrosion of Metals Processed by Directed Energy Beams, Eds. C.R. Clayton and C.M. Preece. TMS-AIME. New York (1982).
2. C.R. Clayton, K.G.K. Doss, H. Herman, S. Prasad, Y-F Wang, J.K. Hirvonen and G.K. Hubler. Ion Implantation Metallurgy, Eds. C.M. Preece and J.K. Hirvonen, p. 65, TMS-AIME. New York (1980).
3. C.R. Clayton, K.G.K. Doss, Y-F Wang, J.B. Warren and G.K. Hubler, Ion Implantation into Metals. Eds. V. Ashworth, W.A. Grant and R.P.M. Proctor, p. 67, Pergamon Press, London (1983).
4. C.R. Clayton, Y-F Wang and G.K. Hubler in Passivity of Metals and Semiconductors. Ed. M. Froment, p. 305, Elsevier, Amsterdam (1983).
5. J.E. Castle and C.R. Clayton, Corrosion Science, 16, 7 (1977).
6. W.K. Chan, C.R. Clayton and J.K. Hirvonen, Corrosion of Metals Processed by Directed Energy Beams. Ed. C.R. Clayton and C.M. Preece, p. 91, TMS-AIME, New York (1982).
7. A. Ali, W.A. Grant and P.J. Grundy, Radiat. Eff., 34, 251 (1977).
8. J.D. Bernal, D.A. Das Gupta and A.L. Mackay, Clay Minerals Bulletin 4, 15 (1959).
9. B. Droste and H.G. Feller in Passivity of Metals. Eds. R.P. Frankenthal and J. Kruger, p. 802, Electrochemical Society, Princeton, (1978).

10. K. Hashimoto, M. Naka, J. Noguchin, K. Asami and T. Masumoto.  
ibid p. 156.
11. K. Hashimoto, K. Osada, T. Masumoto and S. Shimodaira. Corrosion  
Science 16, 71 (1976).
12. P. Marcus and J. Oudar. This publication.
13. K. Hashimoto and K. Asami in Passivity of Metals. Eds. R.P.  
Frankenthal and J. Kruger, p. 749. Electrochemical Society,  
Princeton (1978).
14. G. Okamoto, Corrosion Science 13, 471 (1973).

Section III.C

MODIFICATION OF THE LOCALIZED CORROSION BEHAVIOR OF  
AISI 52100 STEEL BY ION IMPLANTATION

C. R. Clayton and W. K. Chan<sup>1</sup>  
J. K. Hirvonen<sup>2</sup>  
G. K. Hubler<sup>3</sup>  
J. R. Reed<sup>4</sup>

<sup>1</sup>Department of Materials Science and Engineering  
State University of New York at Stony Brook  
Stony Brook, NY 11794

<sup>2</sup>Materials Modification & Analysis Branch  
Condensed Matter & Radiation Sciences Division  
Naval Research Laboratory

Present Address:  
Zymet Corporation  
Danvers, MA 01923

<sup>3</sup>Materials Modification & Analysis Branch  
Condensed Matter & Radiation Sciences Division  
Naval Research Laboratory

<sup>4</sup>Thermostructural Materials Branch  
Material Science and Technology Division  
Naval Research Laboratory

This work was supported at State University of New York by the Office of Naval Research, contract #N0001477C0424 and at Naval Research Laboratory by the Office of Naval Research.

MODIFICATION OF THE LOCALIZED CORROSION BEHAVIOR OF  
AISI 52100 STEEL BY ION IMPLANTATION

C. R. Clayton<sup>1</sup>, W. K. Chan<sup>1</sup>

J. K. Hirvonen<sup>2\*</sup>, G. K. Hubler<sup>2</sup> and J. R. Reed<sup>2</sup>

<sup>1</sup> Department of Materials Science and Engineering  
State University of New York at Stony Brook  
Stony Brook, NY 11794, USA

<sup>2</sup> Naval Research Laboratory  
Washington, D. C. 20375, USA

Abstract

The pitting resistance of AISI 52100 steel in deaerated 0.01M NaCl (pH 6 buffered) solution has been significantly improved following ion implantation with a) Cr, b) Cr + P and c) Ta ions. Cr + P and Ta ion implantation resulted in the formation of amorphous surface alloys. The improvements observed in pitting resistance are discussed in terms of the effect of the ion implantation process on the composition and structure of the carbides and martensitic metal matrix and the nature of the passive films formed on the surface alloys in the Cl<sup>-</sup> solution.

Introduction

AISI 52100 steel is one of the most widely used bearing alloys in aircraft propulsion systems. It is a through-hardened martensitic steel possessing high hardness and good wear resistance. Commonly, corrosion takes the form of localized pitting along the contact region between the rollers and racers (1). Corrosion is also responsible for the severe lowering of the shelf-life of replacement bearings, independent of the type of bearing alloy. This study considers the use of ion implantation as a corrosion protection treatment to improve the passivation behavior of 52100 steel. The choice of ion implantation as a corrosion protection treatment was based on the fact that the technique does not alter the dimensions of the bearings or reduce the contact fatigue resistance (2). Also, several studies have demonstrated that ion implantation may be used to improve the corrosion and mechanical properties of ferrous alloys (3). In this paper, we consider the use of ion implantation with Cr, Cr + P and Ta as a corrosion protection treatment for the purpose of improving localized corrosion resistance. The Cr + P and Ta implantations were carried out with a view to forming amorphous surface alloys, which are commonly found to be more corrosion resistant than crystalline alloys (4).

\*Present Address

Zymet Inc., Danvers, MA 01923

### Experimental

AISI 52100 bearing steel is a martensitic steel containing very little Cr. Its elemental composition is given in Table 1.

Table 1

#### AISI 52100 Steel Composition (% by Wt.)

C	0.96
Mn	0.36
Si	0.22
P	0.01
S	0.01
Cr	1.36
Fe	remainder

Samples of 7 x 7 x 1 mm were cut from rod stock. Polishing was then carried out up the grades finishing with a 1  $\mu$ m diamond polish finish. Samples were then degreased in methanol, rinsed in distilled water and dried. The ion implantation treatments considered in this work are outlined in Table 2. Electrochemically-thinned 3 mm diameter discs suitable for TEM and 4 x 4 x 0.5 mm thin foils for RHEED analysis were also implanted.

Table 2

#### Implantation Conditions

Ion	Fluence ( $10^{17}$ cm <sup>-2</sup> )	Energy (keV)
Cr	2.0	150
Cr <sup>+</sup>	2.0	150
P	0.5	40
Ta	1.0	150

The compositions of the passive films and surface alloys formed by ion implantation were determined by X-ray Photoelectron Spectroscopy (XPS) and Auger Electron Spectroscopy (AES). Depth profiling was carried out with a V.G. Scientific Scanning Auger Microprobe mounted onto a V.G. Scientific ESCA 3 MKII which is fitted with an hemispherical electrostatic analyzer. Auger measurements were carried out in  $5 \times 10^{-10}$  torr background pressure using a rasterable electron gun operating at 3 keV, a beam current of 20  $\mu$ A, and a modulation voltage of 3V. Ion etching was carried out intermittently using Xe ions. The ion gun was operated at 2keV accelerating potential in a background pressure of  $10^{-6}$  torr of Xe. XPS spectra were taken using Al K $_{\alpha 1,2}$  radiation with a power of 200W and the vacuum was better than  $3 \times 10^{-10}$  torr.

In the preparation of the polarization experiments, coupons of 7 x 7 x 1 mm and 4 x 4 x 0.5 mm specimens were mounted onto a "plexi-glass" backed electrochemical probe. Epoxy was used to seal the edges of the samples. The electrolyte used for pitting and passive film studies was a deaerated 0.01 M NaCl (pH 6 acetate buffer) solution. The samples were initially cathodically polarized for 30 minutes at a sufficiently negative potential to yield a cathodic current of 5 mA in order to reduce the air formed oxide films. The samples used in corrosion experiments were then left at open circuit potential for 3-5 minutes prior to potentiodynamic anodic polarization. The scan rate used was 1 mV sec<sup>-1</sup>. In the passive film studies, the specimens were potentiostatically polarized to -300 mV after the removal of the air formed oxide film. The samples were then held at this potential for 10 minutes. All electrode potentials were measured against a Saturated Calomel Electrode (SCE).

## Results and Discussion

### Composition and Structure of Surface Alloys

Auger depth profiles of the surface alloys are presented in figure 1. The Cr concentration is found to increase from 18.5at% at the alloy surface to a maximum value at 26 nm of 25.8at%. The corresponding values for the Cr + P surface alloy was 18.3at% Cr at the surface and 32.3at% at 27nm. Ta implantation resulted in a surface composition of 10at% Ta and a maximum concentration of 20at% at 19 nm.

TEM analysis of ion thinned 3 mm discs of ion implanted AISI 52100 steel was carried out to determine the structure of the surface alloys. This analysis will be fully described elsewhere (5). To summarize this analysis, it was found that the surface alloys formed by Ta and Cr + P implantation were amorphous. Ta is virtually immiscible in Fe and hence the surface alloy is a highly metastable supersaturated amorphous solid solution. The Cr + P surface alloy is also a highly metastable amorphous solid solution. It is important to note that amorphicity was achieved at a lower P fluence than reported in the literature (6) i.e. at  $5 \times 10^{16}$  P<sup>+</sup> ions cm<sup>-2</sup> compared to  $10^{17}$ . The lower fluence was chosen in an attempt to lower the P concentration in the passive film and produce a film based on chromium hydroxide rather than phosphates which have been shown to be highly vulnerable to Cl<sup>-</sup> ion attack (7).

Cr implantation resulted in the formation of a crystalline martensitic surface alloy. An important observation made in this analysis is that surface carbides that are present in the steel before implantation, are severely altered in the near surface regions due to the ion bombardment process. In figure 2 is presented bright field and dark field micrographs obtained from Cr implanted 52100, which shows radiation damage in the metal matrix and amorphization of the

surface layer of the carbides which penetrate the surface of the steel. The bright field image shows the mottled structure of the glassy region and a diffusion "intermixed" interfacial zone. In the dark field the underlying crystallinity of the inner region of the carbide is apparent. The diffraction pattern from the glass region is a double halo typical of a non-crystalline phase.

#### Polarization Experiments in 0.01 M NaCl buffered to pH6

The results of the polarization studies in 0.01 M NaCl solution are summarized in figure 3 and table 3. These studies revealed that the pitting resistance of 52100 was significantly improved by each of the ion implantation treatments. The unimplanted steel exhibited pitting very close to the open circuit potential (OCP). Each of the surface alloys exhibited self-passivation and thus remained highly reflective and unblemished until the onset of pitting. Ion implantation resulted in the following increases in the breakdown potential ( $E_b$ ) of AISI 52100 steel: - Cr, 600 mV, Cr + P, 650 mV and Ta, 880 mV. These improvements in pitting resistance were also reflected in simulated field tests carried out at the Naval Research Laboratories (8).

Table 3

#### Summary of Polarization Data obtained for AISI 52100 in deaerated 0.01 M NaCl (pH6 buffered) solution\*

<u>Sample</u>	<u>OCP (mV)</u>	<u><math>E_b</math> (mV)</u>	<u>Pass. C.D. (<math>\mu A\ cm^{-2}</math>)</u>
52100	- 675	- 650	23
Cr-52100	- 664	- 50	12
Cr + P-52100	- 642	0	30
Ta-52100	- 474	+ 230	20

\* All potentials measure w.r.t. S C E

#### Passive Film Analysis

RHEED analysis was performed on passive films formed during a 10 minute polarization at -300 mV in deaerated 0.01 M NaCl (buffered to pH6) solution during which time no pitting was observed. The three implantation treatments resulted in the formation of amorphous passive films. Figure 4 shows the electron diffraction patterns obtained from two of these passive films. Faint halos were observed in the electron microscope which are indicative of the amorphous state. These halos were not reproduced clearly in the diffraction micrographs due to poor contrast conditions.

Non-destructive variable angle XPS analysis was carried out on each of the passive films, to determine the nature of the cations and

anions. Low photoelectron take-off angles (measured from the plane of the sample) of  $20^\circ$  enhanced the spectra from the outer layers of the films.  $50^\circ$  enhanced the layers at the metal-film interface. The resulting spectra are presented in figure 5. A destructive depth profile analysis was performed on each of the passive films using AES. The profiles are presented in figure 6.

XPS analysis of the passive films formed on the Cr and Cr + P implanted steel showed some distinct differences. The Cr in each film was found to be in the  $\text{Cr}^{3+}$  state, with charge shifting occurring in the film formed on the Cr + P surface alloy.  $\text{Fe}^{2+}$  and  $\text{Fe}^{3+}$  cations were observed in the passive film formed on the Cr implanted steel. Only  $\text{Fe}^{3+}$  ions were found in the passive film formed on the Cr + P surface alloy. The ratios of the areas of the  $2p_{3/2}$  spectra of  $\text{Cr}^{3+}$  to that of  $\text{Fe}^{2+} + \text{Fe}^{3+}$  was 1.9 for the single Cr implant and 3.2 for the Cr + P surface alloy. Hence, P implantation led to the enrichment of the  $\text{Cr}^{3+}$  content of the passive film by approximately 50%. The ratio of the areas of the O1s spectra for  $\text{OH}^-$  to  $\text{O}^-$  was 1.1 for the Cr implant and 1.6 for the Cr + P surface alloy. Hence, P-implantation promoted the formation of a highly hydrated Cr rich passive. The passive films formed on the Cr and Cr + P surface alloys were found to be approximately 1.0 and 0.8 nm respectively. Both films were found to contain incorporated  $\text{Cl}^-$  ions.

The main function of P appears to be the enrichment of Cr in the passive film possibly by the selective dissolution of soluble iron phosphates during the active stage of passivation. A similar behavior has been described by Hashimoto et al for P-bearing amorphous Fe-Cr alloys (9). The consequence of enriching the passive film with Cr is to increase the  $\text{OH}^-$  content, which probably improves the ability of the film to repair local flaws (10). Hence, a greater resistance to  $\text{Cl}^-$  ion attack is achieved.

The Ta surface alloy was found to be the most pitting resistant of the three surface alloys. The passive film was found to be approximately 1.5 nm and was highly enriched in  $\text{Ta}^{5+}$  cations. No  $\text{Cl}^-$  ions were found on the surface or bulk of the passive films. From the O1s spectra it was found that the outer layer of the film was rich in  $\text{OH}^-$  anions which contrasted to the  $\text{O}^-$ -rich inner region. The film was therefore assumed to be an amorphous form of hydrated  $\text{Ta}_2\text{O}_5$ , containing a small concentration of  $\text{Fe}^{3+}$  at the metal-film interface. Hence, the passive film formed on the surface alloy closely resembles the amorphous  $\text{Ta}_2\text{O}_5$  passive film found on pure Ta (11) which provides excellent resistance to pitting due to  $\text{Cl}^-$  ions.

#### The Effect of Surface Carbides on Pitting Resistance

It is also apparent from the passive film depth profiles of figure 6, that some evidence of a low concentration of carbides is seen

in the metal matrix. Most of these carbides are the result of surface carburization resulting from the ion implantation process. A small contribution to the C KLL Auger line would come from the incipient carbides produced in the steel during tempering (12).

In previous work we have shown that carbonaceous contamination in the vacuum of the ion accelerator can deposit on the substrate surface during ion implantation, leading to surface carburization and that carburization can significantly lower the pitting behavior of Cr implanted and Cr Ion beam mixed Fe and AISI 52100 steel (12,13). This is due to disruptions in the passive film by formation of carbides. These carbides which may extend 2-5 nm below the surface, limiting the maximum effect Cr implantation has on pitting resistance. However, the carbides are not as deleterious as would be expected from the influence of incipient carbides present in steels. In steels, the interface between the carbide and metal matrix is a preferential site for localized corrosion. Figure 2 demonstrates the effectiveness of Cr implantation on randomizing the carbide surface structure and causing atomic mixing at the particle-matrix interface. In addition to modifying the structure of the surface of the carbides the implantation process inevitably dopes the carbide with a high concentration of Cr. Thus, it would be expected that galvanic potential differences across the originally discrete metal-carbide interface would be reduced both by doping and atomic mixing, which tends to promote the formation of an interfacial zone. Thus, a Cr-rich passive film is expected to form extending across the metal matrix and carbide surface. The non-crystalline nature of the passive film indicated by RHEED undoubtedly refers to that formed on the metal surface since RHEED probably would not detect the film formed on the carbide surfaces. However, the non-crystalline nature of the carbide surface found by TEM would suggest that an amorphous Cr-rich film probably forms on the carbide surface. Hence, it is conceivable that a relatively homogeneous non-crystalline film is produced on the steel. A similar effect would also be expected of Ta implantation. Furthermore, the apparently beneficial effect of ion bombardment on surface carbides indicated by the TEM analysis would explain why surface carburization due to ion implantation is not as deleterious to the corrosion properties as would be predicted from the behavior of conventional alloys.

#### Conclusions

1. The pitting resistance of AISI 52100 steel in 0.01 M NaCl solution has been significantly improved following ion implantation with Cr, Cr + P and Ta.
2. The improvements in pitting resistance followed the trend: Ta > Cr + P > Cr.
3. Cr + P and Ta implantation resulted in the formation of non-crystalline surface alloys.

4. The improvements in pitting resistance have been related to modifications in the composition and structure of:
  - a) both second phase particles and the metal matrix
  - b) the passive film formed on AISI 52100.
5. The near surface structure of carbide particles was rendered amorphous by radiation-induced disorder. Probably ion beam mixing of the carbide-matrix and doping of the carbides contributed to the lowering of galvanic potential differences between carbide particles and the metal matrix.
6. Ta implantation resulted in the formation of a passive film consisting mainly of amorphous hydrated  $Ta_2O_5$ .
7. The Cr implanted steel produced an amorphous film consisting of hydrated oxides of Cr and Fe.
8. Further implantation with P at a fluence of  $5 \times 10^{16}$  ions  $cm^{-2}$  increased the Cr concentration in the passive film by approximately 50% and tended to support the formation of an M-OH type film, resulting in greater resistance to  $Cl^-$  ion attack and eventual pitting.

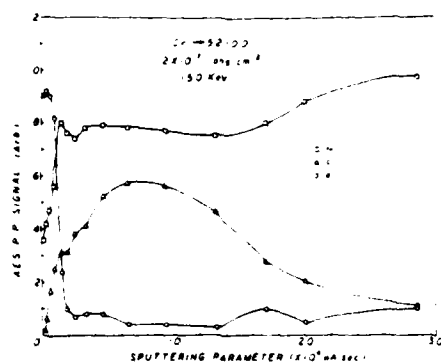
#### Acknowledgments

This work was supported by the U. S. Office of Naval Research, Arlington, Virginia, under the Contract #N0001477C0424 (Dr. P. A. Clarkin). The VGS Electron Spectrometer and VGS 1000 Data System were acquired from equipment awards DMR7718319 and DMR811732 from the National Science Foundation, Washington, D.C., (P. J. Reznik).

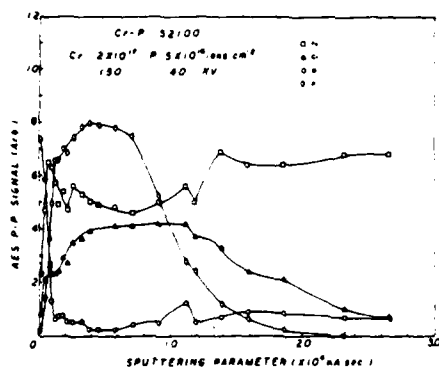
#### References

1. R. Valori and G.K. Hubler, NRL Memorandum Report 4527 June (1981), p. 100.
2. G.K. Hubler, Priv. Comm.
3. J.K. Hirvonen and C.R. Clayton in Surface Modification and Alloying, Ed. M.M. Poate, G. Foti and D.C. Jacobson, NATO conference series, Plenum, New York (1983).
4. R.B. Diegle, N.R. Sorensen, T. Tsor and R.M. Latanision in Corrosion: Aqueous Processes and Passive Films, Vol. 23 Treatise on Materials Science and Technology, Ed. J.C. Scully. Academic Press Inc., London (1983).

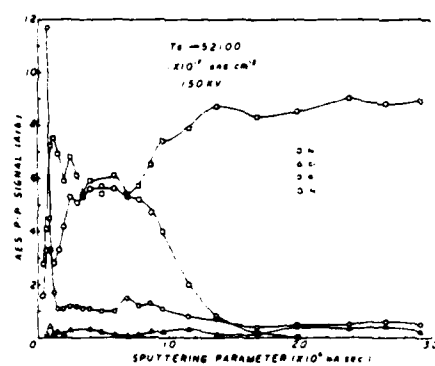
5. C.R. Clayton, W.K. Chan, G.K. Hubler and J. Spragues. To be submitted.
6. J.L. Whitton, W.A. Grant and J.L. Williams. Proc. Int. Conf. on Ion Beam Modification of Materials, Budapest, Hungary (1978).
7. C.R. Clayton, Y-F Wang, and G.K. Hubler. This volume.
8. G.K. Hubler. Priv. Comm.
9. K. Asami, K. Hashimoto, T. Masumoto and S. Shimodaira, Corr. Sci. 16, 909 (1976).
10. H. Saito, T. Shibata and G. Okamoto, Corros. Sci., 19, 693 (1979).
11. L. Young, Anodic Oxide Films, p. 120, Academic Press, London (1961).
12. W.K. Chan, C.R. Clayton and J.K. Hirvonen in: Corrosion of Metals Processed by Directed Energy Beams, Eds. C.R. Clayton and C.M. Preece, p. 91, TMS-AIME, New York (1982).
13. W.K. Chan, C.R. Clayton, R.G. Allas, C.R. Gossett and J.K. Hirvonen, Nuclear Instruments and Methods, 209/210, 857 (1983).



1a



1b



1c

- Fig. 1a. Auger depth profile of Cr implanted  
( $2 \times 10^{17}$  ions  $\text{cm}^{-2}$ ) 52100
- Fig. 1b. Auger depth profile of Cr-P implanted  
( $2 \times 10^{17}$  Cr;  $5 \times 10^{16}$  P ions  $\text{cm}^{-2}$ ) 52100
- Fig. 1c. Auger depth profile of Ta implanted  
( $1 \times 10^{17}$ ) 52100

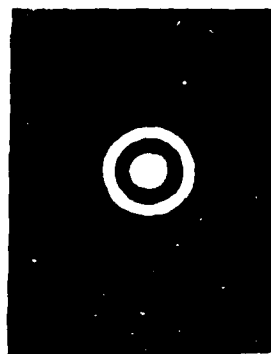
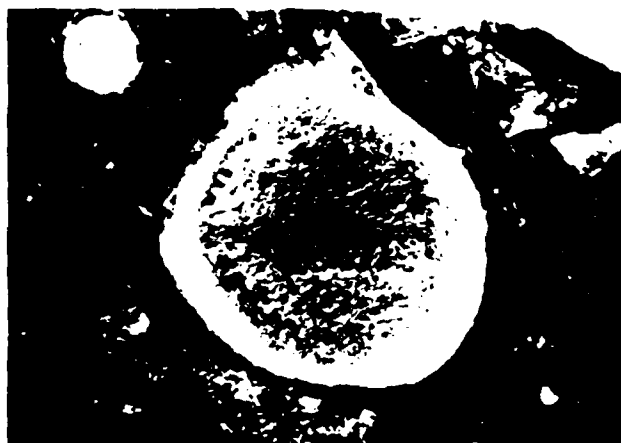
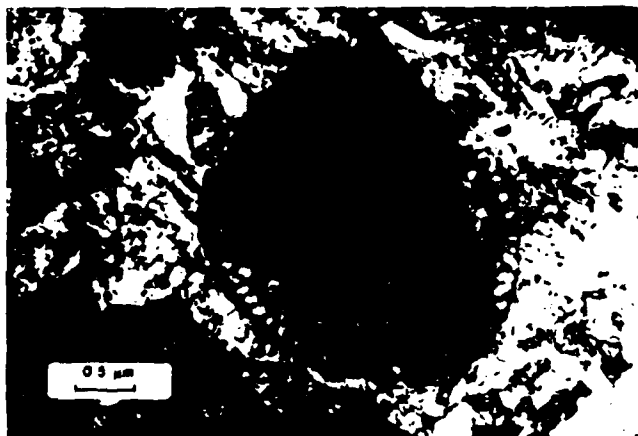


Fig. 2. TEM bright, dark field image and diffraction pattern of amorphous carbide phase found in Cr implanted 52100 passivated at  $-300\text{mV}$  (vs. SCE) for 10 min. in 0.01 M NaCl buffered  $\text{pH}\approx 6.0$

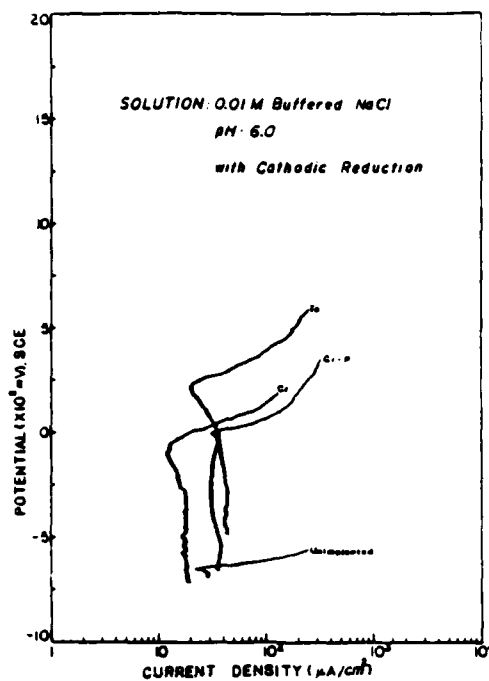


Fig. 3. Anodic polarization curves for AISI 52100 steel and AISI 52100 steel implanted with Cr, Cr + P and Ta in 0.01M NaCl pH6 buffer solution

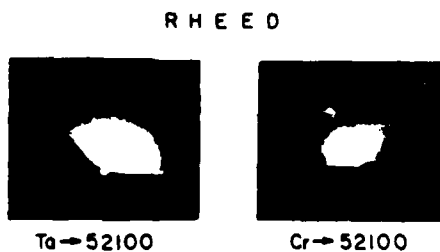
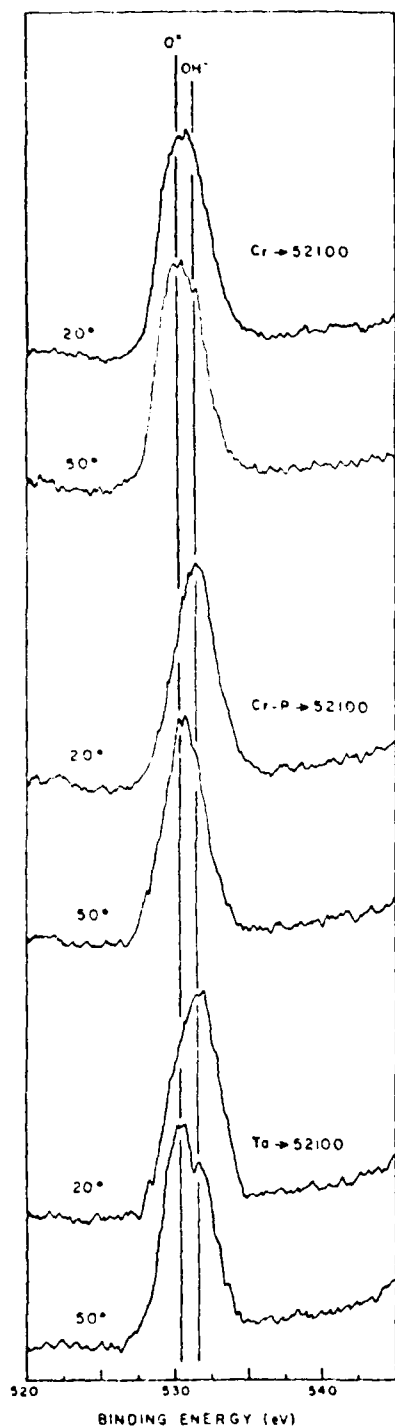
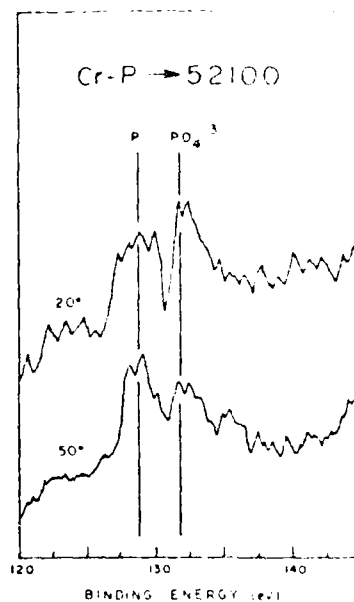


Fig. 4. RHEED pattern of Cr and Ta implanted 52100 steel passivated at -300mV (vs. SCE) for 10 min. in 0.01M NaCl buffered pH=6.0



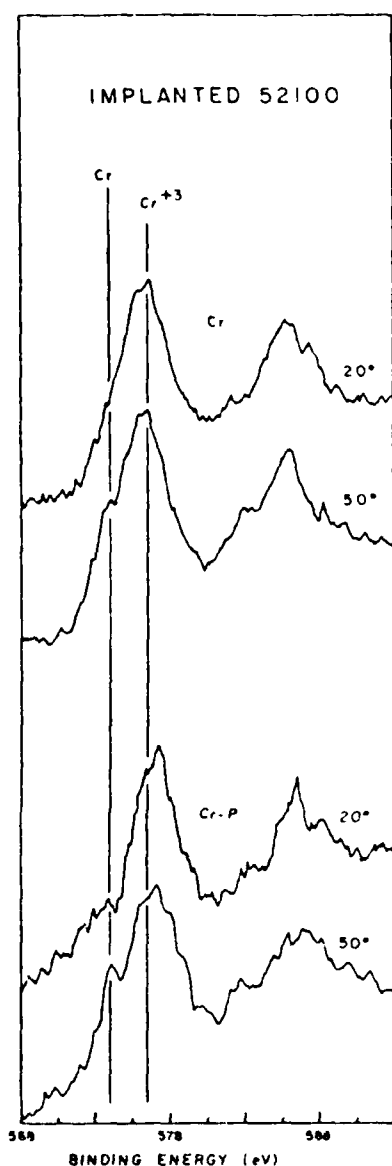
5a



5b

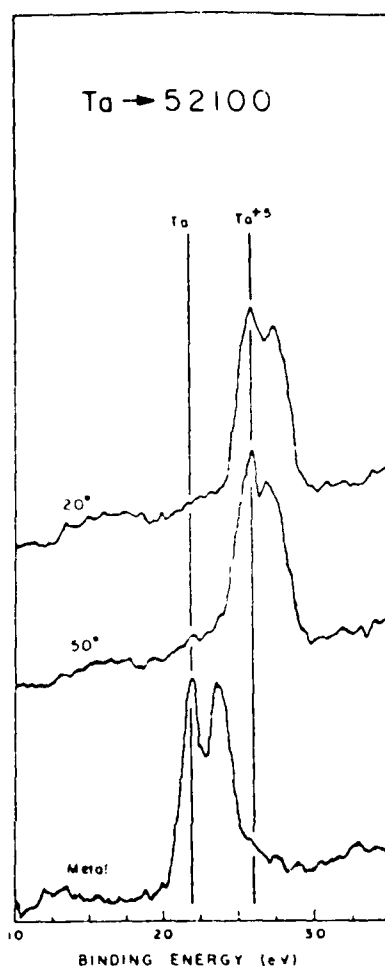
Fig. 5a. The O 1s spectra measured for Cr, Cr-P and Ta implanted 52100 passivated at -300mV (vs. SCE) for 10 min. in 0.01M NaCl buffered pH=6.0

Fig. 5b. The P 2p spectra measured for Cr-P implanted 52100 passivated at -300mV (vs. SCE) for 10 min. in 0.01M NaCl buffered pH=6.0



5c

The Cr 2p spectra measured for Cr and Cr-P implanted 52100 passivated at -300mV (vs. SCE) for 10 min. in 0.01M NaCl buffered pH=6.0



5d

The Ta 4f spectra measured for Ta implanted 52100 passivated at -300mV (vs. SCE) for 10 min. in 0.01M NaCl buffered pH=6.0

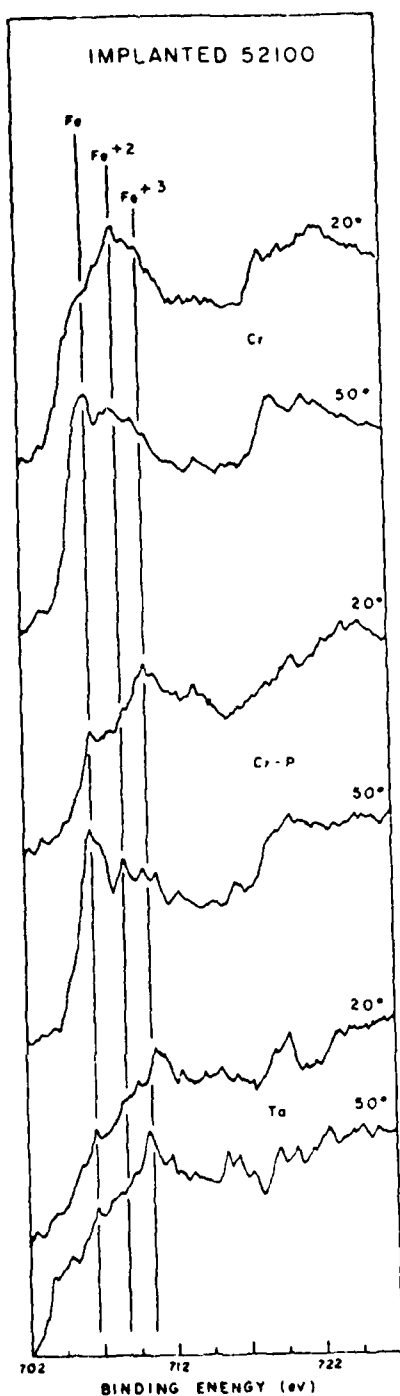
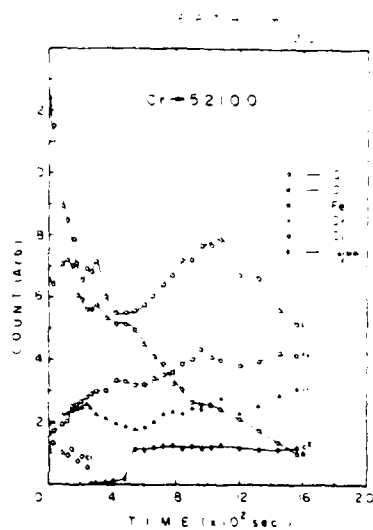
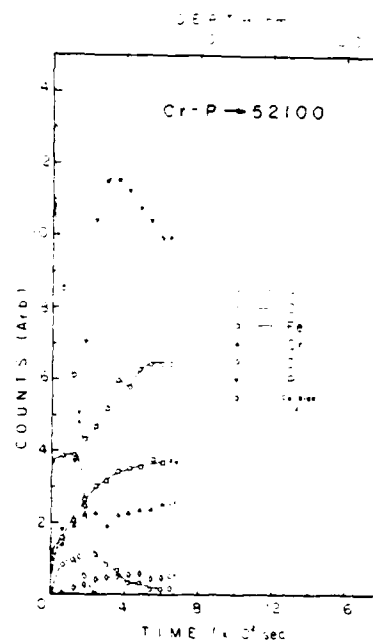


Fig. 5e. The Fe 2p spectra measured for Cr, Cr-P and Ta implanted 52100 passivated at -300mV (vs. SCE) for 10 min. in 0.01M NaCl buffered pH-6.0

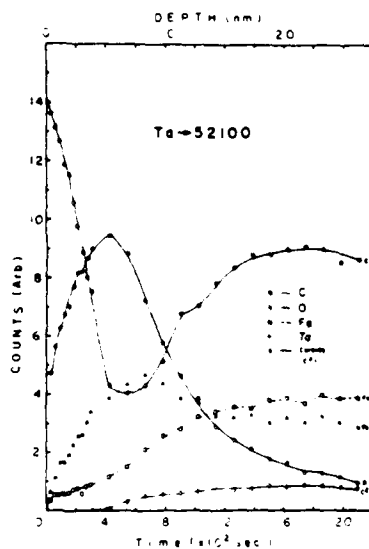
5e



6a



6b



6c

Fig. 6. Auger depth profiles of passive films formed on ion implanted 52100 steel passivated at -300mV (vs. SCE) for 10 min. in 0.01M NaCl buffered pH=6.0  
a) Cr→52100; b) Cr + P→52100; c) Ta→52100

Section III.D

ION IMPLANTING BEARING SURFACES FOR CORROSION RESISTANCE

R. Valori and D. Poggoshev<sup>1</sup>  
G. K. Hubler<sup>2</sup>

<sup>1</sup>Naval Air Propulsion Center  
Trenton, New Jersey

<sup>2</sup>Materials Modification & Analysis Branch  
Condensed Matter & Radiation Sciences Division  
Naval Research Laboratory

This work was supported by the Naval Air Propulsion Center

# Ion Implanting Bearing Surfaces for Corrosion Resistance

R. Valori

D. Popgoshev

Naval Air Propulsion Center,  
Trenton, N. J.

G. K. Hubler

Naval Research Laboratory,  
Washington, D. C.

*A program is currently underway to use ion implantation to improve the tribological and corrosion characteristics of load bearing surfaces in both rolling element bearings and gears used in aircraft propulsion systems. This paper describes that aspect of the program concerned with the use of ion implantation for surface alloying of bearing components in order to alleviate the problem of corrosion in costly M50 steel mainshaft aircraft engine bearings. Results to date indicate that implantation of selected ion species can significantly improve resistance to both generalized and localized (pitting) corrosion without adversely affecting bearing performance or fatigue endurance life.*

## Introduction

Ion implantation as a means of alloying the load bearing surfaces of gears and rolling element bearings used in Navy and aircraft propulsion systems, has the potential for solving costly problems relating to corrosion and premature surface failures.

Ion implantation is a process by which virtually any element can be injected into the near-surface region of any solid by means of a beam of high-velocity ions (usually tens to hundreds of keV in energy) striking a target mounted in a vacuum chamber. The bombarding ions lose energy in collisions with substrate atoms and come to a stop at depths of tens to thousands of angstroms in the host material. The major advantages of ion implantation over coatings and other methods of surface treatments are:

- (a) No change in dimensions or surface character which allows the implantation of existing bearings without further processing.
- (b) None of the interface bonding problems associated with coatings.
- (c) Material bulk properties remain the same.
- (d) Choice of alloying element is not limited by solid solubility or diffusion parameters.

Accordingly, ion implantation offers an attractive method of achieving corrosion resistance and improved tribological characteristics. Consequently the Naval Air Propulsion Center (NAPC) has established and is managing a program to investigate the use of ion implantation for:

- (a) Producing corrosion resistance alloys on M50 steel bearing surfaces.
- (b) Improving the tribological characteristics (wear, scoring, etc.) of bearing and gear surfaces.

The major effort to date and the work described herein is related to the first item listed. This is motivated by the fact

that a major cause of bearing rejection at Naval Air Rework Facilities (NARF's) is corrosion pitting [1]. The estimated yearly cost for replacement of the expensive mainshaft bearings made of M50 steel is several million dollars for both the Navy and Air Force.

The program was designed to:

- (a) Determine optimum implantation parameters (ion energy, species and fluence) most effective of inhibiting corrosion in hardened M50 bearing steel using several types of corrosion tests as a measure of success.
- (b) Develop the methods of implanting all load bearing surfaces of both ball and roller bearings for subsequent testing.
- (c) Conduct full scale bench tests to insure that no deterioration in bearing performance or endurance life occurs as a result of implantation.
- (d) Determine the effectiveness of implantation in inhibiting corrosion of full scale bearings in service, in the long term storage, and in a test cell engine evaluation.

The Naval Research Laboratory is responsible for items (a) and (b). The NAPC and the Naval Air Rework Facility in North Island share responsibilities for items (c) and (d).

## ION IMPLANTATION PARAMETERS

IMPLANTED ELEMENTS	- VIRTUALLY ANY ELEMENT FROM HYDROGEN TO URANIUM CAN BE IMPLANTED
ION ENERGIES	- NORMALLY 2 TO 200 KeV ENERGIES UP TO 5 MeV MAY BE OBTAINED WITH THE VAN DE GRAAFF ACCELERATOR
ION RANGES	- VARY WITH ION ENERGY ION SPECIES AND HOST MATERIAL RANGES NORMALLY 0.01 $\mu$ m TO 10 $\mu$ m
RANGE DISTRIBUTION	- APPROXIMATELY GAUSSIAN CHOICE OF ENERGIES ALLOW TAILORED DEPTH DISTRIBUTION PROFILES
CONCENTRATION	- FROM TRACE AMOUNTS UP TO 50% OR MORE
HOST MATERIAL	- ANY SOLID MATERIAL CAN BE IMPLANTED
SPECIAL EFFECTS	- SPUTTERING RADIATION DAMAGE RADIATION ENHANCED DIFFUSION

Fig. 1 The effect produced by ion implantation depends on a number of factors or parameters. These parameters, together with typical ranges of values, are shown here.

Contributed by the Lubrication Division of THE AMERICAN SOCIETY OF MECHANICAL ENGINEERS and presented at the ASME ASLE Joint Lubrication Conference, Washington, D. C., October 5-7, 1982. Manuscript received by the Lubrication Division, April 1, 1982. Paper No. 82-Lub-23.



Fig. 2 Schematic diagram of research-type ion implantation system

### The Implantation Process

Ion implantation is not a coating technique. Implantation consists of forcibly injecting selected elemental ion species beneath the surface of materials by means of high-energy ion beam from an accelerator (usually at tens to hundreds of kilovolts). This injection process produces an intimate alloy of the implanted and host elements without producing a sharp interface characteristic of most coatings and hence avoids the related adhesion problems. The resultant depth distribution and alloy composition depend on the energy and atomic number of the projectile as well as on the atomic number of the host. Typically, depths of 0.01 to 1.0 micrometers are achievable with concentrations of up to 50 atomic percent. It should be stressed that ion implantation is not a thermodynamical equilibrium process and that metastable alloys can be formed without regard for the conventional considerations of solid solubility and diffusivity; since any elemental species can be implanted into any other material. Heating of the implanted alloy to sufficiently high temperatures will, of course, ensure equilibrium conditions, but several durable metastable (or amorphous) phases with potentially interesting physical properties have been formed by implantation. Figure 1 summarizes many of these factors pertaining to ion implantation for materials modification. The ability to control and reproduce the ion beam parameters listed in Fig. 1 is especially important to its large scale commercial usage for implanting (doping) semiconductor wafers with high reproducibility (typically less than 3 percent dose difference on different wafers or between different points on a single wafer).

Figure 2 shows a schematic diagram of a typical research-type ion implantation system. As depicted, atoms are ionized in an ion source, accelerated to the desired energy, analyzed according to mass by a magnet to select the desired species, and then electrostatically raster scanned over the target to ensure dose uniformity of the implantation. The implanted dose (in terms of impurity atoms per unit volume) is obtained from the ion beam charge, the implanted target area, and the implanted species depth distribution.

### Ion Species Selected for Evaluation

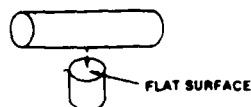
M50 (AMS 6491) is an alloy tool steel used extensively in mainshaft aircraft engines because of its excellent hot hardness characteristics, wear resistance and good contact fatigue life. However, its corrosion resistance is poor. Its elemental composition is shown in Table 1. Ion species and combinations of species which were considered as good candidates for imparting corrosion resistance to M50 steel include Cr, Cr + Mo, Cr + Mo + N, Cr + P, Cr + B, Al, Ti, and Mo. The ion energies used ranged between 12.5 and 150 KeV with fluences between  $1.0 \times 10^{16}/\text{cm}^2$  and  $4 \times 10^{17}/\text{cm}^2$ . The fluences used for Cr, Ti, and Al were sufficient to produce a 15 to 30 atomic percent concentration of the implanted elements in a region from the surface to a depth of about 80 nm. The choice of ions was determined by the well known corrosion behavior of the ions in bulk materials, i.e., chromium produces stainless steel when added to iron based alloys in concentrations greater than 12 percent [2], Mo is known to improve pitting resistance in steels [3], Ti and Al

Table 1

### Elemental composition of M50 tool steel (% by Wt.)

Carbon	0.85
Manganese	0.25
Silicon	0.20
Phosphorous	0.015 (max. allowable)
Sulfur	0.010 (max. allowable)
Chromium	4.00
Vanadium	1.20
Iron	Remainder
Molybdenum	4.30

1. Test pieces (both M50 alloy steel) were placed in contact as indicated by the dotted line.



2. Both pieces in place were immersed in chloride-contaminated oil for 2 hrs., removed, and allowed to dry.

3. A meniscus of contaminated oil was retained between the two parts:

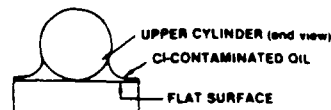


Fig. 3 Laboratory-simulated field service test of corrosion of bearings

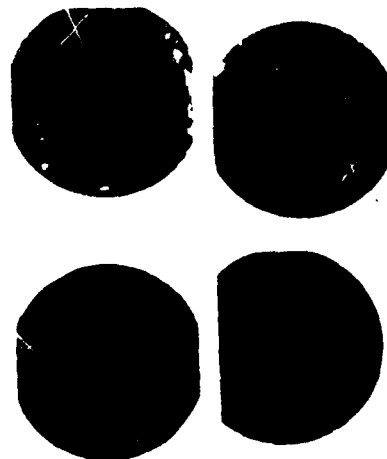


Fig. 4 Optical photographs of the flat surfaces of M50 test samples after a simulated field service test. The two unimplanted samples at the top show pitting under the line of contact. The two CR + Mo + N implanted samples at the bottom show complete immunity. (Magnification 10x).

form stable corrosion resistant oxides [2], P and B stabilize an amorphous phase when alloys with ion [4], and N has been shown to improve pitting resistance of steel [5].

### Corrosion Experiments

Several types of corrosion tests were used to ascertain the degree of improvement in corrosion resistance occurring as a result of ion implantation. To conduct these corrosion tests in actual bearings would have been expensive and time consuming. Therefore, tests are conducted on small M50 hardened specimens on an area of about  $1 \text{ cm}^2$ .

Two types of tests were performed. The first were qualitative field service simulation tests. Those ions which looked promising in simulation tests were further studied by electrochemical polarization and pitting tests. These are described below.

**Simulation Tests.** The tests used herein for simulating the corrosion mechanism which occurs in gas turbine engines was based in the findings of the test method developed by Brown and Feinberg [6]. They found that in a gas turbine engine bearing compartment; (a) corrosion usually occurred statically (i.e., bearing not running) at the conjunction of the bearing rolling element and the race, (b) the lubricant in the form of a miniscus was present at the corrosion site and (c) the lubricant showed typical contamination levels of 3 ppm (wt) of chloride and 600 ppm of water.

Figure 3 shows the arrangement of the simulated geometry corrosion test. The cylindrical surface resting on the flat side of the upright cylinder is intended to simulate the roller on

race contact geometry of an actual bearing. The cylinders are 0.0095M (3/8 in.) diameter M50 rods. The flats (about 0.006M tall) are cut from the rod and consecutively polished down to a mirror finish with a final (3  $\mu$ m) diamond paste. The cylinders were positioned in place and totally immersed for 2 hours in a contaminated neopentyl polyolester gas turbine engine lubricant conforming to specification MIL-L-23699. The oil was contaminated by adding three ppm (wt) of chlorides as ASTM DD665 synthetic seawater to oil and then adjusting the water content to a level of 600 ppm (wt) by the addition of distilled water. The two parts were then removed from the oil and allowed to drip dry. A miniscus of contaminated oil was retained between the two parts as shown in Fig. 3. This system was then exposed to alternate cycles of moist air at 60°C (8 hours) and 4°C (16 hours) for a period of several weeks.

The test shown in Fig. 3 was done for several implanted

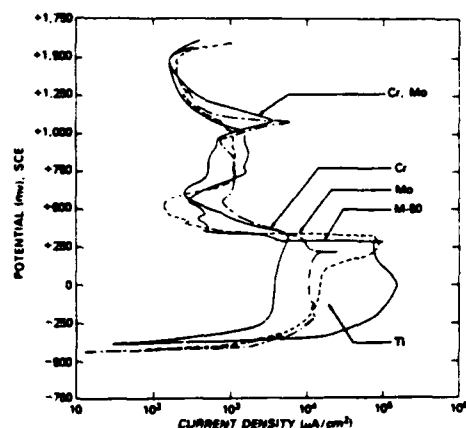


Fig. 5 Potentiokinetic anodic polarization data produced in hydrogen-saturated 1N  $H_2SO_4$  for M50 steel, and for M50 steel implanted with titanium chromium, molybdenum and chromium + molybdenum

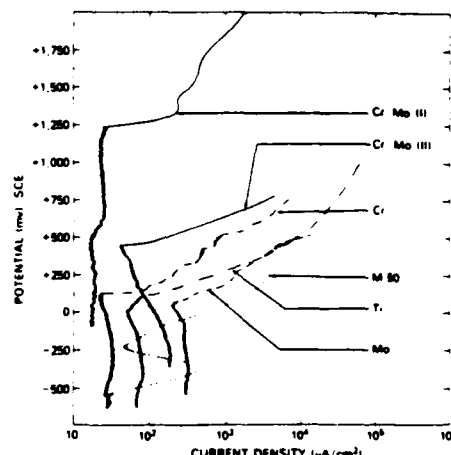


Fig. 6 Potentiokinetic anodic polarization data produced in buffer solution of pH6 containing 0.1 M NaCl for M50 steel, and for M50 steel implanted with titanium, chromium molybdenum and chromium + molybdenum

Table 2 M50 corrosion test results (qualitative ranking)

Sim.	1N $H_2SO_4$	0.1M NaCl (cath.)	0.01M NaCl (no cath.)	0.01M NaCl (cath.)
Cr + P	Cr + Mo	Cr + Mo	Cr + P	Cr
Cr	Cr	Cr	Cr	Cr + P
Cr + Mo + N	Mo	Mo	Cr + Mo	M50
Ti	Ti	Ti	M50	Cr + Mo + N
Cr + Mo	M50	M50	Cr + Mo + N	Cr + Mo
M50				

#### Implantation Parameters

Ion(s)	Fluence ( $\times 10^{17}/cm^2$ )	Energy (keV)
Cr + P	1.5-2.0 0.5-1.0	150 40
Cr	1.5-2.0	150
Cr + Mo + N	1.5-2.0 0.35-0.5 0.1	150 100 12.5
Ti	2.0	55-150
Al	0.6 1.0	50 100

ions and several time periods. Figure 4 shows optical photographs (10 $\times$  magnification) of the corrosion inhibiting effectiveness of an implantation of Cr+Mo+N after a 7 week test (two samples at bottom) as compared to an unimplanted control specimens (two samples at top). The control specimens show severe corrosion. The attack generally occurs in two areas; e.g., a line of pits beneath the line of contact between the cylindrical and flat surfaces, and general corrosion in the thin layer of oil outside this region. A qualitative ordering of the improvement in corrosion resistance found in this simulated field test produced by implanting ions or combinations of ions from best to worst is: Cr+P, Cr+Mo+N, Cr, Ti, Cr+Mo, Al, M50.

**Electrochemical Tests.** Two independent electrochemical characterizations were done to study two types of corrosion behavior. Passivity tests in strong acids provide insight into general corrosion (rusting) behavior and pitting tests in chloride ion solutions give a measure of the resistance to localized corrosion (pitting).

The acid tests were done in 1 Normal H<sub>2</sub>SO<sub>4</sub> at room temperature. Figure 5 shows potentiodynamic polarization scans (1 mV/S) for unimplanted M50 and for Cr, Mo, Ti, and Cr+Mo implants [7]. Notice that all implant samples show a reduction in the maximum current density when compared to the base line M50 curve. Lowering of the maximum current density indicates that the surface is more easily passivated and that improved corrosion resistance may be expected. These tests establish a qualitative ordering of the improvements to be expected in general corrosion behavior which is, from best to worst, Cr+Mo, Cr, Mo, Ti, unimplanted M50.

The chloride ion tests were in a pH6, 0.01, or 0.1 Molar NaCl, buffered solution. The buffer ensured that the pH was constant throughout the measurements. Figure 6 presents potentiodynamic polarization scans (1 mV/S) for the 0.1M NaCl solution for several implants. The salient characteristic of each curve is the breakdown potential, E<sub>b</sub>, which characterizes the metals ability to withstand pitting attack (i.e., higher E<sub>b</sub> indicates better protection). The breakdown potential is that voltage on the curve where there is a sudden increase in current density. The qualitative order of effectiveness is from best to worst, Cr+Mo, Cr+P, Cr, Mo, Ti. The pitting data in a 0.01M NaCl solution for several implant species was performed with two different pretreatments. In one case, the sample was polarized positively im-

mediately upon immersion into the solution so that the air formed film was being tested for pitting. In the other case, the air formed film was removed by polarizing in the negative direction (H<sub>2</sub> charging) for 15 min, then scanned positively allowing a new passive film to form. The latter was the pretreatment for the 0.1M data as well. The former is more realistic since an air formed film would be expected to exist on actual bearings. These test results, for a number of tests similar to those shown in Fig. 6, are summarized in columns 4 and 5 in Table 2 and are discussed below.

Qualitative rankings for the data from the five different tests, (1) simulation tests, (2) 1-normal H<sub>2</sub>SO<sub>4</sub> test (3, 4) the 0.1M and 0.01M NaCl pitting test with cathodic charging, and (5) the 0.01M pitting test on air formed films, are compared in Table 2. Cr and Cr+Mo are found effective in all tests. Chromium implants show good performance in all tests while Cr+Mo perform best in two tests. Cr+P performed best in the simulation tests and the 0.01 NaCl test. Therefore, Cr, Cr+Mo and Cr+P were selected for further examination in full scale rolling element bearings.

### Implantation of Bearings

Bearings selected for implantation are listed in Table 3 along with pertinent information on bearing size where applicable, and function in the overall program. Table 3 also identifies the bearings that have been implanted to date.

There are a number of practical problems to be considered for the successful implantation of the bearings. Obviously, all contacting surfaces must be implanted to protect against the formation of corrosion pits which can act as initiation sites for fatigue spalling. This entails implanting the active surfaces of the bearings (i.e., the inner race outer race and the total area of the rollers and the balls). In order to implant the bearings in a reasonable period of time, very high ion beam currents were developed and used. For Cr a typical beam current is 500  $\mu$ A at 150 keV. This represents 75 watts of incident power which must be dissipated or the bearing will overheat, causing loss of hardness. Fortunately, M50 holds its hardness well in that it has been established that no loss of hardness occurs at temperatures of 800°F for 1000 hours [8]. This enables the heat dissipation to be handled in some cases by radiation losses alone.

During implantation, all the races were clamped tightly to a solid aluminum or brass plate and rotated at 1.5 rpm.

Table 3 Bearings selected for implantation

Application	Type*	Bearing Size - mm			No. Brgs. Implanted	Ions	Function in Program
		O.D.	Bore	Rolling Element Size			
J79 Gas Turbine Engine Thrust Bearing	B	225	150	22.22 (Ball)	1	Cr + Mo	Performance and Field Evaluation
T58 Turboshift Engine - No. 4 Bearing	R	68	40	7 long $\times$ 7 dia	2	Cr + Mo	Performance and Field Evaluation
Modified T58 Bearing	R	68	40	7 long $\times$ 7 dia	10 11	Cr + P Cr	Fatigue Endurance Testing
T63 Gas Turbine Engine Bearing No. 3	B	55	30	16 (Ball)	2	Cr + P	T63 Engine Evaluation in a Test Cell with Contaminated Oil
No. 6	R	42	25	5 long $\times$ 6 dia	2		
Various Engine Gearbox Bearing	B&R	Various Sizes			0		Long Term Storage Tests

\*B = Roller Bearing  
R = Roller

**Table 4 Normal and maximum temperatures reached by bearing components during implantation**

Component	Temperature (°F)	
	T <sub>Normal</sub>	T <sub>Max</sub>
J79 Inner race	400	500
J79 Outer race	400	500
J79 Ball	450	500
T58 Inner race	400	550
T58 Outer race	500	640
T58 Roller	390	650

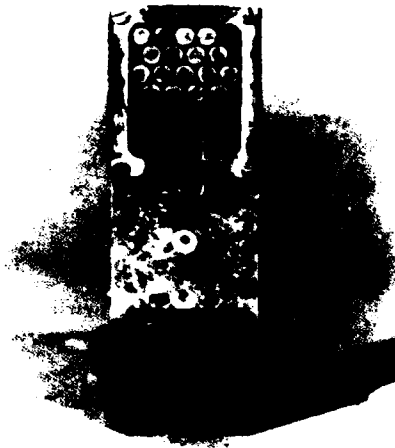


**Fig. 7 Photographs of implantation jig used to implant 18 T-58 bearing roller ends. Stainless steel frame is turned over to implant opposite ends of rollers. The aluminum base is water cooled.**

Typically 60 revolutions are required to finish one race. In this manner, heat was transferred to the plate and both the plate and race then radiated the heat away.

For the races the beam was scanned vertically but not horizontally so that the beam irradiated the bearing races over the vertical extent of the race (1.5 cm for T58; 3 cm for J79) with a width of about 1 cm. Table 4 shows the maximum temperature of each bearing component during implantation. The target chamber vacuum was typically less than  $3 \times 10^{-6}$  Torr during implantation and the target chamber was always vented to atmospheric pressure with dry nitrogen gas after the bearing components had cooled to at least below 550°F.

The T58 rollers were implanted on the ends with the jig shown in Fig. 7. A stainless steel frame held down to an aluminum block contains the rollers which are held tightly in place by a stainless bar pressed against the roller array by two screws. Beneath the rollers is a thin sheet of Mo. Cooling is accomplished by fastening the holder with three screws to a water cooled shaft. Indium foil pressed between the aluminum block and cooled shaft promotes heat conduction from the block. The materials of stainless steel and Mo were chosen to minimize any possible deleterious effects of sputtering of the holder material onto the bearings. Brass and aluminum, which conduct heat much better than stainless, unfortunately sputter very efficiently and would therefore non-uniformly coat the rollers with Cu, Zn, and Al. Mo has a low sputtering coefficient and is innocuous in that the small amount of sputtered Mo contamination on the bearings would

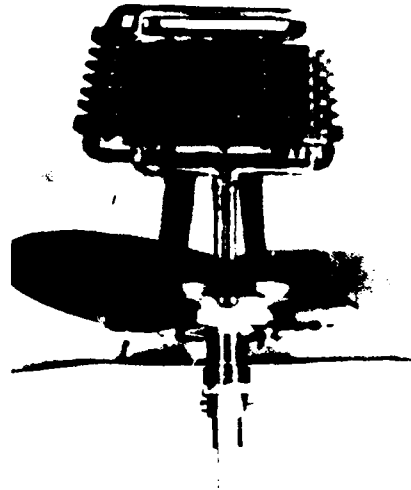


**Fig. 8 Photograph of implantation jig used to implanted up to 48 T-58 rollers at one time. Quarter inch copper tubing provides water cooling and support for stainless steel bars that retain the rollers. Rollers are implanted in four rotations, 90° apart, for complete coverage of the circumference.**



**Fig. 9 Photograph of planetary gear fixture used to implant 24 J-79 balls at one time (expandable to 48 balls). Stainless steel "golf tees" retain the balls and each ball rotates through the beam spot which remains fixed at the dimensions 7/8 in. tall by 2 in. wide. A ball rotates 18.5 times for each rotation of the platform.**

be expected to have a beneficial effect on corrosion resistance. Impurities sputtered onto the bearings from stainless steel are chiefly iron, chromium and nickel which are also compatible with the corrosion prevention purpose of the implanted layer. The sputtering coefficient for P on these materials is much smaller than for Cr and thus was not deemed a problem.

Roller circumferences were implanted in four steps with the jig shown in Fig. 8. Stainless steel tubing supports stainless horizontal struts each of which hold 8 rollers. Water flowing

**Table 5 Test conditions for performance and fatigue endurance testing of implanted bearings**

	Performance Tests		Fatigue Endurance Tests		
	J79 Brg.	T58 Brg.	T58 Modified		
			Group 1	Group 2	Group 3
Implant	Cr + Mo	Cr + Mo	Cr + P	Cr	Untreated
Load					
Radial	900 lbs.	150 lbs.	—	2800 lbs.	—
Thrust	6922 lbs.	0	—		
Speed	7460 rpm	19,500 rpm.	—	7000 rpm	—
Oil in Temp.	300°F	250°F	—	210°F	—
Oil Flow	1.45 gals/mim	0.35 gals/min	—	0.25 gals/min	—
Length of Test	400 hours	400 hours	—	Until Failure	—
No. of Bearings Tested	1	1	10	10	10

Note: Lubrication - MIL-L-23699

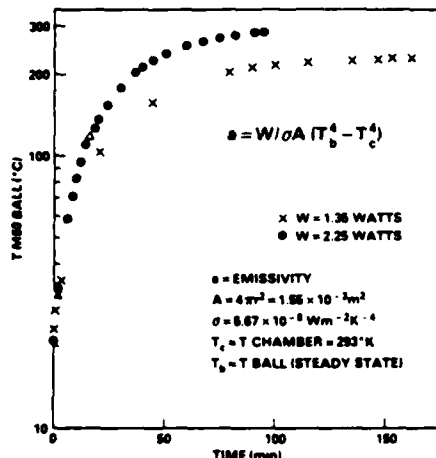


**Fig. 10 The increase in temperature as a function of time of an M50 steel ball from a J-79 main shaft bearing for two different values of the ion beam input power. From this data the emissivity of the M50 ball is determined to be 0.25.**

through the tubing cools the struts which in turn hold and cool the rollers. The roller circumferences are implanted in a cubic geometry such that each of four "sides" receives the same fluence of particles. This results in a  $\pm 15$  percent variation in fluence around the circumference of the roller. For Cr implants, the fluence varies between  $1.5 \times 10^{17}$  and  $2.1 \times 10^{17}/\text{cm}^2$ . We have observed that the corrosion inhibition effects of Cr implants between  $1 \times 10^{17}$  and  $2 \times 10^{17}/\text{cm}^2$  fluences are equal by means of the simulation test mentioned previously. Therefore, the  $\pm 15$  percent variation in fluence is not expected to be a problem. This observation is also consistent with the well known observation that an abrupt improvement in the corrosion resistance of steels occurs at a Cr concentration of 12 percent, so that if this criteria is met by the lowest fluence implant, additional Cr will not substantially further improve the corrosion resistance [2].

Figure 9 shows a planetary gear jig designed to implant up to 48 J79 balls in one operation. It is set up for 24 balls on a

0.19M diameter as shown in Fig. 9. The balls are held in place by gravity in a stainless steel "golf tee" and each ball rotates 18 times for each rotation of the whole assembly. The beam is scanned horizontally and vertically over an area 22 mm high by 51 mm so that at any one time slightly more than 2 balls are being irradiated. The problem of temperature rise is solved by a 12 to 1 duty cycle wherein each ball is irradiated for about 3 seconds and allowed to cool (chiefly by radiation) for about 37 seconds.

The emissivity of the balls was determined by measuring the heating curve of a ball with a thermocouple attached to it in vacuum. Figure 10 presents the data for two different input powers of an Ar ion beam. From the equation in Fig. 10 and knowing the input power and surface area of the ball, an emissivity of 0.25 is computed. From this information an equilibrium temperature of 390°F for a 200  $\mu\text{A}$ , 150 keV, beam was computed. The measured value under the stated implantation conditions of 425°F is in satisfactory agreement with the calculated value. During implantation the temperature of the bearings was measured and continuously monitored by means of an infrared pyrometer sighted on the bearing through a quartz window in the implantation vacuum chamber.

The procedure for implanting the balls with Cr was to (i) implant in a rotating cylindrical geometry to a fluence of  $1 \times 10^{17}/\text{cm}^2$ , (ii) rotate the balls 90 deg with respect to the vertical direction and implant again to an additional fluence of  $1 \times 10^{17}/\text{cm}^2$ . This leaves the ball surface with two poles containing  $2 \times 10^{17}$  ions/ $\text{cm}^2$ , two poles containing  $1 \times 10^{17}$  ions/ $\text{cm}^2$ , and the remainder of the surface with fluences between these two values. This factor of the two nonuniformity in fluence will not be deleterious for the same reasons as discussed for roller bearings. It is envisaged that under production conditions T58 bearings could be implanted at the rate of 4 per hour.

#### Performance and Endurance Testing of Full Scale Bearings

One each of the J79 and T58 engine bearings (first two bearings listed in Table 3), were performance tested for 400 hours at conditions simulating speed, load, and temperatures of actual operating engines.

In addition, 10 each of the modified T58 bearings (Table 3) implanted with either Cr + P or Cr were fatigue endurance

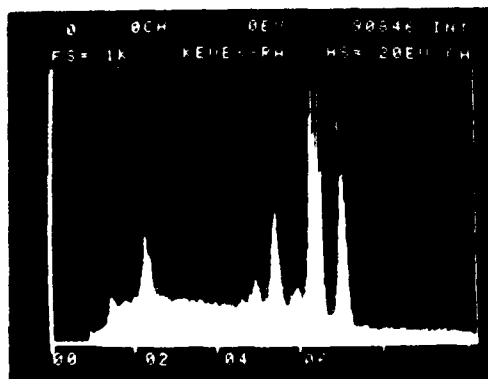
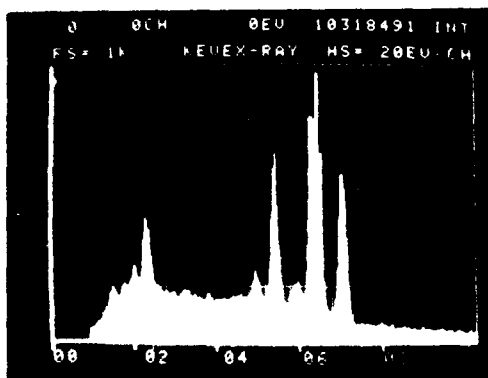
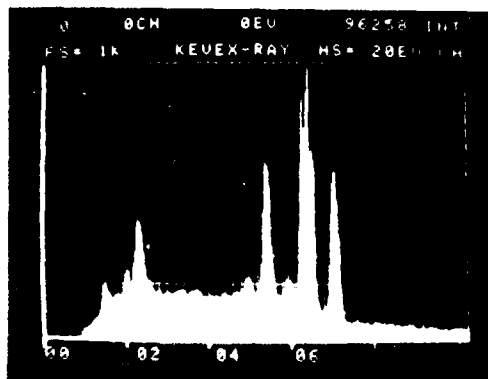


Fig. 11 Energy dispersive X-ray spectra of M50 steel rollers from a T-58 main shaft bearing. Top: Cr+P implanted but not endurance tested. Middle: Cr+P implanted and after 420 hours of endurance testing. Bottom: Not implanted and not endurance tested. The 3 spectra are normalized to the Fe K<sub>α</sub> line for easy comparison. The Cr K<sub>α</sub> line is considerably larger in the top and middle spectra than in the bottom spectrum.

tested. Another group of 10 untreated bearings, also fatigue endurance tested, provided a baseline for comparison. All thirty bearings were made from a single lot of M50 steel and were manufactured at the same time. Differences in en-

Table 6 Results of fatigue endurance tests (hours to failure)

	Cr+P	Cr	Untreated
	81.7	36.2	76.2
	92.6	94.4	86.9
	93.0	127.4	113.2
	100.1	132.8	177.6
	191.4	135.1	177.9
	191.7	150.9	221.9
	278.4	193.4	296.8
	351.8*	252.2	362.4*
	361.2	306.9*	383.8
	420.4*	399.3	394.3*
L <sub>10</sub> Life	67.21	51.27	73.21
90% LCI	22.73	18.84	29.63
90% LCI	256.92	218.46	267.27
L <sub>50</sub> Life	203.39	172.83	216.44
90% LCI	129.60	109.41	144.09
90% LCI	319.38	272.19	323.26
β	1.56	1.44	1.3

\* Bearing test suspended prior to failure.

LCI - Lower Confidence Limit.

LCI - Upper Confidence Limit.

durance life could therefore be attributed only to the implantation process since the material and manufacturing processes were statistically similar among the three groups.

The conditions for the performance and the endurance testing are given in Table 5. Note that in the fatigue endurance testing the loads are much higher than would be expected in actual operation. This is done to accelerate fatigue spalling so that failures will be obtained in a reasonable period of time on a large number of bearings. For simplicity and reliability the machine rotating speed is usually kept low. Bearings in both performance tests successfully completed the schedule 400 hour test without failure and were capable of continued operation. Fatigue test results for the fatigue endurance bearings are shown in Table 6. All bearings experienced a fatigue spall at the endurance life indicated (in hours) except where noted. The data from each group were assumed to be distributed as a Weibull function, which is a population distribution normally used to fit contact fatigue data [9]. For each group of data, Weibull distribution parameters, which are used for comparison between groups, were calculated using a least squares regression analysis. They are the L<sub>10</sub> life, L<sub>50</sub> life, and the Weibull slope (β) and listed in Table 6. These are defined as follows:

- L<sub>10</sub> life - The number of hours exceeded by 90 percent of the population.
- L<sub>50</sub> life - The number of hours exceeded by 50 percent of the population.
- Weibull slope (β) - The slope of the computed Weibull line. This parameter indicates the amount of scatter in the data.

Using the method described in reference [9], a statistical comparison was made of the L<sub>10</sub> and L<sub>50</sub> lives of each implanted group against the baseline unimplanted group. The results show no significant difference in fatigue lives among any of the three groups. This is evident by the large amount of overlap in the 90 percent confidence intervals around the L<sub>10</sub> and L<sub>50</sub> Weibull parameters as shown in Table 6.

Energy dispersive X-ray analysis was conducted to ascertain the Cr content in the surface of one roller before and after endurance testing. The results are shown in the X-ray spectra of Fig. 11 which includes an unimplanted roller for baseline comparison at the bottom, implanted and fatigue tested in the middle, and as implanted at the top. It can be seen that after running for 420 hours, there is very little depletion of Cr in the roller surface.

Evaluation of ion implanted M50 bearings for corrosion protection shows considerable potential and should continue with:

- (a) In-service evaluation of the applications listed in Table 3.
- (b) Testing of a T63 engine in a test cell with chloride and water contaminated oil with two of the seven mainshaft engine bearings implanted with the Cr + P.
- (c) Storage testing of implanted bearings.
- (d) Full scale bearing corrosion tests as described in reference 6. Ion implantation, should be considered for (1) improvement in scuffing resistance of spur gears and (2) corrosion resistances of advanced bearing and gear steels such as CBS600 and CBS1000M.

### Conclusions

Implantation of a single element (chromium) or dual elements (Chromium plus Phosphorous or Molybdenum) substantially improves resistance to both general and pitting corrosion in M50 steel. The improvements are strongly evident in three independent methods, i.e., (1) cylinder-on flat simulation (2) polarization in 1N-H<sub>2</sub>SO<sub>4</sub> and polarization in 0.1M or 0.01M NaCl solution.

Implantation jigs have been designed and built which enable the inner and outer bearing race surfaces, rollers and balls to be implanted to adequate fluences for corrosion protection. The temperature of the bearing components may be adequately controlled during implantation so that there is no loss of hardness.

Twenty-three T58 bearings and one J79 bearing have been successfully implanted. The average time to implant one complete T58 bearing with Cr was about 3 hours beam time. This was under less than optimum production line conditions.

It is estimated that this figure could be improved by a factor of about ten in a production line situation.

The data presented indicate the implantation of the ion species evaluated does not adversely affect either bearing performance or fatigue endurance life under the conditions tested.

### Acknowledgments

The authors gratefully acknowledge the major contributions to this work by Y. F. Wang and C. R. Clayton (electrochemical measurements, S.U.N.Y. - Stony Brook), H. Munson (fatigue and endurance tests, TRW Bearings Div., Jamestown, NY), and the direction and support of J. K. Hirvonen (NRL).

### References

- 1 Cunningham, J. S., and Morgan, M. A., "Review of Aircraft Bearing Rejection Criteria and Causes," *Journal of the American Society of Lubrication Engineers*, Vol. 35, No. 8, Aug. 1979, pp. 435-441.
- 2 Tomashov, N. D., *Theory of Corrosion and Protection of Metals*, Macmillan, New York, 1966.
- 3 Ambrose, J. R., *Corrosion*, NACE, 34, 27, 1978.
- 4 Whitton, J. L., Grant, W. A., and Williams, J. S., *Proc. Int. Conf. on Ion Beam Modification of Materials*, Budapest, Hungary, 1978.
- 5 Truman, J. E., Coleman, M. J., and Pirt, K. R., *Br. Corros. J.*, Vol. 12, 1977, p. 236.
- 6 Brown, C., and Feinberg, F., "Development of Corrosion Inhibited Lubricants for Gas Turbine Engines and Helicopter Transmissions, ASLE Preprint No. 80-AM-6C-3 presented at the 35th Annual Meeting, May 5-8, 1980.
- 7 Wang, Y. E., Clayton, C. R., Hubler, G. K., Lucke, W. H., and Hirvonen, J. K., *Thin Solid Films*, Vol. 63, No. 11, 1979.
- 8 Anderson, N. E., "Long-Term Hot-Hardness Characteristics of Five Through-Hardened Bearing Steels," NASA Tech. Paper 1397, AVRADCOM Tech. Rept. 78-16, Oct., 1978.
- 9 Johnson, L. G., *The Statistical Treatment of Fatigue Experiments*, Elsevier Publishing Co., Amsterdam, London, N.Y., 1961.

Section III.E

HIGH TEMPERATURE OXIDATION OF ION IMPLANTED TANTALUM

E. N Kaufmann, R. G. Musket and J. J. Truhan<sup>1</sup>  
K. G. Grabowski and C. R. Gossett<sup>2</sup>  
I. L. Singer<sup>3</sup>

<sup>1</sup>Lawrence Livermore National Laboratory  
University of California  
Livermore, CA 94550

<sup>2</sup>Materials Modification & Analysis Branch  
Condensed Matter & Radiation Sciences Division  
Naval Research Laboratory

<sup>3</sup>Surface Chemistry Branch  
Chemistry Division  
Naval Research Laboratory

The portion of this work performed at Naval Research Laboratory was supported by the Office of Naval Research and the portion performed at Lawrence Livermore National Laboratory was supported by the Department of Energy.

## HIGH-TEMPERATURE OXIDATION OF ION IMPLANTED TANTALUM

E.N. KAUFMANN, R.G. MUSKET and J.J. TRUHAN

*Lawrence Livermore National Laboratory\*, University of California, Livermore, CA 94550, USA*

K.S. GRABOWSKI, C.R. GOSSETT and I.L. SINGER

*Naval Research Laboratory, Washington, DC 20375, USA*

The oxidation of ion implanted Ta in two different high temperature regimes has been studied. Oxidations were carried out at 500°C in Ar/O<sub>2</sub> mixtures, where oxide growth is known to follow a parabolic rate law in initial stages, and at 1000°C in pure O<sub>2</sub>, where a linear-rate behavior is obtained. Implanted species include Al, Ce, Cr, Li, Si and Zr at fluences of the order of 10<sup>17</sup>/cm<sup>2</sup>. Oxidized samples were studied using Rutherford backscattering, nuclear reaction analysis, Auger spectroscopy, secondary-ion mass spectroscopy, X-ray diffraction and optical microscopy. Significant differences among the specimens were noted after the milder 500°C treatment, specifically, in the amount of oxide formed, the degree of oxygen dissolution in the metal beneath the oxide, and in the redistribution behavior of the implanted solutes. Under the severe 1000°C treatment, indications of different solute distributions and of different optical features were found, whereas the overall oxidation rate appeared to be unaffected by the presence of the solute.

### 1. Introduction

The oxidation of Ta and its alloys had been studied for many years. Reviews covering much of the accumulated data can be found in refs. 1 and 2. Several single and multi-component alloys were developed which display significantly ( $\times 2$  to  $\times 10$ ) enhanced oxidation resistance. Total alloy additions often exceed 50 at.% and thus drastically affect bulk properties. Extremely resistant ( $\times 100$  or better) alloys were also found which, however, did not provide mechanical properties amenable to fabrication of useful parts. In those instances where the ultimate application of the material restricts the bulk properties or where alloy additives add excessive cost, it is reasonable to attempt a surface treatment method on as-fabricated parts. Protective coatings, however, often suffer from adherence difficulties, particularly under high-temperature or temperature-cycling conditions. The use of ion-implanted layers, which are an integral part of the metal surface, may therefore represent a viable alternative.

Tantalum oxidation is a complex process which is not yet wholly understood [1,2]. Complicating factors include a high solubility of oxygen in the metal, the existence of several sub-oxides which are precursors to the normal oxide Ta<sub>2</sub>O<sub>5</sub>, the incursion of oxide platelets into the bulk in advance of the oxide-metal interface, and the transport of oxygen through the oxide by means other than bulk diffusion which leads to a breakdown of parabolic-rate behavior. Resulting oxide scales tend to be non-protective because of mechanical failure at a microscopic level in thin layers, and eventually, in thick layers, the scale will spall.

Little guidance is available for the choice of elements for implantation aside from the behavior of existing alloys. Three qualitative mechanisms can be envisioned for the inhibition of oxidation by an implanted layer in analogy to alloy results. (i) The formation of a continuous alloy layer, of composition corresponding to the most resistant alloys. (ii) The incorporation of the solute in the oxide which will then improve the oxide mechanical properties or slow oxygen transport. (iii) The creation of a high-oxygen-affinity layer which impedes the dissolution of oxygen into the metal. A fourth mechanism which is operative in other systems, that is the preferential formation of the solute-oxide on the surface, was not expected to

\* Work performed under the auspices of the U.S. Department of Energy by the Lawrence Livermore Laboratory under contract number W-7405-ENG-48.

be viable here since  $Ta_2O_5$  is of comparable thermodynamic stability to the oxides of Si, Al and the rare-earths.

The implanted elements Al, Ce, Cr, Li, Si and Zr, have been studied so far. Al, Cr, Si and Zr, as major components of Ta binary and higher-order alloys have imparted oxidation resistance. These also form relatively stable oxides on their own. In addition, Zr (as well as Hf) causes a marked decrease in oxygen dissolution in the alloys. The possibility of formation of stable mixed oxides, such as  $LiTaO_3$ ,  $TaAlO_4$  and  $CeTaO_4$ , which may seal an oxide surface was also considered. The last point as well as more general considerations has been discussed for implanted systems by Dearnaley [3].

## 2. Experimental procedure

A rod of 99.99% pure Ta was obtained from the Materials Research Corporation and machined to a 1 cm diameter. The heat-treatment and extrusion process in the manufacture of the rod resulted in a preferred crystallographic orientation discussed in the following section. Circular specimens of 1 mm thickness were spark-cut from the rod and subsequently lapped and polished to a final 10  $\mu$ m alumina grit finish. A small hole was drilled through some samples near the edge to allow suspension for weight gain measurements. The sharp transition from the face to edge of each disc was blunted to a  $\sim 250$   $\mu$ m radius to reduce the known [2] high-rate oxidation at sharp corners. Most samples thus prepared were mounted in the NRL ion-implantation accelerator and implanted on both faces with the elements listed in table 1, where energies, fluences, and calculated projected ranges are also given. The Si-implanted samples were implanted on one side only by IICO, Inc., Santa Clara, CA. The temperature rise of the samples during implantation is estimated not to be greater than  $\sim 150^\circ\text{C}$ . In most cases (aside from Li) the selected fluence is close to that where saturation due to sputtering occurs. The edges of the specimen remained unimplanted. In some instances half of one sample face was masked to facilitate comparison of implanted with unimplanted regions.

One of each set of samples (except TaSi) was heated to  $500^\circ\text{C}$  for 1 h in a 4:1 mixture of

Table 1

Fluence, energy, and calculated projected range ( $R_p$ ) for implanted species, and measured weight-gain rate at  $1000^\circ\text{C}$  in  $O_2$ .

Element	Energy (keV)	Fluence ( $10^{17}/\text{cm}^2$ )	$R_p$ (nm)	Linear weight-gain rate ( $\text{mg}/\text{cm}^2 \text{ h}$ )
Al	150	2.0	64	210
Ce	150	0.4	19	146
Cr	150	1.5	48	173
Li	60	2.0	112	<sup>b</sup>
Si	184	1.0	73	179 <sup>a</sup>
Sr	150	0.6	25	192
Pure Ta				164

<sup>a</sup> Corrected for only one implanted face, using data for pure Ta.

<sup>b</sup> Reaction was catastrophic.

argon/oxygen gas. In general the oxidized sample was one which had half of one face masked during implantation. These samples and their unoxidized counterparts were analyzed with (i) Rutherford backscattering using  $135^\circ$  scattering of 2.0 MeV He ions and a glancing-exit angle of  $20^\circ$ , (ii) Auger electron spectroscopy for Ta, O, C, and the implanted element using 2 keV Ar-ion sputtering and a 5 kV bias for the electron gun, and (iii) secondary ion mass spectroscopy of the positive ions produced by a primary beam of 5.5 keV Ar ions. In addition, the Al depth distribution was determined using the  $^{27}\text{Al}(p, \gamma)$  nuclear reaction by monitoring the gamma-ray yield as the incident proton energy was varied about the narrow cross section resonance (100 eV) at 992 keV, and the Li distribution was determined using the  $^7\text{Li}(p, \alpha)$  nuclear reaction by energy analyzing the particles produced by a 1.75 MeV proton beam.

Another of each set of samples (with holes near the periphery) was suspended from the balance of a thermogravimetric (TGA) apparatus within a quartz-tube through which pure  $O_2$  flowed. These were heated to  $1000^\circ\text{C}$  in a rapid, reproducible fashion by a quartz-lamp radiant heater and held for five minutes before the heater was switched off. A thermocouple near the sample verified the temperature time sequence in which full temperature was present for  $4\frac{1}{2}$  min. As a result of the exothermic nature of Ta oxidation, a more rapid temperature rise could not be used because of

sample ignition with catastrophic oxidation. Weight-gain data as accumulated represented the combined effects of oxidation on faces and edge. Whereas the appearance of the oxidized faces was a matte grey, the edge showed a relatively voluminous white scale which was easily chipped from the sample and collected. The edge scale was weighed separately and, assuming stoichiometric  $Ta_2O_5$ , the weight of oxygen in the edge scale was obtained.

These samples were characterized using (i) X-ray diffraction with  $CuK\alpha$  radiation (ii) optical microscopy with polarized light, (iii) Auger electron spectroscopy for Ta, O, C and the implanted solute, and (iv) nuclear-reaction analysis for Al using the narrow resonance in the cross section of the  $Al(p, \gamma)Si$  reaction as described above. Use of the strongest gamma-lines in this case suffers from interference with oxygen-reaction gammas, thus lines near 10 MeV were used.

### 3. Results

#### 3.1. Severe case (1000°C, 5 min in $O_2$ )

##### 3.1.1. Thermogravimetric analysis

Fig. 1 shows raw TGA data typical of all samples studied so far. Aside from the initial heating period of  $\sim 40$  s and a slight non-linearity around  $\sim 260$  s, the major portion of the curve is linear. The nonlinearity near the end of the 5 min period was also observed in longer test runs where it was seen to last for  $\sim 1$  min followed by a return to linear behavior with the same slope. Using the weight gain attributable to the edge, the areas of faces and edge, and neglecting the nonlinear por-

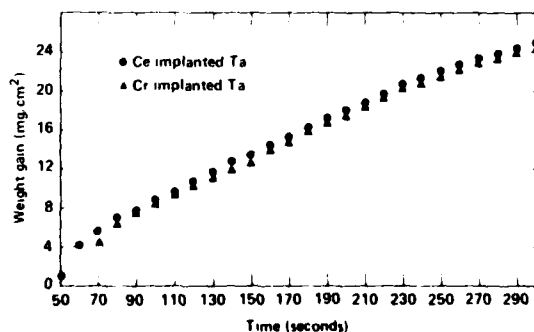


Fig. 1. Raw data typical of that obtained in TGA apparatus.

tions of the data, the experimental slopes were reduced to weight-gain rates applicable to the faces. These data are tabulated in table 1. They may be compared to the literature value [1] of  $140 \text{ mg/cm}^2 \text{ hr}$ . The differences among the several measurements lie within the estimated errors of measurement and the mean value is somewhat greater than the literature value because the weight-gain assigned to edges was probably underestimated. Thus no sizable effect of implantation on overall oxidation rate is observed. Data was not obtained for  $TaLi$  since a catastrophic ignition reaction occurred in spite of the identical temperature time program used for all samples.

##### 3.1.2. X-ray diffraction analysis

Diffraction traces for all samples showed  $Ta_2O_5$  structure. No evidence of Ta metal was seen, implying an oxide layer thickness greater than the extinction depth for the  $CuK\alpha$  radiation employed. A thickness of  $\sim 7.5 \mu\text{m}$  is consistent with this as well as the observed weight gain. Line intensities indicate a high degree of preferred orientation along [010] in the oxide which we attribute to the crystallographic texture in our Ta metal which favored the [110] direction (along the rod axis or) normal to sample faces.

No evidence was found for oxides of the implanted species or for mixed oxides. This does not rule out their presence in the near surface region however, since only  $\sim 6\%$  of total diffracted intensity would originate in the first  $1000 \text{ \AA}$  of material for the range of diffraction angles employed.

##### 3.1.3. Optical microscopy

Notwithstanding the failure to see effects of implantation with the above techniques, the surfaces of the various oxidized specimens did appear different under the optical microscope, particularly with the contrast enhancement of polarized light (orthorhombic  $Ta_2O_5$  would be expected to show anisotropic optical properties). Pure Ta and  $TaCe$  were unremarkable with a mottled light and dark gray appearance.  $TaAl$  showed a finer but similar mottled surface plus distinct inclusions of  $\sim 10 \mu\text{m}$  diameter (see fig. 2a). In  $TaCr$  (fig. 2b) a distinct network of cell-boundaries were observed which showed metallic luster. An outcropping of translucent structures was seen on  $TaSi$  (fig. 2c) surrounded by a dark cell-like network (fig. 2d) with significant relief in the pattern.

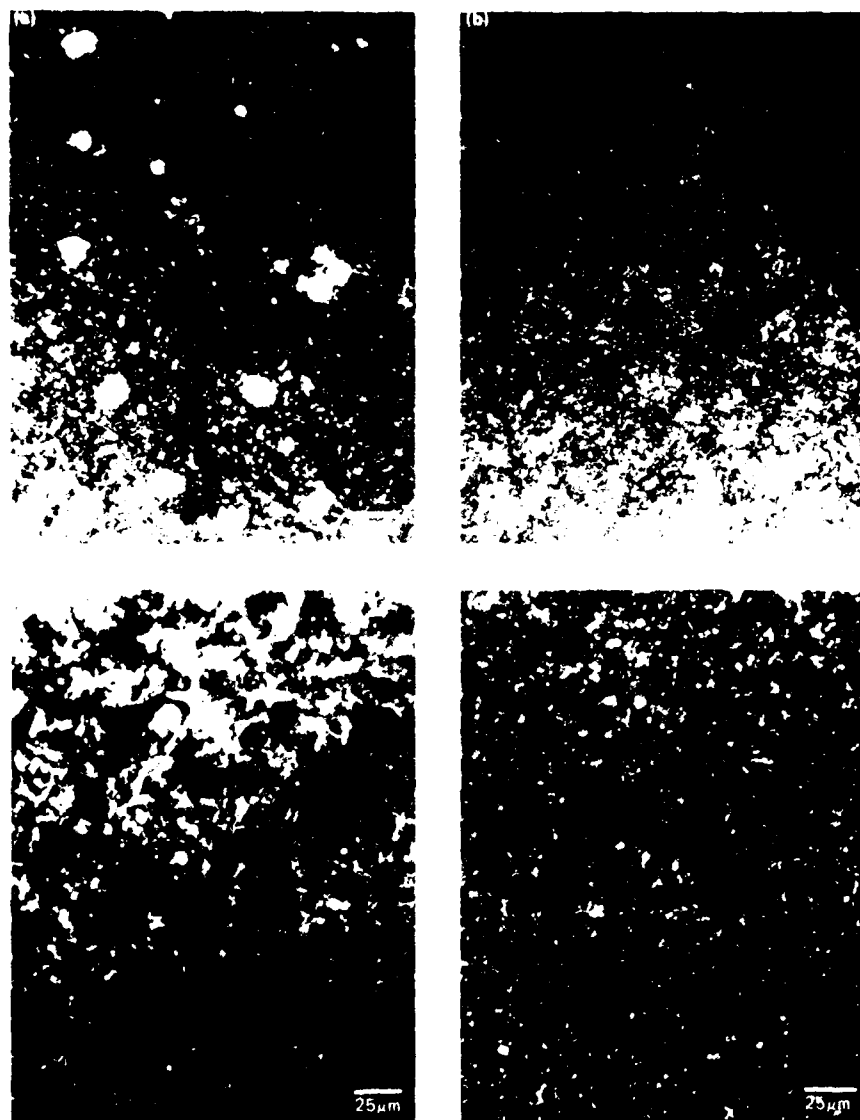


Fig. 2. Optical micrographs of the surface of severely oxidized (a) LaAl, (b) LaCr and (c, d) LaSi. In (a, b) and (c) polarizing filters are crossed at a relative angle of  $146^\circ$ . In (d) which views the identical area as (c) the two filters are coincident ( $0^\circ$ ).

The unimplanted face of the LaSi sample showed no such effects, thus verifying that the various differences in surface appearance result from the implanted solute.

#### 3.1.4. Auger spectroscopy

The thick insulating oxide layer resulted in sample charging effects which required special proce-

dures. We were successful only with samples LaCr and LaCe using low energy (1500 V) exciting electrons and low angle Ar-ion sputtering. Approximate depth scale calibration was derived using a 1000 Å anodic La-oxide film on La. The Ce signal intensity is shown as a function of depth in fig. 3. Quantitative calibration of Ce concentration was not possible at the low excitation voltage, but the

concentration profile is similar to the original implanted-profile in the metal. The Ce seems to have been oxidized in place. Although the Cr signal was too weak to discern a profile shape, its qualitative behavior appeared similar to that of Ce in the first 1600 Å.

### 3.1.5. Nuclear-reaction analysis

The  $^{27}\text{Al}(p, \gamma)^{28}\text{Si}$  reaction was used to profile Al in the as-implanted Ta metal and the oxidized samples. Fig. 4 shows the Al profile for as-implanted and oxidized cases after subtraction of background from a run with an unimplanted-oxidized sample. The figure shows that after oxidation the Al is found distributed throughout the region probed by the analysis beam and probably extends beyond this range.

### 3.2. Mild case (500°C, 1 hour in 4:1 Ar/O<sub>2</sub>)

#### 3.2.1. Rutherford Backscattering Analysis (RBS)

This analysis method takes advantage of differences in atomic mass to distinguish among sample constituents, and of the energy loss of the incident ions within the material to provide depth information. Unfortunately all implanted impurities as well as oxygen itself are of lower mass than the major Ta component. Thus, information must be extracted primarily from scattering by Ta. Referring to the spectra of fig. 5, one sees dilution of unoxidized Ta by some of the implanted species, notably Cr and Al, as evidenced by the reduction

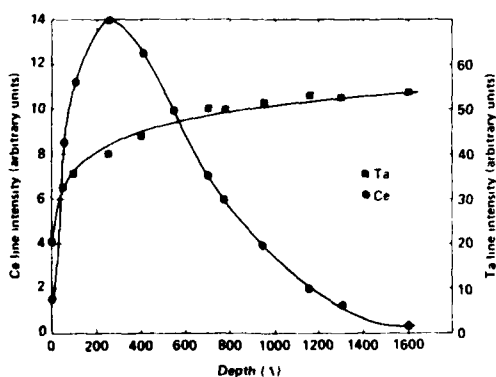


Fig. 3. Auger signal intensity versus sputtered depth for Ce and Ta in severely oxidized TaCe sample. The same arbitrary units apply to both intensity scales. The oxygen signal (not shown) was flat throughout the examined depth.

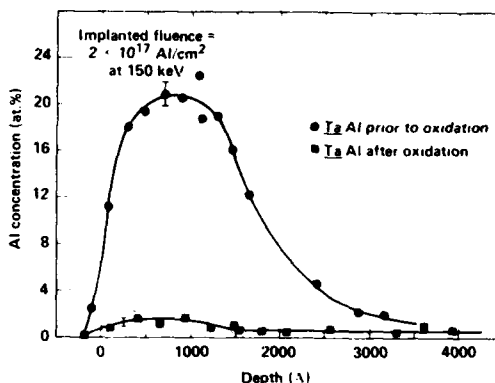


Fig. 4. Concentration profile of Al in as-implanted Ta metal and severely oxidized TaAl obtained by  $(p, \gamma)$  nuclear reaction analysis. Data are background subtracted and concentration scale was determined using a pure Al target.

in scattering yield from Ta, to depths corresponding to the range of the implanted ion. The concentration of Cr deduced from such reductions in TaCr is shown in fig. 5a. Typical features of spectra from oxidized samples include the gradual rise of the Ta signal with increasing depth from that of approximately Ta<sub>2</sub>O<sub>5</sub> toward that of unoxidized Ta metal. One typically sees a knee about 1000 Å below the surface region from which we can infer the presence of an interface between "oxide layer" and "oxygen-bearing-metal". The height of Ta signal in the oxide layer is greater than that expected from Ta<sub>2</sub>O<sub>5</sub>, however, we cannot determine stoichiometry of the layer well since the implant-dilution and stopping power are not known accurately. At the largest depth probed ( $\sim 0.5 \mu\text{m}$ ), the Ta signal corresponds to an average oxygen concentration well in excess of the oxygen solubility limit in Ta at 500°C of about 1 at.% [5]. It is known [2,5] that a complex progression of suboxides of Ta occur at this oxidation temperature. These are probably present in the "interface region" and extend inward and to the surface as well. The interesting aspects of the RBS data are the differences among the various cases.

In the TaAl (fig. 5c), TaZr (fig. 5b) and TaLi (fig. 5d) cases the subsurface interface appears as a sharper spectral feature than for the other systems. This may be a true indication of a more abrupt interface or may indicate greater lateral uniformity in oxide thickness under the area of the analyzing beam. The amount of discernible oxide and the

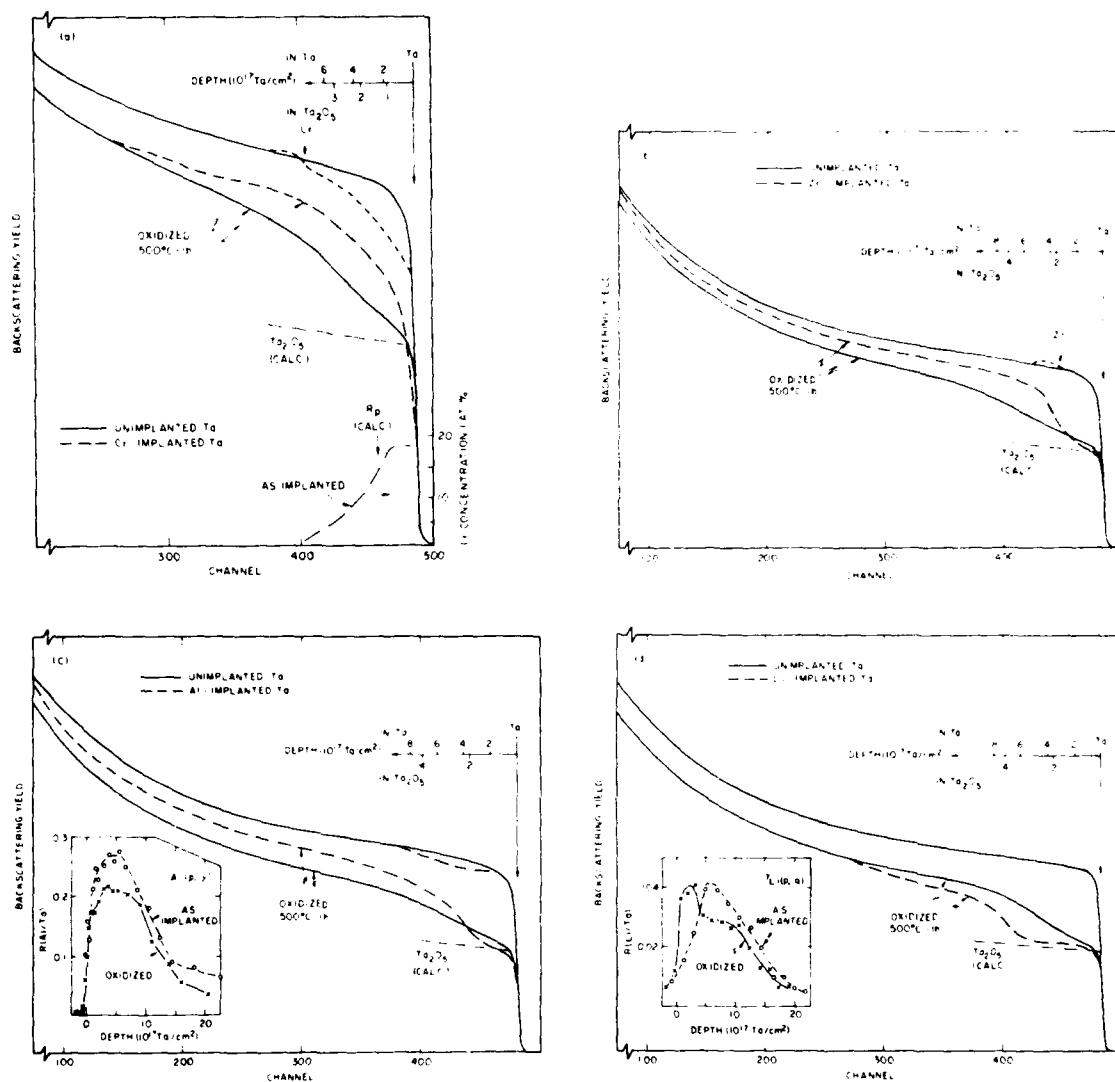


Fig. 5. For mildly oxidized cases: (a) RBS spectrum for  $\text{TaCr}$  and derived Cr distribution; (b) RBS spectrum for  $\text{TaZr}$ ; (c) RBS and nuclear reaction data for  $\text{TaAl}$ ; (d) RBS and nuclear reaction data for  $\text{TaLi}$ .  $1 \times 10^{17} \text{ Ta/cm}^2$  corresponds to 18.1 nm of pure Ta or 44.7 nm of  $\text{Ta}_2\text{O}_5$ . The surface approximation for stopping-power factors was used for the indicated depth scales.

level of oxygen present in the underlying sub-oxides also differ among the samples. Referring to unimplanted Ta as a standard, the  $\text{TaCe}$  (not shown) appears about the same. In  $\text{TaAl}$ , the oxide appears  $\sim 20\%$  thinner and oxygen present in suboxides is less by a factor of  $\sim 2$ . In  $\text{TaZr}$ , a similar oxygen-in-suboxides reduction as in  $\text{TaAl}$  is seen but oxide thickness is about one-half the

standard. A different effect is seen in  $\text{TaCr}$  (fig. 5a) where oxygen is only reduced in the interface region and the oxide layer is too thin to be resolved.

The case of  $\text{TaLi}$  is unusual in that oxidation enhancement is seen. The oxide layer is thicker than pure Ta by  $\sim 50\%$  and the oxygen level in the interface region is higher, approaching that seen in

pure oxidized Ta at greater depths. This sample's surface displayed a blue-iridescent hue.

### 3.2.2. Nuclear-reaction analysis

The  $(p, \gamma)$  reaction noted in sect. 2 was used on the TaAl samples where no Al redistribution on oxidation was seen (fig. 5c). The slight discrepancy between the Al concentrations in the two samples is believed to be caused by the simplifying assumptions used in the calculation. Note that the oxide layer resides within the first 25% of the Al distribution.

The  ${}^7\text{Li}(p, \alpha){}^4\text{He}$  reaction was applied to the TaLi sample and showed Li to be enriched in the oxide layer at the expense of Li just beneath the layer (fig. 5d). It was observed that only about 25% of implanted Li was retained following ion implantation.

### 3.2.3. Auger Electron Spectroscopy (AES)

Samples studied by this method include unimplanted oxidized Ta and samples implanted with Al, Ce, Cr and Zr in both as-implanted and post-oxidation conditions. The Auger lines of Ta, oxygen and solute were monitored as a function of depth by sputter-etching the samples. In all cases some degree of carbon contamination was noted beneath the surface which probably arose from implantation vacuum conditions. The carbon was in all cases considerably closer to the surface than the implant range. Corroboration of RBS data was found in all respects. Ce and Al remained essentially in the implanted concentration profile after oxidation. As shown in fig. 6, Cr was found to segregate to the oxide surface where the Ta signal was correspondingly less. Through the oxide, and in the metal immediately below, the Cr was depleted. Zr did not provide a sufficiently strong line to profile in as-implanted or oxidized samples. As seen in RBS data, the oxidized TaCr, TaZr, and TaAl samples displayed a sharp interface between the oxide layer and metal with a reduced oxygen tail into the metal. This interface was diffuse, and a deep oxygen tail was seen in TaCe and unimplanted Ta. The relative intensities of Ta and oxygen lines were initially roughly consistent with that known to obtain for  $\text{Ta}_2\text{O}_5$ , where preferential sputtering affects the observed ratio. After sputter etching a few nm of oxide, however, significant deviations from  $\text{Ta}_2\text{O}_5$  stoichiometry were observed, suggesting the presence of Ta suboxides.

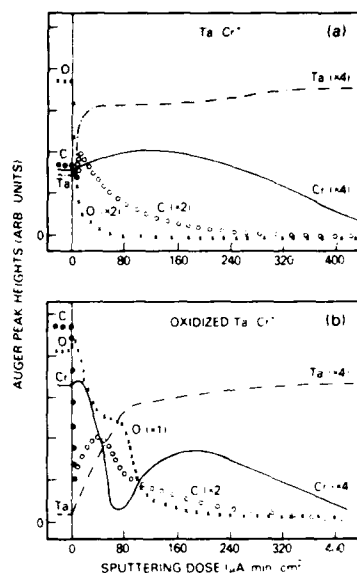


Fig. 6. Auger depth profiles for (a) unoxidized and (b) mildly oxidized TaCr specimens. (The solid circles refer to adventitious carbon, whereas the open circles refer to carbon in a carbide as deduced from Auger line shape. The peak concentration of carbon in carbide in the unoxidized (a) case was found to be  $\sim 20$  at.% using a sensitivity factor of 0.32.)

Unfortunately, this method, like RBS, cannot distinguish whether oxygen in the metal is in solution or in suboxide platelets, nor whether apparent interface diffuseness results from oxide thickness nonuniformity or from a truly gradual transition in Ta/O ratio.

### 3.2.4. Secondary Ion Mass Spectroscopy (SIMS)

SIMS analysis of unimplanted oxidized Ta and of samples implanted with Al, Ce, and Cr substantiated the results previously obtained by AES on these samples. Analysis of the Li and Zr implanted specimens provided new information due to the greater sensitivity for these elements of SIMS. Li was found to segregate to the surface of the oxide layer at the expense of subsurface Li concentration, much as implanted Cr had. Zr retained its initial implantation profile following oxidation, as Ce and Al had.

#### 4. Discussion

The linear oxidation rate for Ta as a function of temperature indicates a change in mechanism between  $\sim 600$  and  $800^\circ\text{C}$  as shown in fig. 7. It is generally believed [2] that in the low temperature regime, the progressive formation of various suboxides controls oxidation, whereas at high temperature, the direct formation of  $\text{Ta}_2\text{O}_5$  from the oxygen-contaminated metal occurs. It is thus not surprising that the degree to which oxidation is influenced by implanted species also differs in the two temperature regions.

At the lower temperature, we have shown that Zr and Cr significantly impede oxide-layer growth whereas Li accelerates it. Also, the dissolution of oxygen in the underlying metal is reduced by implantation of Zr and Al. The presence of Ce had little effect. Differences in the post-oxidation distribution of the solute may be related to this behavior. Cr and Li, for example, move preferentially to the surface, indicating mobility of the solute, whereas Ce, Zr and Al tend to retain their implanted distribution through the oxide.

We can speculate on possible mechanisms whereby implantation causes these results. The implanted layer may block oxygen transport into the metal or make the oxide itself less permeable in those cases where oxidation is reduced. Lauf

and Altstetter [6] have shown, for example, that Zr solute in the Ta-like metal, Nb, can trap oxygen and retard its diffusion. Some work in progress indicates that Cr solute in Ta can also trap oxygen [7]. It is also known that the morphology of the suboxides entails the incursion of suboxide platelets along particular habit planes of the metal. The solute may interfere with this directly or through the stress or lattice disorder which attends implantation. Since  $500^\circ\text{C}$  is roughly 25% of the absolute melting point of Ta, long range migration of solute atoms or lattice annealing effects would not be expected to erase the effects of implantation, particularly on so thin an oxidation layer as is created under these relatively mild conditions. It should be noted that whereas all of the implanted Ce and Zr were enveloped in the growing oxide layer, considerable amounts of Al, Li, and Cr remained beneath this layer because of their deeper penetration into Ta during ion implantation.

At high temperature, the rate of oxidation far exceeds the diffusion rate of both the implanted solutes and of oxygen in Ta metal. Therefore any beneficial effect of the implanted layer would have to result from it providing a rather impenetrable barrier for an extended period. This implies both the need to form an alloy with extreme resistance or a thin oxide with extremely slow oxygen transport, and the need to maintain lateral continuity of the layer. Since no remarkable effect on net oxidation rate was seen, these criteria were not met. The optical micrographs of fig. 2 imply lateral segregation of solute and/or solute oxides near the surface. In addition, from the modest degree to which Cr, Zr, or Al were protective at  $500^\circ\text{C}$  in 20%  $\text{O}_2$ , one would not expect significant protection at  $1000^\circ\text{C}$  in 100%  $\text{O}_2$ . For protection at these severe conditions, it is probably necessary to form the type of ternary or higher alloy at the surface which shows rates of  $< 0.4 \text{ mg/cm}^2/\text{h}$  (ref. 1, p. 439).

Some points of similarity exist between the high and low temperature data. Ce was seen to be essentially immobile in both cases. And, the enhancement of oxidation by Li at  $500^\circ\text{C}$  could account for the sample ignition at  $1000^\circ\text{C}$ . A disparity is noted for Al which strongly redistributed at the higher temperature, but not at the lower.

Additional studies on the specimens described here as well as on other systems are in progress.

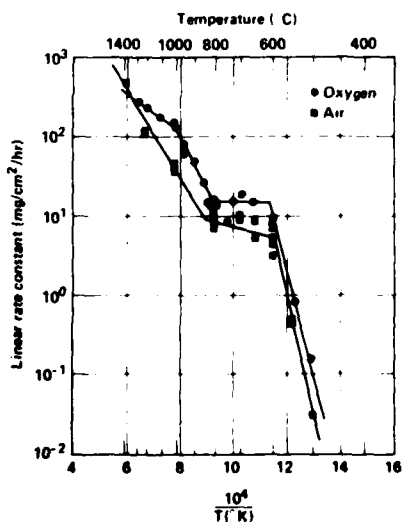


Fig. 7. Temperature variation of linear rate constants for tantalum oxidation in oxygen and air from Schmidt et al. [4].

We gratefully acknowledge useful discussions with Dr. J. Stringer and the technical assistance of E. Lilly, S. Aceves, T. Schmidt, R.G. Patterson, J. Fischer, P. Curtis, G.S. Smith, C. Wagner and C. Farrell of LLNL and of T. M. Barlack of NRL.

## References

- [1] F.E. Bacon and P.M. Moanfeldt, in: *Columbium and Tantalum*, eds., F.T. Sisco and E. Epremian (Wiley, New York, 1963) ch. 9, p. 347.
- [2] J. Stringer, *Reviews on High-Temperature Materials* 1, No. 3 (1973) 256.
- [3] G. Dearnaley, *Nucl. Instr. and Meth.* 182/183 (1981) 899.
- [4] F.F. Schmidt, W.D. Klopp, W.M. Albrecht, F.C. Holden, H.R. Ogden and R.I. Jaffee, U.S. Air Force Technical Report WADD-TR-59-13 (1959) 152 pp.
- [5] G. Hörz, *Acta Metall.* 27 (1979) 1893.
- [6] R.J. Lauf and C.J. Altstetter, *Acta Metall.* 27 (1979) 1157.
- [7] Private communication with C.J. Altstetter, University of Illinois, Urbana, IL 61801, USA.

Section IV.A

MAGNETIC PROPERTIES OF IRON-IMPLANTED GRAPHITE

N. C. Koon<sup>1</sup>  
P. Pehrsson<sup>2</sup>  
D. Weber<sup>3</sup>  
A. I. Schindler<sup>4</sup>

<sup>1</sup>Metal Physics Branch  
Condensed Matter & Radiation Sciences Division  
Naval Research Laboratory

<sup>2</sup>Catholic University of America  
Washington, D.C. 20064

<sup>3</sup>Inorganic & Electrochemistry Branch  
Chemistry Division  
Naval Research Laboratory

<sup>4</sup>Material Science & Component Technology Directorate  
Naval Research Laboratory

This work was supported by the Office of Naval Research.

# Magnetic properties of iron-implanted graphite

N. C. Koon, P. Pehrsson, D. Weber, and A. I. Schindler  
Naval Research Laboratory, Washington, DC 20375

We have measured the magnetic properties of highly oriented pyrolytic graphite (HOPG) implanted with fluences of 25-keV iron atoms ranging from  $10^{16}$  to  $10^{17}$  atoms/cm<sup>2</sup>. The lowest fluence specimen was paramagnetic down to 2 K, with evidence for clusters of only a few spins, while the highest fluence specimen was clearly ferromagnetic, with magnetization curves resembling those of a set of randomly oriented soft magnetic planes. The critical fluence for formation of a ferromagnetic state appears to be between 1 and  $3 \times 10^{16}$  atoms/cm<sup>2</sup> at 25 keV. These results can be qualitatively understood based on the critical density for percolation of near neighbor exchange interactions.

PACS numbers: 75.70. — i, 75.50. — y

## INTRODUCTION

In recent years the modification of crystallographically layered materials by intercalation of foreign species, principally by chemical means, has been the subject of intense interest. Intercalated graphitic compounds have been extensively studied because of the great variety of physical, chemical, electrical, and magnetic phenomena which they exhibit. Many species, however, cannot be intercalated by chemical means. Ion implantation offers an alternative method for insertion of foreign species into a host material, although for a variety of reasons it cannot really be considered equivalent to chemical intercalation. One of the principal differences is in the damage produced by the high kinetic energy required for insertion. At a critical level of damage in carbon systems there seems to be quite generally a transition to an amorphous state, which in the case of ion implantation implies an amorphous surface layer.<sup>1-3</sup> For ions as heavy as iron implanted at 100 keV, for example, Raman scattering measurements<sup>3</sup> have shown that an amorphous layer results with fluences as low as  $1 \times 10^{14}$  atoms/cm<sup>2</sup>. In any event the implanted atoms will generally come to rest in heavily radiation damaged if not fully amorphous regions near the surface.

The purpose of the present work was to explore the magnetic properties of iron implanted into graphite. Because of the typically strong nature of the exchange coupling between iron spins, even in amorphous materials, it was expected that the magnetic properties would provide useful information about the structure and separation of the implanted atoms.

## EXPERIMENT

The samples were prepared by implantation at a fixed energy of 25 keV normal to the graphite face. The depth distribution of implanted atoms was estimated using the theory of Lindhard, Scharff and Schiott (LSS).<sup>4</sup> Fitting a Gaussian to the calculated distribution gave the center of the distribution at a depth of 147 Å, with a Gaussian width of 47 Å, assuming no sputtering at the surface. Samples were prepared with fluence levels of 1, 3, 6, and  $10 \times 10^{16}$  atoms/cm<sup>2</sup>. The atomic concentrations of iron at the maximum of the

distributions were calculated to be 6.5, 17.3, 29.5, and 41.1 at. %, respectively.

The ion-implanted surfaces were removed in an inert atmosphere and sealed in quartz tubes under vacuum. Magnetic measurements were made using a vibrating sample magnetometer and a superconducting solenoid. For experimental reasons the data were limited to temperatures less than 150 K.

## RESULTS

The fluence levels chosen for investigation resulted in samples whose magnetic properties spanned the range from clearly ferromagnetic at the highest fluence level ( $10^{17}$  atoms/cm<sup>2</sup>) to paramagnetic at the lowest ( $10^{16}$  atoms/cm<sup>2</sup>). Magnetization curves taken at 2 K for the highest fluence sample are shown in Fig. 1. The linear diamagnetic signal from graphite has been subtracted from the data. One rather striking feature of the data is a rapid change in magnetization at low fields. This is consistent with what would be expected from a randomly oriented arrangement of thin magnetic films with low coercive forces. Because of the low demagnetizing factor in the plane, there would be an initial

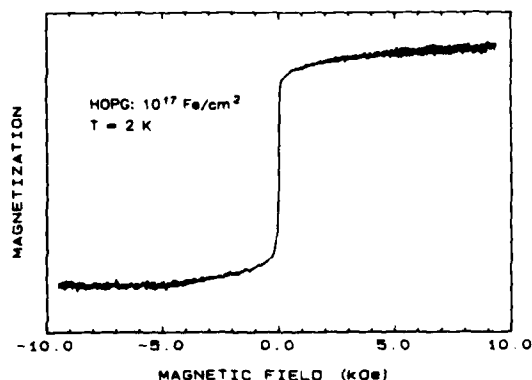


FIG. 1 Magnetization vs applied magnetic field at 2 K for HOPG implanted with  $10^{17}$  atoms/cm<sup>2</sup> of iron. The diamagnetic signal from the graphite has been subtracted.

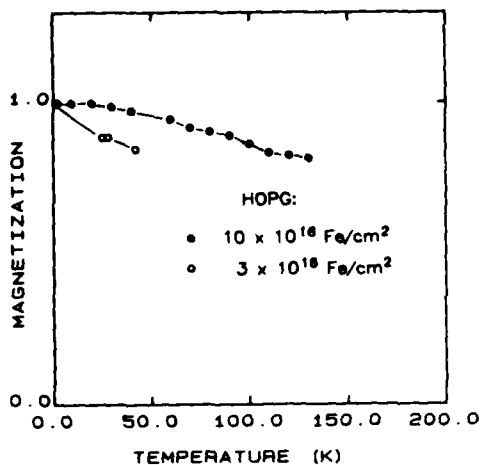


FIG. 2. Relative spontaneous magnetization vs temperature for HOPG implanted with  $3 \times 10^{16}$  (○) and  $10^{17}$  (●) atoms/cm<sup>2</sup> of iron.

sharp rise in magnetization to 78.5% of saturation as the moment of each plane rotated in the plane to maximize the component parallel to the applied field. There would then be a slower increase with applied field as the moments rotate out of the plane. Similar results were observed for a fluence of  $6 \times 10^{16}$  atoms/cm<sup>2</sup>, except that the coercive force was somewhat greater. The coercive force at 2 K reached a maximum of 550 Oe at a fluence of  $3 \times 10^{16}$  atoms/cm<sup>2</sup>, which is probably close to the critical fluence for formation of a ferromagnetic state. The rise in coercive force near this critical concentration probably reflects the fact that near that concentration the magnetic state of the system more nearly resembles a collection of weakly coupled magnetic clusters than a uniform ferromagnetic sheet.

The temperature dependence of the spontaneous moments, as shown in Fig. 2 for the  $3$  and  $10 \times 10^{16}$  atoms/cm<sup>2</sup> samples, also suggest that  $3 \times 10^{16}$  is approaching the critical fluence for the formation of a ferromagnetic state. The two highest fluence samples had a very weakly temperature dependent spontaneous moment at low temperatures, suggesting that almost all of the implanted Fe atoms in those specimens experience rather strong ferromagnetic exchange interactions. The specimen with  $3 \times 10^{16}$  atoms/cm<sup>2</sup> has a magnetization which drops off much more rapidly with increasing temperature, suggesting a much larger percentage of weakly coupled spins. Extensions of the data to higher temperatures could not be done reliably due to experimental limitations and to the complex field dependence of the magnetization, especially of the lower concentration sample.

The magnetization of the lowest fluence specimen ( $10^{16}$  atoms/cm<sup>2</sup>) is shown in Fig. 3. It is strikingly different from the other three in that there is no evidence for a spontaneous moment even at the lowest temperature measured. The susceptibility varies more slowly than  $1/T$ , but still increases rapidly with decreasing temperature. Higher field data suggests that the average moment size per spin is larger than two Bohr magnetons, indicating there is exchange coupling between spins, but the average number of spins in each exchange coupled cluster is rather small.

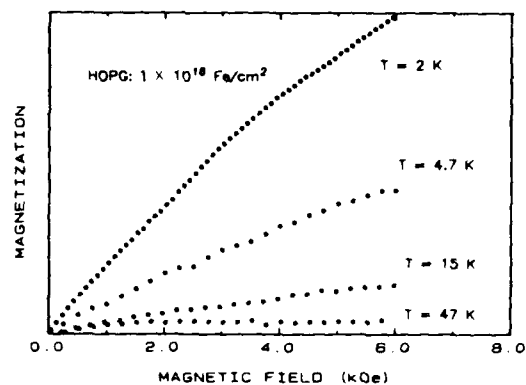


FIG. 3. Magnetization vs applied magnetic field at various temperatures for HOPG implanted with  $10^{17}$  atoms/cm<sup>2</sup> of iron. The diamagnetic signal from the graphite has been subtracted.

## DISCUSSION

The results of this study can be reasonably understood based on the assumption that only neighboring iron spins in the heavily radiation damaged (and probably amorphous) layer are strongly exchange coupled. The variation in magnetic properties with concentration then depends mainly on how this strong exchange propagates through the lattice. In this model ferromagnetism only occurs at iron concentrations greater than the percolation concentration, where the exchange interactions can propagate to infinity. The percolation problem has been treated extensively for a variety of physical processes,<sup>5,6</sup> usually for the case of regular lattices. In the present case, where the structure is poorly defined, it is useful to note the results of Sher and Zallen<sup>7</sup> who defined a critical density for percolation, which turns out to be close to 15 vol. % for a wide variety of lattice types. While the exact relative volumes occupied by the iron and carbon atoms is clearly not known for the radiation damaged layer, it is probably reasonable for qualitative discussion to assume they occupy equal volumes, in which case the atomic concentration is the same as the relative atomic density. The remaining problem in making contact with the Sher and Zallen<sup>7</sup> theory is in relating the relative atomic density to the absolute fractional volume occupied by the iron. For the purpose of discussion we assume the two are equal, which is certainly not precisely correct. With that assumption it is interesting to note that in the maximum iron concentration region the three high fluence specimens are all well above the iron percolation density and are clearly ferromagnetic, while the lowest fluence specimen is well below the iron percolation limit and is clearly paramagnetic. The magnetic properties observed in the present case therefore seem to correlate reasonably well with the structural characteristics expected for iron implanted into graphite, although it should be pointed out that the LSS depth distributions constitute only a qualitative and semiquantitative guide. The actual depth distribution of implanted iron atoms may very well differ from the LSS theory due to the highly anisotropic nature of the graphite structure and bonding.

- <sup>1</sup>B. L. Crowder, J. E. Smith, Jr., M. H. Brodsky, and M. I. Nathan, *Proceedings of the Second International Conference on Ion Implantation in Semiconductors* (Garmisch-Partenkirchen, Federal Republic of Germany, 1970), p. 255; J. E. Smith, Jr., M. H. Brodsky, B. L. Crowder, and M. I. Nathan, *J. Non-Cryst. Solids* **9-10**, 179 (1972).
- <sup>2</sup>R. B. Wright, R. Varma, and D. M. Gruen, *J. Nucl. Mater.* **63**, 415 (1976).
- <sup>3</sup>B. S. Elman, M. S. Dresselhaus, G. Dresselhaus, E. W. Maby, and H. Mazurek, *Phys. Rev.* **24**, 1027 (1981).
- <sup>4</sup>J. Lindhard, M. Scharff, and H. E. Schiott, *Kgl. Danske Vid. Selsk. Mat.-Fys. Medd.* **33**, 14 (1963).
- <sup>5</sup>H. L. Frisch and J. M. Hammersley, *J. Soc. Ind. Appl. Math.* **11**, 894 (1963).
- <sup>6</sup>R. J. Elliott, B. R. Heap, D. J. Morgan, and G. S. Rushbrooke, *Phys. Rev. Lett.* **5**, 366 (1960).
- <sup>7</sup>H. Shur and R. Zallen, *J. Chem. Phys.* **53**, 3759 (1970).

Section IV.B

PHYSICAL PROPERTIES OF TWO METASTABLE  
STATES OF AMORPHOUS SILICON

G. K. Hubler and T. A. Kennedy<sup>1</sup>  
C. N. Waddell and W. G. Spitzer<sup>2</sup>  
J. E. Fredrickson<sup>3</sup>

<sup>1</sup>Materials Modification & Analysis Branch  
Condensed Matter & Radiation Sciences Division  
Naval Research Laboratory

<sup>2</sup>Physics and Materials Science Departments  
University of Southern California  
Los Angeles, California

<sup>3</sup>Physics-Astronomy Department  
California State University  
Long Beach, California

The portion of this research performed at NRL was supported by the Office of Naval Research and the research conducted at University of Southern California and California State were partially supported by the Joint Services Electronics Program under contract #F44620-76C-0061.

## PHYSICAL PROPERTIES OF TWO METASTABLE STATES OF AMORPHOUS SILICON

G.K. Hubler\*, C.N. Waddell\*\*, W.G. Spitzer\*\*, J.E. Fredrickson\*\*\*, and T.A. Kennedy\*

\*Naval Research Laboratory, Washington, D.C.; \*\*Physics and Materials Science Departments, University of Southern California, Los Angeles, California; \*\*\*Physics-Astronomy Department, California State University, Long Beach, California

### ABSTRACT

Characterization of the two metastable states of amorphous Si produced by ion implantation is extended to include electron paramagnetic resonance, fundamental absorption edge, and density measurements in addition to infrared reflection. It is found that the properties of the two a-Si states are not dependent upon the mass of the incident ion ( $^{12}\text{C}$ ,  $^{29}\text{Si}$ ,  $^{31}\text{P}$ ,  $^{120}\text{Sn}$ ) or upon the anneal temperature for  $400^\circ < T_A < 600^\circ\text{C}$ . The dangling-bond density drops about a factor of 2, the absorption coefficient drops by more than a factor of 5, but the density does not change when the a-Si makes a transition between the two states.

### INTRODUCTION

In previous work [1] a number of Si samples were implanted at either 200K or room temperature with Si or P ions which had incident energies between 200keV and 2.7MeV and fluences between  $1.0 \times 10^{16}$  and  $10.0 \times 10^{16}$  ions/cm<sup>2</sup>. In all cases the amorphous (a-Si) produced by the implantation process had an infrared refractive index,  $n_I(\nu)$  (see curve in Fig. 1) which was independent of the fluence and the implanted ion, and was 12% larger than the crystalline value at the frequency  $\nu$  corresponding to a wave number of  $4000\text{cm}^{-1}$ .

In subsequent studies [2,3] it was found that annealing the implanted samples for about 2 hours at  $500^\circ\text{C}$  caused the index of refraction to decrease to a new value,  $n_{II}(\nu)$ , also shown in Fig. 1. The ratio  $n_{II}/n_I = 0.96$  at  $\nu = 4000\text{cm}^{-1}$  indicates that annealing causes the refractive index to drop about 1/3 of its original implantation induced increase from the crystalline value  $n_C(\nu)$ . The values of  $n_{II}(\nu)$  were also independent of the implantation parameters and did not change with further annealing. These two optical states were identified as (I), the defect-saturated (as-implanted) and (II), the thermally-stabilized (annealed) states of a-Si [4]. For this work, we define these states as a-Si-I and a-Si-II, respectively.

In a recent study [5] the infrared refractive indices, the strength of the electron paramagnetic resonance (EPR) dangling-bond signal, and the changes in density of the a-Si were measured as a function of annealing time at  $T_A = 500^\circ\text{C}$  for  $^{29}\text{Si}$ -implanted samples of Si. These

measurements indicated that the dangling bond density behaved in a manner similar to that of the refractive index, i.e., a large drop in the early stages (first two hours) of the 500°C anneal, and only slight further changes resulting from prolonged anneal times. However, there was no corresponding change in density.

The results presented here extend those of Ref. 5 in two ways. Firstly, because there was an indication in the literature that the refractive index of a-Si-I depends upon the mass of the implanted ion [6], it is important to determine if these properties of a-Si-I and II are

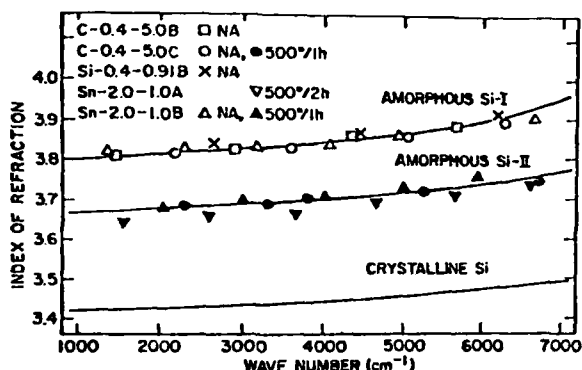


Fig. 1. Indices of refraction of crystalline Si, a-Si-I (as-implanted), and a-Si-II (thermally stabilized). The curves are from Ref. [1,2] and the data points are measurements of C, Si, and Sn implanted samples in the as-implanted state and after annealing at 500°C.

dependent upon the ion mass. Group IV ( $^{12}\text{C}$ ,  $^{29}\text{Si}$ ,  $^{120}\text{Sn}$ ) ions were chosen to avoid complications of electrical doping effects. Secondly, since the transition between the two states had only been studied for  $500 \leq T_A \leq 550^\circ\text{C}$ , we studied the annealing process over a wider temperature range ( $300 \leq T_A \leq 600^\circ\text{C}$ ) to determine whether the properties of the thermally stabilized state (a-Si-II) are dependent upon the anneal temperature employed. If the several properties of a-Si-II are independent of all implantation parameters and of the annealing temperature, then the results would suggest that a definable and unique thermodynamic state has been produced.

#### Experimental Procedures

The techniques used are essentially the same as those used previously [1-3,5,7] and therefore they will be reviewed here only briefly. The implanted samples are identified in Figs. 1, 2, and 3 by the designation of: implanted ion, incident ion energy in MeV, fluence in units of  $10^{16}$  ions/cm<sup>2</sup>, and if there is more than one sample, by A,B, etc. Thus, C-0.4-5-A is a C ion-implanted Si sample, where the C-ion energy is 400 keV, the fluence is  $5 \times 10^{16}$ /cm<sup>2</sup>, and "A" indicates that this is the first such implanted sample. The starting material was single crystal Si having an initial resistivity  $> 10 \Omega\text{cm}$ . Multiple energy implantations between 25 and 400 keV were used in some cases to achieve more uniform ion and damage density profiles within the implanted layer. The sample temperature was maintained near 200K during implantation and, to reduce channeling, the incident ion beam direction was approximately  $8^\circ$  off of the high symmetry directions.

Room temperature, near-normal incidence, reflection measurements were made over the wave number range  $400 < \nu < 7000 \text{ cm}^{-1}$ . The reflected intensity varies strongly with  $\nu$  because of interference between the reflections at the air-amorphous and amorphous-crystalline interfaces. Computer analyses of the reflection spectra yields precise values for (i) the

refractive-indices of the a-Si and the recrystallized region, (ii) the depth of the amorphous layer, and (iii) the width of the transition between the a-Si and c-Si regions [7].

During implantation a mask covered a small portion of the surface of each sample. The swelling of the implanted region produces a sharp step in surface height at the edge of the mask. Because the thickness of the implanted region is very small compared to the lateral dimensions of the implanted region, only the thickness of the sample is significantly affected by the radiation damage [8]. Using this model the change in density,  $\% \rho$ , is given by  $\% \rho = \rho_c (\text{step height}) / (\text{a-Si thickness})$  where  $\rho_c$  is the crystalline Si density. The thickness of the a-Si region was determined from the infrared reflection measurements, and a Sloan Dektak profilometer was used to determine the step height to an accuracy of  $\sim 25 \text{ \AA}$  per measurement. The latter measurements contributed most of the inaccuracy in the determination of  $\% \rho$ . For our implantation conditions we estimate that 5 to 11 Å of Si was removed by sputtering for  $^{29}\text{Si}$  implants, 18 Å for C implants, and 38 Å for Sn implants. Since step heights for the as-implanted samples were usually between 100 to 160 Å, the correction to the density would be negligible for Si, 10% for C and about 20% for Sn. Since the step height measurements themselves are accurate only to about 20%, and the sputtering coefficient estimates are accurate only to 50%, we have not applied the correction.

The EPR measurements were made at room temperature with a Varian E3 spectrometer at 9GHz. The signal from a-Si, which has an isotropic  $g = 2.0055$ , has been attributed to dangling bonds [9]. To obtain relative spin density values, the EPR signal strength is divided by the a-Si volume which is obtained by using the sample surface area and the layer thickness determined from the infrared reflection measurements. Infrared band edge absorption measurements were made at 77K by directly comparing the infrared transmission of the implanted sample with that of an identical, non-implanted sample.

## Results

The curves in Fig. 1 show the refractive indices  $n_I(\nu)$  of a-Si-I (as-implanted),  $n_{II}(\nu)$  of a-Si-II (thermally stabilized, 500°C), and  $n_C(\nu)$  for crystalline Si, all as previously reported for Si and P implants. The data points are the refractive indices obtained for several of the samples from this study implanted with  $^{12}\text{C}$ ,  $^{29}\text{Si}$ , or  $^{120}\text{Sn}$  ions. Both the as-implanted and the 500°C anneal refractive indices for all samples are in excellent agreement with our previously published results [1-3,5]. Thus, there is no discernible dependence upon the mass of the incident ion ( $^{12}\text{C} \rightarrow ^{120}\text{Sn}$ ), or the use of a single ion energy or multiple energies during amorphization.

For  $^{12}\text{C}$ ,  $^{29}\text{Si}$ , and  $^{120}\text{Sn}$  implanted samples, the measured absorption for non-annealed samples in the region of the absorption edge was close to  $\alpha \sim 5 \times 10^{-13} \text{ cm}^{-1}$  in agreement with the previous results for P-implanted Si [1], and there was no detectable dependence upon which ion is used for the implantation. The implanted samples were annealed for 2 hours at 500°C to produce the change from  $n_I(\nu)$  to  $n_{II}(\nu)$  and the absorption edge was remeasured. It was not possible to detect a difference between the absorption of the annealed implanted samples and the crystalline reference samples. Therefore, we were unable to obtain

meaningful values for  $\alpha_{II}$ , the absorption coefficient for the thermally stabilized state. We estimate that  $\alpha_{II}(\nu)$  is less than  $\alpha_I(\nu)/5$  or  $\approx \alpha_c(\nu)$  for all cases.

EPR measurements for some of the  $^{12}\text{C}$ ,  $^{29}\text{Si}$ , and  $^{120}\text{Sn}$  implanted samples are presented in Table I. The values for  $^{29}\text{Si}$  are the same as those given previously [5], and it was indicated there that the as-implanted value corresponds to a dangling bond density of  $\sim 2 \times 10^{19} \text{cm}^{-3}$ . When the samples are annealed (500°C/2h) the spin density drops about a factor of 2. There are variations in the values measured for both as-implanted and annealed samples, but no trend due to ion mass is discernible. Therefore, the decrease in the spin density is also attributed to the transition between the two states of the a-Si. The spin densities of a-Si-I and a-Si-II compare to within a factor of 3 for pure films evaporated onto substrates held at room temperature [9].

To characterize the changes in the indices of refraction  $n(\nu)$  we define a single parameter  $f_D = n(\nu)/n_I(\nu)$ . The value of this parameter was determined at  $\nu = 4000 \text{ cm}^{-1}$ , the average frequency of the infrared measurements. The results of annealing  $^{12}\text{C}$ ,  $^{29}\text{Si}$ , and  $^{120}\text{Sn}$  implanted samples of at 400°C are shown in Fig. 2. The  $f_D$  measurements in Fig. 2a clearly show the change in the index of refraction that occurs when the a-Si makes a transition between the two states. There is no

TABLE I: Relative Dangling-Bond Densities<sup>a)</sup>

Anneal/Ion $^{29}\text{Si}$ Average	$^{12}\text{C}$ $^{120}\text{Sn}$
as-implanted	299
353 <sup>b)</sup>	252
310 $\pm$ 38	
325	
320	
500°C/2h	150
136 148	
500°C/8h	163
$\sim 100$	
140 $\pm$ 22	
Ratio	0.45 $\pm$ 0.10

<sup>a)</sup> (The isotropic  $g = 2.0055$  EPR signal)/(a-Si volume).

<sup>b)</sup> This value corresponds to a spin density of  $\sim 2 \times 10^{19} \text{cm}^{-3}$ .

discernible difference due to the implanted ion specie or the duration of the annealing time. The average value of  $f_D = 0.965$  is in good agreement with the previously determined values [3].

The density measurements shown in Fig. 2b indicate that there is no change in the density of the a-Si layer when the transition in states occurs. Note that for an anneal time of two hours, large changes are observed for  $f_D$  and the EPR spin density. There is also no observed density effect due to the implanted ion specie. There is a correlation between the magnitude of  $\rho/\rho_c$  and the calculated magnitude of the sputtering corrections, but the large errors mentioned earlier preclude an accurate sputtering correction. The density of a-Si-I and a-Si-II is  $2.0 \pm 0.5\%$  less than crystalline Si. Very similar results for  $f_D$  and  $\rho/\rho_c$  to those in Fig. 2 were obtained for 500°C anneals except that the transition occurred much more rapidly.

Figure 3 shows the results obtained when  $^{29}\text{Si}$  implanted samples are isothermally annealed at temperatures between 300°C and 600°C. Again the  $f_D$  values indicate similar values of index of refraction  $n_{II}(\nu)$  for the annealed state for  $T_A = 400^\circ$  to  $600^\circ\text{C}$ . However, at  $T_A = 300^\circ\text{C}$  the transition rate is much slower, and the index of refraction remained at  $f_D = 0.974$  after 118h which is significantly greater than the value  $f_D = 0.965 \pm 0.005$  obtained at the higher temperatures. These results suggest that the annealing mechanism responsible for the transition between states may be different at the lowest anneal temperature.

### Discussion

The experimental results presented here and in previous publications support the view that the physical properties being measured are intrinsic to two distinct states of a-Si. The refractive index of as-implanted amorphous silicon,  $n_I(\nu)$ , is independent of ion mass ( $^{12}\text{C}$  -  $^{120}\text{Sn}$ ), implantation dose and energy ( $3 \times 10^{15}$  to  $10^{17}$  Si, P/cm<sup>2</sup>; 200 to 2700 keV P) [1-3] and implantation temperature (100K to 300K for Si implants). The refractive index of thermally stabilized a-Si,  $n_{II}(\nu)$ , is independent of the above parameters and is unique for annealing temperatures  $400 \leq T_A \leq 600^\circ\text{C}$ . For 300°C annealing the final  $n_{II}(\nu)$  state is not quite achieved. If we assume the change in refractive index,  $n_c(\nu) \rightarrow n_I(\nu)$ , is caused by the introduction of  $\sim 2 \times 10^{19} \text{cm}^{-3}$  dangling bonds and to the decrease in dipole moment/volume caused by the observed 2% decrease in mass density, one calculates that the dangling bond polarizability must increase by a factor of 2500 over that of a normal bond. This result is physically unreasonable and indicates that the dangling bonds are not responsible for the change in indices of refraction. Averaged over the entire lattice one finds that there is an increase of  $\sim 28\%$  in the average bond polarizability for the change from c-Si to a-Si-I, and a decrease of  $\sim 8\%$  for the change from a-Si-I to a-Si-II. The observed decrease in the near band edge absorption after the a-Si-I  $\rightarrow$  a-Si-II transition occurs appears to be consistent with the proposal of a network reorganization in which there is a reduction in disorder [5]. The absorption in this region is often associated with the fluctuations in the atomic configurations [10] which cause shifts in electronic states and give rise to band tails. The reduction in disorder by network reorganization thus appears to be the cause for the reduction in absorption and the  $\sim 8\%$  decrease in average bond polarizability. The decrease in dangling bond density seems to be directly related to the annealing of defects within the amorphous structure.

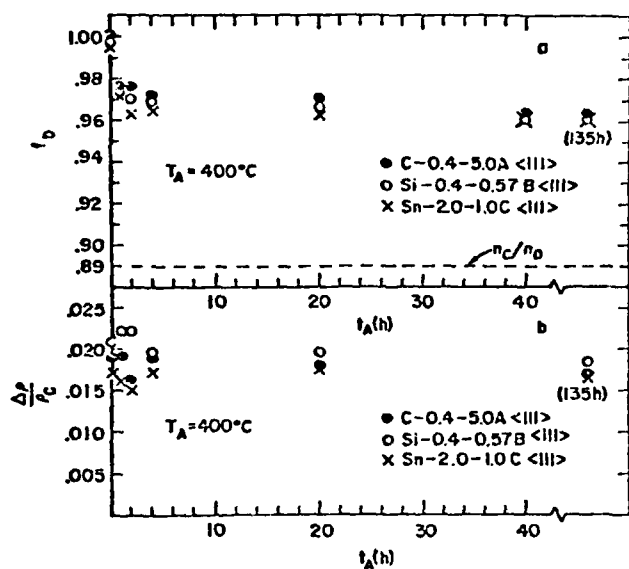
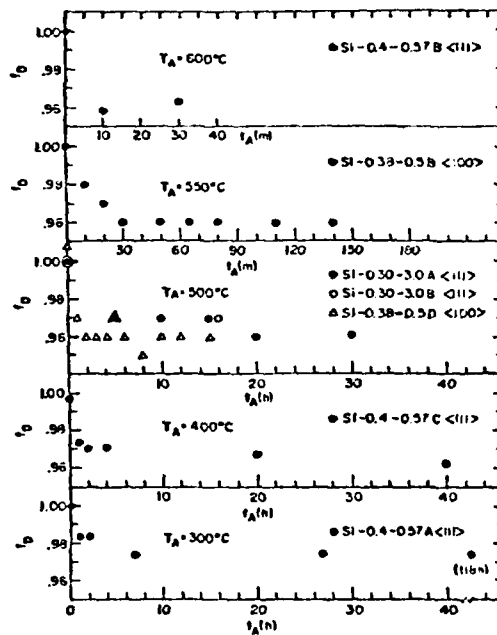


Fig. 2. The relative change in index of refraction,  $n_D$ , and mass density,  $\% \rho/\rho_C$  for C, Si, and Sn implanted samples annealed at  $400^\circ\text{C}$  as a function of anneal time  $t_A$ .

Fig.3. Comparison of the changes in index of refraction,  $n_D$ , for anneal temperatures  $T_A = 300^\circ, 400^\circ, 500^\circ, 550^\circ$  and  $600^\circ\text{C}$ .



If the transition to a-Si-II is a phase transition, one might expect a release of heat during the phase change. Using differential scanning calorimetry, Donovan et al. [11] has measured the heat of crystallization of a-Si and a-Ge prepared by ion implantation. For a-Ge, they observe a substantial heat of stabilization prior to crystallization, (1/2 of the heat released during crystallization) but no heat of stabilization is observed for a-Si prior to crystallization. Our preliminary refractive index data for as-implanted and thermally stabilized a-Ge [12] shows a similar relaxation to that occurring in Si. It is therefore puzzling that there is no heat of stabilization measured for Si and indicates that the mechanism producing the relaxation is different for the two materials.

Given that two distinct states of a-Si can be produced, it is appropriate to speculate on the effects that the two states may have on other material properties. For example, in pulse laser annealing, the coupling of the radiation prior to melting would change due to changes in the optical constants, especially if the light can penetrate to a-c boundary and back to the front surface to interfere with the incident wave. Also, any enthalpy decrease (probably small) between a-Si-I and a-Si-II will increase the melting temperature of a-Si-II; and/or, the apparent melting temperature of a-Si-II might be larger than a-Si-I because advantageous sites for heterogeneous and homogeneous nucleation of the liquid are reduced which allows the a-Si-II to be more readily superheated [13] in a fast pulse anneal. In addition, Cspregi et al. have observed that the crystalline quality of epitaxially recrystallized amorphous layers on (111) Si can be improved by performing a 550°C, 1h anneal prior to performing the normal 950°C, 1h anneal [14]. Our work shows that this pre-anneal should produce the a-Si-II state before recrystallization occurs. While we have no evidence that the production of a-Si-II is related to the results of Cspregi et al., it is possible that the nucleation of microtwins and polycrystallites [14] is suppressed in the relaxed "structure" of a-Si-II such that epitaxial regrowth and simple defect annealing can occur at 550 and 950°C without competition from polycrystallite and microtwin formation. This deserves further study.

In any case, it is clear that refractive index changes induced by the thermal annealing of a-Si provide a physical basis for systematic investigations of the effects of two-step thermal processing on the properties of recrystallized Si and other semiconductors as well [12].

This work was partially supported by the joint Services Electronics Program under contract No. F44620-76C-0061 monitored by the Air Force Office of Scientific Research. We would like to thank J.M. Poate and E.P. Donovan for useful discussions.

# REFERENCES

1. G.K. Hubler, C.N. Waddell, W.G. Spitzer, J.E. Fredrickson, S. Prussin and R.G. Wilson, J. Appl. Phys. 50, 3294 (1979).
2. J.E. Fredrickson, C.N. Waddell, W.G. Spitzer and G.K. Hubler, Appl. Phys. Lett. 40, 172 (1982).
3. C.N. Waddell, W.G. Spitzer, G.K. Hubler and J.E. Fredrickson, J. Appl. Phys. 53, 5851 (1982).
4. M. Janai, D.D. Atired, D.C. Booth and B.O. Seraphin, Solar Energy Mat. 1, 11 (1979).
5. W.G. Spitzer, G.K. Hubler and T.A. Kennedy, Nucl. Instr. Meth. 209/210, 309 (1983).
6. W. Wesch and G. Gotz, Radiat. Eff. 49, 137 (1980).
7. G.K. Hubler, P.R. Malmberg, C.N. Waddell, W.G. Spitzer and J.E. Fredrickson, Radiat. Eff. 60, 35 (1982).
8. K.N. Tu, P. Chaudhari, K. Lal, B.L. Crowder and S.I. Tan, J. Appl. Phys. 43, 4262 (1972).
9. P.A. Thomas, M.H. Brodsky, D. Kaplan and D. Lepine, Phys. Rev. B 18, 3059 (1978.)
10. G.A.N. Connell, "Optical Properties of Amorphous Semiconductors", in Amorphous Semiconductors, ed. M.H. Brodsky, (Springer Verlag, Berlin, 1979). pg. 73.
11. E.P. Donovan, F. Spaepen, and D. Turnbull, these proceedings.
12. K-W. Wang, W.G. Spitzer, and G.K. Hubler, unpublished.
13. D. Turnbull, Metastable Materials Formation by Ion Implantation, eds. S.T. Picraux and W.J. Choyke (North Holland, 1983) 103.
14. L. Csepregi, W.K. Chu, H. Muller, and J.W. Mayer, Rad. Eff. 28, 227 (1976).

## BIBLIOGRAPHY

1. E. A. Wolicki, C. R. Gossett, K. W. Marlow, and M. E. Toms, "Capabilities for Nonnuclear Applications with Nuclear Facilities at NRL," NRL Report 6599, 17 October 1967.
2. I. Manning and D. Padgett, "Transport Theory of Penetration by Heavy Ions," NRL Memorandum Report 2631, August 1973.
3. I. Manning and G. P. Mueller, "Depth Distribution of Energy Deposition in Ion Bombardment," *Comp. Phys. Comm.* **7**, 85 (1974).
4. G. P. Mueller, "Total Cross-Section Corresponding to the Differential Cross-Section of Lindhard, Nielsen and Scharff," *Radiat. Eff.* **21**, 253 (1974).
5. J. W. Butler, "Ion Implantation and Tribology," *Proceedings of ONR-NRL Tribology Workshop*, Washington, DC, 14-16 October 1975.
6. H. W. Kugel, L. Eytel, G. K. Hubler, and D. E. Murnick, "The Temperature Dependence of Hyperfine Fields at Rare Earth Nuclei in Iron and Nickel," *Phys. Rev. B* **13**, 3697 (1976).
7. J. W. Butler, "Ion Implantation and Wear," *Reports, Memoranda and Technical Notes of the Materials Research Council Summer Conference*, La Jolla, CA (University of Michigan Document 005020, 1976) p. 255.
8. Irwin Manning, Mervine Rosen, and J. E. Westmoreland, "Adaptation of a Program for Depth Distribution of Energy Deposition by Ion Bombardment: Calculation of Ion Lateral Ranges," *Comp. Phys. Comm.* **12**, 335 (1976).
9. I. Manning, M. Rosen, and J. E. Westmoreland, "Computer Code for the Calculation of Lateral Range of a PKA," NRL Memorandum Report 3358, September 1976.
10. J. M. Poate, J. A. Borders, A. G. Cullis, and J. K. Hirvonen, "Ion Implantation as an Ultrafast Quenching Technique for Metastable Alloy Production: The Ag-Cu System," *Appl. Phys. Letters* **30**, 365 (1977).
11. G. P. Mueller and Mervine Rosen, "A Boltzmann Transport Code for Ion Penetration in Matter," NRL Memorandum Report 3556, July 1977.
12. J. K. Hirvonen, "Spinodal Decomposition in Amorphous Au-Implanted Pt," *Appl. Phys. Letters* **32**, 25 (1978).
13. A. G. Cullis, J. A. Borders, J. K. Hirvonen, and J. M. Poate, "Metastable Alloy Layers Produced by Implantation of Ag<sup>+</sup> and Ta<sup>+</sup> Ions into Cu Crystals," *Phil. Mag.* **B32**, 615 (1978).
14. J. K. Hirvonen, "Ion Implantation in Tribology and Corrosion Science," *J. Vac. Sci. Technol.* **15**, 1662 (1978).
15. Wen-Wei Hu, C. R. Clayton, H. Herman, and J. K. Hirvonen, "Fatigue-Life Enhancement by Ion Implantation," *Ser. Met.* **12**, 697 (1978).

16. E. McCafferty and G. K. Hubler, "Electrochemical Behavior of Palladium-Implanted Titanium," *J. Electrochem. Soc.* **125**, 1892 (1978).
17. J. W. Butler, "Some Effects of Ion Implantation on Fluid-Solid Surface Interactions," Proceedings of the Fourth Symposium on Fluid-Solid Surface Interactions, sponsored by the U.S. Department of the Navy and the West Germany Federal Ministry of Defense, 18-20 October 1978, National Bureau of Standards, Gaithersburg, MD, p. 267.
18. J. K. Hirvonen, C. A. Carosella, R. A. Kant, I. L. Singer, R. Vardiman, and B. B. Rath, "Improvement of Metal Properties by Ion Implantation," *Thin Solid Films* **63**, 5 (1979).
19. G. K. Hubler, P. R. Malmberg, and T. P. Smith, III, "Refractive Index Profiles and Range Distributions of Silicon Implanted with High-Energy Nitrogen," *J. Appl. Phys.* **50**, 7147 (1979).
20. G. K. Hubler, C. N. Waddell, W. G. Spitzer, J. E. Fredrickson, S. Prussin, and R. G. Wilson, "High-Fluence Implantations of Silicon: Layer Thickness and Refractive Indices," *J. Appl. Phys.* **50**, 3294 (1979).
21. R. A. Kant, J. K. Hirvonen, A. R. Knudson, J. S. Wollam, "Surface Hardening of Beryllium by Ion Implantation," *Thin Solid Films* **63**, 27 (1979).
22. W. G. Spitzer, J. S. Ko, C. N. Waddell, G. K. Hubler, and J. E. Fredrickson, "Plasma Region in High-Fluence Implants of Phosphorus in Amorphized Silicon," *J. Appl. Phys.* **50**, 3775 (1979).
23. Y. F. Wang, C. R. Clayton, G. K. Hubler, W. H. Lucke, and J. K. Hirvonen, "Applications of Ion Implantation for the Improvement of Localized Corrosion Resistance of M50 Bearing Steel," *Thin Solid Films* **63**, 11 (1979).
24. J. K. Hirvonen, "Implantation Into Metals - Mechanical Property Changes," Proceedings of the 1st Conference on Ion Beam Modification of Materials, eds., J. Gyulai, T. Lohner, and E. Pasztor, Central Research Institute for Physics, H-1525, Budapest 114 POB 49, Hungary, Vol. III, p. 1753 (1979).
25. J. K. Hirvonen and J. W. Butler, "Improved Corrosion and Mechanical Behavior of Alloys by Ion Implantation," 1978 Science and Engineering Symposium Proceedings (Joint Air Force and Navy), Vol. IV (Basic Research), Navy Material Command and Air Force Systems Command, p. 981 (1979).
26. J. K. Hirvonen, J. W. Butler, T. P. Smith, III, R. A. Kant, and V. C. Westcott, "Sliding-Wear Reduction by Ion Implantation," Proceedings of the 1st Conference on Ion Beam Modification of Materials, eds., J. Gyulai, T. Lohner, and E. Pasztor, Central Research Institute for Physics, H-1525, Budapest 114, POB 49, Hungary, Vol. III, p. 1973 (1979).
27. J. K. Hirvonen, J. M. Poate, Z. L. Liau, and J. W. Mayer, "Sputtering Limitations for High-Dose Implantations," Proceedings of the 1st Conference on Ion Beam Modification of Materials, eds., J. Gyulai, T. Lohner, and E. Pasztor, Central Research Institute for Physics, H-1525, Budapest 114, POB 49, Hungary, Vol. III, p. 1519 (1979).

28. G. K. Hubler, P. R. Malmberg, C. A. Carosella, T. P. Smith, III, W. G. Spitzer, C. N. Waddell, and C. N. Phillippi, "Optical Effects Resulting from Deep Implants of Silicon with Nitrogen and Phosphorus," Proceedings of the 1st Conference on Ion Beam Modification of Materials, eds., J. Gyulai, T. Lohner, and E. Pasztor, Central Research Institute for Physics, H-1525, Budapest 114, POB 49, Hungary, Vol. II, p. 1323 (1979).
29. W. W. Hu, C. R. Clayton, H. Herman, J. K. Hirvonen, and R. A. Kant, "Fatigue-Life Enhancement of Steel by Nitrogen Implantation," Proceedings of the 1st Conference on Ion Beam Modification of Materials, eds., J. Gyulai, T. Lohner, and E. Pasztor, Central Research Institute for Physics, H-1525, Budapest 114, POB 49, Hungary, Vol. III, p. 1977 (1979).
30. D. J. Land, D. G. Simons, J. G. Brennan, M. D. Brown, and J. K. Hirvonen, "Range Distribution for 25-100 keV  $^{14}\text{N}^+$  Ions," Proceedings of the 1st Conference on Ion Beam Modification of Materials, eds., J. Gyulai, T. Lohner, and E. Pasztor, Central Research Institute for Physics, H-1525, Budapest 114, POB 49, Hungary, Vol. I, p. 93 (1979).
31. E. McCafferty, G. K. Hubler, and J. K. Hirvonen, "Corrosion Control by Ion-Implantation," Proceedings of the 1978 Tri-Service Conference on Corrosion, ed. by M. Levy and J. Brown, Materials and Ceramics Information Center, Battelle, OH, p. 435, May 1979.
32. R. G. Vardiman, R. A. Kant, and T. W. Crooker, "The Effect of Ion Implantation on Fatigue Behavior of Ti/6Al/4V Alloy," Report of NRL Progress, p. 4, May 1979.
33. I. Manning, "Use of Range Distributions to Approximate Energy Distributions," F. A. Smidt and L. A. Beach, Coordinators, Cooperative Radiation Effects Simulation Program (Annual Progress Report) NRL Memorandum Report 4080 (October 1979), p. 2.
34. I. Manning, "Approximation for Energy Deposition in Ion Beam Bombardment," F. A. Smidt and L. A. Beach, Coordinators, Cooperative Radiation Effects Simulation Program (Annual Progress Report) NRL Memorandum Report 4080 (October 1979), p. 8.
35. M. Zamanzadeh, A. Allan, H. W. Pickering, and G. K. Hubler, "Effect of Helium-, Iron-, and Platinum-Ion Implantation on Permeation of Hydrogen Through Ion Membranes," ONR Technical Report No. 10 (Contract No. N00-14-75-C-0264), July 1979.
36. G. K. Hubler and E. McCafferty, "The Corrosion Behaviour and Rutherford Backscattering Analysis of Palladium-Implanted Titanium," Corros. Sci. 20, 103 (1980).
37. R. N. Bolster and I. L. Singer, "Surface Hardness and Abrasive Wear Resistance of Nitrogen-Implanted Steels," Appl. Phys. Letters 36, 208 (1980).
38. I. L. Singer and J. S. Murday, "The Chemical State of Ion-Implanted Nitrogen in Fe<sub>18</sub>Cr<sub>8</sub>Ni Steel," J. Vac. Sci. Technol. 16, 330 (1980).
39. G. P. Mueller, "New Analytical Calculation of Displacement Damage," Nucl. Instr. and Methods 170, 389 (1980).

40. G. P. Mueller, "Differential Cross Section and Related Integrals for the Moliere Potential," *Radiat. Eff. Letters* **50**, 87 (1980).
41. W. N. Allen, P. Brant, C. A. Carosella, J. J. DeCorpo, C. T. Ewing, F. E. Saalfeld, and D. C. Weber, "Ion Implantation Studies of  $(\text{SN})_x$  and  $(\text{CH})_x$ ," *Synthetic Metals* **1**, 151 (1979/80).
42. L. Buene, J. M. Poate, D. C. Jacobson, C. W. Draper, and J. K. Hirvonen, "Laser Irradiation of Nickel Single Crystals," *Appl. Phys. Lett.* **37**, 385 (1980).
43. J. K. Hirvonen, J. M. Poate, A. Greenwald, R. Little, "Pulsed Electron Beam Irradiation of Ion Implanted Copper Single Crystals," *Appl. Phys. Lett.* **36**, 564 (1980).
44. G. K. Hubler, P. R. Malmberg, C. A. Carosella, T. P. Smith, III, W. G. Spitzer, C. N. Waddell, and C. N. Phillippi, "Optical Effects Resulting from Deep Implants of Silicon with Nitrogen and Phosphorus," *Radiat. Eff.* **48**, 81 (1980).
45. G. K. Hubler and E. McCafferty, "The Corrosion Behavior and Rutherford Backscattering Analysis of Pd-Implanted Titanium," *Corrosion Science* **20**, 103 (1980).
46. M. Zamanzadeh, A. Allam, H. W. Pickering, and G. K. Hubler, "Effect of Helium, Iron, and Platinum Implantation on the Absorption of Hydrogen by Iron," *J. Electrochem. Soc.* **127**, 1688 (1980).
47. C. A. Carosella, I. L. Singer, R. C. Bowers, and C. R. Gossett, "Friction and Wear Reduction of Bearing Steel via Ion Implantation," *Ion Implantation Metallurgy*, eds. C. M. Preece and J. K. Hirvonen, (The Metallurgical Society of AIME, 1980), p. 103.
48. C. R. Clayton, K. G. K. Doss, H. Herman, S. Prasad, Y-F. Wang, J. K. Hirvonen, and G. K. Hubler, "Modification of the Corrosion Behavior of 304 Stainless Steel by Phosphorus Implantation," *Ion Implantation Metallurgy*, eds. C. M. Preece and J. K. Hirvonen, (The Metallurgical Society of AIME, 1980), p. 65.
49. J. K. Hirvonen, "Introduction," *Ion Implantation*, Treatise on Materials Science and Technology **18**, 1-16, Academic Press (1980).
50. J. K. Hirvonen, ed., *Ion Implantation*, Treatise on Materials Science and Technology **18**, Academic Press (1980).
51. J. W. Mayer, S. S. Lau, B-Y Tsaur, J. M. Poate, and J. K. Hirvonen, "High-Dose Implantation and Ion-Beam-Mixing," *Ion Implantation Metallurgy*, eds., C. M. Preece and J. K. Hirvonen, (The Metallurgical Society of AIME, 1980), p.37.
52. W. W. Hu, H. Herman, C. R. Clayton, J. Kozubowski, R. A. Kant, J. K. Hirvonen, and R. K. MacCrone, "Surface-Related Mechanical Properties of Nitrogen-Implanted 1018 Steel," *Ion Implantation Metallurgy*, eds. C. M. Preece and J. K. Hirvonen, (The Metallurgical Society of AIME 1980), p.92.
53. C. M. Preece and J. K. Hirvonen, Editors, *Ion Implantation Metallurgy*, (The Metallurgical Society of the AIME, 1980).

54. I. L. Singer, R. N. Bolster, and C. A. Carosella, "Abrasive Wear Resistance of Ti and N Implanted 52100 Steel Surfaces," Thin Solid Films 73,p.283(1980).
55. G. K. Hubler, J. K. Hirvonen, I. L. Singer, R. C. Bowers, C. R. Gossett, M. R. Weller, C. R. Clayton, and Y. A. Wang, " Application of Ion Implantation for the Improvement of Localized Corrosion Resistance of M50 Steel Bearings," NRL Memorandum Report 4481, Mar 1980.
56. I. L. Singer, J. S. Murday, H. Ravner, J. K. Hirvonen, and N. L. Jarvis, "New Opportunities in Tribology," Naval Research Reviews 32,p.4(1980).
57. I. L. Singer and R. N. Bolster, "Surface Hardness and Abrasive Wear Resistance of Nitrogen-Implanted Steels," Ion Implantation Metallurgy, eds. C. M. Preece and J. K. Hirvonen, The Metallurgical Society of AIME, p.116,(1980).
58. J. H. Harding and R. H. Bassel, "A Theoretical Study of the Defect Structure of Praseodymium Chromite," TP.862, Theoretical Physics Division, AERE Harwell, Oxfordshire, United Kingdom, July 1980.
59. F. A. Smidt, "The Use of Ion Implantation for Materials Processing," Semi-annual Progress Report for Period 1 Oct. 1979 - 31 Mar. 1980, NRL Memorandum Report 4341, Oct. 6, 1980.
60. L. Buene, D. C. Jacobson, S. Nakahara, J. M. Poate, C. W. Draper, and J. K. Hirvonen, "Laser Irradiation of Ni: Defect Structures and Surface Alloying," pp. 583-590 in Laser and Electron-Beam Interactions and Materials Processing, eds. Gibbons, Hess, Sigmon, Elsevier North Holland, Inc., 1981.
61. G. K. Hubler, "Use of Ion Beam Analysis in Metal Modification By Means of Ion Implantation," Nucl. Instrum. Methods 191,p.101(1981).
62. F. A. Smidt, "The Use of Ion Implantation for Materials Processing," Semi-annual Progress Report for the Period 1 Apr. 1980 - 30 Sept. 1980, NRL Memorandum Report 4527, June 24, 1981.
63. F. A. Smidt, J. K. Hirvonen, and S. Ramalingam, "Preliminary Evaluation of Ion Implantation as a Surface Treatment to Reduce Wear of Tool Bits," NRL Memorandum Report 4616, Naval Research Laboratory, 25 Sep 1981.
64. M. Rosen and G. P. Mueller, "Calculation of Self Sputtering of High Energy Copper Ions," 1981 NRL Review. pp.152-154.
65. I. L. Singer, C. A. Carosella, and J. R. Reed, "Friction Behavior of 52100 Steel Modified by Ion Implanted Ti," Nuclear Instruments and Methods 182/183, pp.923-932(1981).
66. I. L. Singer, "Surface Morphologies Produced by Ion Milling on Ion-Implanted 18Cr8Ni Steels," J. Vac. Sci. Technol. 18 (2), p.175(1981).
67. R. N. Bolster and I. L. Singer, "Surface Hardness and Abrasive Wear Resistance of Ion-Implanted Steels," ASLE Trans. 24, p.526(1981).

68. R. G. Allas, A. R. Knudson, J. M. Lambert, P. A. Treado, and G. W. Reynolds, "Self-Ion Sputtering Yields for Copper, Nickel, and Aluminum," Nucl. Instrum. Methods 194, p.615(1982).
69. P. Trzaskoma, E. McCafferty, G. K. Hubler, and I. L. Singer, "Electrochemical Behavior of an Amorphous Fe-Ti-C Surface in Titanium-Implanted Steel," Ion Implantation Into Metals, eds., V. Ashworth, W. A. Grant, and R. P. M. Proctor, Pergamon Press, NY, pp.24-34,(1982).
70. R. G. Vardiman, D. Creighton, G. Saliver, A. Effatian, and B. B. Rath, "The Effect of Ion Implantation on Fretting Fatigue in Ti-6Al-4V," in STP 780 Symposium on Materials Evaluation Under Fretting Conditions, Ed. S. R. Brown, American Soc. for Testing and Materials, Philadelphia, Pa., p.138,(1982).
71. J. E. Fredrickson, C. N. Waddell, W. G. Spitzer, and G. K. Hubler, "Effects of Thermal Annealing on the Refractive Index of Amorphous Silicon Produced by Ion Implantation," Appl. Phys. Lett. 40,172,(1982).
72. G. K. Hubler, P. R. Malmberg, C. N. Waddell, W. G. Spitzer, and J. E. Fredrickson, "Electrical and Structural Characterization of Implantation Doped Silicon by Infrared Reflection," Radiat. Eff. 60,35,(1982).
73. R. G. Vardiman, R. N. Bolster, and I. L. Singer, "The Effect of Nitrogen Implantation on Martensite in 304 Stainless Steel," in Metastable Materials Formation by Ion Implantation, Eds. S. T. Picraux and W. J. Choyke, Elsevier Science Publishing Co., NY, p.269,(1982).
74. R. G. Vardiman and R. A. Kant, "The Improvement of Fatigue Life in Ti-6Al-4V by Ion Implantation," J. Appl. Physics 53,pp.690-694,(1982).
75. C. N. Waddell, W. G. Spitzer, G. K. Hubler, and J. E. Fredrickson, "Infrared Studies of Isothermal Annealing of Ion-Implanted Silicon: Refractive Indices, Regrowth Rates, and Carrier Profiles," J. Appl. Phys. 53, pp.5851-5862,(1982).
76. C. R. Clayton, K. G. K. Doss, Y-F Wang, J. B. Warren, and G. K. Hubler, "RHEED, AES, and XPS Studies of the Passive Films Formed on Ion-Implanted Stainless Steel," Ion Implantation into Metals, eds., V. Ashworth, W. A. Grant, and R. P. M. Proctor, Pergamon Press, NY, pp.67-76,(1982).
77. C. R. Gossett, "Near Surface Analysis with Energetic Ion Beams," in ACS Symposium Series, No. 199, Industrial Applications of Surface Analysis, eds. L. A. Casper and C. J. Powell, American Chemical Society, Washington, DC, pp.49-68,(1982).
78. K. S. Grabowski and L. E. Rehn, "Ion Implantation Effects on the Thermal Oxidation of Metals," in Corrosion of Metals Processed by Directed Energy Beams, eds. C. R. Clayton and C. M. Preece, The Metallurgical Society of AIME, p.23,(1982).

79. G. K. Hubler, "DOD Applications of Implantation-Modified Materials," in Metastable Materials Formation by Ion Implantation, eds., S. T. Picraux and W. J. Choyke, Elsevier Science Publishing Co., NY, pp.341-354,(1982).
80. F. A. Smidt, "The Use of Ion Implantation for Materials Processing," Annual Progress Report for the Period 1 Oct. 1980 - 30 Sept. 1981, NRL Memorandum Report 4821, 2 July 1982.
81. R. A. Kant, A. R. Knudson, and K. Kumar, "Mechanical and Microstructural Properties of Boron Implanted Beryllium," in Metastable Materials Formation by Ion Implantation, eds., S. T. Picraux and W. J. Choyke, Elsevier Science Publishing Co., NY, pp.253-259,(1982).
82. E. McCafferty, P. G. Moore, J. D. Ayers, and G. K. Hubler, "Effect of Laser Processing and Ion Implantation on Aqueous Corrosion Behavior," in Corrosion of Metals Processed by Directed Energy Beams, eds., C. R. Clayton and C. M. Preece, AIME, pp.1-21,(1982).
83. G. W. Reynolds, F. R. Vozzo, R. G. Allas, A. R. Knudson, and J. M. Lambert, "The Surface Behavior of a Binary Alloy by Ion Implantation," in Metastable Materials Formation by Ion Implantation, eds., S. T. Picraux and W. J. Choyke, Elsevier Science Publishing Co., NY, pp.51-57,(1982).
84. W. K. Chan, C. R. Clayton, R. G. Allas, C. R. Gossett, and J. K. Hirvonen, "Electrochemical and A. E. S. Studies of Fe-Cr Surface Alloys Formed on AISI 52100 Steel by Ion Beam Mixing," Nucl. Instr. Methods 209-210, pp.857-865,(1983).
85. E. N. Kaufmann, R. G. Musket, J. J. Truhan, K. S. Grabowski, C. R. Gossett, and I. L. Singer, "High-Temperature Oxidation of Ion-Implanted Tantalum," Nucl. Instr. Methods, 209/210, pp.953-961,(1982).
86. M. Rosen, G. P. Mueller and W. A. Fraser, "Computer Study of Self Sputtering of Cu and Ni at 90 KeV," Nucl. Inst. Methods, 209/210, p.63,(1983).
87. K. S. Grabowski and R. A. Kant, "Methods to Control Target Heating During Ion Implantation," Ion Implantation: Equipment and Techniques, eds. H. Ryssel and H. Glawischnig, Springer Series in Electrophysics Vol. XI, Springer-Verlag, New York, p. 364,(1983).
88. D. Popgoshev, R. Valori, and G. K. Hubler, "Ion Implantation of Bearing Surfaces for Corrosion Resistance," ASME, J. Lub. Technology 105, pp.534-541,(1983).
89. J. M. Lambert, P. A. Treado, D. Trbojevic, R. G. Allas, A. R. Knudson, G. W. Reynolds, and F. R. Vozzo, "Sputtering Analysis with PIXE," IEEE Trans. Nucl. Sci. NS-30, pp.1285-1290,(1983).
90. G. W. Reynolds, R. G. Allas, J. M. Lambert, and P. A. Treado, "Sputtering from Binary Alloys - A Technique for Evaluating Change in Surface Binding Energy," IEEE Trans. Nucl. Sci. NS-30, pp.1285-1290,(1983).

91. N. E. W. Hartley and J. K. Hirvonen, "Wear Testing Under High Load Conditions," Nucl. Instr. Methods 209/210, pp.933-940,(1983).
92. W. G. Spitzer, G. K. Hubler, and T. A. Kennedy, "Properties of Amorphous Silicon Produced by Ion Implantation: Thermal Annealing," Nucl. Instr. Methods 209/210, p.309,(1983).
93. C. R. Clayton, Y-F Wang, and G. K. Hubler, "An Electrochemical Study of Amorphous Ion Implanted Stainless Steels," Passivity of Metals and Semiconductors ed. by M. Froment, Elsevier, Science Publishers, Amsterdam, Netherlands, pp.305-310,(1983).
94. R. G. Vardiman and I. L. Singer, "Transformation of Stress-Induced Martensite in 304 Stainless Steel by Ion Implantation," Materials Letters 2, pp.150-154,(1983).
95. J. K. Hirvonen and C. R. Clayton, "Materials Modification by Ion Implantation" Ch. 12 in Surface Modification and Alloying ed. by J. M. Poate, G. Foti and D. C. Jacobson, Plenum Press, N.Y., pp.323-384,(1983).
96. I. L. Singer and R. A. Jeffries, "Surface Chemistry and Friction Behavior of Ti-implanted 52100 Steel," J. Vac. Sci. Technol. A1, p.317-321,(1983).
97. I. L. Singer, "Carburization of Steel Surfaces During Implantation of Ti Ions At High Fluences," J. Vac. Sci. Technol. A1, p.419-422,(1983).
98. I. L. Singer and T. M. Barlak, "Absorption of Carbon from Residual Gases During Ti-Implantation of Alloys," Appl. Phys. Letts. 43, pp.457-459,(1983).
99. I. L. Singer, Discussion of "Tribological Properties of Ion-Implanted 52100 Steel," by T. E. Fischer, et al. ASLE Trans. 26, pp.473-474,(1983).
100. I. L. Singer and R. A. Jeffries, "Effects of Implantation Energy and Carbon Concentration on the Friction and Wear of Titanium-Implanted Steel," Appl. Phys. Letts. 43, pp.925-927,(1983).
101. S. A. Dillich and I. L. Singer, "Effect of Ti-Implantation on the Friction and Surface Chemistry of A Co-Cr-W-C Alloy," Thin Solid Films 108, pp.219-227,(1983).
102. B. D. Sartwell, G. K. Hubler and E. McCafferty, "High Dose Ion Implantation and the Corrosion Behavior of Ferrous Metals", Proceedings of the Workshop on Ion Mixing, Sandia Report SAND 83-1230, pp.136-149,(1983).
103. K. S. Grabowski, R. J. Colton, W. K. Chan and C. R. Clayton, "Ion Mixing of Cr Layers on Steel: Effect of Impurities During Ion Mixing," Proc. Workshop on Ion Mixing and Surface Layer Alloying, SAND 83-1230, p. 117,(1983).
104. N. C. Koon, P. Pehrsson, D. Weber and A. I. Schindler, "Magnetic Properties of Iron-Implanted Graphite," J. Appl. Phys. 55, pp.2497-2499,(1984).

105. F. A. Smidt., "The Use of Ion Implantation for Materials Processing Annual Progress Report for the Period 1 Oct. 1981-30 Sept. 1982," NRL Memorandum Report 5177, Sept. 28, 1983.
106. R. N. Bolster and I. L. Singer, "Polishing Wear Studies of Coating Materials," Material Failure Prevention Group Symposium, N.B.S., Gaithersburg, MD, May 1983.
107. S. A. Dillich, R. N. Bolster and I. L. Singer, "Effects of Ion-Implantation on the Tribological Behavior of a Cobalt-Based Alloy," NATO-ASI Surface Engineering Conference, Les Arcs, France, 3 July 1983.
108. R. H. Bassel, K. S. Grabowski, M. Rosen, M.L. Roush and F. Davarya, "Carburization During Cr Self Implantation in a  $^{13}\text{CO}$  Atmosphere," Int. Conf. Atomic Collisions in Solids, Bad Iburg, F.R. Germany, July 18-22, 1983.
109. P. R. Malmberg, R. G. Allas, J. M. Lambert, P. A. Treado, and G. W. Reynolds, "Effects of Non-Normal Incidence on the Implantation of Copper with Gold and Tantalum," 10th International Conference on Atomic Collisions in Solids, Bad Iburg, F.R. Germany, July 18-22, 1983.
110. G. W. Reynolds, F. R. Vozzo, R. G. Allas, P. A. Treado and J. M. Lambert, "A Model of the Surface Binding Energy For A Ternary Alloy Produced by Ion Implantation," 10th International Conference on Atomic Collisions in Solids, Bad Iburg, F.R. Germany, July 18-22, 1983.
111. M. Rosen and R. H. Bassel, "Binary Collision Cascade Calculation of Sputtering from Cu-Ni Alloys by 90 keV Cu and Ni Ions", 10th International Conference on Atomic Collisions in Solids, Bad Iburg, F.R. Germany, July 18-22, 1983.
112. G. R. Johnston, P. L. Mart, J. L. Cocking, J. A. Sprague and K. S. Grabowski, "The High-Temperature Oxidation of Nickel and Magnesium-Ion Implanted Nickel and X-Nickel-Silicon Alloys," Electrochem. Soc. Meeting, Oct. 9-14, 1983, Washington, D.C.
113. C. R. Clayton, Y-F Wang, G. K. Hubler, "Modification of Passivity of 316 S.S. by Boron and Phosphorus Implantation," Electrochemical Society Symposium "Fundamental Aspects of Corrosion Protection by Surface Modification," Washington, D.C., Oct. 1983.
114. C. R. Clayton, W. K. Chan, J. K. Hirvonen, G. K. Hubler and J. R. Reed, "Modification of the Localized Corrosion Behavior of AISI 52100 Steel by Ion Implantation," Electrochemical Society Symposium "Fundamental Aspects of Corrosion Protection by Surface Modification," Washington, D.C., Oct. 1983.
115. C. N. Waddell, W. G. Spitzer, J. E. Fredrickson, G. K. Hubler and T. A. Kennedy, "Amorphous Silicon Produced by Ion-Implantation: Effects of Ion Mass and Thermal Annealing", J. Appl. Phys. in press.
116. I. Manning, "Migration Currents and Implant Densities in Steady-State Ion Implantation," J. Appl. Phys., to be published.

117. G. K. Hubler, C. N. Waddell, W. G. Spitzer, T. P. Smith and J. E. Frederickson, "Physical Properties of Two Metastable States of Amorphous Silicon," Ion Implantation and Ion Beam Processing of Materials, eds. G. K. Hubler, O. W. Holland, C. R. Clayton and C. W. White, in press.
118. I. Manning, "Boltzmann Approach to Cascade Mixing," Ion Implantation and Ion Beam Processing of Materials, eds. G. K. Hubler, O. W. Holland, C. R. Clayton and C. W. White, in press.
119. N. C. Koon, D. C. Weber, P. E. Pehrsson, and A. I. Schindler, "Magnetic Properties of Ion Implanted Materials," Ion Implantation and Ion Beam Processing of Materials, eds. G. K. Hubler, O. W. Holland, C. R. Clayton and C. W. White, in press.
120. R. A. Kant and B. D. Sartwell, "Surface Modification by Ion Beam Enhanced Deposition," Ion Implantation and Ion Beam Processing of Materials, eds. G. K. Hubler, O. W. Holland, C. R. Clayton and C. W. White, in press.
121. D. Farkas, M. Rangaswamy and I. L. Singer, "Computer Modeling of High Fluence Ti Implantation and Vacuum Carburization in Steel," Ion Implantation and Ion Beam Processing of Materials, eds. G. K. Hubler, O. W. Holland, C. R. Clayton and C. W. White, in press.
122. K. S. Grabowski, N. E. W. Hartley, C. R. Gossett and I. Manning, "Retention of Ions Implanted At Non-Normal Incidence," Ion Implantation and Ion Beam Processing of Materials, eds. G. K. Hubler, O. W. Holland, C. R. Clayton and C. W. White, in press.
123. I. L. Singer and R. A. Jeffries, "Processing Steels for Tribological Applications by Titanium Implantation," Ion Implantation and Ion Beam Processing of Materials, eds. G. K. Hubler, O. W. Holland, C. R. Clayton and C. W. White, in press.
124. R. G. Vardiman, "Wear Improvement in Ti-6Al-4V by Ion Implantation," Ion Implantation and Ion Beam Processing of Materials, eds. G. K. Hubler, O. W. Holland, C. R. Clayton and C. W. White, in press.
125. K. Kumar, H. Newborn and R. A. Kant, "Wear Behavior of Flat and Graded Profile Boron Implanted Beryllium," Ion Implantation and Ion Beam Processing of Materials, eds. G. K. Hubler, O. W. Holland, C. R. Clayton and C. W. White, in press.
126. S. Dillich, R. N. Bolster, and I. L. Singer, "Friction and Wear Behavior of Hardface Materials Implanted with Ti or N," Ion Implantation and Ion Beam Processing of Materials, eds. G. K. Hubler, O. W. Holland, C. R. Clayton and C. W. White, in press.
127. I. L. Singer, "Tribomechanical Properties of Ion Implanted Alloys: Approaches, Present Knowledge and Future Directions," Ion Implantation and Ion Beam Processing of Materials, eds. G. K. Hubler, O. W. Holland, C. R. Clayton and C. W. White, in press.

128. W. C. Oliver, R. Hutchings, J. B. Pethica, I. L. Singer and G. K. Hubler, "Hardness as a Measure of Wear Resistance," Ion Implantation and Ion Beam Processing of Materials, eds. G. K. Hubler, O. W. Holland, C. R. Clayton and C. W. White, in press.
129. I. L. Singer and R. A. Jeffries, "Friction, Wear and Deformation of Soft Steels Implanted with Ti and N," Ion Implantation and Ion Beam Processing of Materials, eds. G. K. Hubler, O. W. Holland, C. R. Clayton and C. W. White, in press.
130. K. S. Grabowski and C. R. Gossett, "Effect of Cr<sup>+</sup> Implantation on the Thermal Oxidation of Ta," Ion Implantation and Ion Beam Processing of Materials, eds. G. K. Hubler, O. W. Holland, C. R. Clayton and C. W. White, in press.

**DATE**  
**FILME**